Doctoral Disseration

Syntheses of Chiral Polymers and Direct Observation of Single-Polymer-Chains Dynamics

Ryoga Hori

Supervisor: Ken-ichi Shinohara

Graduate School of Advanced Science and Technology

Japan Advanced Institute of Science and Technology

Materials Science

March 2025

Abstract

The functions of biomolecules have been significantly elucidated by single-molecule imaging and measurement techniques. Recently, it has been recognized that the structure of individual polymer chains strongly influences their physical properties, even in synthetic polymers, making single-molecule imaging an area of great interest. Conventional spectroscopic methods and microscopy could only provide static information, but the development of fast-scanning atomic force microscopy (FS-AFM) has allowed the simultaneous observation of function and structure. This advance has rapidly revealed polymer structures and dynamics that were previously inaccessible, establishing FS-AFM as a highly effective tool in the analysis of synthetic polymers. However, the number of studies using FS-AFM remains limited.

If molecular motors driven by thermal fluctuations that perform mechanical work could be realized, they could find applications in artificial muscles and molecular transport systems. In addition, because these systems are driven by thermal fluctuations, they have great potential as a powerful means to address energy-related challenges. In biological systems, molecular motor systems driven by thermal fluctuations, such as actomyosin and microtubule-kinesin, have been realized. In synthetic molecules, molecular machines such as rotaxanes and light-driven molecular rotors have been developed, but none has demonstrated practical functionality comparable to that of biomolecular motors.

This study aims to elucidate the dynamics of single synthetic polymer chains using FS-AFM and to develop synthetic polymer motors. In addition, to further understand the functions of synthetic polymers, force measurements of interaction between synthetic polymer chains were performed using an optical trapping system. Overviews of each chapter are as follows:

Chapter 1: This chapter explains the general background of the study and provides an overview of the apparatus.

Chapter 2: A chiral helical poly(phenylacetylene) with amide groups and bulky cholesteryl groups as pendant was synthesized, and FS-AFM imaging was performed. Although the structure was expected to form a rigid structure, dynamic analysis revealed that the molecule exhibited flexible micro-Brownian motion.

Chapter 3: Structural analysis of poly(pseudo-rotaxane) composed of high molecular weight poly(ethylene glycol) (PEG) and α-cyclodextrin (α-CD), which has been difficult to analyze in solution using conventional methods, was performed at the solid-liquid interface. Dynamic analysis revealed structural changes involving the shuttling of α-CD. Furthermore, these structural changes were simulated by MD calculations.

Chapter 4: A chiral helical poly(phenylacetylene) with cholesteryl groups as pendants was synthesized and FS-AFM imaging was performed. Observations revealed molecular motor functionality, with long-range translational motion driven by thermal fluctuations in an organic solvent at room temperature. This discovery suggests the potential for creating synthetic polymer molecular motors comparable to biomolecular motors.

Chapter 5: Two types of porphyrin-based supramolecular polymers with cholesteryl groups as pendants and coordinated with either Cu or Zn were synthesized, and microscopic imaging was performed. Both supramolecular polymers exhibited multiple types of higher-order structures, leading to the proposal of a stepwise growth process based on their structural features. Furthermore, FS-AFM imaging revealed intermolecular interactions between polymer chains, which are thought to be the origin of the molecular motor functionality.

Chapter 6: Molecular motor functionality induced by electrostatic interactions between the cationic polymer and the anionic polymer was observed using FS-AFM. In addition, the unidirectional motion of composite molecular chains formed by the interaction of these polymers was confirmed. Furthermore, an optical trapping system was used to demonstrate that these phenomena involve mechanical work.

Chapter 7: This chapter provides a general discussion of the overall study and explains how the newly discovered phenomena relate to societal issues and challenges in polymer field.

Keywords: Single-Molecule Imaging, Polymer Molecular Motor, Polymer Dynamics, Chiral Polymer, Supramolecular Polymer

Table of Contents

Chapter 1. General Introduction

1.1 Chiral Helical Polymer

1.1.1 Chirality

Since Pasteur's discovery of the chirality of tartaric acid, the properties of chirality have been studied extensively by many researchers.[1,2] The amino acids that make up proteins also exhibit chirality, making this field extremely important, as properties such as taste, smell, and pharmacological efficacy are greatly influenced by chirality.[3–5]

Chirality manifests in various structural forms. Tartaric acid, discovered by Pasteur, exhibits the simplest form of chirality, known as point chirality (**Fig. 1.1A**), with two chiral centers. The presence of a chiral center is not essential for chirality to occur. Compounds like allenes and bis(diphenylphosphino)-1,1'-binaphthyl (BINAP) exhibit a type of chirality known as axial chirality, despite lacking a chiral center (**Fig. 1.1B**).[6] Additionally, cyclophanes, such as those with benzene rings substituted with specific groups, display planar chirality even without a chiral center (**Fig. 1.1C**).[7] In recent years, the topological chirality observed in interlocked compounds, such as rotaxanes composed of two achiral components, has also been recognized as a valuable chiral source (**Fig. 1.1D**).[8]

Another type of chirality, known as "helicity," occurs without any chiral points, axes, or planes (**Fig. 1.1E**). For example, helicenes lack chiral points, axes, and planes, yet they possess right-handed and left-handed enantiomers. Due to its relatively large spatial structure compared to other forms of chirality, helicity generally exhibits strong optical activity. Moreover, this spatially extensive chirality is valuable for enantioselective recognition and as a chiral environment.

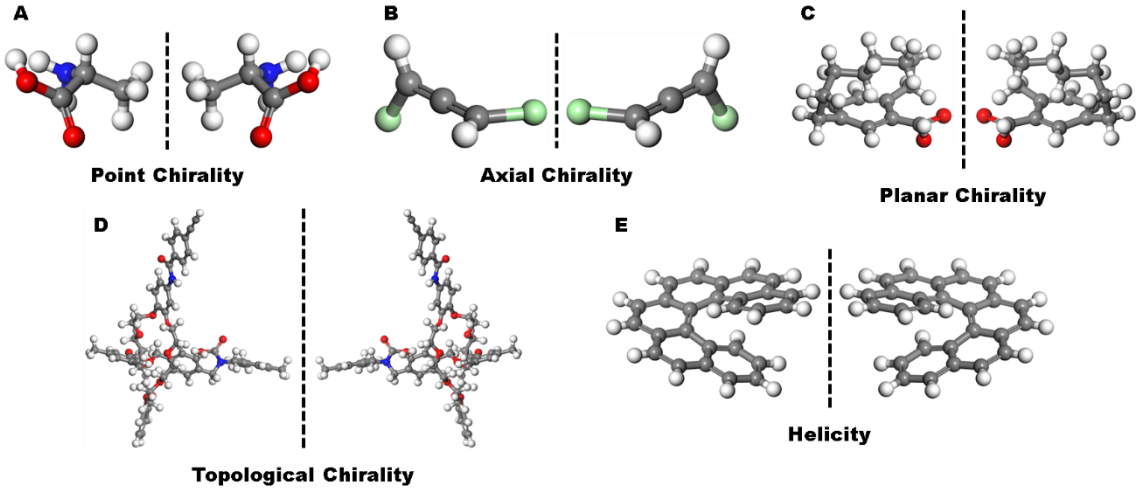

Fig. 1.1 The types of Chirality. (A) Alanine exhibiting point chirality, (B) 1,3-dichloroallene exhibiting axial chirality, (C) 10-carboxy-[8]paracyclophane exhibiting planar chirality, (D) rotaxane exhibiting topological chirality composed of two achiral compounds, and (E) helicene exhibiting helicity.

1.1.2 Synthetic Chiral Helical Polymer

Around the same time as the discovery of the α-helix structure in the natural polymer protein[9] and the double helix in DNA,[10] Natta discovered the helical structure formation in the synthetic polymer isotactic poly(propylene).[11] Since then, various synthetic helical polymers have been developed, focusing on inducing helical structures and stabilizing them.[12,13]

There are three primary methods for synthesizing helical polymers. The first method involves the use of chiral monomers (**Fig. 1.2A**), which was the approach employed for many early chiral helical polymers. The second method utilizes chiral molecules in the polymerization initiator or solvent (**Fig. 1.2B**). Okamoto and colleagues achieved the synthesis of a one-handed helical polymer by polymerizing an achiral methyl methacrylate with bulky substituents (triphenylmethyl groups) using an initiator containing a chiral ligand.[14] The third method induces helical structures through non-covalent interactions (**Fig. 1.2C**). Okamoto's team also demonstrated that adding chiral amines to a

solution of poly[(4-carboxyphenyl)acetylene], which typically forms a random coil, induces a one-handed helical structure in the polymer chain.[15] The helical structure formed by this method is a dynamic helical polymer in which the direction of the helix can be controlled by the added chiral agent. Generally, bulky substituents and a rigid backbone are required to stabilize the helical structure in such polymers regardless of the method used.

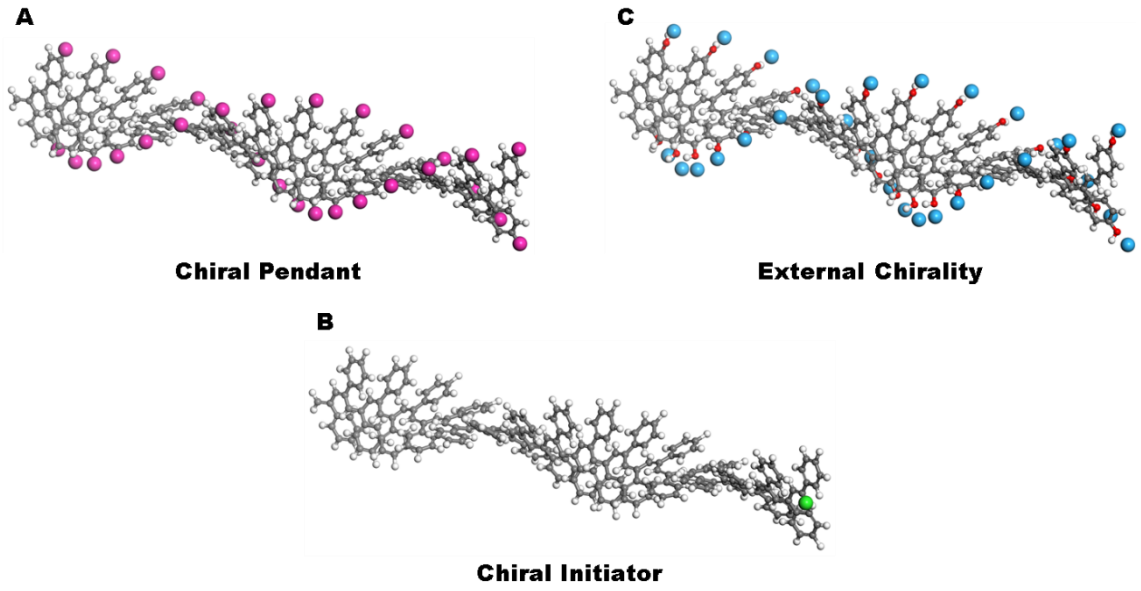

Fig. 1.2 The types of induction of single-helical structures. (A) Induction by a chiral pendant. (B) induction by a chiral initiator. (C) induction by an external chiral factor.

Poly(phenyl acetylene) derivatives possess the rigidity in the main chain and the bulky side chains necessary for helix formation. Aoki and colleagues achieved the first synthesis of a one-handed helical poly(phenyl acetylene) through the polymerization of phenyl acetylene bearing a menthyl group as pendant moiety.[16] The chiral, bulky monomers they developed induced helical structures even in copolymerization with achiral phenyl acetylene monomers. Furthermore, because these derivatives are soluble in various organic solvents, they overcome the molding limitations typically associated with traditional polyacetylene. Given that polyacetylene, as the repeating unit, is a type of conductive polymer, applications in electronic devices are anticipated.[17] Consequently, interest is directed not only

at the synthesis method but also at the polymer's structural characteristics. Shinohara and colleagues successfully analyzed the single-molecule structure of poly(phenyl acetylene) with menthoxycarbonylamino groups as pendants using scanning tunneling microscopy (STM).[18,19] They observed that the polymer forms a right-handed double-helical structure. Additionally, they imaged the same polymer using fast-scanning atomic force microscopy (FS-AFM) and elucidated the dynamics of the photodecomposition reaction.[20]

1.2 Supramolecule

1.2.1 Host–Guest Chemistry

In 1967, Pedersen reported the synthesis of crown ethers, which are cyclic polyethers, and their ability to include metal ions (**Fig. 1.3A**).[21] Crown ethers are large cyclic ethers that contain multiple oxygen atoms, allowing them to form coordinate bonds with cations. Due to the size of the ring, they exhibit high selectivity for specific metal ions, attracting attention for this property. This led to various applications, including cryptands with high inclusion ability and selectivity developed by Lehn (**Fig. 1.3B**),[22] and inclusion compounds with chiral recognition capabilities created by Cram.[23] Inclusion is driven not only by coordinate bonds but also by various non-covalent interactions, leading to extensive research on diverse host–guest molecules. For example, compounds known as cyclodextrins are molecules where α-glucose units are cyclically connected by 1,4-glycosidic bonds. These molecules have hydrophilic groups on the outer surface and hydrophobic groups on the interior, enabling them to include hydrophobic components within their cavities through hydrophobic interactions (**Fig. 1.3C**). Such including molecules are referred to as host molecules, while the included molecules are called guest molecules. The chemistry related to molecular recognition between hosts and guests is known as host–guest chemistry. Additionally, molecules assembled through non-covalent interactions are termed supramolecules.

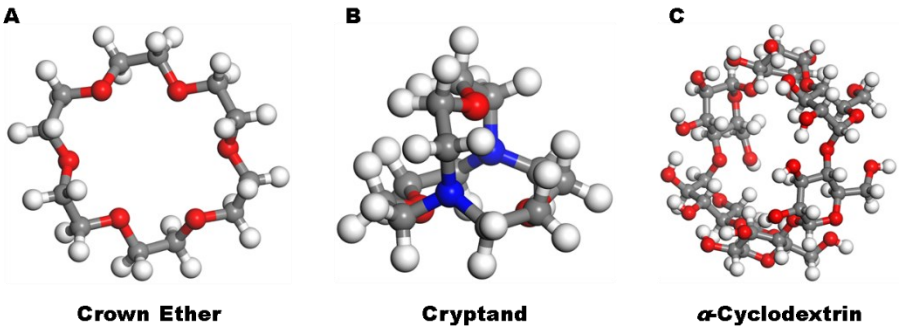

Fig. 1.3 A host molecule with inclusion ability. (A) Crown ether, (B) cryptand, and (C) *α*-cyclodextrin

1.2.2 Polyrotaxane

In 1981, Ogino reported a high-yield synthesis method for rotaxanes based on the concept of host–guest chemistry. In this method, cyclic host molecules incorporate guest molecules as axial components, and bulky substituents are introduced at both ends of the axial components to prevent the cyclic components from excluding.[24] Rotaxanes lack covalent bonds between the cyclic and axial components, allowing the cyclic components to move along the axial components. This movement can be driven and controlled by various external stimuli such as pH changes, light irradiation, and polarity changes, making them promising for applications in molecular switches and artificial muscles.

In recent years, research on polyrrotaxanes where multiple cyclic molecules include a polymer used as the axial component has been actively conducted due to their ability to exhibit high-performance functions not found in conventional polymer materials. Polyrrotaxanes display dynamic properties absent in traditional polymer materials because the cyclic components can freely slide. Among these, rotaxanes utilizing polyethylene glycol as the axial component and *α*-cyclodextrin as the cyclic component are frequently used, as they can be easily prepared by simply allowing them to stand in aqueous solution (**Fig. 1.4**).

Fig. 1.4 The model of polypseudorotaxane consisting of poly(ethylene glycol) and α-cyclodextrin.

For example, the slide-ring gel formed by two axial components penetrating an 8-shaped cyclic component, reported by Ito et al., differs from physical gels formed solely by the entanglement of polymer chains or chemical gels with crosslinking points introduced by covalent bonds. [25] In this slide-ring gel, the cyclic components serving as crosslinking points can move freely. Additionally, the ends of the axial components are blocked by bulky substituents, preventing the crosslinking points from excluding from the axial components. This specificity imparts high swelling capacity and high elongation properties.

Furthermore, Harada et al. developed self-healing polymer materials by leveraging the dynamic properties of polyrrotaxanes.[26] The gel composed of polyrrotaxanes with hydroxyl groups on the cyclic components and polyolefins with benzene boronic acid as pendant forms a chemical gel through dynamic covalent bonds between the cyclic components and polyolefins. Even when the gel is cut, the high mobility of the cyclic components allows the dynamic covalent bonds between the cyclic components and polyolefins to rapidly reform. This results in a self-healing function that is far more efficient than that of conventional polymer materials.

1.2.3 Supramolecular Polymer

In recent years, the development of supramolecular polymers, which apply the concept of supramolecular chemistry to polymer synthesis, has been actively pursued. Typically, a "polymer"

refers to a molecule composed of long chains connected by covalent bonds, formed by polymerizing small repeating units using catalysts. In contrast, supramolecular polymers do not contain covalent bonds between monomers but are linked through reversible non-covalent interactions (**Fig. 1.5**). This reversible linkage not only enables the expression of high-performance functions, such as self-healing capabilities,[27] but also offers advantages over conventional polymer materials in terms of ease of handling and high reusability.

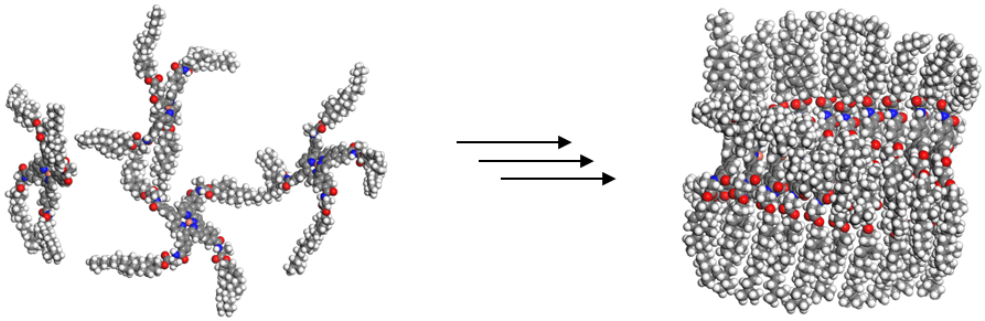

Fig. 1.5 Schematic diagram of supramolecular polymer formation.

In 1988, Aida et al. developed porphyrin derivatives that spontaneously assemble and arrange in a one-dimensional fashion in aqueous solutions.[28] Porphyrins are known to exhibit strong π–π interactions due to their extensive conjugated planes. By arranging multiple porphyrin units cofacially through π–π interactions, they formed supramolecular polymers.

In 1997, Meijer et al. developed telechelic monomers that form robust linkages through cooperative hydrogen bonding and reported the physical properties of the resulting supramolecular polymers.[29] These supramolecular polymers are formed by one-dimensional linkage through complementary hydrogen bonds between ureidopyrimidinone units located at both ends of each monomer. They exhibit viscoelastic properties similar to those of conventional polymers and demonstrate behavior akin to thermoplastics due to the temperature-dependent changes in their self-assembled states. This indicates that supramolecular polymers can exhibit the excellent functions unique to supramolecular systems while also displaying material properties comparable to traditional polymer materials,

allowing them to be used in the same manner as conventional materials.

1.3 *Single-Molecular Measurement*

1.3.1 *Atomic Force Microscopy*

Because the shape of polymer chains is closely related to the physical properties of polymer materials, the structural analysis of single polymer chains has attracted attention, and atomic force microscopy (AFM) is an effective method for analyzing single-chain structures. AFM scans the surface of a sample with a probe attached to the end of a cantilever and detects surface irregularities through the deflection of the cantilever (**Fig. 1.6**).[30] Due to the characteristics of the device, it can observe a wide range of subjects, including metals, organic materials, and biomacromolecules, without regard to the conductivity of the target and without requiring specific observation environments.

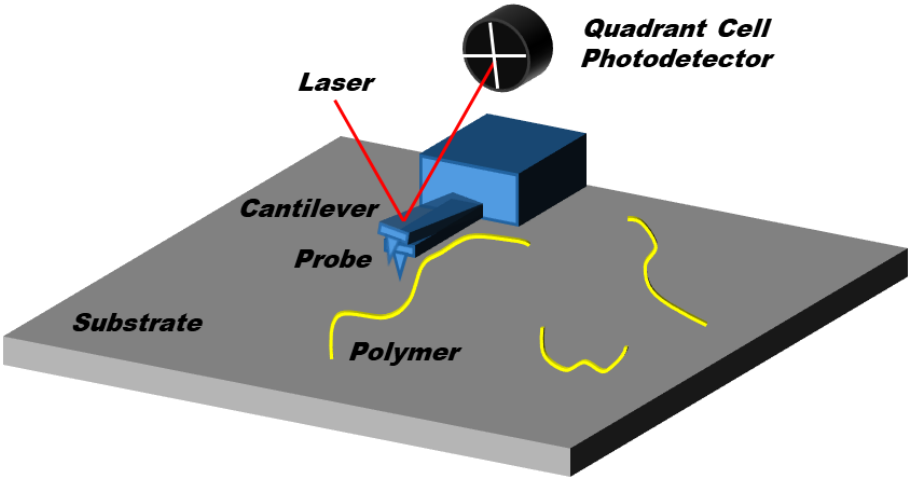

Fig. 1.6 The principle of atomic force microscopy.

Single-molecule analysis of synthetic polymers was achieved by Kumaki et al. in 1996.[31] They cast a polystyrene–poly(methyl methacrylate) block copolymer onto a mica substrate, allowed it to stand under humidity-controlled conditions, and then observed it in air. As a result of the observation, they confirmed a condensed polystyrene (PS) core and extended poly(methyl methacrylate) (PMMA)

blocks, successfully measuring the length of the PMMA chains.

In recent years, the observation of helical structures and higher-order structures formed by polymer chains has been accomplished, making it indispensable for the structural analysis of synthetic polymers. Additionally, AFM is frequently used for the structural analysis of not only polymers but also supramolecular polymers. In 2018, Meijer et al. synthesized a porphyrin-based supramolecular polymer that forms a one-handed helical structure in methylcyclohexane and analyzed its structure using AFM.[32] The analysis results revealed a one-handed helical structure formed by an individual supramolecular polymer chain. Furthermore, a superhelical structure, where a single supramolecular polymer chain forms higher-order helices, was also confirmed, and measurements of the size and pitch of the periodic structure were achieved.

1.3.2 Imaging of Polymer Dynamics using Fast-Scanning AFM

Conventional AFM takes several minutes to obtain a single image, limiting the obtained information to static structures and making it impossible to observe molecular movements. To address this, fast-scanning AFM (FS-AFM) was developed, featuring microcantilevers with low spring constants and high resonance frequencies in liquid, as well as devices with increased response speeds.[33,34] FS-AFM can acquire dozens of images per second, allowing the visualization of molecular movements as videos.

Originally developed for imaging proteins, FS-AFM was utilized by Shinohara et al. to perform video imaging and dynamic analysis of synthetic polymers in aqueous solutions.[35] They synthesized Poly[9,10-anthracenediyl-ethynylene-1,4-phenylene-ethynylene-rotaxa-(α-CD)], which has a phenylene ethynyl backbone included by α-CD.[36] The synthesized polymer formed long supramolecular polymers through interactions between the anthracene end groups of the chains. Observations using FS-AFM revealed flexible movements driven by thermal fluctuations. Additionally, when the probe was pressed firmly, the polymer chains were severed, strongly supporting that the supramolecular polymers are linked by non-covalent interactions. Detailed motion analysis

and fitting of the mean squared displacement plots indicated that the flexible movements of the polymer chains follow Einstein's Brownian motion. The ability to observe the Brownian motion of single molecules suggests that FS-AFM is an excellent analytical method for creating molecular devices driven by thermal fluctuation.

Furthermore, They elucidated the long-chain branching structure of low-density polyethylene (LDPE) using FS-AFM, which is optimized for observing single polymer chains in organic solvents.[37] LDPE has a branched structure, and its physical properties significantly change depending on this structure;[38,39] however, this structure had remained unclear until then. They spin-cast a polymer's toluene solution onto a mica substrate and performed observations in decamethyltetrasiloxane (DMTS). As a result, they successfully imaged the branching structure and measured the positions, lengths, and intervals between branches of each side chain. Additionally, They used FS-AFM to elucidate the molecular structure and dynamics of modified styrene-butadiene rubber (SBR) chains for high-performance tires at the nanoscale.[40]

1.3.3 Force Measurement using Optical Trapping System

One of the devices that has significantly advanced the elucidation of biological molecule functions is the optical trapping system.[41–43] The optical trapping system measures the displacement that occurs when interactions are activated between substrates by bringing microbeads, which have substrates attached and are trapped by an infrared laser, into proximity with a glass substrate that has a different substrate attached (**Fig. 1.7**). By modifying both the beads and the substrates with fluorescent labels, these interactions can be imaged using a fluorescence microscope. Since the trapped beads behave like springs, the work can be calculated using the following equation.

$$E = \frac{1}{2}kx^2\ [pN \cdot nm] = \frac{kx^2}{2 \times 4.1}\ [k_BT]$$

Here, k is the trap stiffness and x is the displacement.

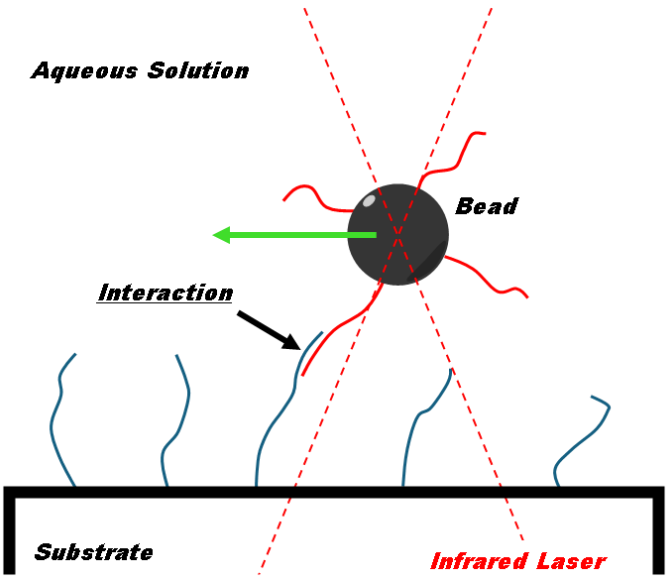

Fig. 1.7 The principle of optical trapping system.

To date, force measurements have been successfully conducted on several types of proteins; however, there have been no reports of mechanical measurements on synthetic molecules. This lack of achievement is primarily due to several factors: the characteristics of the device cause molecules with small molecular weights to become obscured by the irregularities of the microbeads, making them unusable; the sample preparation method is optimized for measurements in aqueous solutions, thereby limiting the types of molecules that can be used; and the difficulty in fluorescent labeling prevents the imaging of interactions.

1.4 Molecular Machine

1.4.1 Biomolecular Machine

Within living organisms, there exist proteins such as actomyosin[42,44] and microtubule–kinesin,[43] which perform dynamic movements using adenosine triphosphate (ATP). These proteins possess highly sophisticated mechanical movements and functions, and are referred to as "molecular motors"

(**Fig. 1.8**).

Fig. 1.8 The walking mechanism of molecular motors.

The movements of motor proteins have been elucidated by observing fluorophores attached to individual molecules using single-molecule fluorescence microscopy.[45] On the other hand, the structures of proteins have been studied using X-ray crystallography and NMR; however, these analytical methods only provide static information.[46–48] Ando et al. achieved the simultaneous observation of the structure and dynamics of myosin V using FS-AFM.[44] Myosin V is a two-headed motor protein that was suggested to move along actin filaments in a two-legged walking manner,[49,50] but until then, there had been no direct observations of its movement. The structure of myosin observed by Ando was in good agreement with that observed using electron microscopy,[51] and the walking of myosin along actin filaments in 36 nm steps was confirmed.

In addition to their movements, the functions of motor proteins have also been elucidated. Hirokawa et al. performed force measurements of the movement of kinesin KIF1A, a single-headed motor protein, using an optical trapping system.[43] KIF1A was attached to microbeads, which were optically trapped using an infrared laser, and the displacement of the beads resulting from interactions with microtubules attached to a substrate was measured. The measurements revealed that KIF1A exhibits minimal movement when dissociating from microtubules accompanied by ATP hydrolysis. Subsequently, KIF1A undergoes one-dimensional diffusion along the microtubule and exhibits directional movement upon releasing ADP and binding to the microtubule.

1.4.2 Synthetic Molecular Machine

In recent years, the development of synthetic molecular machines that perform controlled movements using synthetic molecules, mimicking biological molecules, has been actively pursued. Biomolecular motors are composed of proteins and thus can only be driven under highly restricted environments, such as aqueous solutions containing ATP at appropriate temperatures. In contrast, synthetic molecular machines have the advantage of being able to operate under various environments by modifying substituents.

Stoddart et al. developed molecular shuttles utilizing rotaxanes with axle components bearing multiple substituents that allow the cyclic component to halt on the axial component.[52–54] Rotaxanes based on the molecular recognition between dialkylammonium salts and crown ethers can shuttle the cyclic component through deprotonation/protonation of the ammonium groups, making them commonly used for creating pH-responsive rotaxanes (**Fig. 1.9A**). The molecular elevator developed by Stoddart et al. is an end-capped rotaxane where three benzocrown ethers connected in a triangular manner are threaded through three axial components bearing diammine and bipyridinium units.[55] By deprotonating the ammonium groups on the axial component using a base, the cyclic component is driven to move to the bipyridinium unit through host–guest interactions. Reprotonation with acid then prompts the cyclic component to revert to the ammonium unit. Thermodynamic analysis estimated that this movement generates a force of up to 200 pN. In addition to rotaxanes, which exhibit shuttling motions, synthetic molecular machines that perform rotational motions also exist. Feringa et al. developed a rotary molecular machine (**Fig. 1.9B**) that rotates unidirectionally through photoisomerization of double bonds and precise steric hindrance control induced by temperature changes.[56] This molecular machine can perform continuous unidirectional rotation when irradiated with light of appropriate wavelengths and maintained at suitable temperatures. Furthermore, they discovered that molecular machines with similar structures are effective in inducing helices in cholesteric liquid crystals.[57] When the molecular machines are rotated, the texture oriented in one

direction also rotates, and this rotation can be utilized to rotate micron-sized fine glass pieces placed on a liquid crystal film.

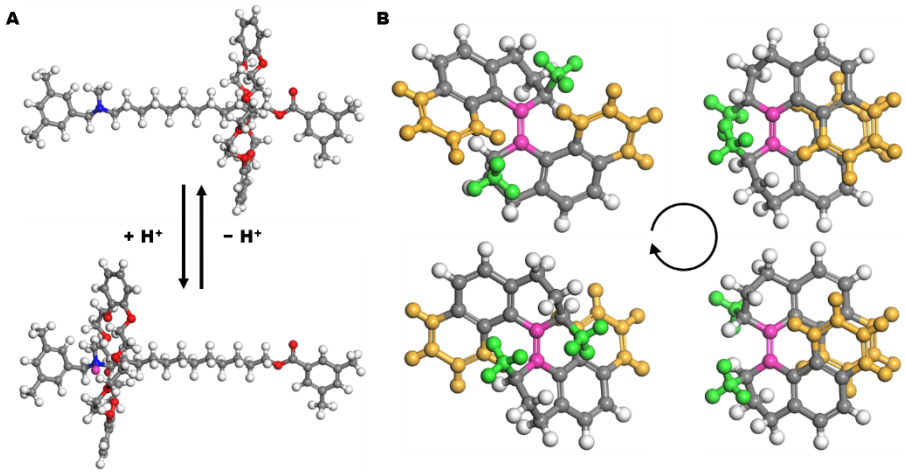

Fig. 1.9 The model of synthesized molecular motor. (A) Acid-base driven rotaxane, and (B) light-driven monodirectional molecular rotor

1.5 Purpose of This Research

The purpose of this study was to analyze the dynamics of single polymer molecules, which had not been elucidated previously, and to discover new functionalities. FS-AFM not only enables the elucidation of polymer chain structures that were previously unobservable but also allows for the direct observation of their movements, thereby serving as a novel method for evaluating material properties.[40] Among commonly used polymer materials, such as LDPE, some are utilized without a clear understanding of their detailed structures. The application of FS-AFM to polymer imaging is expected to provide a new approach to resolving these issues. Therefore, in this study, we conducted FS-AFM imaging and dynamic analysis on ionic polymers (**Chapter 6**), two types of chiral helical polymers (**Chapter 2** and **Chapter 4**), poly pseudo-rotaxanes (**Chapter 3**), and porphyrin-based supramolecular polymers (**Chapter 5**).

Synthetic molecular machines have yet to develop practical functionalities, and the utilization of polymers is essential to achieve dynamic movements similar to those of biomolecular motors.

Consequently, in this study, we used synthetic polymers that exhibit strong non-covalent interactions between polymer chains to observe (**Chapter 4**, **Chapter 5** and **Chapter 6**) and perform force measurements (**Chapter 6**) of molecular motor functions. As outlined in **Chapter 1.4.1**, the elucidation of the functions of biological molecular machines has advanced significantly through direct observation and force measurements. In this study, imaging polymer motors using FS-AFM is expected to lay the foundation for understanding polymer motor functionalities. Additionally, this study represents the first attempt to perform force measurements at the single-molecule level of synthetic polymers using an optical trapping system. Demonstrating that commonly used polymers, previously considered mere structural entities, can generate energy constitutes a novel advancement and lays the groundwork for the development of new molecular systems.

1.6 Reference

1 V. Prelog, Chirality in Chemistry. *Science* **1976**, *193* (4247), 17–24. https://www.science.org/doi/10.1126/science.935852

2 L. Pasteur, Recherches sur les relations qui peuvent exister entre la forme cristalline, la composition chimique et les sens de la polarisation rotatoire. *Ann. Chim. Phys.* **1848**, 3 (24), 442–460.

3 M. Kawai, Y. Sekine-Hayakawa, A. Okiyama, Y. Ninomiya, Gustatory sensation of L- and D-amino acids in humans. *Amino Acids* **2012**, *43* (6), 2349–2358. https://doi.org/10.1007/s00726-012-1315-x

4 R. Bentley, The Nose as a Stereochemist. Enantiomers and Odor. *Chem. Rev.* **2006**, *106* (9), 4099–4112. https://doi.org/10.1021/cr050049t

5 B. Kasprzyk-Hordern, Pharmacologically Active Compounds in the Environment and Their Chirality. *Chem. Soc. Rev.* **2010**, *39* (11), 4466–4503. https://doi.org/10.1039/C000408C

6 J. Ye, S. Ma, Conquering Three-Carbon Axial Chirality of Allenes. *Org. Chem. Front.* **2014**, *1* (10), 1210–1224. https://doi.org/10.1039/C4QO00208C

7 K. Kanda, K. Endo, T. Shibata, Enantioselective Synthesis of Planar-Chiral 1,*n*-Dioxa[*n*]paracyclophanes via Catalytic Asymmetric *ortho*-Lithiation. *Org. Lett.* **2010**, *12* (9), 1980–1983. https://doi.org/10.1021/ol100444u

8 F. Ishiwari, K. Nakazono, Y. Koyama, T. Takata, Induction of Single-Handed Helicity of Polyacetylenes Using Mechanically Chiral Rotaxanes as Chiral Sources. *Angew. Chem. Int. Ed.* **2017**, *56* (47), 14858–14862. https://doi.org/10.1002/anie.201707926

9 L. Pauling, R. B. Corey, H. R. Branson, The Structure of Proteins; Two Hydrogen-Bonded Helical Configurations of the Polypeptide Chain. *Proc. Natl. Acad. Sci. USA* **1951**, *37* (4), 205–211. https://doi.org/10.1073/pnas.37.4.205

10 J. D. Watson, F. H. C. Crick, Molecular Structure of Nucleic Acids: A Structure for Deoxyribose Nucleic Acid. *Nature* **1953**, *171* (4356), 737–738. https://doi.org/10.1038/171737a0

11 G. Natta, P. Pino, P. Corradini, F. Danusso, G. Moraglio, E. Mantica, G. Mazzanti, Crystalline High Polymers of α-Olefins. *J. Am. Chem. Soc.* **1955**, *77* (6), 1708–1710. https://doi.org/10.1021/ja01611a109

12 T. Nakano, Y. Okamoto, Synthetic Helical Polymers: Conformation and Function. *Chem. Rev.* **2001**, *101* (12), 4013–4038. https://doi.org/10.1021/cr0000978

13 E. Yashima, K. Maeda, H. Lida, Y. Furusho, K. Nagai, Helical Polymers: Synthesis, Structures, and Functions. *Chem. Rev.* **2009**, *109* (11), 6102–6211. https://doi.org/10.1021/cr900162q

14 Y. Okamoto, K. Suzuki, K. Ohta, K. Hatada, H. Yuki, Optically Active Poly (Triphenylmethyl Methacrylate) with One-Handed Helical Conformation. *J. Am. Chem. Soc.* **1979**, *101* (16), 4763–4765. https://doi.org/10.1021/ja00510a072

15 E. Yashima, T. Matsushima, Y. Okamoto, Poly((4-Carboxyphenyl)Acetylene) as a Probe for Chirality Assignment of Amines by Circular Dichroism. *J. Am. Chem. Soc.* **1995**, *117* (46), 11596–11597. https://doi.org/10.1021/ja00151a032

16 T. Aoki, M. Kokai, K. Shinohara, E. Oikawa, Chiral Helical Conformation of the Polyphenylacetylene Having Optically-Active Bulky Substituent. *Chem. Lett.* **1993**, *22* (12), 2009–2012. https://doi.org/10.1246/cl.1993.2009

17 H. Shirakawa, E. J. Louis, A. G. MacDiarmid, C. K. Chiang, A. J. Heeger, Synthesis of electrically conducting organic polymers: halogen derivatives of polyacetylene, $(CH)_x$. *J. Chem. Soc., Chem. Commun.* **1977**, *16*, 578–580. https://doi.org/10.1039/C39770000578

18 K. Shinohara, S. Yasuda, G. Kato, M. Fujita, H. Shigekawa, Direct Measurement of the Chiral Quaternary Structure in a π-Conjugated Polymer at Room Temperature. *J. Am. Chem. Soc.* **2001**, *123* (15), 3619–3620. https://doi.org/10.1021/ja003023m

19 K. Shinohara, T. Kitami, K. Nakamae, Direct Measurement of Structural Diversity in Single Molecules of a Chiral Helical π-Conjugated Polymer. *J. Polym. Sci. A Polym. Chem.* **2004**, *42* (16), 3930–3935. https://doi.org/10.1002/pola.20247

20 K. Shinohara, N. Kodera, T. Oohashi, Single-Molecule Imaging of Photodegradation Reaction in a Chiral Helical π-Conjugated Polymer Chain. *J. Polym. Sci. A Polym. Chem.* **2010**, *48* (18), 4103–4107. https://doi.org/10.1002/pola.24201

21 C. J. Pedersen, Cyclic Polyethers and Their Complexes with Metal Salts. *J. Am. Chem. Soc.* **1967**, *89* (26), 7017–7036. https://doi.org/10.1021/ja01002a035

22 J. M. Lehn, J. P. Sauvage, [2]-Cryptates: Stability and Selectivity of Alkali and Alkaline-Earth Macrobicyclic Complexes. *J. Am. Chem. Soc.* **1975**, *97* (23), 6700–6707. https://doi.org/10.1021/ja00856a018

23 E. B. Kyba, K. Koga, L. R. Sousa, M. G. Siegel, D. J. Cram, Chiral Recognition in Molecular Complexing. *J. Am. Chem. Soc.* **1973**, *95* (8), 2692–2693. https://doi.org/10.1021/ja00789a051

24 H. Ogino, Relatively High-Yield Syntheses of Rotaxanes. Syntheses and Properties of Compounds Consisting of Cyclodextrins Threaded by α, ω-Diaminoalkanes Coordinated to Cobalt(III) Complexes. *J. Am. Chem. Soc.* **1981**, *103* (5), 1303–1304. https://doi.org/10.1021/ja00395a091

25 O. Yasushi, K. Ito. The Polyrotaxane Gel: A Topological Gel by Figure-of-Eight Cross-links. *Adv. Mater.* **2001**, *13* (7), 485 - 487. https://doi.org/10.1002/1521-4095(200104)13:7<485::AID-ADMA485>3.0.CO;2-T

26 M. Nakahata, S. Mori, Y. Takashima, H. Yamaguchi, A. Harada, Self-Healing Materials Formed by Cross-Linked Polyrotaxanes with Reversible Bonds. *Chem* **2016**, *1* (5), 766–775. https://doi.org/10.1016/j.chempr.2016.09.013

27 F. Herbst, D. Döhler, P. Michael, W. H. Binder, Self-Healing Polymers via Supramolecular Forces. *Macromol. Rapid. Commun.* **2013**, *34* (3), 203–220. https://doi.org/10.1002/marc.201200675

28 T. Aida, A. Takemura, M. Fuse, S. Inoue, Synthesis of a Novel Amphiphilic Porphyrin Carrying Water-Soluble Polyether Side Chains of Controlled Chain Length. Formation of a Cofacial Molecular Assembly in Aqueous Media. *J. Chem. Soc., Chem. Commun.* **1988**, *5*, 391–393. https://doi.org/10.1039/C39880000391

29 R. P. Sijbesma, F. H. Beijer, L. Brunsveld, B. J. B. Folmer, J. H. K. K. Hirschberg, R. F. M. Lange, J. K. L. Lowe, E. W. Meijer, Reversible Polymers Formed from Self-Complementary Monomers Using Quadruple Hydrogen Bonding. *Science* **1997**, *278* (5343), 1601–1604. https://doi.org/10.1126/science.278.5343.1601

30 G. Binnig, C. F. Quate, C. Gerber, Atomic Force Microscope. *Phys. Rev. Lett.* **1986**, *56* (9), 930–933. https://doi.org/10.1103/PhysRevLett.56.930

31 J. Kumaki, Y. Nishikawa, T. Hashimoto, Visualization of Single-Chain Conformations of a Synthetic Polymer with Atomic Force Microscopy. *J. Am. Chem. Soc.* **1996**, *118* (13), 3321–3322. https://doi.org/10.1021/ja9538593

32 M. F. J. Mabesoone, A. J. Markvoort, M. Banno, T. Yamaguchi, F. Helmich, Y. Naito, E. Yashima, A. R. A. Palmans, E. W. Meijer, Competing Interactions in Hierarchical Porphyrin Self-Assembly Introduce Robustness in Pathway Complexity. *J. Am. Chem. Soc.* **2018**, *140* (25), 7810–7819. https://doi.org/10.1021/jacs.8b02388

33 T. Ando, N. Kodera, E. Takai, D. Maruyama, K. Saito, A. Toda, A High-Speed Atomic Force Microscope for Studying Biological Macromolecules. *Proc. Natl. Acad. Sci. USA* 2001, *98* (22), 12468–12472. https://doi.org/10.1073/pnas.211400898

34 T. Ando, T. Uchihashi, T. Fukuma, High-Speed Atomic Force Microscopy for Nano-Visualization of Dynamic Biomolecular Processes. *Prog. Surf. Sci.* **2008**, *83* (7–9), 337–437. https://doi.org/10.1016/j.progsurf.2008.09.001

35 K. Shinohara, N. Kodera, T. Ando, Single Molecular Imaging of a Micro-Brownian Motion and a Bond Scission of a Supramolecular Chiral π-Conjugated Polymer as a Molecular Bearing Driven by Thermal Fluctuations. *Chem. Lett.* **2007**, *36* (11), 1378–1379. https://doi.org/10.1246/cl.2007.1378

36 K. Shinohara, T. Suzuki, T. Kitami, S. Yamaguchi, Simultaneous Imaging of the Structure and Fluorescence of a Supramolecular Nanostructure Formed by the Coupling of π-Conjugated Polymer Chains in the Intermolecular Interaction. *J. Polym. Sci. A Polym. Chem.* **2006**, *44* (2), 801–809. https://doi.org/10.1002/pola.21175

37 K. Shinohara, M. Yanagisawa, Y. Makida, Direct Observation of Long-Chain Branches in a Low-Density Polyethylene. *Sci. Rep.* **2019**, *9* (1), 1–5. https://doi.org/10.1038/s41598-019-46035-9

38 C. Gabriel, H. Münstedt, Influence of Long-Chain Branches in Polyethylenes on Linear Viscoelastic Flow Properties in Shear. *Rheol. Acta* **2002**, *41* (3), 232–244. https://doi.org/10.1007/s00397-001-0219-6

39 F. J. Stadler, J. Kaschta, H. Münstedt, Thermorheological Behavior of Various Long-Chain Branched Polyethylenes. *Macromolecules* **2008**, *41* (4), 1328–1333. https://doi.org/10.1021/ma702367a

40 K. Shinohara, Y. Makida, Direct Observation of Dynamic Interaction between a Functional Group in a Single SBR Chain and an Inorganic Matter Surface. *Sci. Rep.* **2018**, *8* (1), 1–8. https://doi.org/10.1038/s41598-018-32382-6

41 M. Nishiyama, E. Muto, Y. Inoue, T. Yanagida, H. Higuchi, Substeps within the 8-Nm Step of the ATPase Cycle of Single Kinesin Molecules. *Nat. Cell Biol.* **2001**, *3* (4), 425–428. https://doi.org/10.1038/35070116

42 M. Kaya, H. Higuchi, Nonlinear Elasticity and an 8-Nm Working Stroke of Single Myosin Molecules in Myofilaments. *Science* **2010**, *329* (5992), 686–689. https://doi.org/10.1126/science.1191484

43 Y. Okada, H. Higuchi, N. Hirokawa, Processivity of the Single-Headed Kinesin KIF1A through Biased Binding to Tubulin. *Nature* **2003**, *424* (6948), 574–577. https://doi.org/10.1038/nature01804

44 N. Kodera, D. Yamamoto, R. Ishikawa, T. Ando, Video Imaging of Walking Myosin V by High-Speed Atomic Force Microscopy. *Nature* **2010**, *468* (7320), 72–76. https://doi.org/10.1038/nature09450

45 C. Joo, H. Balci, Y. Ishitsuka, C. Buranachai, T. Ha, Advances in Single-Molecule Fluorescence Methods for Molecular Biology. *Annu. Rev. Biochem.* **2008**, *77*, 51–76. https://doi.org/10.1146/annurev.biochem.77.070606.101543

46 I. Rayment, H. M. Holden, M. Whittaker, C. B. Yohn, M. Lorenz, K. C. Holmes, R. A. Milligan, Structure of the Actin-Myosin Complex and Its Implications for Muscle Contraction. *Science* **1993**, *261* (5117), 58–65. https://doi.org/10.1126/science.8316858

47 D. R. Knighton, J. Zheng, L. F. T. Eyck, N. H. Xuong, S. S. Taylor, J. M. Sowadski, Structure of

a Peptide Inhibitor Bound to the Catalytic Subunit of Cyclic Adenosine Monophosphate-Dependent Protein Kinase. *Science* **1991**, *253* (5018), 414–420. https://doi.org/10.1126/science.1862343

48 J. Reed, J. S. D. Ropp, J. Trewhella, D. B. Glass, W. K. Liddle, E. M. Bradbury, V. Kinzel, D. A. Walsh, Conformational analysis of PKI(5–22)amide, the active inhibitory fragment of the inhibitor protein of the cyclic AMP-dependent protein kinase. *Biochem J.* **1989**, *264* (2) 371–380. https://doi.org/10.1042/bj2640371

49 A. Yildiz, J. N. Forkey, S. A. McKinney, T. Ha, Y. E. Goldman, P. R. Selvin, Myosin V Walks Hand-over-Hand: Single Fluorophore Imaging with 1.5-Nm Localization. *Science* **2003**, *300* (5628), 2061–2065. https://doi.org/10.1126/science.10843

50 J. N. Forkey, M. E. Quinlan, M. A. Shaw, J. E. T. Corrie, Y. E. Goldman, Three-Dimensional Structural Dynamics of Myosin V by Single-Molecule Fluorescence Polarization. *Nature* **2003**, *422* (6930), 399–404. https://doi.org/10.1038/nature01529

51 M. L. Walker, S. A. Burgess, J. R. Sellers, F. Wang, J. A. Hammer, J. Trinick, P. J. Knight, Two-Headed Binding of a Processive Myosin to F-Actin. *Nature* **2000**, *405* (6788), 804–807. https://doi.org/10.1038/35015592

52 P. L. Anelli, N. Spencer, J. F. Stoddart, A Molecular Shuttle. *J. Am. Chem. Soc.* **1991**, *113* (13), 5131–5133. https://doi.org/10.1021/ja00013a096

53 R. A. Bissell, E. Córdova, A. E. Kaifer, J. F. Stoddart, A Chemically and Electrochemically Switchable Molecular Shuttle. *Nature* **1994**, *369* (6476), 133–137. https://doi.org/10.1038/369133a0

54 C. J. Bruns, J. F. Stoddart, Rotaxane-Based Molecular Muscles. *Acc. Chem. Res.* **2014**, *47* (7), 2186–2199. https://doi.org/10.1021/ar500138u

55 J. D.; Bacljić, V. Balzani, A. Credi, S. Silvi, J. F. Stoddart, A Molecular Elevator. *Science* **2004**, *303* (5665), https://doi.org/10.1126/science.1094791

56 N. Koumura, R. W. J. Zijistra, R. A. V. Delden, N. Harada, B. L. Feringa, Light-Driven Monodirectional Molecular Rotor. *Nature* **1999**, *401* (6749), 152–155. https://doi.org/10.1038/43646

57 R. Eelkema, M. M. Pollard, J. Vicario, N. Katsonis, B. S. Ramon, C. W. M. Bastiaansen, D. J. Broer, B. L. Feringa, Nanomotor Rotates Microscale Objects. *Nature* **2006**, *440* (7081), 163–163. https://doi.org/10.1038/440163a

Chapter 2. Synthesis and Direct Observation of a micro-Brownian Motion of a Chiral Helical Polymer Chain

2.1 Introduction

The direct observation of single molecule deepens the understanding of the structure and function of molecules.[1] In the field of biophysics, the understanding of the function of protein has progressed drastically from the study of single molecule imaging for biopolymers.[2-4] Inspired by such biological studies, the author has been studying the imaging of single polymer molecule using scanning probe microscopy[5,6], total reflection fluorescence microscopy[7-9] and so forth. The imaging of single polymer molecule for chiral substituted phenyl acetylene has already been studied by Aoki et al. as the first report[10] In the present study, the structural dynamics of single chiral helical polymer chain was clarified using the single molecule imaging method. Specifically, para-substituted phenyl acetylene polymer with cholesteryl group at the pendant [(+)-poly(ChOCAPA)] was synthesized. Then, the imaging for its single polymer chain was conducted using fast-scanning AFM (FS-AFM). The diffusion coefficients were determined by measuring the micro-Brownian motion based on the dynamic analysis. In addition, from the measurement of three-point angles for the three measuring points, the motility of each domain in the polymer chain was determined.

2.2 Experimental

2.2.1 Materials

(–)-Cholesterol, 4-bromobenzoic acid, 2-methyl-3-butyn-2-ol, copper(II) acetate, triphenylphosphine, tetrahydrofuran and triethylamine were purchased from Kanto Kagaku (Tokyo, Japan). Bis(triphenylphosphine)palladium(II) chloride, sodium hydride were from Wako Pure Industries (Osaka, Japan).Diphenylphosphoryl azide was from TCI (Tokyo, Japan). Bicyclo[2.2.1]hepta-2,5-diene-rhodium(I) chloride dimmer {$[Rh(nbd)Cl]_2$} was from Sigma-Aldrich (Missouri, USA).

2.2.2 Synthesis of (+)-Poly(ChOCAPA)

Method: (+)-Poly(ChOCAPA) was prepared following section, its weight average molecular mass (M_w) and molecular weight distribution (M_w/M_n) was determined by GPC (SEC) equipped with TSKgel GMH_{XL} column (Tosoh, Tokyo, Japan) in tetrahydrofuran with polystyrene standards calibration. ^1H NMR spectra were recorded on an AVANCE III 400 MHz (Bruker, MA, USA). Mass spectra were measured using surface-assisted laser desorption/ionization fourier transform ion cyclotron resonance mass spectrometry (SALDI-FT-ICR-MS) scimaX (Bruker, MA, USA). IR spectra were obtained using Perkin Elmer (MA, USA) Spectrum One FT-IR spectrometer. CD spectra were measured using a J-820 spectropolarimeter (Jasco, Tokyo, Japan). Concentration of polymer tetrahydrofuran solution is 1.0×10^{-4} mol/L and the concentration of (+)-poly(ChOCAPA) was calculated based on the monomer units.

(+)-Poly(ChOCAPA) was synthesized as follows (**Scheme 2.1**).

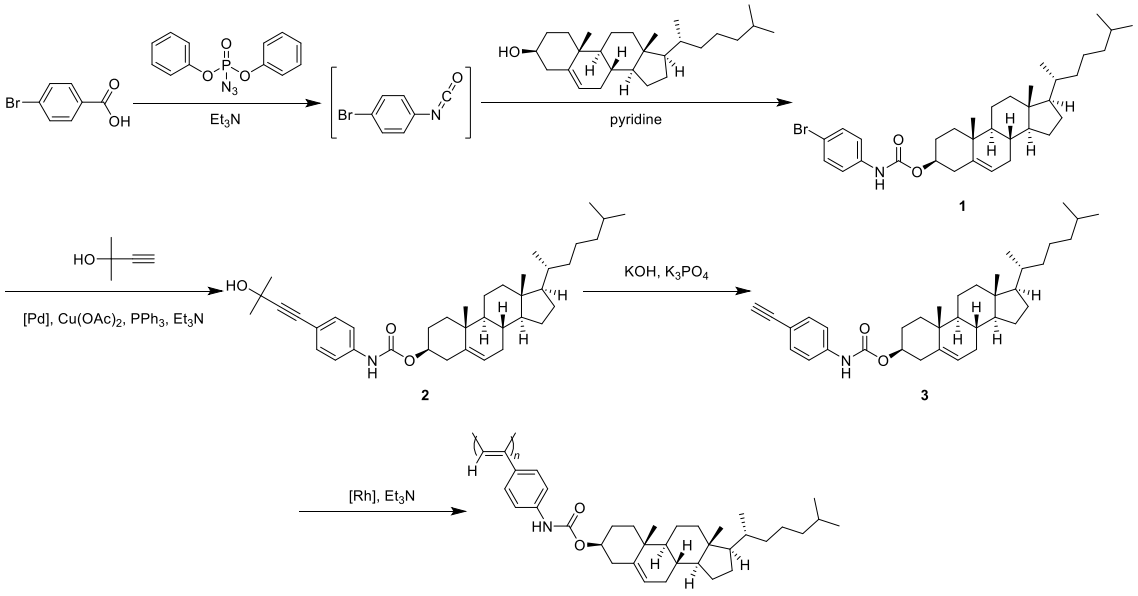

Scheme 2.1 Synthesis of (+)-Poly(ChOCAPA.

Synthesis of (–)-4-cholesteryloxycarbonylamino-1-bromobenzene (1)

A mixture of 4-bromobenzoic acid (1.04 g, 5.17 mmol), dry triethylamine (1.80 mL, 12.9 mmol), diphenylphosphoryl azide (DPPA) (1.66 ml, 7.72 mmol) and dry THF (10.0 mL) was refluxed for 4.5 h. After addition of pyridine (0.63 mL, 7.82 mmol) and (–)-cholesterol (1.00 g, 2.59 mmol) in dry THF (5.00 mL), the reaction mixture was further refluxed for 18 h and concentrated under reduced pressure. The residue was dissolved in dichloromethane and the solution was washed with 1 M aqueous HCl, saturated aqueous $NaHCO_3$, and brine. The organic layer was dried with Mg_2SO_4 and concentrated under reduced pressure. The residue was purified by reprecipitation from a dichloromethane solution into methanol. The product was a white solid. Yield: 69%; $[\alpha]_D^{20}$ = –20.8º (c 1.00, chloroform); ^{1}H NMR ($CDCl_3$, 400 MHz, TMS) δ 7.40 (d, *J* = 8.8 Hz, 2H, Ar-H ortho to NH), 7.28 (d, *J* = 8.8 Hz, 2H, Ar-H meta to NH), 6.53 (s, 1H, NH), 5.46–5.36 (m, 1H, =CH), 4.66–4.53 (m, 1H, OCH), 2.48–2.27 (m, 2H), 2.09–0.69 (m, 38H), 0.68 (s, 3H, CH_3); ^{13}C NMR ($CDCl_3$, 100 MHz, TMS) δ 152.8 (CO), 139.5 (C=), 137.2 (Ar-NH), 132.0 (Ar ortho to NH), 122.9 (=CH), 120.1 (Ar meta to NH), 115.7 (Ar para to NH), 75.2 (OCH), 56.7, 56.1, 50.0, 42.3, 39.7, 39.5, 38.4, 37.0, 36.6, 36.2, 35.8, 31.92, 31.87, 28.2, 28.1, 28.0, 24.3, 23.8, 22.8, 22.6, 21.1, 19.3, 18.7, 11.9**;** MS (SALDI-FT-ICR): m/z calcd. for $C_{34}H_{50}BrNO_2$ ($[M^+K]^+$) 624.264; found 624.265.

Synthesis of (–)-cholesteryloxy-*N*-[4-(3-hydroxy-3-methylbut-1-ynyl)phenyl]carboxamide (2)

(1) (1.01 g, 1.73 mmol) and 2-methyl-3-butyn-2-ol (335 μl, 3.45 mmol) were dissolved in dry triethylamine (10.0 mL). To this solution, dry THF (5.53 mL) solution of bis(triphenylphosphine)palladium(II) chloride (12.2 mg, 17.3 μmol), cuprous acetate (19.5 mg, 107 μmol), triphenylphosphine (32.3 mg, 123 μmol) was added. The solution was stirred for 21 h at the reflux temperature. The resulting salt was removed by filtration and the solvent of the filtrate was evaporated to yield a crude product, which was purified by silica-gel chromatography using ethyl acetate/*n*-hexane = 1/4 (*v*/*v*) and 1/1 (*v*/*v*), and **(2)** was obtained from the ethyl acetate/*n*-hexane = 1/1

(*v*/*v*) eluate. The product was white solid. Yield: 50%; $[\alpha]_D^{20} = -18.4^o$ (c 1.00, chloroform); ^{1}H NMR ($CDCl_3$, 400 MHz, TMS) δ 7.39–7.29 (m, 4H, Ar-H), 6.59 (s, 1H, NH), 5.46–5.35 (m, 1H, =CH), 4.68–4.53 (m, 1H, OCH), 2.48–2.27 (m, 2H), 2.08–0.80 (m, 45H), 0.68 (s, 3H, CH_3); ^{13}C NMR ($CDCl_3$, 100 MHz, TMS) δ 152.7 (CO), 139.5 (C=), 138.1 (Ar-NH), 132.5 (Ar ortho to NH), 122.9 (=CH), 118.0 (Ar meta to NH), 117.3 (Ar para to NH), 93.0 (acetylene), 81.9 (acetylene), 75.2 (OC), 65.7 (C-OH), 56.7, 56.1, 50.0, 42.3, 39.7, 39.5, 38.4, 37.0, 36.6, 36.2, 35.8, 31.92, 31.87, 31.5 (COH(CH_3)$_2$), 28.2, 28.1, 28.0, 24.3, 23.8, 22.8, 22.6, 21.1, 19.3, 18.7, 11.88; MS (SALDI-FT-ICR): m/z calcd. for $C_{39}H_{57}NO_3$ ($[M^+K]^+$) 626.398; found 626.398.

Synthesis of (–)-cholesteryloxy-*N*-(4-ethynylphenyl)carboxamide (3)

A mixture of **(2)** (100 mg, 171 μmol), potassium hydroxide (9.7 mg, 173 μmol), tripotassium phosphate (36.3 mg, 171 μmol) and dry toluene (6.80 mL) was refluxed for 5 h. The resulting solution was filtered through celite and concentrated under reduced pressure. The crude product was purified with silica-gel chromatography using dichloromethane/*n*-hexane = 1/5 (*v*/*v*) and 2/3 (*v*/*v*), and **(3)** was obtained from the dichloromethane/*n*-hexane = 2/3 (*v*/*v*) eluate. The product was white solid. Yield: 64%; $[\alpha]_D^{20} = -50.4^o$ (c 0.100, chloroform); ^{1}H NMR ($CDCl_3$, 400 MHz, TMS) δ 7.43 (d, J = 8.8 Hz, 2H, Ar-H ortho to NH), 7.34 (d, J = 8.8 Hz, 2H, Ar-H meta to NH), 6.59 (s, 1H, NH), 5.46-5.37 (m, 1H, =CH), 4.67–4.55 (m, 1H, OCH), 3.02 (s, 1H, C≡CH), 2.47–2.29 (m, 2H), 2.08–0.79 (m, 38H), 0.68 (s, 3H, CH_3); ^{13}C NMR ($CDCl_3$, 100 MHz, TMS) δ 152.7 (CO), 139.5 (C=), 138.6 (Ar-NH), 133.0 (Ar ortho to NH), 122.9 (=CH), 118.0 (Ar meta to NH), 116.6 (Ar para to NH), 83.5 (C≡), 76.4 (≡CH), 75.2 (OC), 56.7, 56.1, 50.0, 42.3, 39.7, 39.5, 38.4, 37.0, 36.6, 36.2, 35.8, 31.92, 31.88, 28.2, 28.1, 28.0, 24.3, 23.8, 22.8, 22.6, 21.1, 19.3, 18.7, 11.9; MS (SALDI-FT-ICR): m/z calcd. for $C_{36}H_{51}NO_2$ ($[M^+K]^+$) 568.356; found 568.356.

Synthesis of (+)-poly[4-(cholesteryloxycarbonylamino)phenylacetylene] [(+)-Poly(ChOCAPA)]

To the monomer **(3)** (100 mg, 0.189 mmol) in dry THF (0.76 mL) was added the [Rh(norbornadiene)Cl]$_2$ (0.174 mg, 3.78×10^{-4} mmol) in dry triethylamine (0.10 ml), and the solution was stirred for 1 h at room temperature. The polymerization mixture was poured into acetone, and the polymer was purified by reprecipitation from THF solution into acetone and then dried *in vacuo* for 24 h. The product was yellow solid. Yield: 84%; $[\alpha]_D^{20}$ = +280º (c 0.0200, THF); ^{1}H NMR ($CDCl_3$, 400 MHz, TMS) δ 6.81–5.71 (br, 5H, Ar-H and NH), 5.62–5.02 (br, 2H, HC=C- in main-chain and =CH), 4.78–4.45 (br, 1H, OCH), 2.46–2.28 (br, 2H) 2.12–0.67 (br, 41H); GPC: M_w = 1.69 x 10^6, M_w/M_n = 3.07.

(+)-Poly(ChOCAPA) had a chiral structure in main-chain as shown in **Fig. 2.1**, that is, one-handed helical structure.

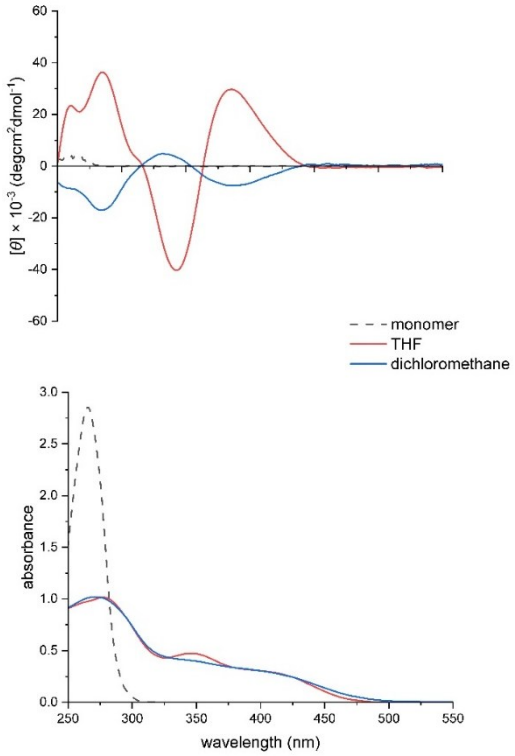

Fig. 2.1 CD and UV-vis. spectra of (+)-poly(ChOCAPA) (1.00×10^{-4} mol/L) in THF (blue line) and $CHCl_3$ (red line) and monomer (1.00×10^{-4} mol/L) in THF at 25 ºC.

2.2.3 FS-AFM Video Imaging

To observe the single molecule of the polymer chain, we modified the specifications of an NVB500 fast-scanning atomic force microscope (FS-AFM) (Olympus, Tokyo, Japan) in dynamic (tapping) mode.[11] An ultra-small cantilever with a low spring constant of approximately 0.1 N/m and a high resonance frequency of over 1 MHz in air was used (AC-10EGS, Olympus, Tokyo, Japan or USC-F1.2-k0.15, NanoWorld AG, Neuchâtel, Switzerland). FS-AFMs offer outstanding performance for investigating the structural dynamics of single molecules in aqueous solutions.[3] However, we modified the AFM for use in organic solvents,[11] enabling us to observe the structural dynamics of a single polymer chain (**Fig. 2.2**).[11,12]

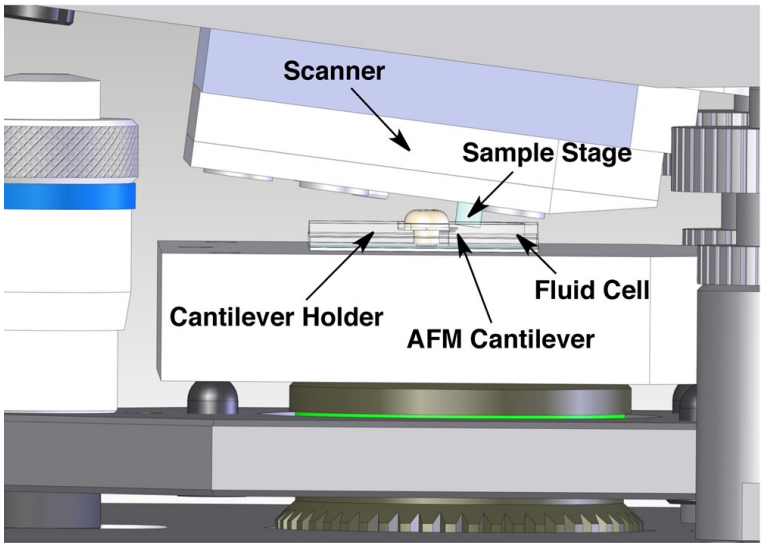

Fig. 2.2 AFM head with a fluid cell.

The polymer was dissolved in tetrahydrofuran (THF) to prepare a solution with a concentration of approximately 1×10^{-6} mol/L. The polymer solution was cast on the surface of a 3-aminopropyltriethoxysilane (APS)-coated mica substrate[11] to prepare a sample for AFM video imaging. Subsequently, FS-AFM images were obtained in *n*-octylbenzene at 25 ± 1°C (**Fig. 2.3**). A line profile is shown in **Fig. 2.4**.

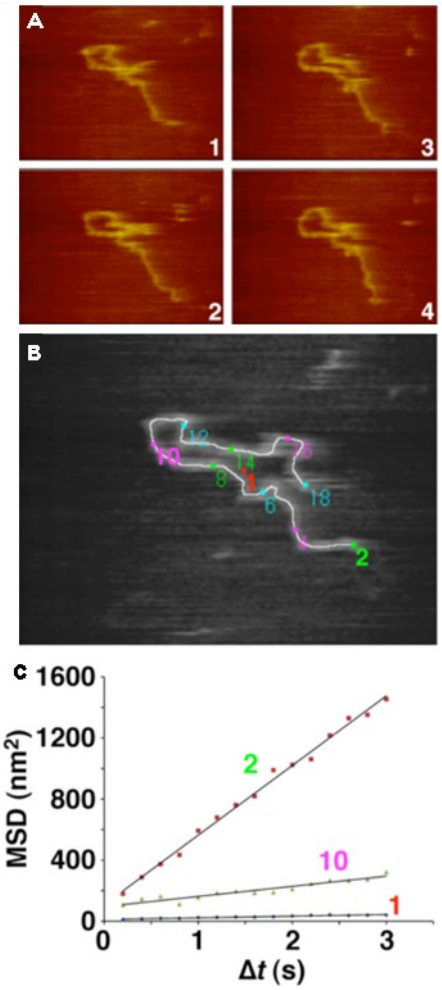

Fig. 2.3 FS-AFM imaging of a single molecule of (+)-poly(ChOCAPA) at rate of 5.0 fps on mica at 25 ± 1°C. (A) Continuous AFM images in a movie. (B) Measurement points of a polymer chain for two-dimensional diffusion. FS-AFM image: x = 280 nm, y = 210 nm, z = 16.8 nm. (C) Mean-square displacement (MSD)-Δ*t* plots for the positions of 1, 2 and 10 in (B). The diffusion constant (*D*) can be calculated from the slope of the MSD/Δ*t* line.

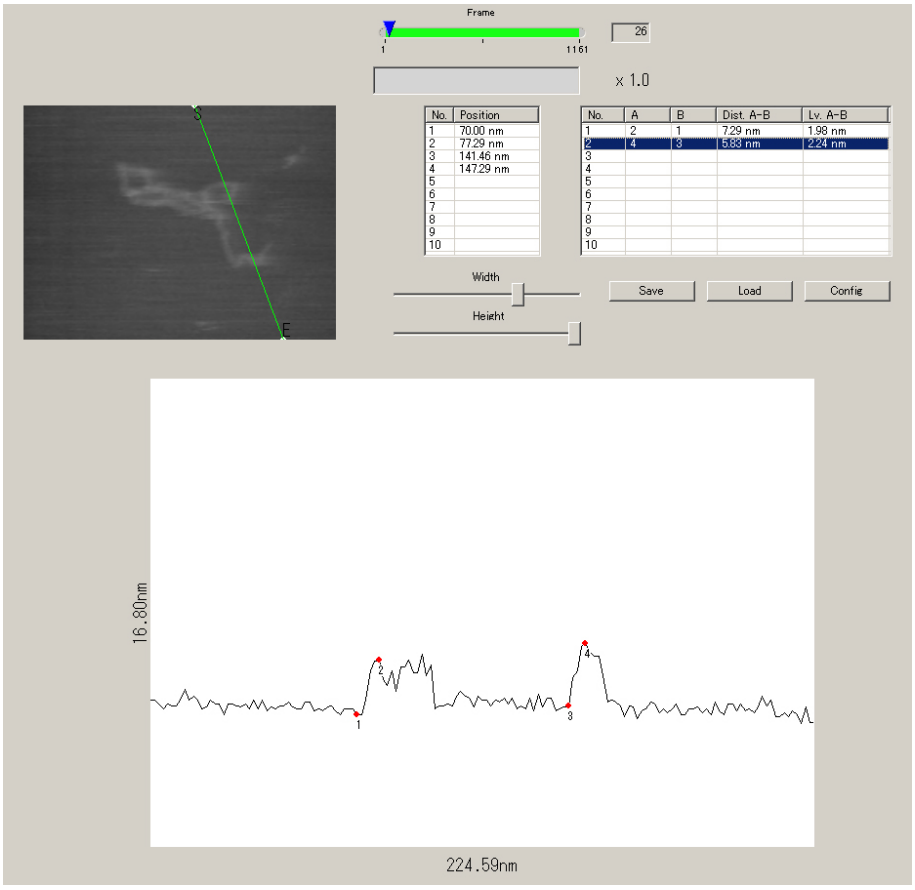

Fig. 2.4 Line profile of a polymer chain.

2.2.4 MSD plots

To determine the dynamics of the polymer chain, the measurement point of the video-imaged short chain was tracked and the mean square displacement (MSD) for a certain time Δt was plotted against Δt,

$$MSD(\Delta t) = \overline{[\Delta x(\Delta t)]^2 + [\Delta y(\Delta t)]^2}.$$

The diffusion coefficient D (nm^2/s) was calculated by dividing the slope of the linearly approximating the MSD-Δt plots of the measurement point by four (**Fig. 2.3C**). Measurement points for displacement were set at equal intervals along the trunk of the single chain [a chain end to the other chain end (2-18)], and also set at the chain centroid (1) (**Fig. 2.3B**). The mobility of each point

determined based on the trajectory data for the single chain was measured by AFM video imaging.

2.2.5 All-Atom MD Simulation

All-atom molecular dynamics (MD) simulations were carried out using the Forcite module of the BIOVIA Materials Studio 2023 (Dassault Systèmes BIOVIA, San Diego, CA, USA) on a supercomputer system (PowerEdge R6525, Dell Technologies Inc., Round Rock, TX, USA). A model of (+)-poly(ChOCAPA) was built by use of the Polymer Builder module. The torsion angle between monomer units was set to -155 degree. A 20-mer model of (+)-poly(ChOCAPA) in a MD cell. The MD cell was built by means of usual procedure of the Amorphous Cell module. The MD cell length and angle were (a = 90 å, b = 60 Å, c = 60 Å) and ($\alpha = 90^{o}$, $\beta = 90^{o}$, $\gamma = 90^{o}$), respectively. Here, single polymer chain was put in the center of the cell, and the solvent molecules of *n*-octylbenzene were packed in the cell at density of 0.858 g cm^{-3}. Sequentially, the geometry of the MD cell was optimized. Simulation in the NVT ensemble (constant number of atoms, volume and temperature) was conducted at 300 K for 100 ps (time step of 0.5-fs, 200,000 steps) and the NPT ensemble (constant number of atoms, pressure and temperature) was conducted at pressure of 1.013×10^{-4} GPa and at 300 K for 100 ps (time step of 1.0-fs, 100,000 steps) to equilibrate the MD cell. The Nose thermostat was used to control the temperature. The Berendsen barostat was used to control the pressure. After the equilibration at 300 K, simulation in the NVE ensemble (constant number of atoms, volume and energy) was conducted for 50 ns (time step of 1.0-fs, 50,000,000 steps) as the production run. The COMPASS III (ver. 1.2) forcefield was used, and the charges were assigned by the forcefield. A snapshot structure was indicated in **Fig. 2.5**.

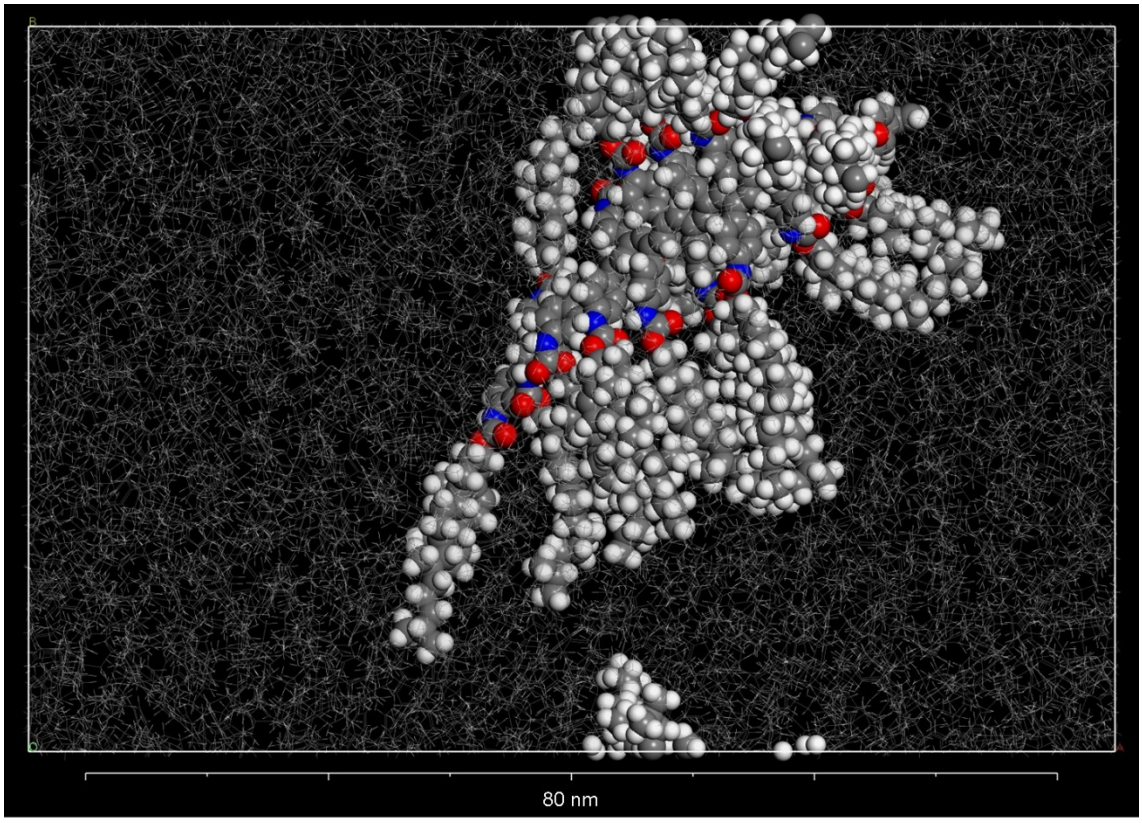

Fig. 2.5 A snap shot of all-atom MD simulation at 50.0 ns.

2.3 Results and Discussion

Single chiral helical polymer [(+)-poly(ChOCAPA)] chain in *n*-octylbenzene at 25 ± 1 ºC was observed using a FS-AFM that was remodeled for observing polymers (**Fig. 2.3A**). From the line-profile analysis of the AFM images, chain length, and size of the molecular model obtained by the all-atom molecular dynamics (MD) calculation (**Fig. 2.5**), it was confirmed that this polymer chain is a single chain polymer. Next, the polymer chain trunk was equally divided and the trajectory of each point was measured (**Fig. 2.3B**). In this figure, the points 1, 2, and 10 represent the measuring points of the center of gravity, the end of the chain, and the center of the chain, respectively. The mean square displacement (MSD) in a certain time (Δt) was plotted as a function of Δt (**Fig. 2.3C**). From the measurements, $D_1 = 2.7$ nm^2/s, $D_2 = 110$ nm^2/s, and $D_{10} = 17$ nm^2/s were obtained, indicating that the diffusion coefficient of the micro-Brownian motion at the end of the polymer chain is about seven

times larger than that at the center. The motion of the polymer chain at the center of gravity, i.e., the diffusion coefficient D_1 of the Brownian motion, was about 1/40 of D_2 at the chain end. It can be said that this method is a new characterization for the precise analysis of polymers at solid-liquid interfaces. In addition, MSD plots for the other measuring points were shown in **Fig. 2.6**.

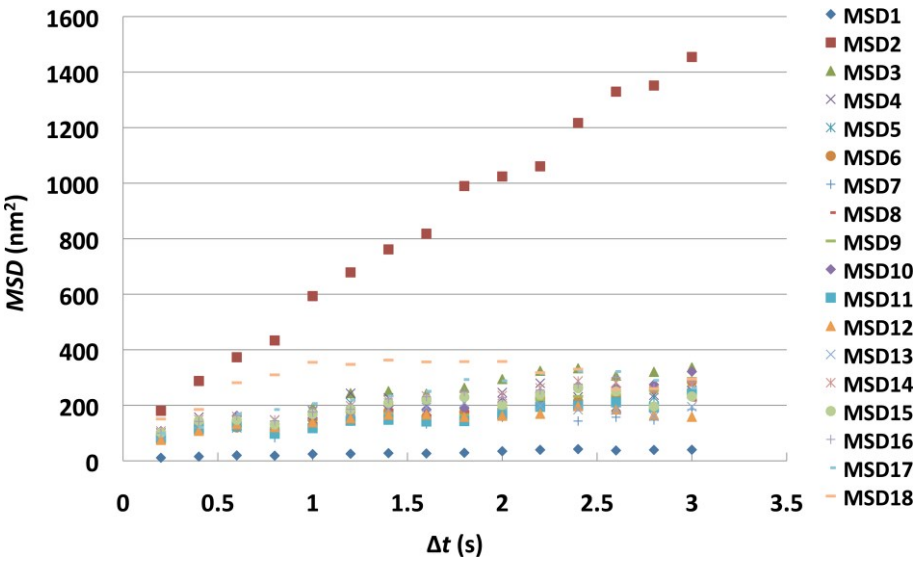

Fig. 2.6 MSD plots of a polymer chain.

Further, the three-point angles for the measuring points were analyzed as histograms (**Fig. 2.7**). For the polymer chain of (+)-poly(ChOCAPA), the average values and the standard deviations calculated from the distribution of three-point angles were as follows. Here, the time average and the standard deviation for three-point angles (2-4-6) are represented as $\theta_{2\text{-}4\text{-}6}$ and $\sigma_{2\text{-}4\text{-}6}$, respectively. Those values at other measuring points were also shown in the same manner.

end of the chain：$\theta_{2\text{-}4\text{-}6} = 135°$, $\sigma_{2\text{-}4\text{-}6} = 30.0$

inside of the chain：$\theta_{6\text{-}8\text{-}10} = 160°$, $\sigma_{6\text{-}8\text{-}10} = 17.2$

inside of the chain：$\theta_{10\text{-}12\text{-}14} = 62.6°$, $\sigma_{10\text{-}12\text{-}14} = 26.1$

end of the chain：$\theta_{14\text{-}16\text{-}18} = 152°$, $\sigma_{14\text{-}16\text{-}18} = 20.4$

whole chain：$\theta_{2\text{-}10\text{-}18} = 40.2°$, $\sigma_{2\text{-}10\text{-}18} = 14.5$

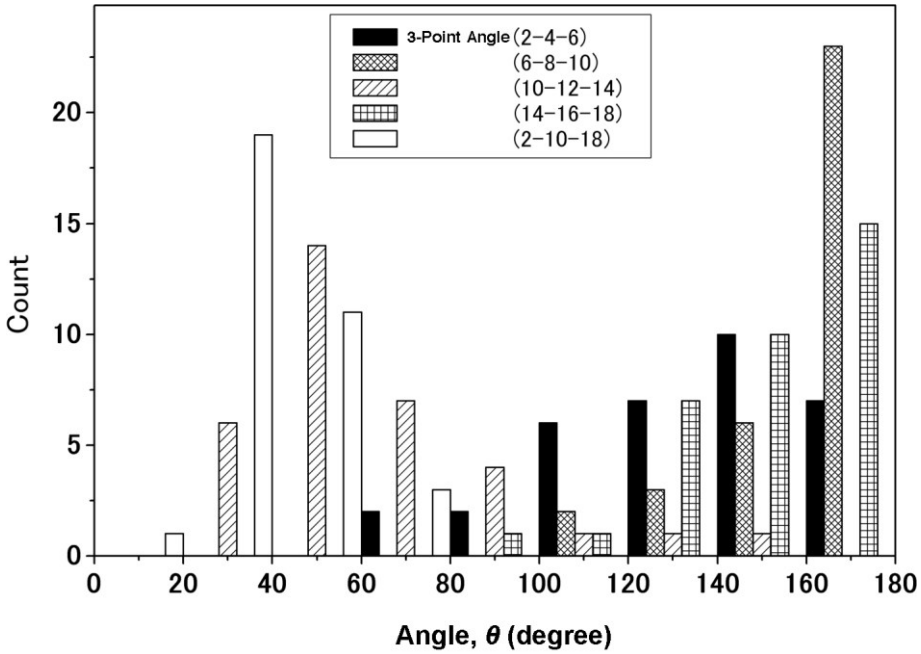

Fig. 2.7 The histogram of three-point angles for the measuring points.

At the solid-liquid interface, relatively large time average angles (θ: 135° and 152°) were observed for both ends of the (+)-poly(ChOCAPA) polymer chain, suggesting that the average structure is relatively linear. However, the difference in the standard deviations (σ : 30.0 and 20.1) was observed, which means that there is a difference in the degree of the mobility (flexibility). From these results, it was elucidated that there is diversity in helical structures with π conjugated system.[12]

Furthermore, it was found that the values inside the polymer chain differ considerably depending on the domain. While there were linear domains with little movement (θ: 60°, σ: 17.2), highly flexible domains with relatively large movement (θ: 62.6°, σ: 26.1) were also confirmed, indicating the diversity of the structural dynamics inside the polymer chain at the solid-liquid interface. This result confirmed that the helical structure with π conjugated system is relatively flexible.

Furthermore, it was found that (+)-poly(ChOCAPA) as a whole polymer chain has high flexibility and its motion is relatively little (θ: 40.2°, σ: 14.5).

The MSD-Δt analysis makes the dynamic analysis at a single point in a polymer chain possible. The three-point angle analysis makes the dynamic analysis at a certain domain in a polymer chain possible.

By performing the MSD-Δ*t* analysis and the three-point angle analysis, it became possible to conduct deeper investigations on the polymer chain dynamics at solid-liquid interfaces.

2.4 Conclusion

(+)-Poly(ChOCAPA) chain was predicted to have a rigid-rod polymer chain structure due to the hydrogen bonds among amid bonds between pendants, the intramolecular interaction by van der Waals force between cholesteryl groups, and rigidity by π conjugate system in the main chain. However, this study elucidated that a (+)-poly(ChOCAPA) chain has a "flexible" structure with relatively large degree of dynamics at the molecular level. Many molecular machines have already been reported,[13-18] the macromolecular dynamics could be analyzed by this study method to develop the molecular machines such as molecular motors, etc. driven by thermal fluctuations.

2.5 *Spectral Data*

2.5.1 *^{1}H and ^{13}C NMR Spectra*

(–)-4-Cholesteryloxycarbonylamino-1-bromobenzene (1)

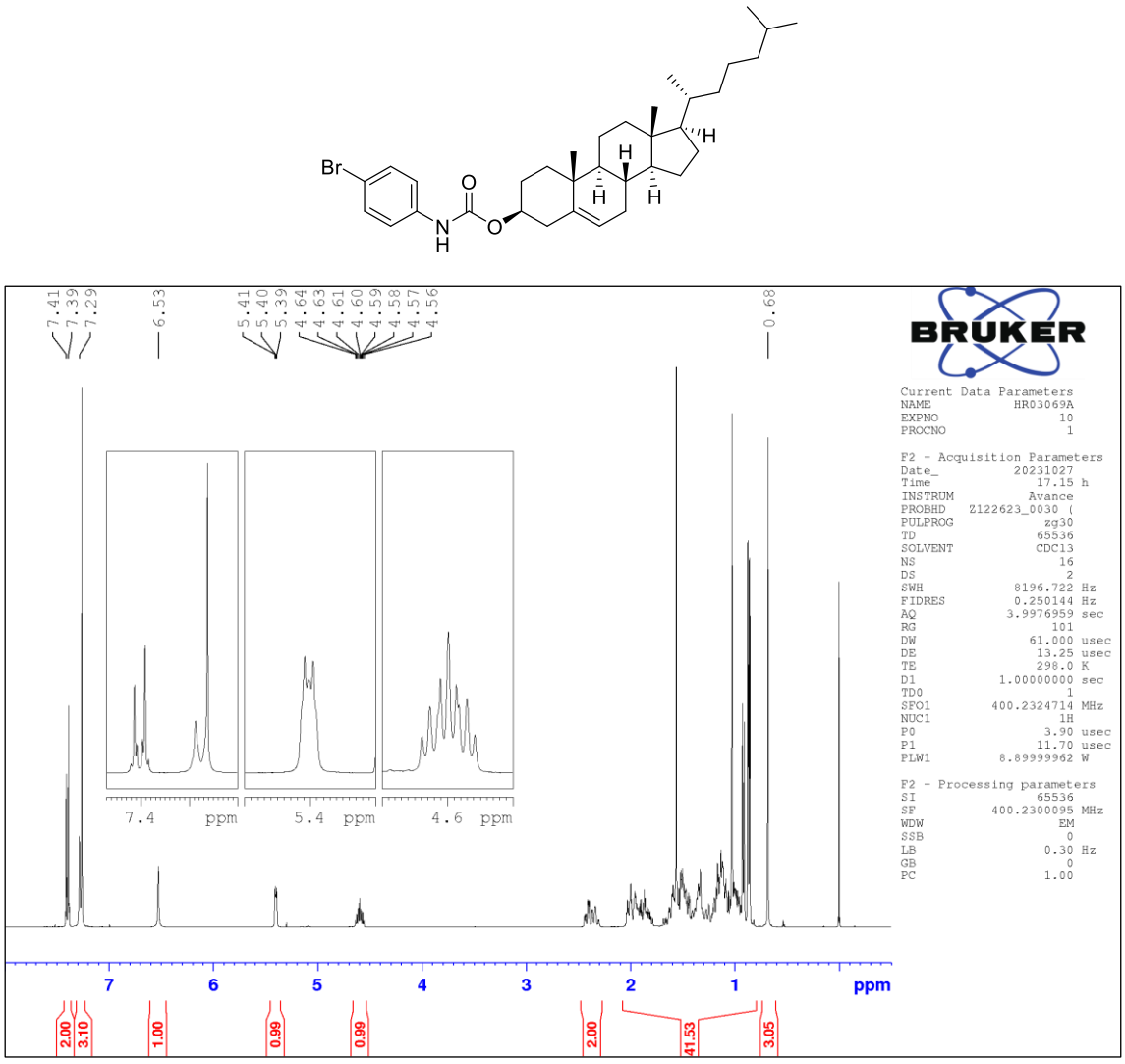

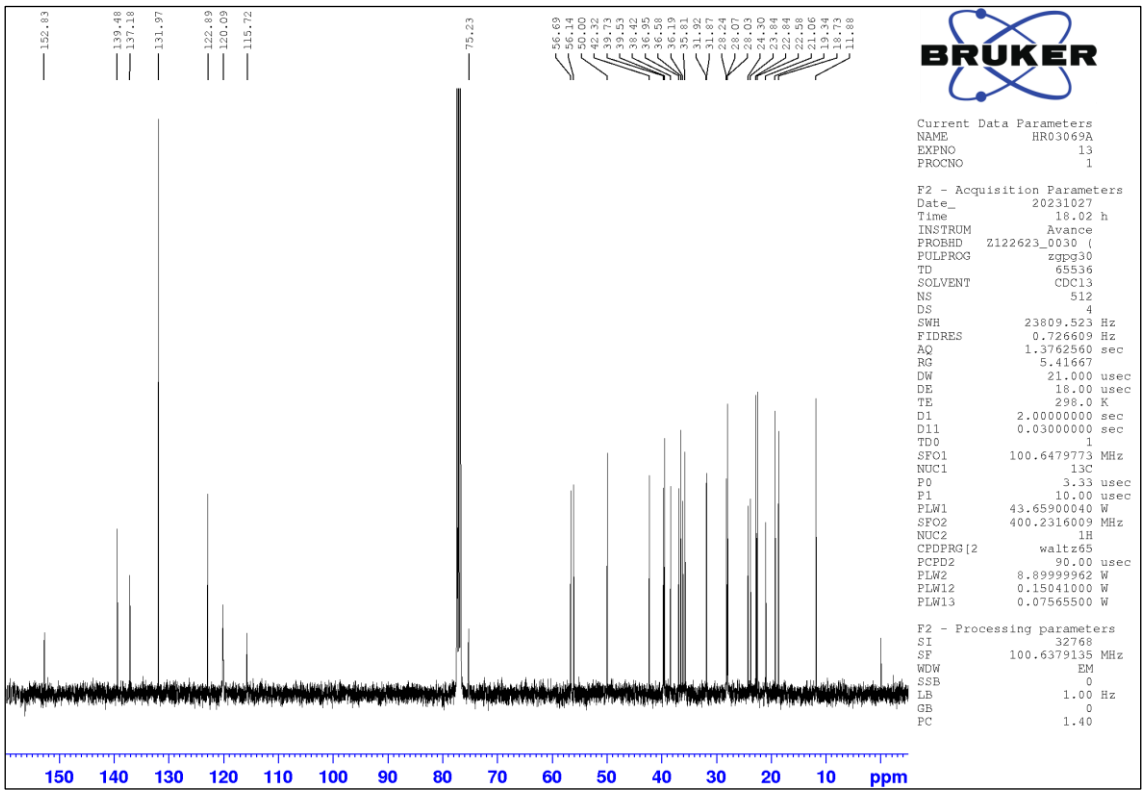
152.83
139.48
137.18
131.97
122.89
120.09
115.72
75.23
56.69
56.14
50.00
42.32
39.73
39.53
38.42
36.95
36.58
35.19
35.01
31.92
31.87
28.24
28.07
28.03
24.30
23.84
22.84
22.58
21.06
19.44
18.73
11.88
150 140 130 120 110 100 90 80 70 60 50 40 30 20 10 ppm
BRUKER
Current Data Parameters
NAME HR03069A
EXPNO 13
PROCNO 1
F2 - Acquisition Parameters
Date_ 20231027
Time 18.02 h
INSTRUM Avance
PROBHD Z122623_0030 (
PULPROG zgpg30
TD 65536
SOLVENT CDC13
NS 512
DS 4
SWH 23809.523 Hz
FIDRES 0.726609 Hz
AQ 1.3762560 sec
RG 5.41667
DW 21.000 usec
DE 18.00 usec
TE 298.0 K
D1 2.00000000 sec
D11 0.03000000 sec
TD0 1
SFO1 100.6479773 MHz
NUC1 13C
P0 3.33 usec
P1 10.00 usec
PLW1 43.65900040 W
SFO2 400.2316009 MHz
NUC2 1H
CPDPRG[2 waltz65
PCPD2 90.00 usec
PLW2 8.89999962 W
PLW12 0.15041000 W
PLW13 0.07565500 W
F2 - Processing parameters
SI 32768
SF 100.6379135 MHz
WDW EM
SSB 0
LB 1.00 Hz
GB 0
PC 1.40

(–)-Cholesteryloxy-*N*-[4-(3-hydroxy-3-methylbut-1-ynyl)phenyl]carboxamide (2)

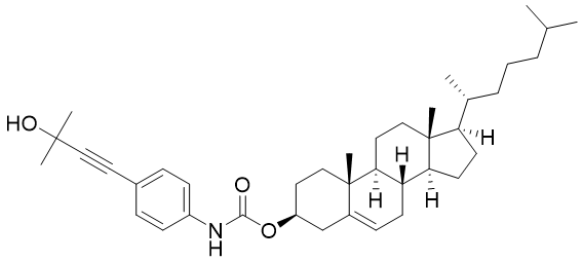

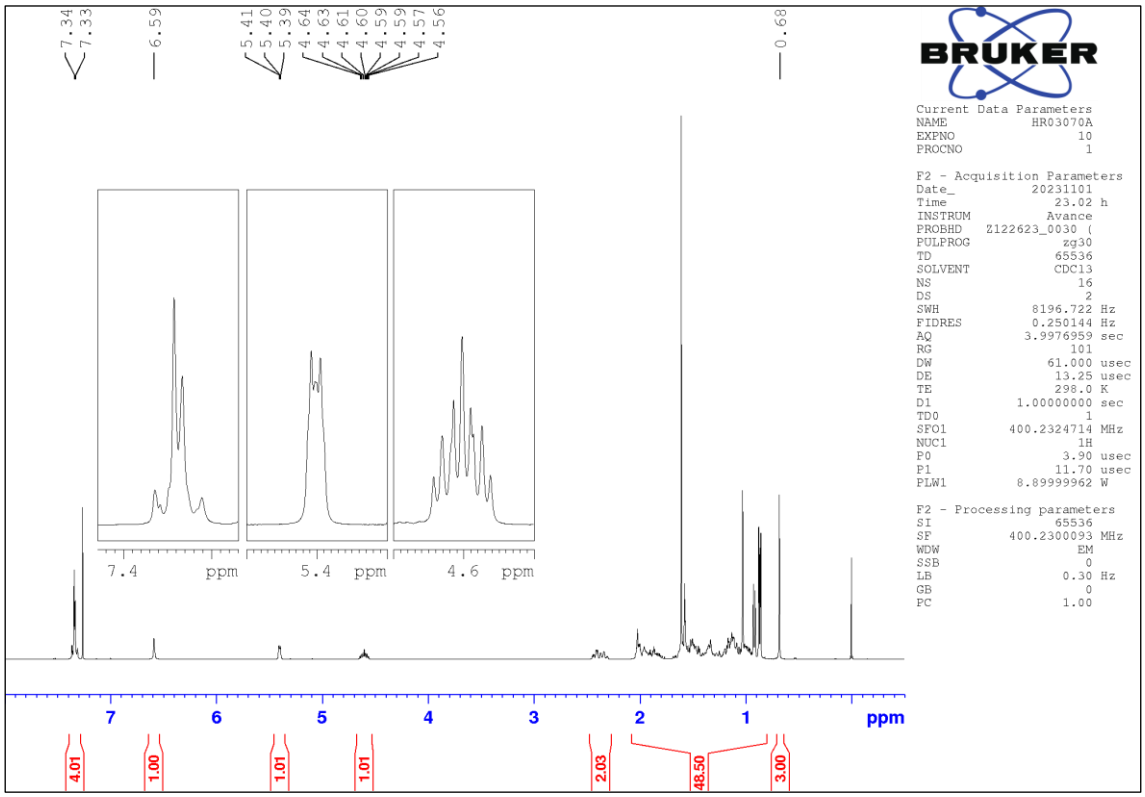

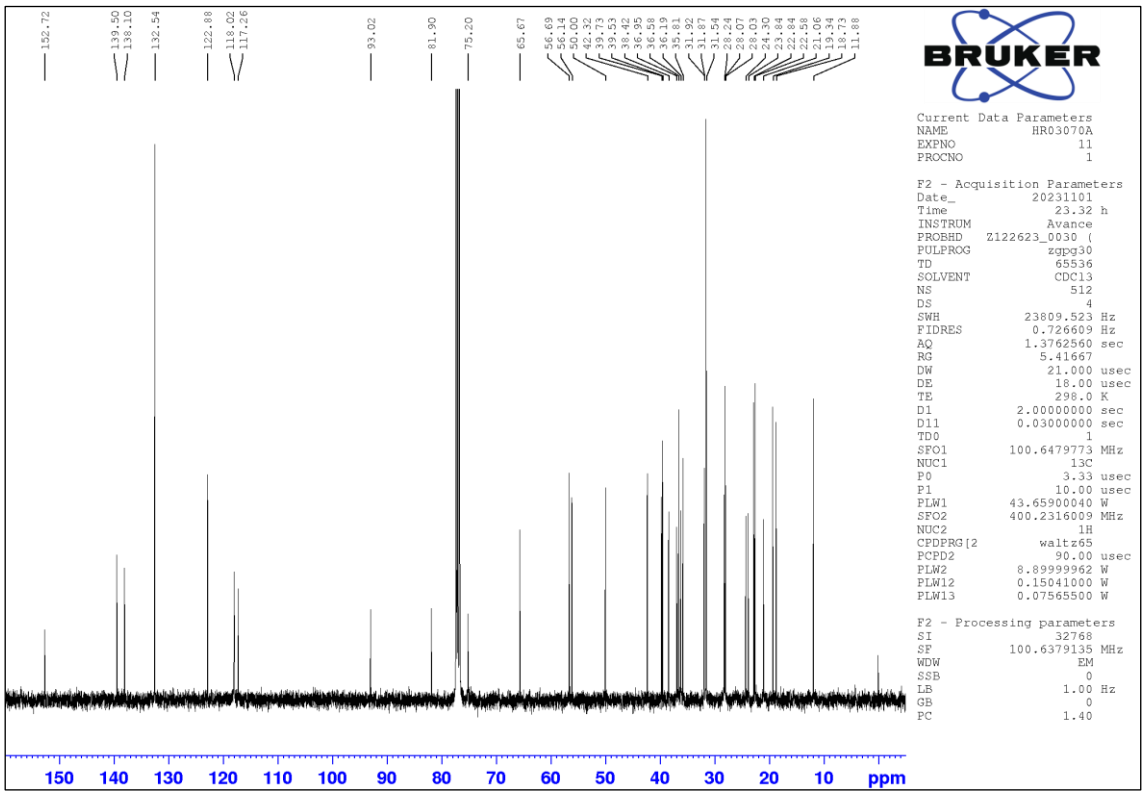
152.72
139.50
138.10
132.54
122.88
118.02
117.26
93.02
81.90
75.20
65.67
56.69
56.14
50.00
49.32
43.73
39.53
38.42
36.95
36.58
36.19
35.81
31.92
31.87
31.54
28.24
28.07
28.03
24.30
23.84
22.84
22.58
21.06
19.34
18.73
11.88
150
140
130
120
110
100
90
80
70
60
50
40
30
20
10
ppm
BRUKER
Current Data Parameters
NAME HR03070A
EXPNO 11
PROCNO 1
F2 - Acquisition Parameters
Date_ 20231101
Time 23.32 h
INSTRUM Avance
PROBHD Z122623_0030 (
PULPROG zgpg30
TD 65536
SOLVENT CDCl3
NS 512
DS 4
SWH 23809.523 Hz
FIDRES 0.726609 Hz
AQ 1.3762560 sec
RG 5.41667
DW 21.000 usec
DE 18.00 usec
TE 298.0 K
D1 2.00000000 sec
D11 0.03000000 sec
TD0 1
SFO1 100.6479773 MHz
NUC1 13C
P0 3.33 usec
P1 10.00 usec
PLW1 43.65900040 W
SFO2 400.2316009 MHz
NUC2 1H
CPDPRG[2 waltz65
PCPD2 90.00 usec
PLW2 8.89999962 W
PLW12 0.15041000 W
PLW13 0.07565500 W
F2 - Processing parameters
SI 32768
SF 100.6379135 MHz
WDW EM
SSB 0
LB 1.00 Hz
GB 0
PC 1.40

(–)-Cholesteryloxy-*N*-(4-ethynylphenyl)carboxamide (3)

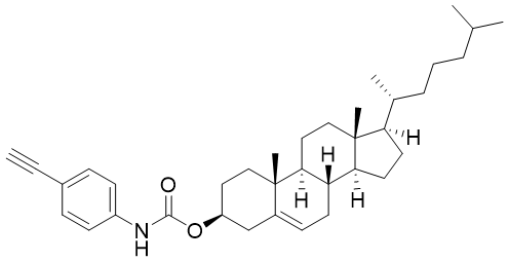

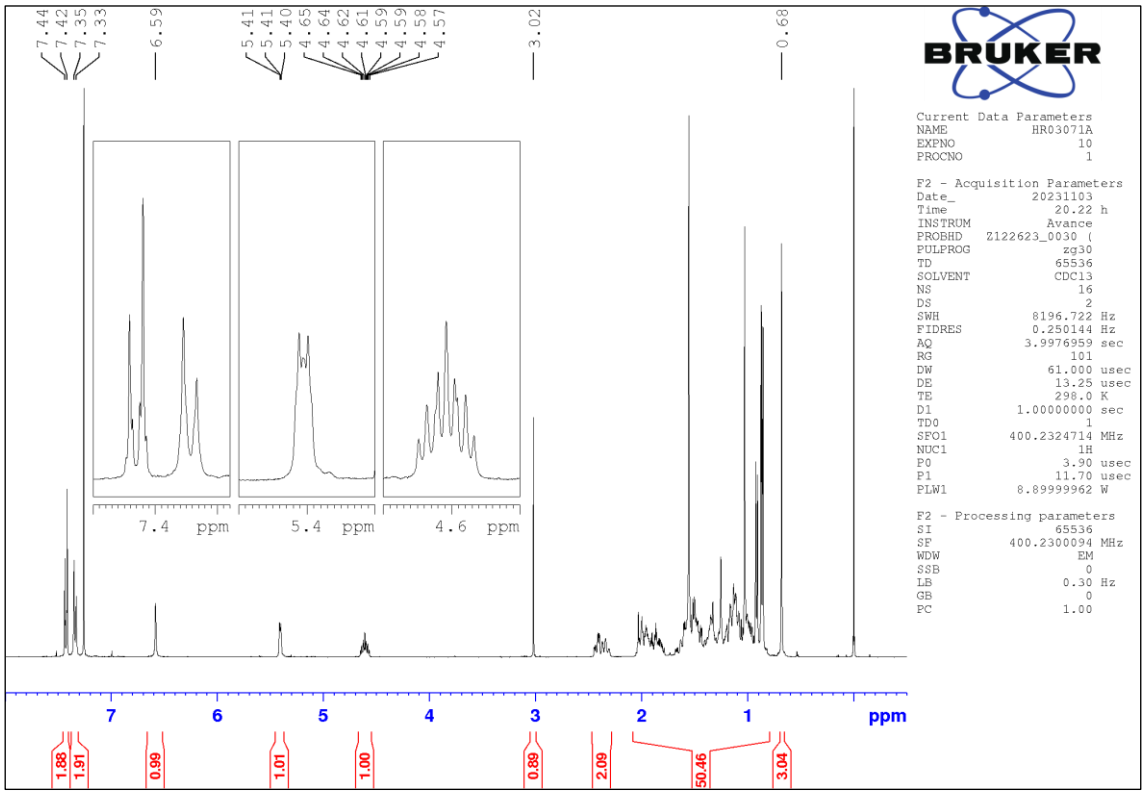

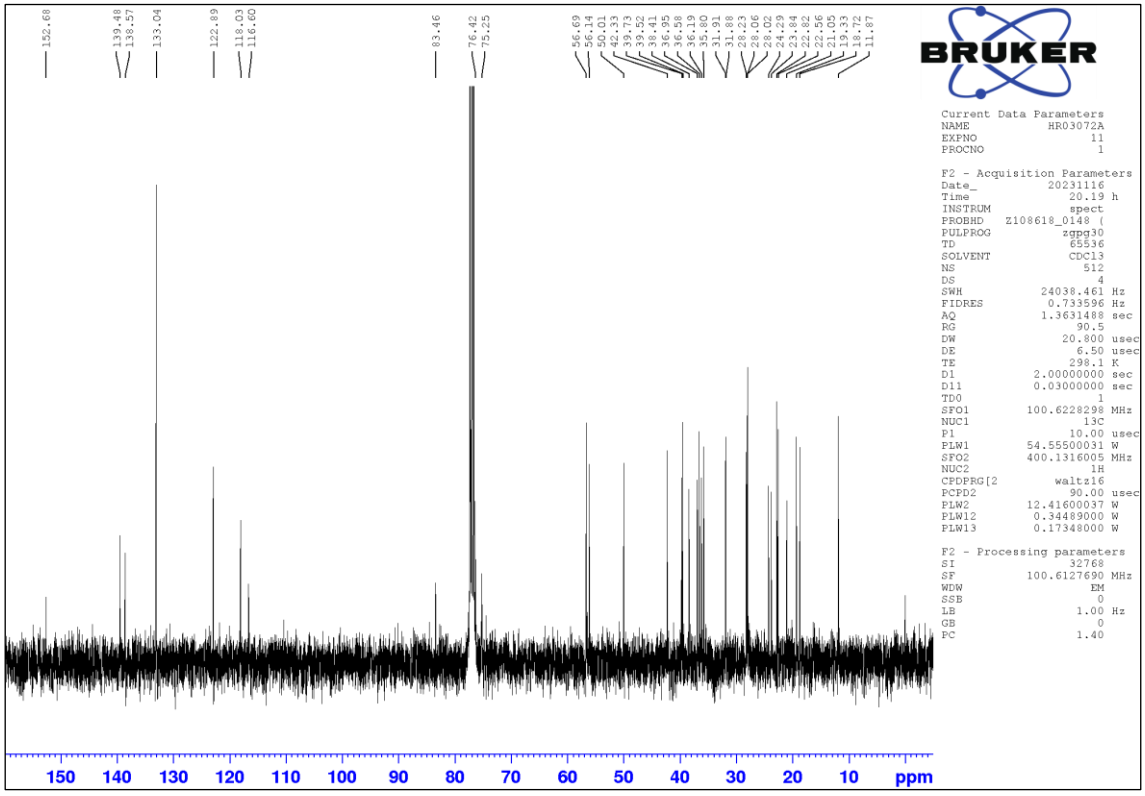
152.68
139.48
138.57
133.04
122.89
118.03
116.60
83.46
76.42
75.25
56.69
56.14
50.01
49.73
39.52
38.41
36.95
36.58
36.19
35.80
31.91
31.88
28.23
28.06
24.20
24.29
23.84
22.82
22.56
21.05
19.33
18.72
11.87
150
140
130
120
110
100
90
80
70
60
50
40
30
20
10
ppm
BRUKER
Current Data Parameters
NAME HR03072A
EXPNO 11
PROCNO 1
F2 - Acquisition Parameters
Date_ 20231116
Time 20.19 h
INSTRUM spect
PROBHD Z108618_0148 (
PULPROG zgpg30
TD 65536
SOLVENT CDCl3
NS 512
DS 4
SWH 24038.461 Hz
FIDRES 0.733596 Hz
AQ 1.3631488 sec
RG 90.5
DW 20.800 usec
DE 6.50 usec
TE 298.1 K
D1 2.00000000 sec
D11 0.03000000 sec
TD0 1
SFO1 100.6228298 MHz
NUC1 13C
P1 10.00 usec
PLW1 54.55500031 W
SFO2 400.1316005 MHz
NUC2 1H
CPDPRG[2 waltz16
PCPD2 90.00 usec
PLW2 12.41600037 W
PLW12 0.34489000 W
PLW13 0.17348000 W
F2 - Processing parameters
SI 32768
SF 100.6127690 MHz
WDW EM
SSB 0
LB 1.00 Hz
GB 0
PC 1.40

(+)-Poly[4-(cholesteryloxycarbonylamino)phenylacetylene]

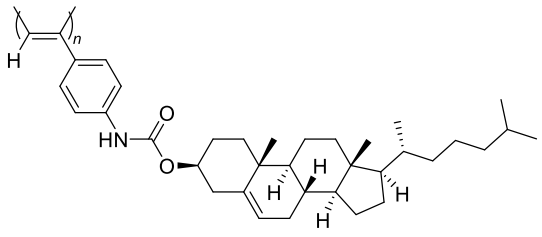

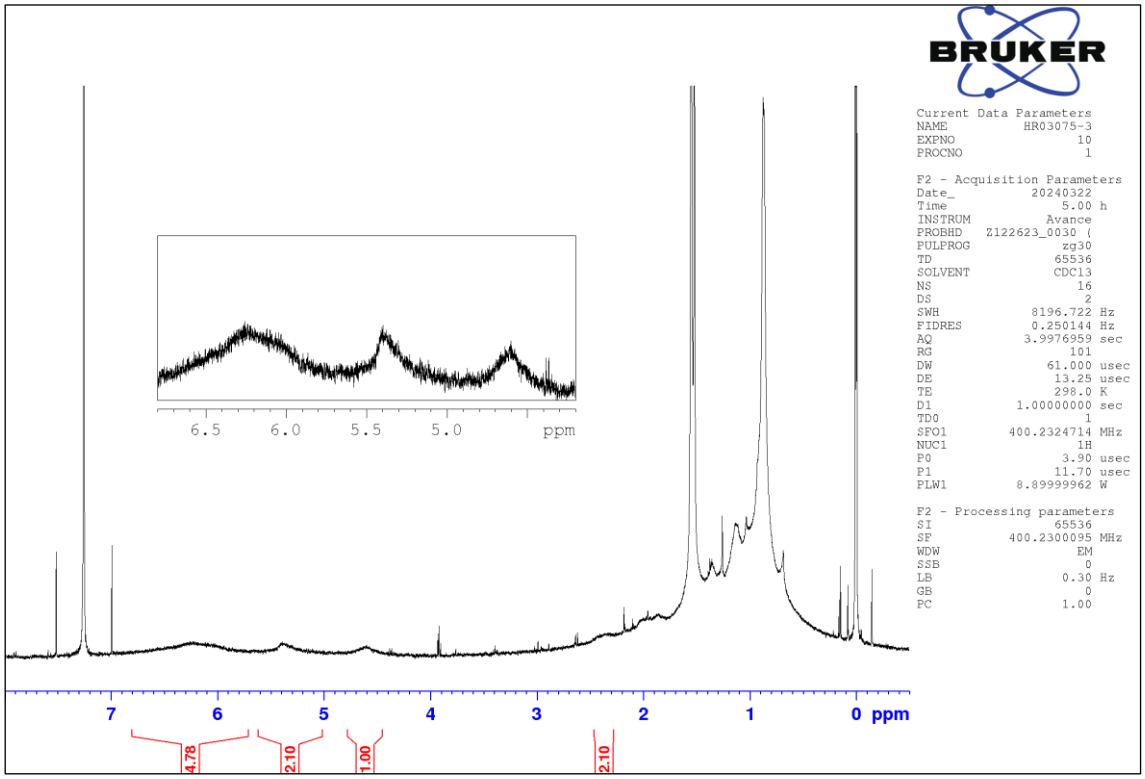

2.5.2 IR Spectra

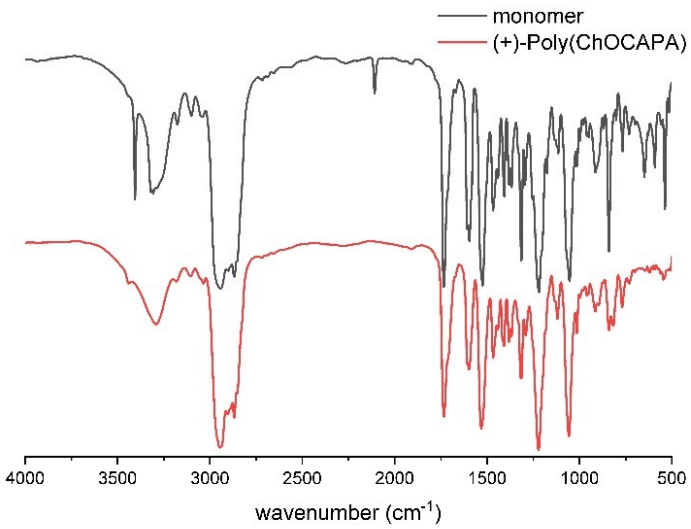

2.6 Reference

1. K. Shinohara, Single-Molecule Imaging of a Polymer: Direct Observation of Structure and Dynamics in a Polymer Chain. *Kobunshi Ronbunshu* **2016**, *73*, 491–504. https://doi.org/10.1295/koron.2016-0034
2. M. Kaya, H. Higuchi, Nonlinear Elasticity and an 8-nm Working Stroke of Single Myosin Molecules in Myofilaments. *Science* **2010**, *329*, 686–689. https://doi.org/10.1126/science.1191484
3. N. Kodera, D. Yamamoto, R. Ishikawa, T. Ando, Video imaging of walking myosin V by high-speed atomic force microscopy. *Nature* **2010**, *468*, 72–76. https://doi.org/10.1038/nature09450
4. Y. Okada, H. Higuchi, N. Hirokawa, Processivity of the single-headed kinesin KIF1A through biased binding to tubulin. *Nature* **2003**, *424*, 574–577. https://doi.org/10.1038/nature01804
5. K. Shinohara, *Applied Scanning Probe Methods X -Biomimetics and Industrial Applications*, Chapter 31: Scanning Probe Microscope Application for Single Molecules in a π-Conjugated Polymer toward the Molecular Devices based on Polymer Chemistry, pp 153–182, B. Bhushan,

H. Fuchs, M. Tomitori (Eds.), Springer (Berlin, Heidelberg), ISBN: 978-3-540-74084-1 (2008).

6. K. Shinohara, S. Yasuda, G. Kato, M. Fujita, H. Shigekawa, Direct Observation of the Chiral Quaternary Structure in a π-Conjugated Polymer at Room Temperature, *J. Am. Chem. Soc.* **2001**, *123*, 3619–3620. https://doi.org/10.1021/ja037733e
7. K. Shinohara, H. Higuchi, Direct Observation of Dynamic Behavior of Single Molecules of a Linear π-Conjugated Polymer with a Total Internal Reflection Fluorescence Microscope. *Trans. Mater. Res. Soc. Japan* **2000**, *25*, 825–828.
8. K. Shinohara, S. Yamaguchi, H. Higuchi, Single Molecule Imaging of a π-Conjugated Polymer in Tetrahydrofuran Solution at Room Temperature. *Polym. J.* **2000**, *32*, 977–979. https://doi.org/10.1295/polymj.32.977
9. K. Shinohara, S. Yamaguchi, T. Wazawa, Syntheses and Enantioselective Recognition of Chiral Poly(phenyleneethynylene)s bearing Bulky Optically Active Menthyl Groups. *Polymer* **2001**, *42*, 7915–7918. https://doi.org/10.1016/S0032-3861(00)00391-8
10. T. Aoki, M. Kokai, K. Shinohara, E. Oikawa, Chiral Helical Conformation of the Polyphenylacetylene Having Optically Active Bulky Substituent, *Chem. Lett.* **1993**, *22*, 2009–2012. https://doi.org/10.1246/cl.1993.2009
11. K. Shinohara, Y. Makida, T. Oohashi, R. Hori, Single-Molecule Unidirectional Processive Movement along a Helical Polymer in Non-aqueous Medium, *Langmuir* 2022, *38*, 12173–12178. https://doi.org/10.1021/acs.langmuir.2c01704
12. K. Shinohara, T. Kitami, K. Nakamae, Direct Measurement of a Structural Diversity in Single Molecules of a Chiral Helical π-Conjugated Polymer, *J. Polym. Sci. Part A: Polym. Chem.* **2004**, *42*, 3930–3935. https://doi.org/10.1002/pola.20247
13. M. Cesario, C. O. Dietrich-Buchecker, J. Guilhem, C. Pascard, J. P. Sauvage, Molecular structure of a catenand and its copper(I) catenate: complete rearrangement of the interlocked macrocyclic ligands by complexation. *J. Chem. Soc., Chem. Commun.* **1985**, *5*, 244–247. https://doi.org/10.1039/C39850000244
14. P. R. Ashton, D. Philp, N. Spencer, J. F. Stoddart, A new design strategy for the self-assembly of

molecular shuttles. *J. Chem. Soc., Chem. Commun.* **1992**, *16*, 1124–1128. https://doi.org/10.1039/C39920001124

15. N. Koumura, R. W. J. Zijlstra, R. A. van Delden, N. Harada, B. L. Feringa, Light-driven monodirectional molecular rotor. *Nature* **1999**, *401*, 152–155. https://doi.org/10.1038/43646
16. T. Kudernac, N. Ruangsupapichat, M. Parschau, B. Maciá, N. Katsonis, S. R. Harutyunyan, K. Ernst, B. L. Feringa, Electrically driven directional motion of a four-wheeled molecule on a metal surface. *Nature* **2011**, *479*, 208–211. https://doi.org/10.1038/nature10587
17. L. Zheng, H. Zhao, Y. Han, H. Qian, L. Vukovic, J. Mecinović, P. Král, WTS Huck, Catalytic transport of molecular cargo using diffusive binding along a polymer track, *Nat. Chem.* **2019**, *11*, 359–366. https://doi.org/10.1038/s41557-018-0204-7
18. M. Samperi, B. Bdiri, C. D. Sleet, R. Markus, A. R. Mallia, L. Pérez-García, D. B. Amabilino, Light-controlled micron-scale molecular motion, *Nat. Chem.* **2011**, *13*, 1200–1206. https://doi.org/10.1038/s41557-021-00791-2

Chapter 3. Direct Observation of "End-Capping Effect" of a PEG@α-CD Polypseudorotaxane in aqueous media

3.1 Introduction

Supramolecular materials have attracted attention because they can exhibit advanced functionalities, such as self-healing properties.[1] In particular, poly(ethylene glycol) (PEG)-based polypseudorotaxane, using α-cyclodextrin (α-CD) as the ring component, has been widely used because it can be easily prepared by standing in aqueous solution.[2, 3] However, when high-molecular-weight PEG is used as the axial component, the low solubility and dissociation of α-CD make it difficult to analyze the structure in solution, particularly with conventional spectroscopic techniques.[4] Consequently, it is often necessary to synthesize end-capped rotaxanes to stabilize the structure and achieve more accurate structural analysis in solution.

Many commonly used polymer materials have unclear molecular structures and dynamics. To optimize the performance of these materials, it is essential to understand their molecular structure, and single-chain structural analysis has frequently been conducted.[5, 6] Elucidating the functions at the single-molecule level is also important. Research on biomolecules, such as motor proteins, has made considerable progress by using techniques such as microscopic imaging and force measurements with laser trapping.[7-9] In particular, fast-scanning atomic force microscopy (FS-AFM) is useful for elucidating functions visually at the single-molecule level. Furthermore, single-molecule imaging using FS-AFM can be performed at lower concentrations ($<10^{-6}$ mol/L) than spectroscopic methods, making it effective for low-solubility samples.

Although PEG@α-CD polypseudorotaxane is widely used, to the best of our knowledge, there are no studies that address the structural changes associated with the shuttling of the α-CD ring along the polymer chain. Spectroscopic analysis provides averaged values for the entire system,[4, 10-12] making it difficult to conduct localized structural analysis at the single-molecule level, and thus localized structural changes remain unclear. Therefore, the mechanisms of the functionalities of supramolecular materials are still ambiguous, and elucidating the structural changes caused by the shuttling of the ring component will contribute to improving functionality. Moreover, PEG@α-CD polypseudorotaxane exhibits intermolecular hydrogen bonding.[13] Our recently reported synthetic polymer motor achieves

long-range translational motion by using non-covalent interactions between polymer chains and thermal fluctuations.[14, 15] Therefore, elucidating the structure of PEG@α-CD polypseudorotaxane at the solid–liquid interface in this study will contribute to the development of synthetic polymer motors driven by thermal fluctuations. Molecular machines operating through thermal fluctuations at room temperature could contribute to achieving the Sustainable Development Goals published by the United Nations.[16]

In this study, we conducted single-molecule imaging of PEG@α-CD polypseudorotaxane in aqueous solution using FS-AFM. FS-AFM allowed the structural analysis of polypseudorotaxane with high-molecular-weight PEG as the axial component, which has low solubility. We analyzed the micro-Brownian motion within a polypseudorotaxane, and we confirmed the end-capping effect caused by globules at the chain ends. To validate the observation results, we conducted all-atom molecular dynamics (MD) simulations in water. Based on these results, we discussed the interdependence between the micro-Brownian motion of the polypseudorotaxane chains and the shuttling motion of α-CD at the solid–liquid interface.

3.2 Experimental

3.2.1 Materials

Polyethylene oxide ($M_w = 1.0 \times 10^5$ g/mol) was purchased from Thermo Fisher Scientific (Waltham, MA, USA). α-CD was purchased from Junsei Chemical (Tokyo, Japan). Potassium chloride was purchased from Kanto Kagaku (Tokyo, Japan).

3.2.2 Preparation of PEG_{100k}@α-CD Polypseudorotaxane

A saturated aqueous solution of α-CD was mixed with PEG_{100k} (1.0 *w*/*v*%), ultrasonicated for 30 min, and then left to stand for more than 6 h. The precipitated white solid was separated by centrifugation, and the supernatant was discarded. The residue was washed three times by adding a

small amount of distilled water, shaking, and then centrifuging to remove the supernatant.

3.2.3 FS-AFM Imaging

To observe a single polymer chain molecule, we modified the specifications of a FS-AFM system (NVB500, Olympus, Tokyo, Japan) in dynamic (tapping) mode (**Fig. 3.1**).[17, 18] An ultra-small cantilever (AC-10EGS, Olympus, or USC-F1.2-k0.15, NanoWorld AG, Neuchâtel, Switzerland) with a low spring constant of approximately 0.1 N/m and a high resonance frequency of over 1 MHz in air was used.

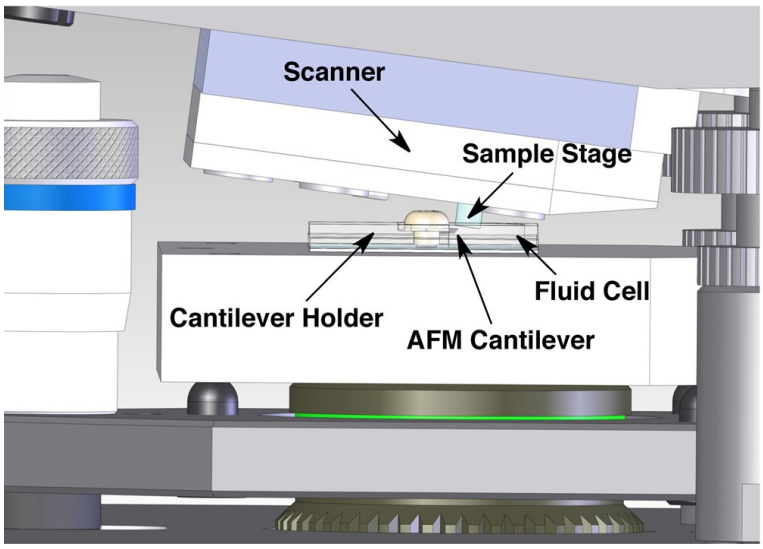

Fig. 3.1 AFM head with a fluid cell.

For PEG_{100k}, the sample solution was prepared by dissolving it in water at a concentration of 2×10^{-9} mol/mL. For PEG_{100k}@α-CD polypseudorotaxane, the sample solution was prepared by adding the precipitate to water and using the soluble portion. The polymer solutions were then cast on the surface of a mica substrate to prepare samples for AFM video imaging. Subsequently, FS-AFM images were obtained in 15 mM KCl aqueous solution at 25 ± 1 °C (for PEG_{100k} see **Fig. 3.2**, and the line profile in **Fig. 3.3**; for PEG_{100k}@α-CD polypseudorotaxane see **Fig. 3.4**, and the line profile in **Fig. 3.5**).

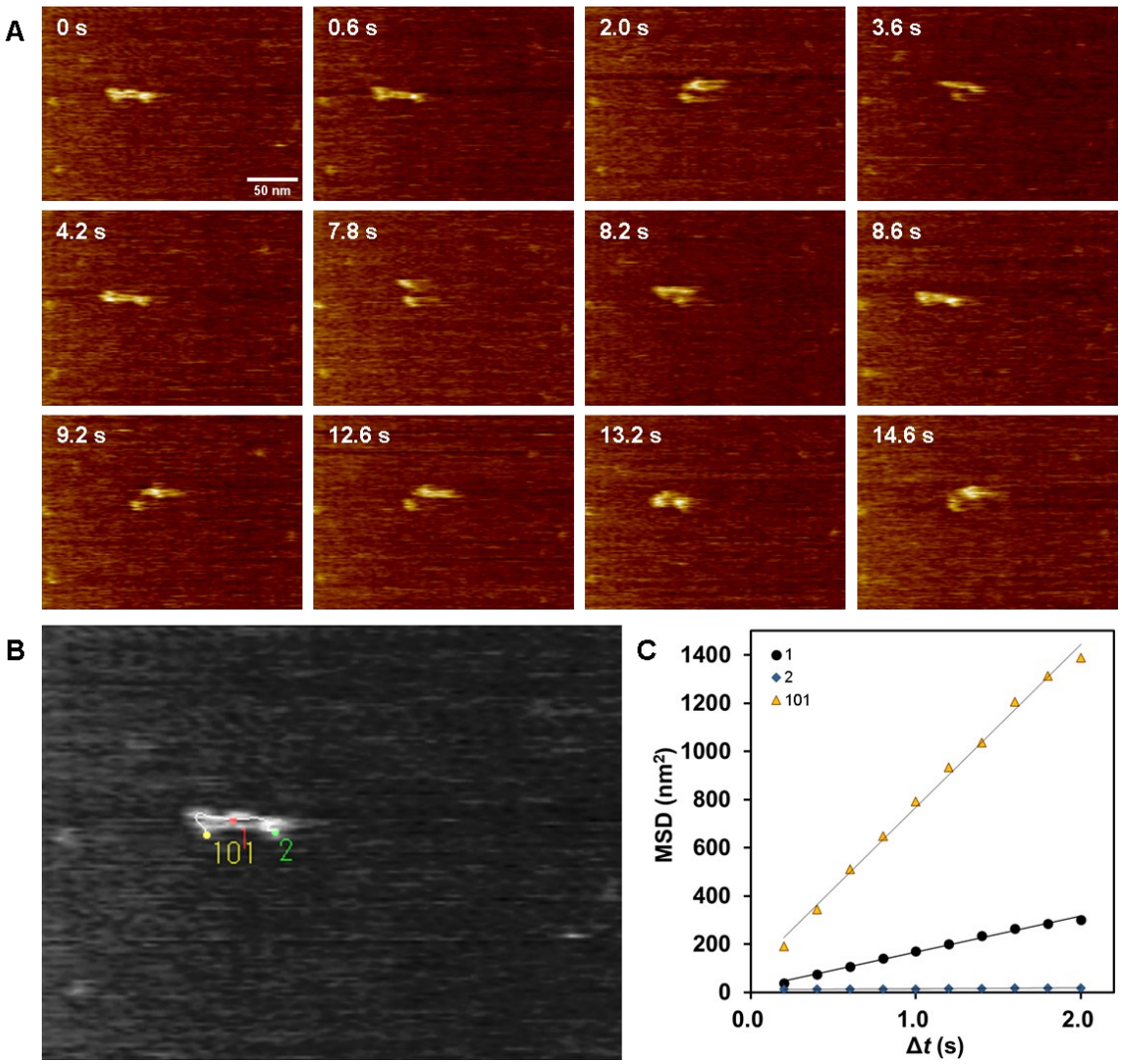

Fig. 3.2 FS-AFM imaging of a single molecule of PEG_{100k} at rate of 5.0 fps on mica 25 ± 1 °C. (A) AFM images from a movie. (B) Measurement points on a polymer chain for two-dimensional diffusion. FS-AFM image: x = 256 nm, y = 192 nm, z = 18.0 nm. (C) MSD–Δt plots for points 1, 2, and 101 in (B). D was calculated from the slope of the MSD/Δt line.

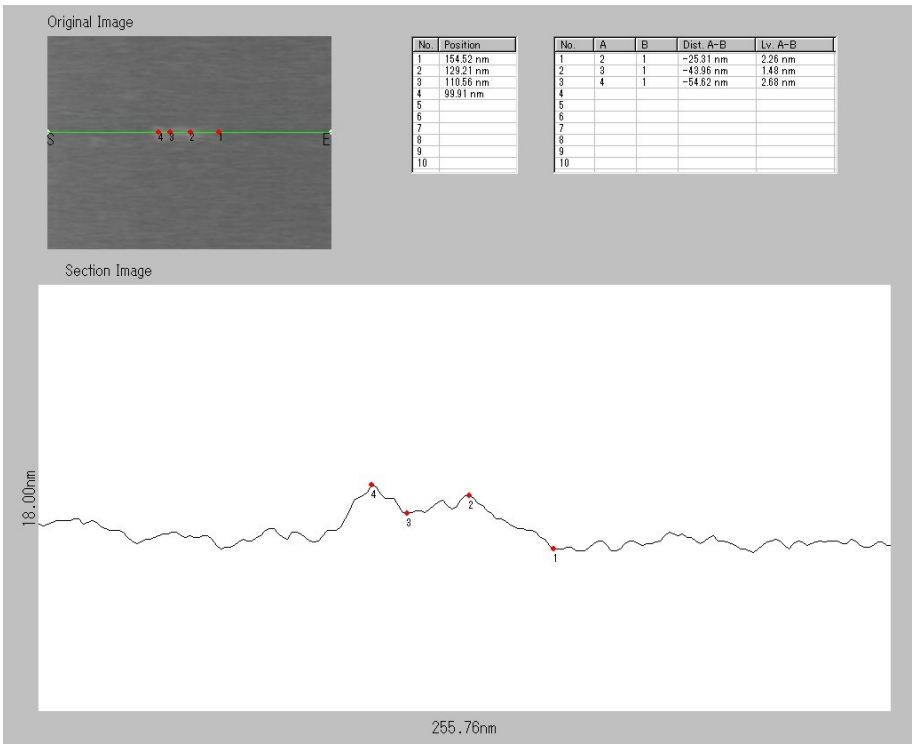

Fig. 3.3 Line profile of PEG_{100k}.

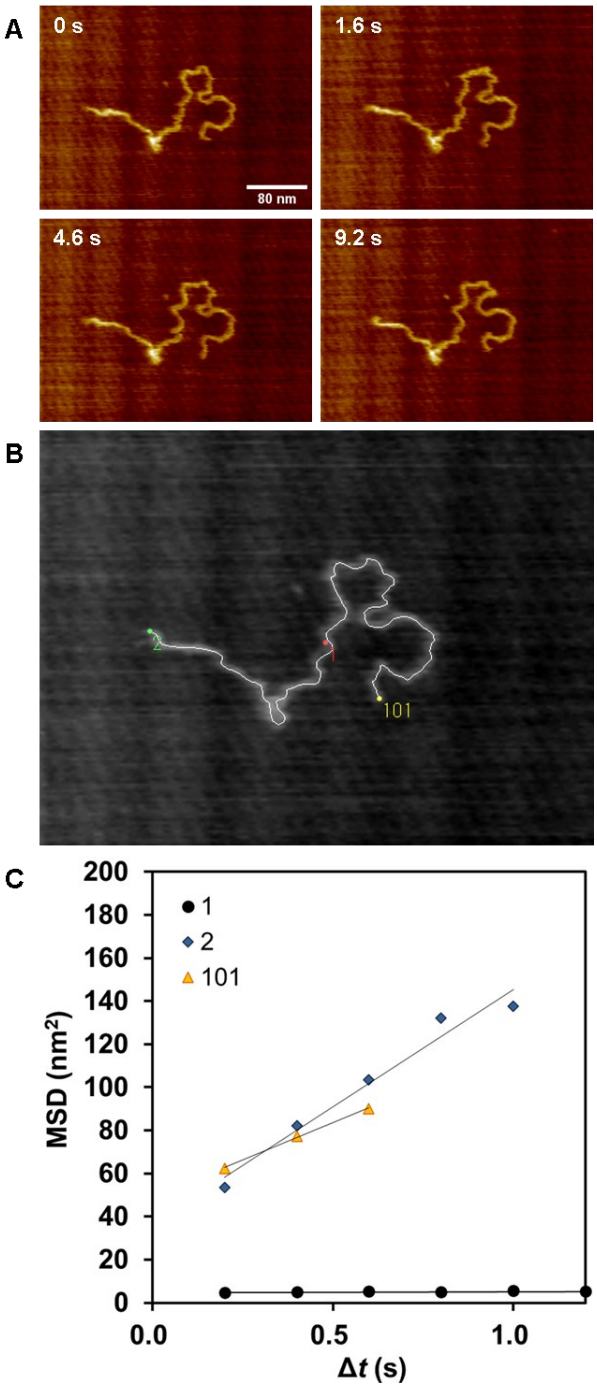

Fig. 3.4 FS-AFM imaging of a single molecule of PEG_{100k}@*α*-CD polypseudorotaxane at rate of 5.0 fps on mica 25 ± 1 °C. (A) AFM images from a movie. (B) Measurement points on a polymer chain for two-dimensional diffusion. FS-AFM image: x = 356 nm, y = 267 nm, z = 9.0 nm. (C) MSD–Δt plots for points 1, 2, and 101 in (B). D was calculated from the slope of the MSD/Δt line.

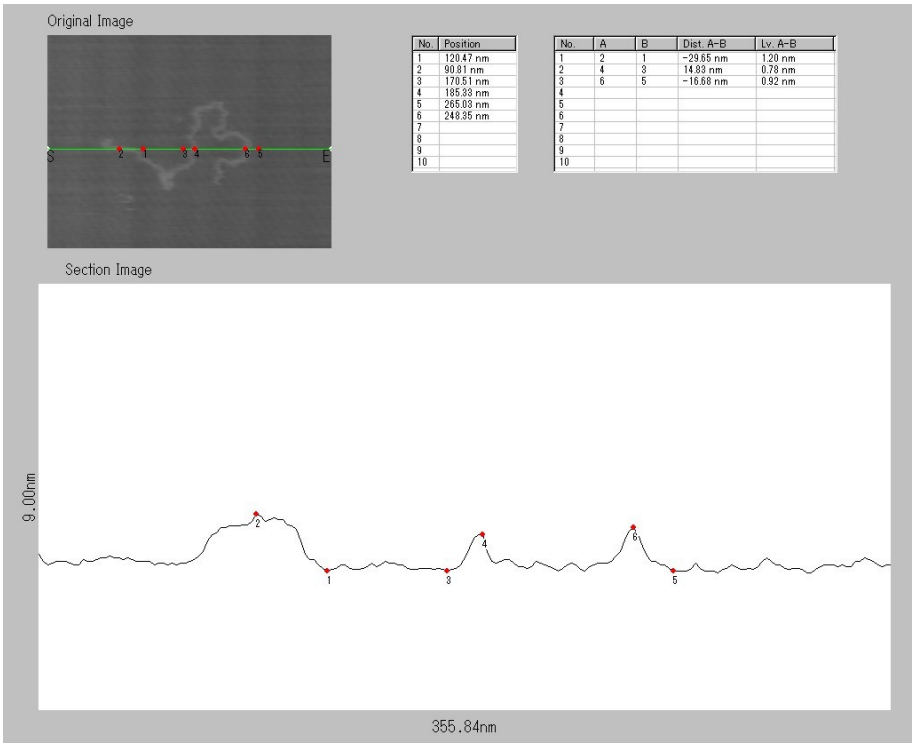

Fig. 3.5 Line profile of PEG$_{100k}$@*α*-CD polypseudorotaxane.

3.2.4 MSD plots

The dynamics of the polymer chain were determined by tracking the measurement point and plotting the mean square displacement (MSD) against Δt,

$$MSD(\Delta t) = \overline{\left[\Delta x(\Delta t)\right]^2 + \left[\Delta y(\Delta t)\right]^2} \tag{3.1}$$

where x and y are the coordinates of the tracked points. Diffusion coefficient D (nm^2/s) was calculated by dividing the slope of the linearly approximated MSD-Δt plots of the measurement points by four.[17] Measurement points for displacement were set at the chain ends (2, 101) and at the chain centroid (1) (for PEG$_{100k}$ see **Fig. 3.2B**, for PEG$_{100k}$@*α*-CD polypseudorotaxane see **Fig. 3.4B**). The mobility of each point determined from the trajectory data for the single chain was measured by AFM video imaging.

3.2.5 All-atom MD simulations

All-atom MD simulations were performed using the Forcite module of BIOVIA Materials Studio 2023 (Dassault Systèmes BIOVIA, San Diego, CA, USA) on a supercomputer system (PowerEdge R6525, Dell Technologies Inc., Round Rock, TX, USA). See the Supporting Information for more details (for PEG_{100k} see **Fig. 3.6**; for PEG_{100k}@α-CD polypseudorotaxane see **Fig. 3.7**).

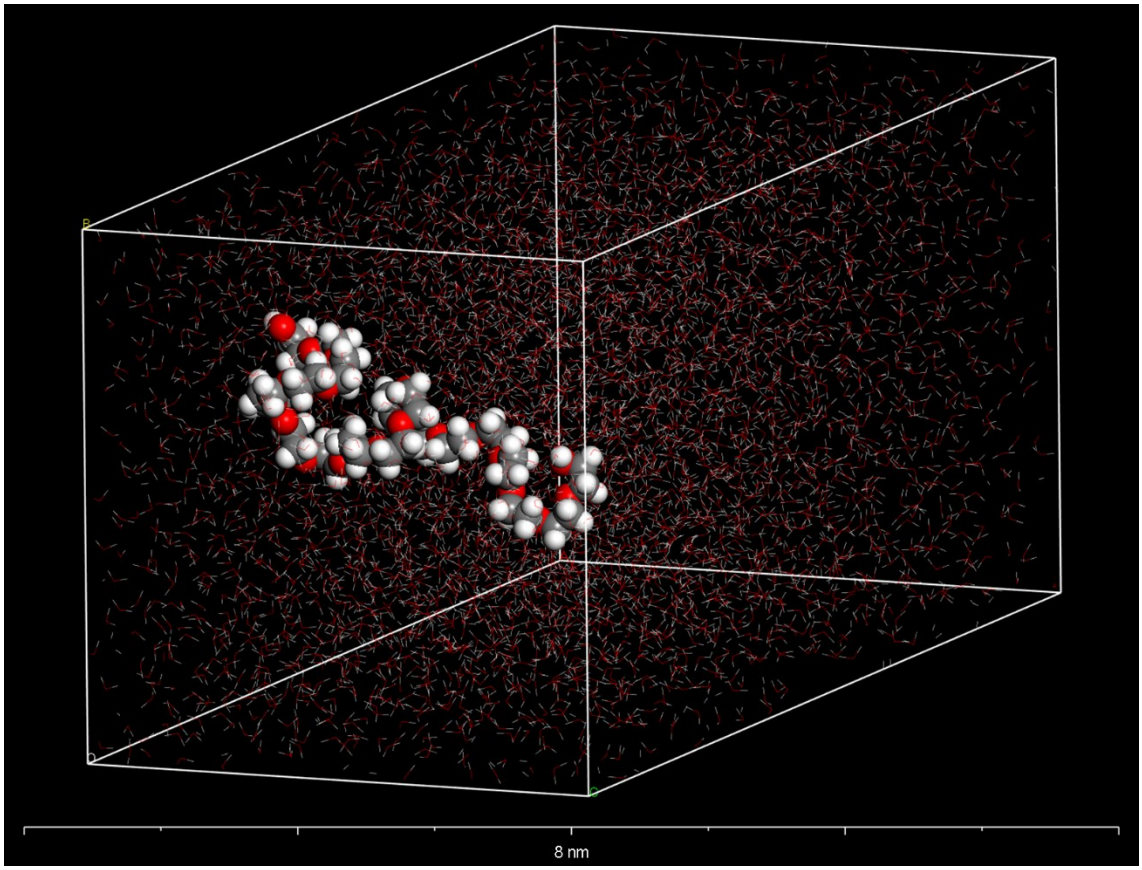

Fig. 3.6 A snapshot of all-atom MD simulation for PEG-20 mer at 50.0 ns.

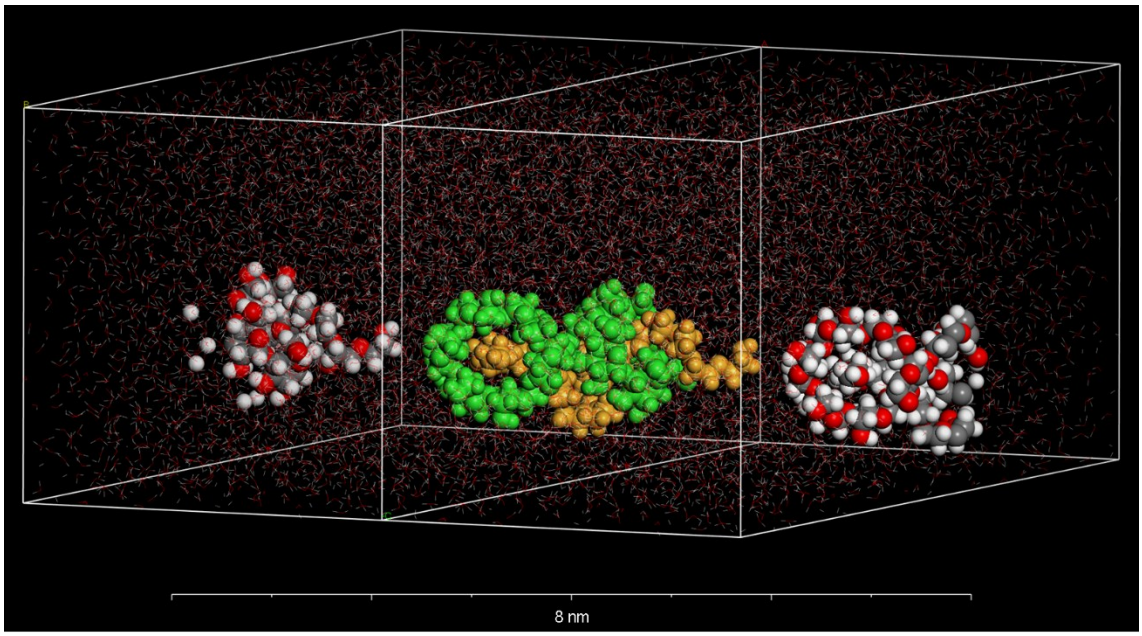

Fig. 3.7 A snapshot of all-atom MD simulation for PEG-20 mer (orange) included by two *α*-CDs (green) at 50.0 ns.

Fig. 3.8 shows the detailed sizes of each model after structural optimization calculation.

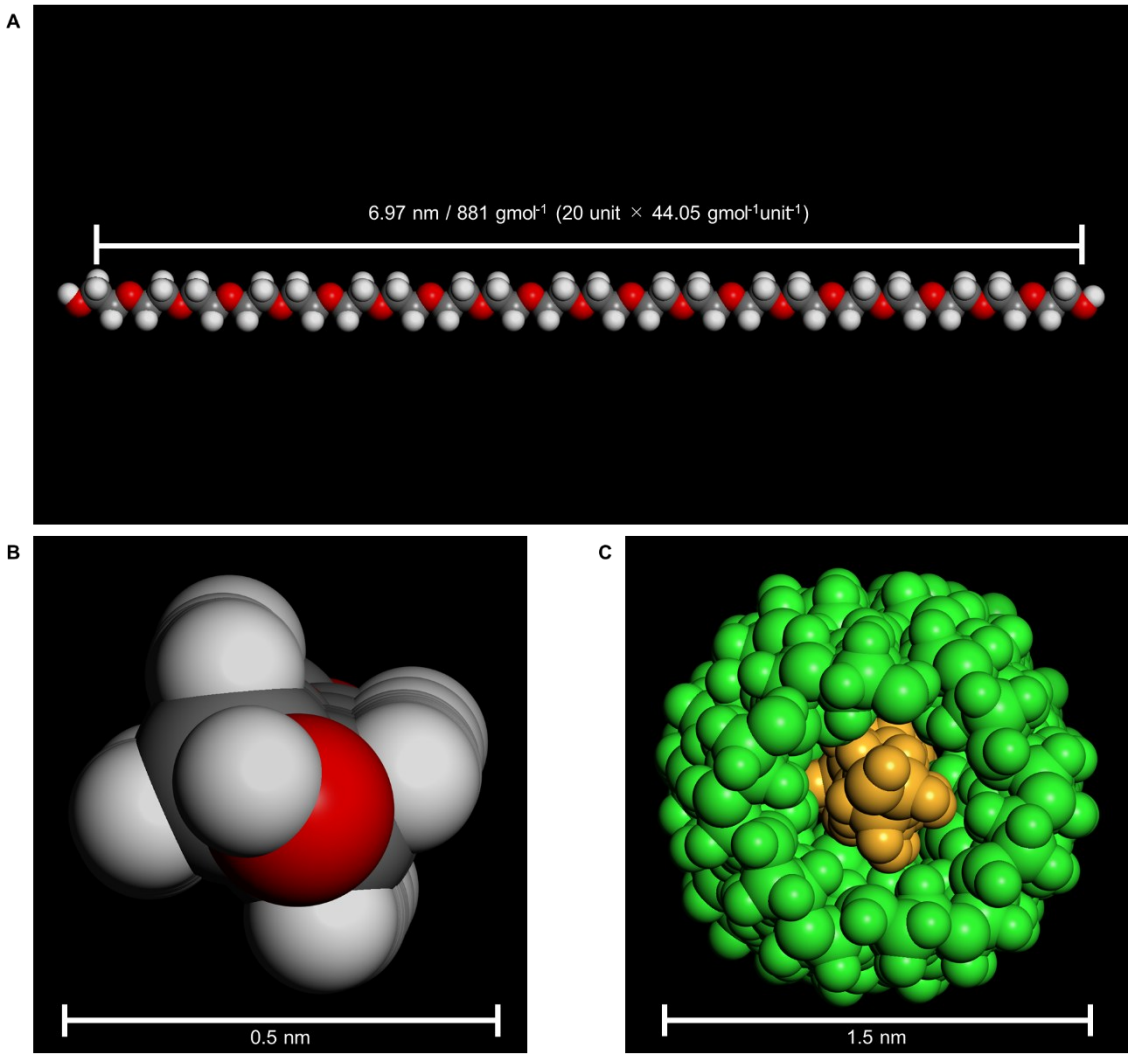

Fig. 3.8 The sizes of the models after structural optimization calculation. (A) The length of a model of PEG 20-mer. (B) The thickness of a model of PEG 20-mer. (C) The thickness of a model of PEG 20-mer (orange) included by 10 *α*-CDs (green).

3.3 Results and Discussion

Using an FS-AFM system modified for polymer observation, a single PEG_{100k} chain was observed in 15 mM KCl solution at 25 ± 1 °C (**Fig. 3.2**). Both ends of the polymer chain formed bulky globules, creating a dumbbell-shaped structure. The polymer chain length was measured in each frame, and the

minimum was 27.6 nm, the maximum was 69.7 nm, the average was 48.1 nm, and the standard deviation was 9.38 nm (**Fig. 3.9A** and **B**). The length of PEG_{100k} was measured as 48.1 nm, which was substantially smaller than the calculated value of 6.97 nm/881 g mol^{-1} × (1.0 × 10^6 g mol^{-1}) ≅ 790 nm (**Fig. 3.8A**). The difference between the observed (>1.4 nm, **Fig. 3.3**) and calculated (<0.5 nm, **Fig. 3.8B**) thicknesses supported the self-shrinking behavior of the PEG chain. To understand this behavior better, a length‑time plot revealed spring-like shrinking and extending motions (**Fig. 3.9C**). The trajectories of both ends of the polymer chain (points 2 and 101) and its centroid (point 1) were tracked and measured (**Fig. 3.2B**). No plot was made for the center of the chain because it was difficult to track the location owing to the length changes. The MSD was plotted against time interval Δt (**Fig. 3.2C**). From the measurements, diffusion coefficients for the points were obtained as D_1 = 37.3 nm²/s, D_2 = 0.8 nm²/s, and D_{101} = 169.2 nm²/s. D_{101} for one end of the chain (point 101) was about 212 times larger than that for the other end (point 2), highlighting considerable asymmetry in chain mobility. D_1 for the centroid, representing the polymer chain's Brownian motion, was approximately 47 times larger than D_2 and about one-quarter (1/4.5) of D_{101}. The large difference arose because the micro-Brownian motion of one end of the molecule (point 2) was suppressed because it adhered strongly to the substrate, whereas the other end (point 101) moved relatively freely because it interacted weakly with the substrate. At the solid–liquid interface, fixing one end of a flexible polymer chain that does not bind strongly to the substrate surface produces a mushroom conformation at low concentrations,[19, 20] and PEG exhibits similar behavior in water.[21, 22] In the present study, the MSD plot results demonstrated that the behavior resembled that of a polymer chain with one end fixed. Consequently, the contracted PEG chain probably also exhibited a mushroom conformation.

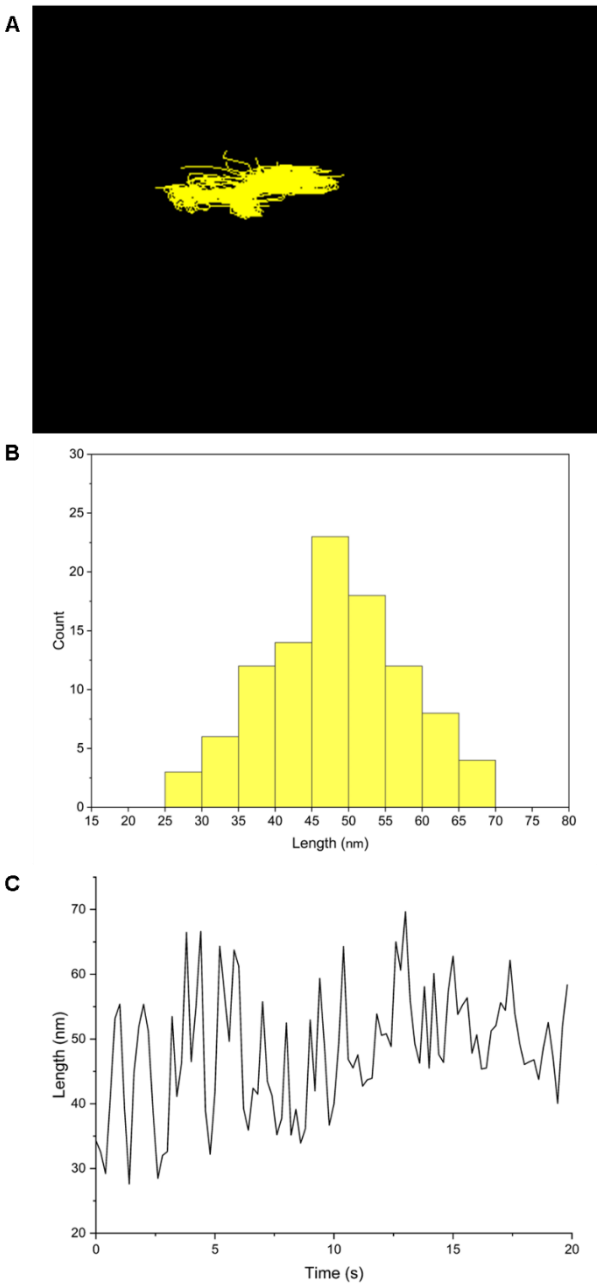

Fig. 3.9 Motion analysis of PEG_{100k}. (A) Trajectory of the Brownian motion of PEG_{100k} on mica. (B) Length histogram of PEG_{100k}. (C) Plot of PEG_{100k} length versus time.

A single PEG_{100k}@α-CD polypseudorotaxane chain was observed by FS-AFM in 15 mM KCl solution at 25 ± 1 °C (**Fig. 3.4**). The chain length was measured in each frame, and the minimum was 472.4 nm, the maximum was 528.4 nm, the average was 499.6 nm, and the standard deviation was 11.4 nm (**Fig. 3.10A** and **B**). The observed length of the polymer chain was 499.6 nm, which was close

to the calculated value (790 nm, **Fig. 3.8**), suggesting that the polymer chain adopted an extended structure. If the chain were a PEG chain without α-CD, the thickness would be close to the calculated value (<0.5 nm, **Fig. 3.8B**); however, the value measured from the line profile was approximately 1 nm (**Fig. 3.5**). Considering the effects of tapping,[23] this value closely matched the calculated thickness of PEG@*α*-CD polypseudorotaxane (approximately 1.5 nm, **Fig. 3.8C**). Additionally, the increased rigidity and linearity of the observed polymer chain compared with PEG_{100k} (**Fig. 3.2**) and the absence of the extended structures seen in **Fig. 3.10** for PEG_{100k} without *α*-CD supported the identification of the chain as PEG_{100k}@*α*-CD polypseudorotaxane.[24] Therefore, we concluded that the observed polymer chain was PEG_{100k}@*α*-CD polypseudorotaxane. A length–time plot showed that the polypseudorotaxane also exhibited shrinking and extending motions, clarifying the dynamic behavior of this structure further (**Fig. 3.10C**). To determine whether this length change was caused by violent motion at the ends of the molecular chain or changes in the central part of the chain, the length excluding both ends was measured. The minimum length was 388.4 nm, the maximum was 435.2 nm, the average was 411.3 nm, and the standard deviation was 8.2 nm (**Fig. 3.10D** and **E**). The initial and end points of the central part were defined as the points that interacted strongly with the substrate and were not affected by chain-end movement. MSD plots of the initial and end points of the central part are shown in **Fig. 3.11**. A length–time plot revealed that the central part of the polypseudorotaxane chain also exhibited shrinking and extending motions (**Fig. 3.10F**). If the entire PEG chain were tightly included by the *α*-CDs, this type of bending or stretching would not occur. Maeda and Ito reported that in a polypseudorotaxane with high-molecular-weight PEG, portions of the axial components remained exposed to gain entropy.[25] Therefore, we inferred that exposed PEG segments formed random coils or globules in the chain, and that the shrinking and extending motions were caused by repeated expansion and re-shrinking from the self-shrinking state, driven by the shuttling of *α*-CD. This inference was supported by the continuous height change observed in FS-AFM imaging (**Fig. 3.12** and

Table 3.1). Additionally, no major reduction in the polymer chain length was observed during the imaging, likely because there were end-cap structures at the ends of the polypseudorotaxane similar to the globules at both ends of the PEG chain (**Fig. 3.2A**). This end-capping effect suppressed the release of α-CD. Next, the trajectories of both ends of the polymer chain (points 2 and 101) and its centroid (point 1) were tracked and measured (**Fig. 3.4B**). As with the PEG_{100k} chain, the central part of the molecular chain was not plotted due to the difficulty in tracing the same location caused by length changes. The MSD was plotted against time interval Δt (**Fig. 3.4C**). From the measurements, diffusion coefficients D_1 = 0.3 nm²/s, D_2 = 27.3 nm²/s, and D_{101} = 17.3 nm²/s were obtained. D_{101} for one end of the chain (point 101) was approximately 1.6 times larger than D_2 for the other end (point 2). D_1 for the centroid, representing the Brownian motion of the polymer chain, was approximately 1/273 of D_2 and 1/173 of D_{101}. The difference in diffusion coefficients at both ends was attributed to the difference in the shapes of the globules at the chain ends.

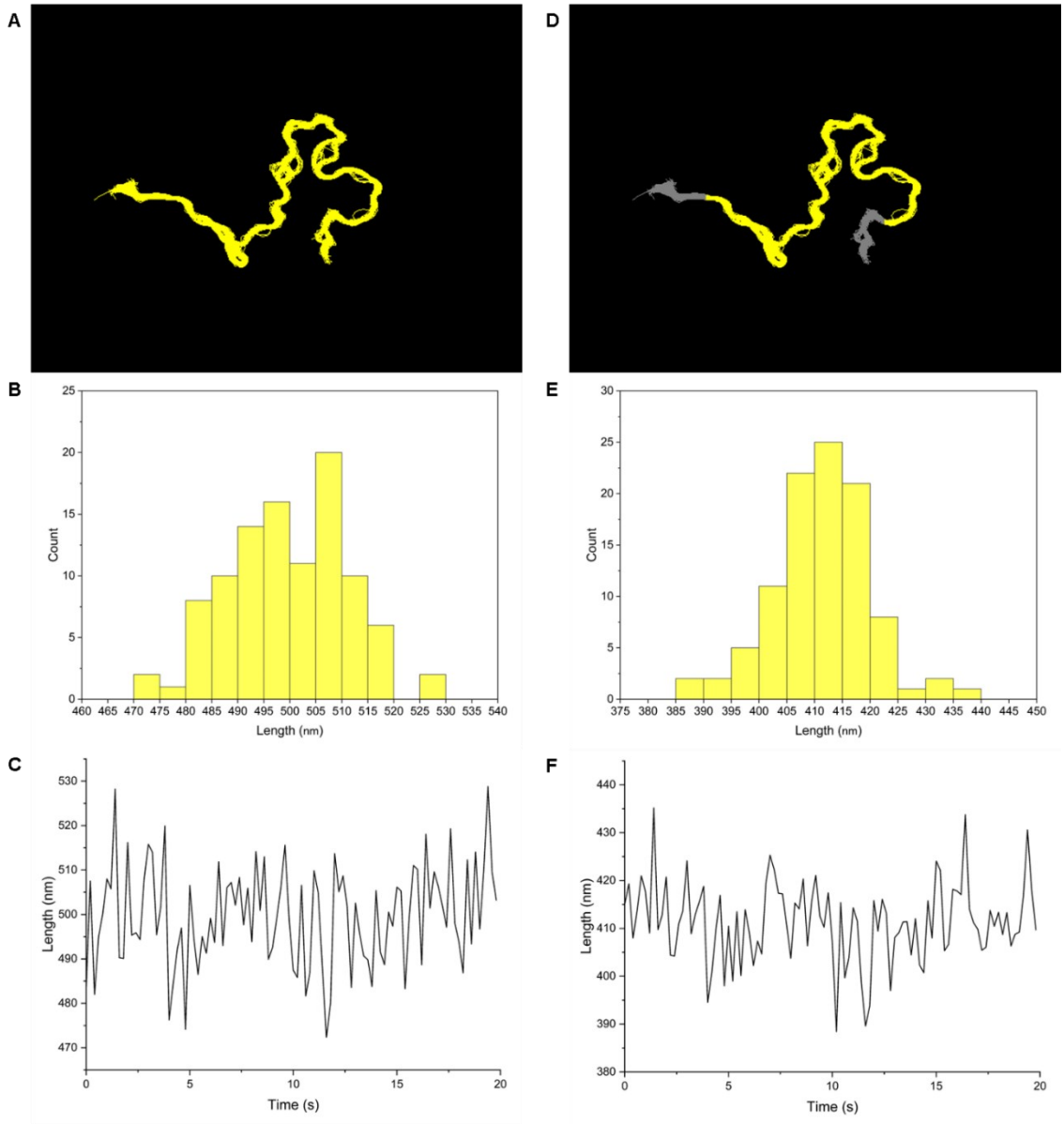

Fig. 3.10 Motion analysis of the entire PEG_{100k}@*α*-CD polypseudorotaxane chain. (A) Trajectory of the Brownian motion of the entire polypseudorotaxane chain on mica. (B) Length histogram of the entire polypseudorotaxane chain. (C) Plot of the entire polypseudorotaxane chain length versus time. (D) Trajectory of the Brownian motion of the polypseudorotaxane chain, excluding the chain ends on mica. (E) Length histogram of the polypseudorotaxane chain, excluding the chain ends. (F) Plot of the length versus time for the polypseudorotaxane chain, excluding the chain ends.

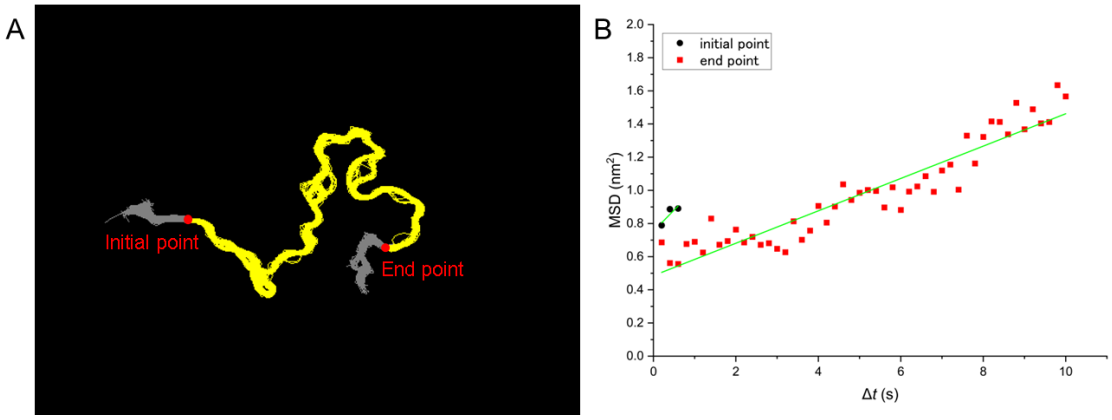

Fig. 3.11 MSD plots for the initial and end points of the central part of the polypseudorotaxane chains, excluding the chain ends. (A) Locations of the initial and end points. (B) MSD plots.

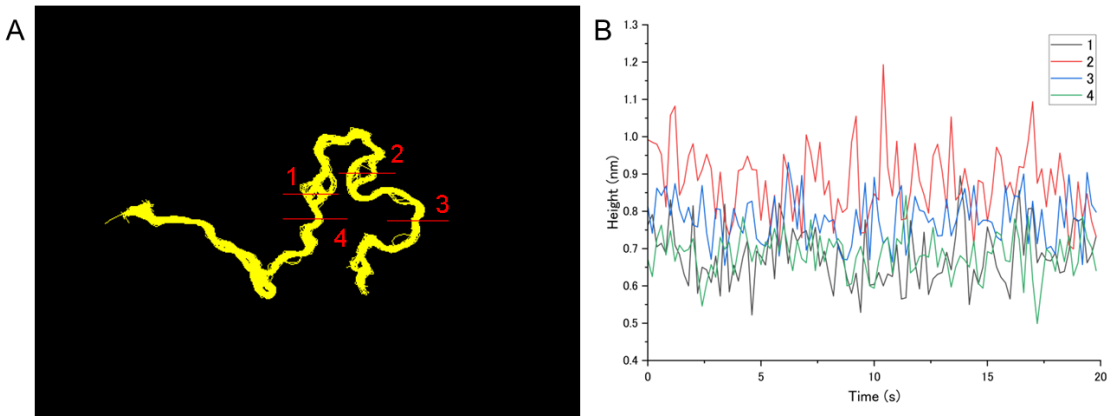

Fig. 3.12 Height changes at positions showing different mobilities. (A) Positions of high mobility (points 1 and 2) and low mobility (points 3 and 4) where height changes were measured. (B) Height–time plots of each position.

Table 3.1 Height changes of each position in Fig. 3.12.

	Min. (nm)	Max. (nm)	Ave. (nm)	σ (nm)
1	0.52	0.90	0.68	0.08
2	0.46	0.82	0.62	0.07
3	0.66	0.93	0.78	0.07
4	0.50	0.84	0.68	0.06

All-atom MD simulations corroborated the FS-AFM observations, showing that PEG segments alternated between self-shrinking and extended states as α-CDs shuttled along the chain. Throughout the calculation, the entire 20-mer PEG chain remained self-shrunk (**Fig. 3.6** and **Fig**. 3.13). The structure was highly flexible, reproducing the dynamics of the PEG chain observed by FS-AFM. The structure and the shrinking and extending motions closely resembled those reported in previous studies.[26, 27]

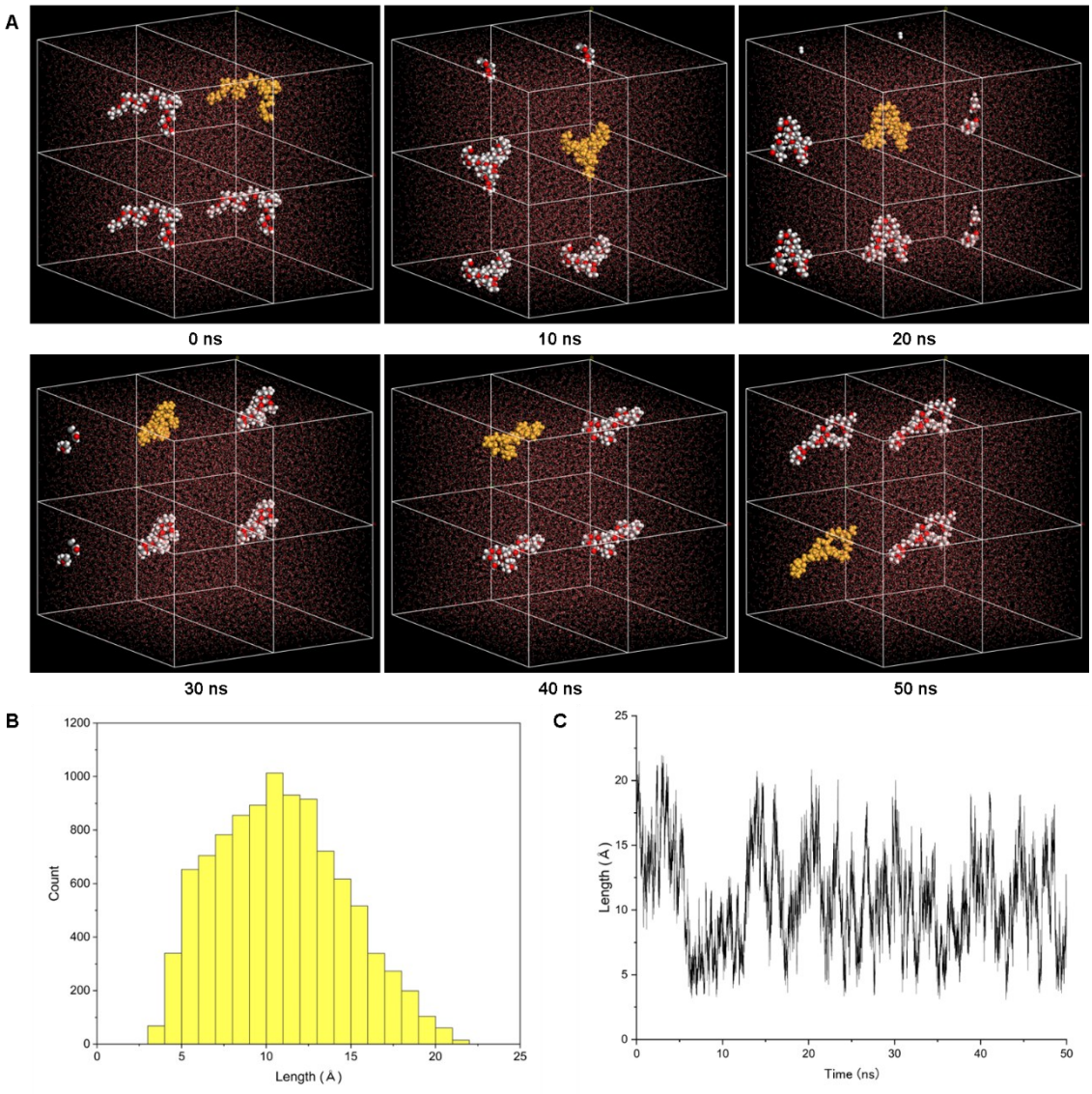

Fig. 3.13 Motion analysis for the model of the PEG 20-mer, excluding terminal 6-mers, simulated by all-atom MD. (A) Snapshots of all-atom MD by the microcanonical ensemble (NVE) after equilibration at 298 K in water. (B) Length histogram of the PEG chain, excluding terminal 6-mers (*n*=10001). (C) The plot of the length versus time for the PEG chain, excluding terminal 6-mers.

In the polypseudorotaxane chain with two α-CDs including the 20-mer PEG chain, the PEG ends remained self-shrunk, and the central part of the molecular chain without α-CDs also formed a self-shrunk structure (**Fig. 3.14**). The contraction of the exposed PEG segments has also been confirmed

in several studies, supporting the accuracy of our calculation results.[28, 29] The end-to-end distance of the central 8-mer, excluding the 6-mers at both PEG chain ends, was measured as a minimum of 0.29 nm, maximum of 2.47 nm, and average of 1.53 nm, with a standard deviation of 0.43 nm (**Fig. 3.14B**). A plot of the distance between the chain ends of the central 8-mer of PEG versus time also revealed shrinking and extending motions (**Fig. 3.14C**). Furthermore, a strong negative correlation (correlation coefficient = −0.74, **Fig. 3.14E**) was observed between the distance between chain ends of central 8-mer of PEG (**Fig. 3.14C**) and the sum of the distances from the central atom of the PEG chain to the centroids of the two α-CDs (**Fig. 3.14D**). In other words, the farther the two α-CDs moved away from the center of the PEG chain (exclusion of the central part of the PEG chain), the more the central part of the PEG chain self-shrunk, shortening the end-to-end distance of the central 8-mer. Conversely, the closer the α-CDs moved toward the center of the PEG chain (inclusion of the PEG chain center), the more the central part of the PEG chain tended to adopt a rigid, fully extended structure. These results strongly support the conclusion that the shrinking and extending motions of the polypseudorotaxane are linked to the shuttling motion of the α-CDs.

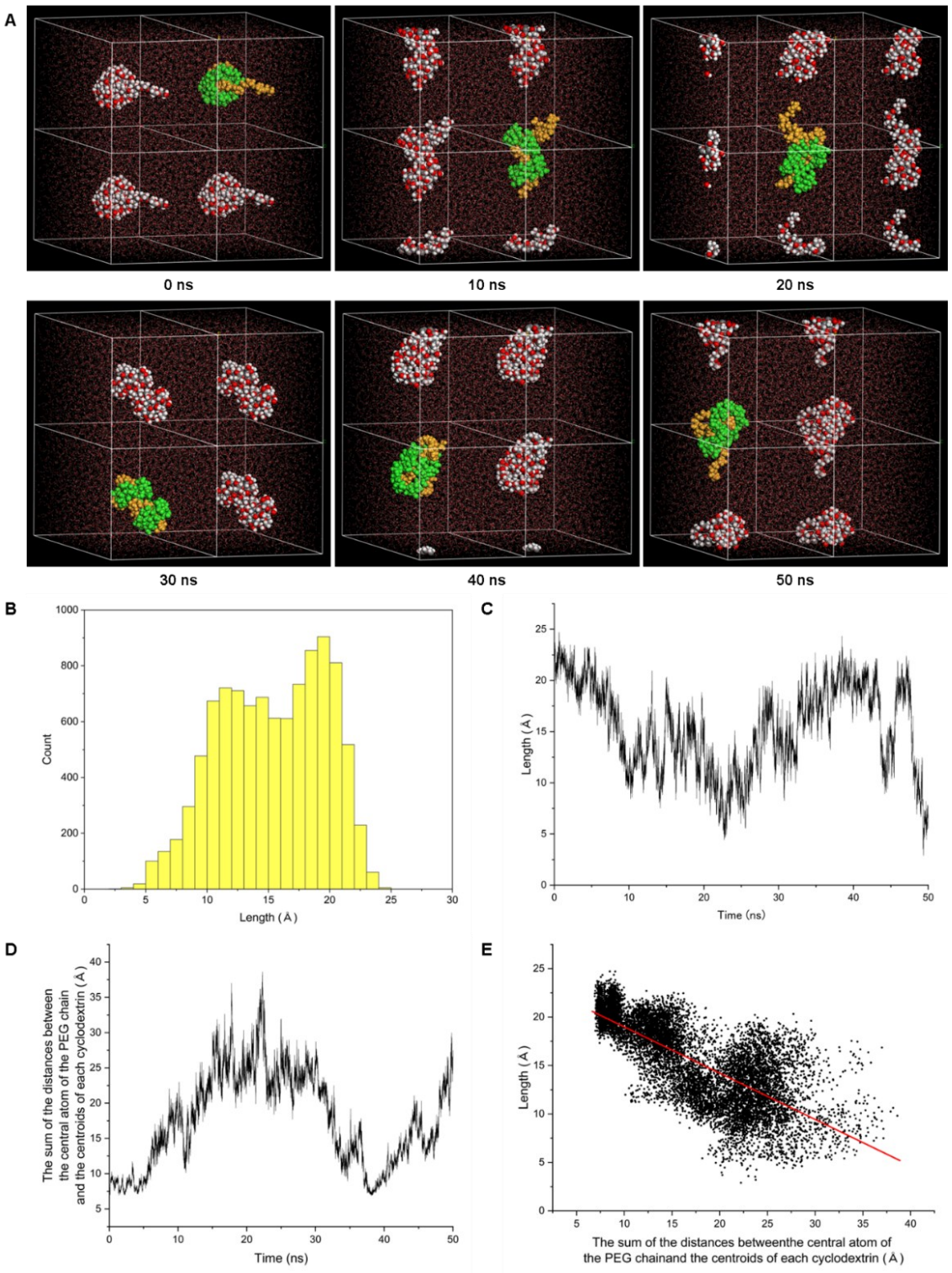

Fig. 3.14 Motion analysis for the model of the PEG 20-mer included in two *α*-CDs, excluding terminal 6-mer units, simulated by all-atom MD. (A) Snapshots from all-atom MD simulations in the microcanonical ensemble (NVE) after equilibration at 298 K in water. (B) Length

histogram of the polypseudorotaxane chain, excluding terminal 6-mers (*n* = 10,001). (C) Plot of the distance between chain ends of the PEG central 8-mer versus time, excluding terminal 6-mers. (D) Plot of the sum of the distances between the central atom of the PEG chain and the centroids of each cyclodextrin versus time for the polypseudorotaxane chain, excluding terminal 6-mers. (E) Scatter plot of the distance between chain ends of the PEG central 8-mer versus the sum of the distances between the central atom of the PEG chain and the centroids of each cyclodextrin (*n* = 10,001; correlation coefficient = −0.74).

3.4 Conclusion

The PEG@*α*-CD polypseudorotaxane, with high-molecular-weight PEG (M_w = 1.0 × 10^5 g/mol) as the axial component, remained stable in aqueous solution due to the end-capping effect caused by globule formation at the chain ends. Because the polypseudorotaxane maintained a stable, linear structure at the solid–liquid interface, it has the properties required for use as a rail molecule in synthetic polymer motors, suggesting its potential application as a synthetic polymer motor driven by thermal fluctuations. The polypseudorotaxane chain contained exposed, self-shrinking PEG segments and the chain exhibited shrinking and extending motions driven by *α*-CD shuttling. The discovery of the local structural changes driven by *α*-CD shuttling improves our understanding of rotaxane-based polymer materials and their functional properties. Furthermore, major differences were observed in the structure and dynamics between PEG_{100k} and PEG_{100k}@*α*-CD polypseudorotaxane. This indicates that FS-AFM is a promising method for analyzing supramolecular materials, especially where conventional spectroscopic techniques are unsuitable for structural analysis.

3.5 Reference

1. M. Nakahata, S. Mori, Y. Takashima, H. Yamaguchi and A. Harada, Self-Healing Materials Formed by Cross-Linked Polyrotaxanes with Reversible Bonds. *Chem* **2016**, *1* (5), 766-775. https://doi.org/10.1016/j.chempr.2016.09.013

2. A. Harada and M. Kamachi, Complex formation between poly(ethylene glycol) and α-cyclodextrin. *Macromolecules* **1990**, *23* (10), 2821-2823. https://doi.org/10.1021/ma00212a039
3. A. Harada, Y. Takashima and H. Yamaguchi, Cyclodextrin-based supramolecular polymers. *Chem. Soc. Rev.* **2009**, *38*, 875-882. https://doi.org/10.1039/B705458K
4. T. Zhao and H. W. Beckham, Direct Synthesis of Cyclodextrin-Rotaxanated Poly(ethylene glycol)s and Their Self-Diffusion Behavior in Dilute Solution. *Macromolecules* **2003**, *36* (26), 9859-9865. https://doi.org/10.1021/ma035513f
5. K. Shinohara, M. Yanagisawa and Y. Makida, Direct Observation of Long-Chain Branches in a Low-Density Polyethylene. *Sci Rep* **2019**, *9*, 9791. https://doi.org/10.1038/s41598-019-46035-9
6. K. Shinohara and Y. Makida, Direct observation of dynamic interaction between a functional group in a single SBR chain and an inorganic matter surface. *Sci Rep* **2018**, *8*, 13982. https://doi.org/10.1038/s41598-018-32382-6
7. N. Kodera, D. Yamamoto, R. Ishikawa, T. Ando, Video imaging of walking myosin V by high-speed atomic force microscopy. *Nature* **2010**, ***468***, 72-76. https://doi.org/10.1038/nature09450
8. M. Kaya, H. Higuchi, Nonlinear Elasticity and an 8-nm Working Stroke of Single Myosin Molecules in Myofilaments. *Science* **2010**, *329*, 686-689. https://doi.org/10.1126/science.1191484
9. Okada, Y., Higuchi, H. & Hirokawa, N. Processivity of the single-headed kinesin KIF1A through biased binding to tubulin. *Nature* **2003**, *424*, 574-577. https://doi.org/10.1038/nature01804
10. M. Ceccato, P. L. Nostro, C. Rossi, C. Bonechi, A. Donati and P. Baglioni, Molecular Dynamics of Novel α-Cyclodextrin Adducts Studied by ^{13}C-NMR Relaxation. *J. Phys. Chem.* **1997**, *101* (26), 5094-5099. https://doi.org/10.1021/jp9638447
11. T. Karino, Y. Okumura, C. Zhao, T. Kataoka, K. Ito and M. Shibayama, SANS Studies on Deformation Mechanism of Slide-Ring Gel. *Macromolecules* **2005**, *38* (14), 6161-6167. https://doi.org/10.1021/ma050624v
12. K. Mayumi, N. Osaka, H. Endo, H. Yokoyama, Y. Sakai, M. Shibayama and K. Ito, Concentration-Induced Conformational Change in Linear Polymer Threaded into Cyclic

Molecules. *Macromolecules* **2008**, *41* (17), 6480-6485. https://doi.org/10.1021/ma801021g

13. J. Araki and K. Ito, Recent advances in the preparation of cyclodextrin-based polyrotaxanes and their applications to soft materials. *Soft Matter* **2007**, *3*, 1456-1473. https://doi.org/10.1039/B705688E
14. K. Shinohara, Y. Makida, T. Oohashi and R. Hori, Single-Molecule Unidirectional Processive Movement along a Helical Polymer Chain in Non-aqueous Medium. *Langmuir* **2022**, *38* (40), 12173-12178. https://doi.org/10.1021/acs.langmuir.2c01704
15. R. Hori, K. Higashimine, O. Notoya and K. Shinohara, Synthesis and Direct Observation of Chiral Supramolecular Polymer of Porphyrin Having Cholesteryl Groups. *Langmuir* **2024**, *40* (10), 5535-5544. https://doi.org/10.1021/acs.langmuir.4c00164
16. Transforming our world: the 2030 Agenda for Sustainable Development. Resolution adopted by the UN General Assembly, September 25, 2015. https://sustainabledevelopment.un.org/post2015/transformingourworld (accessed December 22, 2023).
17. K. Shinohara, Single-Molecule Imaging of a Polymer: Direct Observation of Structure and Dynamics in a Polymer Chain. *Kobunshi Ronbunshu* **2016**, *73*, 491-504. https://doi.org/10.1295/koron.2016-0034
18. K. Shinohara, *Applied Scanning Probe Methods X -Biomimetics and Industrial Applications*, Chapter 31: Scanning Probe Microscope Application for Single Molecules in a π-Conjugated Polymer toward the Molecular Devices based on Polymer Chemistry, pp 153-182, B. Bhushan, H. Fuchs, M. Tomitori (Eds.), Springer (Berlin, Heidelberg), ISBN: 978-3-540-74084-1 (2008). https://doi.org/10.1007/978-3-540-74085-8_5
19. P. G. de Gennes, Conformations of Polymers Attached to an Interface. *Macromolecules* **1980**, *13*, 1069–1075. https://doi.org/10.1021/ma60077a009
20. P.G. de Gennes, Polymers at an interface; a simplified view. *Adv. Colloid Interface Sci.* **1987**, *27* (3–4), 189–209. https://doi.org/10.1016/0001-8686(87)85003-0
21. A. A. D'souza and R. Shegokar, Polyethylene glycol (PEG): a versatile polymer for

pharmaceutical applications. *Expert Opin. Drug Deliv.* **2016**, *13* (9), 1257–1275. https://doi.org/10.1080/17425247.2016.1182485

22. J. V. Jokerst, T. Lobovkina, R. N. Zare and S. S. Gambhir, Nanoparticle PEGylation for Imaging and Therapy. *Nanomed.* **2011**, 6(4), 715–728. https://doi.org/10.2217/nnm.11.19
23. Y. C. Chang, C. S. Chang, D. C. Wang, M. H. Lee, T. F. Wang, M. Y. Wu, T. Y. Fu, and T. T. Tsong, Nanoscale Imaging of Biomolecules by Controlled Carbon Nanotube Probes. *Jpn. J. Appl. Phys.* **2004**, *43*, 4517–4520. https://doi.org/10.1143/JJAP.43.4517
24. K. Mayumi, Molecular dynamics and structure of polyrotaxane in solution. *Polym J.* **2021**, *53*, 581–586. https://doi.org/10.1038/s41428-020-00457-9
25. S. Uenuma, R. Maeda, H. Yokoyama and K. Ito, Formation of Isolated Pseudo-Polyrotaxane Nanosheet Consisting of α-Cyclodextrin and Poly(ethylene glycol). *Macromolecules* **2019** *52* (10), 3881–3887. https://doi.org/10.1021/acs.macromol.9b00491
26. H. Lee, R. M. Venable, A. D. MacKerell Jr. and R. W. Pastor, Molecular Dynamics Studies of Polyethylene Oxide and Polyethylene Glycol: Hydrodynamic Radius and Shape Anisotropy. *Biophys. J.* **2008**, *95* (4), 1590–1599. https://doi.org/10.1529/biophysj.108.133025
27. S.A. Oelmeier, F. Dismer and J. Hubbuch, Molecular dynamics simulations on aqueous two-phase systems - Single PEG-molecules in solution. *BMC Biophys* **2012**, *5*, 14. https://doi.org/10.1186/2046-1682-5-14
28. X. Cai, H. Liu and G. Zhang, Control of the threading ratio of rings in a polypseudorotaxane: A computer simulation study. *Polymer* **2023**, *22*, 125705. https://doi.org/10.1016/j.polymer.2023.125705
29. N. Urakami, J. Imada, T. Yamamoto, Simulation of pseudopolyrotaxane formation and orientational order between pseudopolyrotaxanes. *J. Chem. Phys.* **2010**, *132*, 054901. https://doi.org/10.1063/1.3298995

Chapter 4. Single-Molecule Unidirectional Processive Movement along a Helical Polymer in Non-aqueous Medium

4.1 Introduction

If a single molecule can move unidirectionally to generate force, a molecular motor can be created to transport material and effect morphological change. In living systems, not only are these functions already realized, they are often highly organized. A synthetic molecular machine with even some of the biological function would require an innovative design concept. The principles by which proteins work in the fields of molecular biology and biophysics are being clarified.[1-3] By applying these concepts to the design of synthetic molecules, it should be possible to create molecular machines with characteristics that respond to environmental changes such as stimuli and load that are comparable to biomolecular machines.

Synthetic molecular machines reported recently include catenane,[4] a molecular shuttle called rotaxane,[5] a light-driven molecular rotor that rotates in one direction,[6] and nanocar,[7] which glides on metal substrates. However, these are small molecules, and are limited in terms of the development of more advanced functions such as substance transport and the generation of force. A molecular motor in which a molecule "walks" along a molecular rail requires the control of intermolecular interactions with the solvent. However, the interaction points in low-molecular-weight molecules are small, and the secondary bonds between molecules dissociate owing to collisions with the surrounding solvent molecules. Therefore, the motor function disappears. However, it is expected that molecular motors could be produced using polymers capable of dynamic multipoint interactions between molecules.

The motor protein actomyosin, which is found in muscles, is an example of a biomacromolecule. It comprises a complex of the rail protein F-actin and the walking molecule myosin,[2] and enables physical exercise. However, artificial synthetic molecules (polymers) have still not been used as molecular motors. We speculated whether it would be possible to artificially create molecular motors like actomyosin. The function of a molecular motor comprising a synthetic polymer could be dictated by molecular design according to the method of organic synthesis used, and appropriate stability could be expected.

In the biomolecular motor described above, the actin filament (F-actin) of the rail is formed by the polymerization of spherical G-actin, and the resulting molecule has a chiral helix structure. Myosin

walks unidirectionally along F-actin while fluctuating in an aqueous solution, with each step using energy derived from the hydrolysis of adenosine triphosphate (ATP). That is, actomyosin is a molecular motor that is driven by biased Brownian motion.[2]

For a molecular motor to function, a rail comprising a periodic structure is required on the surface to function as a scaffold for the walking molecules. Therefore, to fulfil the expected intermolecular interaction we designed a main chain polymer with a periodic surface structure comprising a helix, and a polymer with pendant cholesteryl groups.

4.2 Experimental

4.2.1 Materials

(–)-Cholesterol, 4-bromobenzoic acid, 2-methyl-3-butyn-2-ol were purchased from Kanto Kagaku (Tokyo, Japan). Bis(triphenylphosphine)palladium(II) chloride, sodium hydride were from Wako Pure Industries (Osaka, Japan). Thionyl chloride was from Nacalai tesque (Kyoto, Japan). Bicyclo[2.2.1]hepta-2,5-diene-rhodium(I) chloride dimmer {$[Rh(nbd)Cl]_2$} was from Sigma-Aldrich (Missouri, USA).

4.2.2 Synthesis of a Chiral Helical Polymer

Method: (–)-Poly(ChOCPA) was prepared following section, its weight average molecular mass (M_w) and molecular weight distribution (M_w/M_n) was determined by GPC (SEC) equipped with TSKgel GMH_{XL} column (Tosoh, Tokyo, Japan) in tetrahydrofuran with polystyrene standards calibration. ^1H NMR spectra were recorded on an AVANCE III 400 MHz (Bruker, MA, USA). Mass spectra were measured using surface-assisted laser desorption/ionization time-of-fight mass spectra (SALDI-TOF-MS) ultrafleXtreme (Bruker, MA, USA). IR spectra were obtained using Perkin Elmer (MA, USA) Spectrum One FT-IR spectrometer. CD spectra were measured using a J-820 spectropolarimeter (Jasco, Tokyo, Japan). Concentration of polymer tetrahydrofuran solution is 1.0×10^{-4} mol/L and the concentration of (+)-poly(ChOCPA) was calculated based on the monomer units.

(−)-Poly(ChOCPA) was synthesized as follows (**Scheme 4.1**).

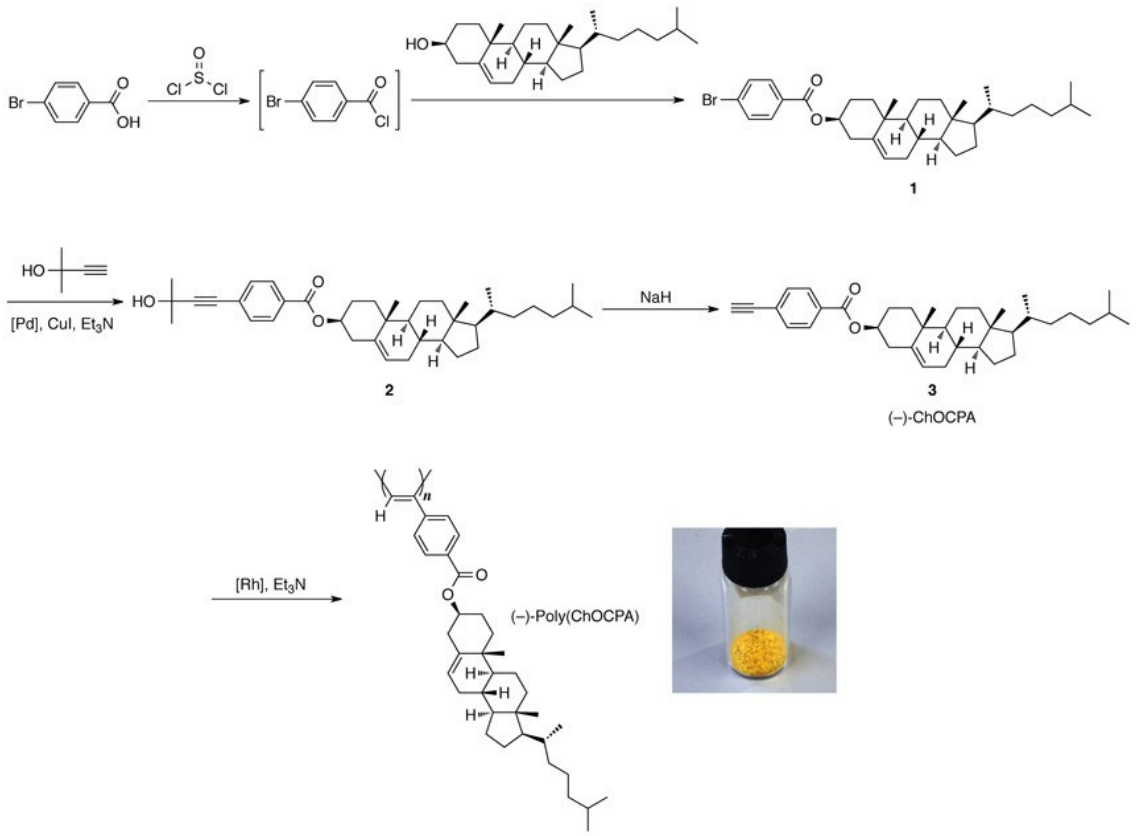

Scheme 4.1 Synthesis of (–)-poly(ChOCPA).

4-{(–)-Cholesteryloxycarbonyl}bromobenzene (1)

Thionyl chloride (10.0 mL, 139 mmol) was added to 4-bromobenzoic acid (1.00 g, 4.97 mmol) and stirring was continued at the reflux temperature for 3 h. The remaining thionyl chloride was evaporated to give a white solid, which was added to a toluene (10.0 mL) solution of (–)-cholesterol (1.92 g, 4.97 mmol). This solution was stirred for 12 h at the reflux temperature. The solvent was evaporated, and the crude product was purified by recrystallization using hexane and reprecipitation from THF solution into methanol. The resulting product was white crystal. Yield: 46%; $[\alpha]_D^{20}$ = –8.90º (c 1.00, chloroform); ^{1}H NMR (400 MHz, $CDCl_3$, TMS) δ (ppm) 7.90 (d, J = 8.65 Hz, 2H, *o*-COAr*H*), 7.57 (d, J = 8.65 Hz, 2H, *m*-COAr*H*), 5.49–5.39 (m, 1H, C=C*H*), 4.91–4.79 (m, 1H, O–C*H*), 2.53–2.39 (m, 2H, CH_2–C=CH), 2.08–0.84 (m, 38H), 0.69 (s, 3H, CH_3–CH–C_8H_{17}); ^{13}C NMR (100 MHz, $CDCl_3$, TMS) δ (ppm) 165.3 (*C*=O), 139.5 (*C*=CH), 131.6 (*o*-CO*Ar*), 131.1 (*m*-CO*Ar*), 129.7 (*C*–CO),

127.8 (*C*–Br), 122.9 (C=*C*H), 74.9 (COO*C*), 56.7, 56.1, 50.0, 42.3, 39.7, 39.5, 38.2, 37.0, 36.6, 36.2, 35.8, 31.93, 31.86, 28.2, 28.0, 27.8, 24.3, 23.8, 22.8, 22.6, 21.1, 19.4, 18.7, 11.9; MS (SALDI-TOF): *m*/*z* calcd. for $C_{34}H_{49}BrNaO_2$ ($[M^+Na]^+$), 591.281; found 591.229.

(–)-Cholesteryl 4-(3-hydroxy-3-methyl-1-butynyl)benzoate (2)

(1) (1.00 g, 1.76 mmol) and 2-methyl-3-butyn-2-ol (0.340 mL, 3.52 mmol) were dissolved in triethylamine (10.0 mL). To this solution, tetrahydrofuran (5.5 mL) solution of bis(triphenylphosphine)palladium(II) chloride (12.3 mg, 17.6×10^{-3} mmol), copper(II) acetate (19.1 mg, 0.105 mmol), triphenylphosphine (32.2 mg, 0.123 mmol) was added. The solution was stirred for 30 min at the reflux temperature. The resulting salt was removed by filtration and the solvent of the filtrate was evaporated to yield a crude product, which was purified by silica-gel chromatography using eluents gradient from chloroform to THF. The product was viscous liquid. Yield: 68%; $[\alpha]_D^{20}$ = –10.4º (c 1.00, chloroform); ^{1}H NMR (400 MHz, $CDCl_3$, TMS) δ (ppm) 7.97 (d, J = 8.65 Hz, 2H, *o*-COAr*H*), 7.46 (d, J = 8.65 Hz, 2H, *m*-COAr*H*), 5.48–5.36 (m, 1H, C=C*H*), 4.91–4.79 (m, 1H, O–C*H*), 2.53–2.39 (m, 2H, CH_2–C=CH), 2.08–0.83 (m, 45H), 0.69 (s, 3H, CH_3–CH–C_8H_{17}); ^{13}C NMR (100 MHz, $CDCl_3$, TMS) δ (ppm) 165.4 (*C*=O), 139.6 (*C*=CH), 131.5 (*m*-CO*Ar*), 130.3 (*C*–CO), 129.4 (*o*-CO*Ar*), 127.2 (*Ar*–C≡C), 122.9 (C=*C*H), 96.5 (Ar–C≡*C*), 81.6 (Ar–*C*≡C), 74.8 (COO*C*), 65.7 (*C*–OH), 56.7 , 56.1, 50.0, 42.3, 39.7, 39.5, 38.2, 37.0, 36.6, 36.2, 35.8, 31.93, 31.87, 31.4, 28.2, 28.0, 27.9, 24.3, 23.8, 22.8, 22.6, 21.0, 19.4, 18.7, 11.9; MS (SALDI-TOF): *m*/*z* calcd. for $C_{39}H_{56}NaO_3$ ($[M^+Na]^+$), 595.413; found 595.334.

(–)-*p*-Cholesteryloxycarbonylphenylacetylene (3) [(–)-ChOCPA]

Sodium hydride (60wt%, 89.2 mg, 2.23 mmol) was added to a toluene solution (10.0 mL) of **(2)** (0.500 g, 0.873 mmol), and the mixture was heated to 90 ºC with stirring for 30 min. After the usual work up, the product was purified with silica-gel chromatography using toluene as an eluent. White crystal was obtained in 60% yield. $[\alpha]_D^{27}$ = –2.4º (c 1.00, chloroform); ^{1}H NMR (400 MHz, $CDCl_3$, TMS) δ (ppm) 7.99 (d, J = 8.56 Hz, 2H, *o*-COAr*H*), 7.54 (d, J = 8.56 Hz, 2H, *m*-COAr*H*), 5.46–5.39 (m, 1H, C=C*H*), 4.91–4.81 (m, 1H, O–C*H*), 3.22 (s, 1H, *H*C≡C), 2.51–2.42 (m, 2H, CH_2–C=CH),

2.07–0.83 (m, 38H), 0.69 (s, 3H, C*H*$_3$–CH–C$_8$H$_{17}$); ^{13}C NMR (100 MHz, $CDCl_3$, TMS) δ (ppm) 165.3 (*C*=O), 139.5 (*C*=CH), 132.0 (*m*-CO*Ar*), 130.8 (*C*–CO), 129.4 (*o*-CO*Ar*), 126.5 (*C*–C≡CH), 122.9 (C=*C*H), 82.9 (HC≡*C*), 79.9 (H*C*≡C), 74.5 (COO*C*), 56.7, 56.1, 50.0, 42.3, 39.7, 39.5, 38.2, 37.0, 36.6, 36.2, 35.8, 31.92, 31.86, 28.2, 28.0, 27.8, 24.3, 23.8, 22.8, 22.6, 21.0, 19.3, 18.7, 11.9; MS (SALDI-TOF): *m*/*z* calcd. for $C_{36}H_{50}NaO_2$ ($[M^+Na]^+$), 537.371; found 537.323.

Synthesis of (–)-poly[4-(cholesteryloxycarbonyl)phenylacetylene] [(–)-Poly(ChOCPA)].

To the monomer **(3)** (100 mg, 0.194 mmol) in dry chloroform (0.760 ml) was added the [Rh(norbornadiene)Cl]$_2$ (0.174 mg, 3.78×10^{-4} mmol) in dry triethylamine (0.100 ml, 0.718 mmol), and the solution was stirred for 1 h at room temperature. The polymerization mixture was poured into acetone, and the polymer was purified by reprecipitation from chloroform solution into acetone and then dried *in vacuo* for 24 h. Yellow solid was obtained in 92.4% yield. $[\alpha]_D^{30}$ = –125º (c 0.0200, chloroform); ^{1}H NMR (400 MHz, $CDCl_3$, TMS) δ (ppm) 7.93–7.44 (br, 2H, *o*-COAr*H*), 6.98–6.20 (br, 2H, *m*-COAr*H*), 5.97–5.59 (br, 1H, –*H*C=C– in main chain), 5.58–5.20 (br, 1H, C=C*H*), 4.88–4.53 (br, 1H, O–C*H*), 2.78–0.31 (br, 43H); IR (cm^{-1}, ATR) 2936 (C-H), 1717 (C=O); GPC: M_w = 1.19 x 10^6, M_w/M_n = 1.67; *Cis*% = 96.0 (^{1}H NMR).

(–)-Poly(ChOCPA) had a chiral structure in main-chain as shown in **Fig. 4.1**, that is, one-handed helical structure.

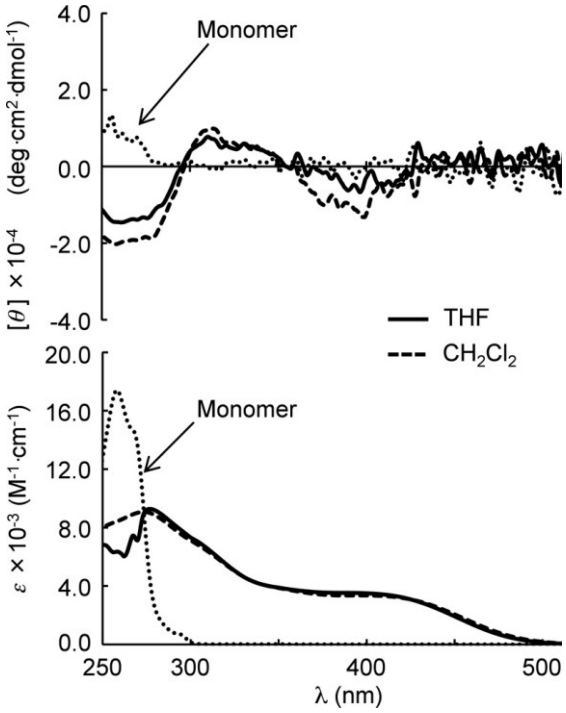

Fig. 4.1 CD and UV-vis. spectra of (−)-poly(ChOCPA) (1.00×10^{-4} mol/L) in THF (line) and $CHCl_3$ (dashed line) and monomer (1.00×10^{-4} mol/L) in THF at 25 ºC.

4.2.3 FS-AFM Video Imaging

To observe the single molecule walking along the polymer chain, we modified the specifications of an NVB500 FS-AFM (Olympus, Tokyo, Japan) in dynamic (tapping) mode.[8,9] An ultra-small cantilever with a low spring constant of approximately 0.1 N/m and a high resonance frequency of over 1 MHz in air was used (AC-10EGS, Olympus, Tokyo, Japan or USC-F1.2-k0.15, NanoWorld AG, Neuchâtel, Switzerland). FS-AFMs offer outstanding performance for investigating the structural dynamics of single molecules in aqueous solutions.[2] However, we modified the AFM for use in organic solvents,[10] enabling us to observe the structural dynamics of a single polymer chain (**Fig. 4.2**).[11,12]

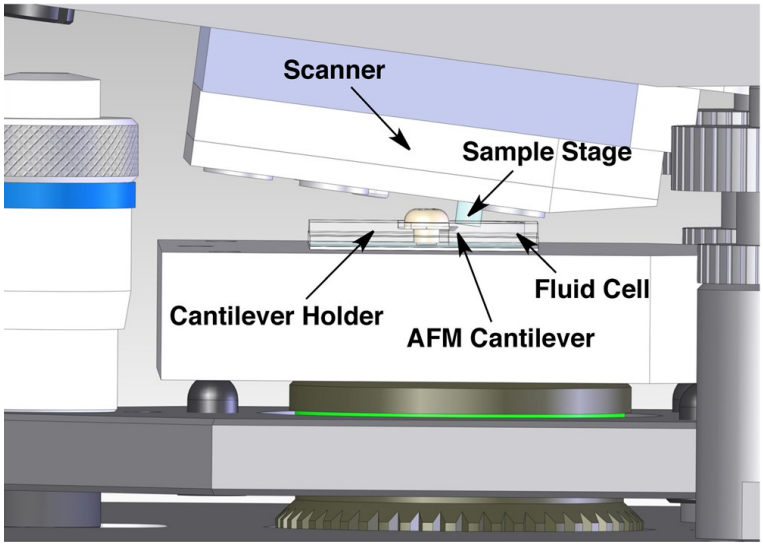

Fig. 4.2 AFM head with a fluid cell.

The polymer was dissolved in tetrahydrofuran (THF) to prepare a solution with a concentration of approximately 1×10^{-6} mol/L. The polymer solution was cast on the surface of a 3-aminopropyltriethoxysilane (APS)-coated mica substrate[13] to prepare a sample for AFM video imaging. A line profile is shown in **Fig. 4.3**.

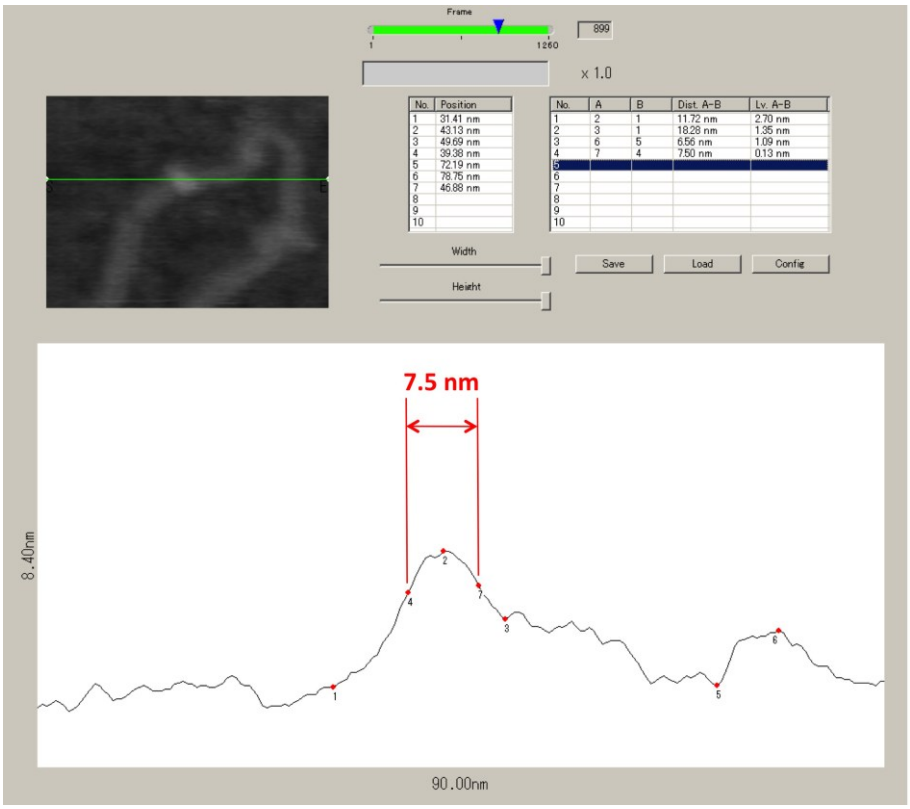

Fig. 4.3 Line profile of a short chain on a rail of a long chain. AFM image on APS-coated mica in *n*-octylbenzene at 25 ± 1 °C. XY: 90.0 nm × 67.5 nm. Z: 8.40 nm.

4.2.4 MSD plots

To determine the dynamics of the walking short chain, the measurement point of the video-imaged short chain was tracked and the mean square displacement (MSD) for a certain time Δt was plotted against Δt,

$$MSD(\Delta t) = \overline{[\Delta x(\Delta t)]^2 + [\Delta y(\Delta t)]^2}.$$

The diffusion coefficient D (nm^2/s) was calculated by dividing the slope of the linearly approximating the MSD-Δt plots of the measurement point by four.

4.2.5 All-Atom MD Simulation

All-atom molecular dynamics (MD) simulations were carried out using the Forcite module of the BIOVIA Materials Studio 2019 (Dassault Systèmes BIOVIA, San Diego, CA, USA) on a supercomputer system (PRIMERGY CX2570 M4, Fujitsu, Tokyo, Japan). A model of (–)-poly(ChOCPA) was build by use of the Polymer Builder module. The torsion angle between monomer units was set to +155 degree. A 35-mer model was put on the infinite-chain of (–)-poly(ChOCPA) in a MD cell. The MD cell was built by means of usual procedure of the Amorphous Cell module. The MD cell length and angle were (a = 113 å, b = 130 Å, c = 90 Å) and (α = 90º, β = 90º, γ = 90º), respectively. Here, single polymer chain was put in the center of the cell, and the solvent molecules of *n*-octylbenzene were packed in the cell at density of 0.858 g cm^{-3}. Sequentially, the geometry of the MD cell was optimized. Simulation in the NVT ensemble (constant number of atoms, volume and temperature) was conducted at 298 K for 200 ps (time step of 0.2-fs, 1,000,000 steps) and the NPT ensemble (constant number of atoms, pressure and temperature) was conducted at pressure of 1.013×10^{-4} GPa and at 298 K for 200 ps (time step of 0.2-fs, 1,000,000 steps) to equilibrate the MD cell. The Nose thermostat was used to control the temperature. The Berendsen barostat was used to control the pressure. After the equilibration at 298 K, simulation in the NVE ensemble (constant number of atoms, volume and energy) was conducted for 60 ns (time step of 1.0-fs, 60,000,000 steps) as the production run. The COMPASS II (ver. 1.2) forcefield was used, and the charges were assigned by the forcefield. A snapshot structure was indicated in **Fig. 4.4**.

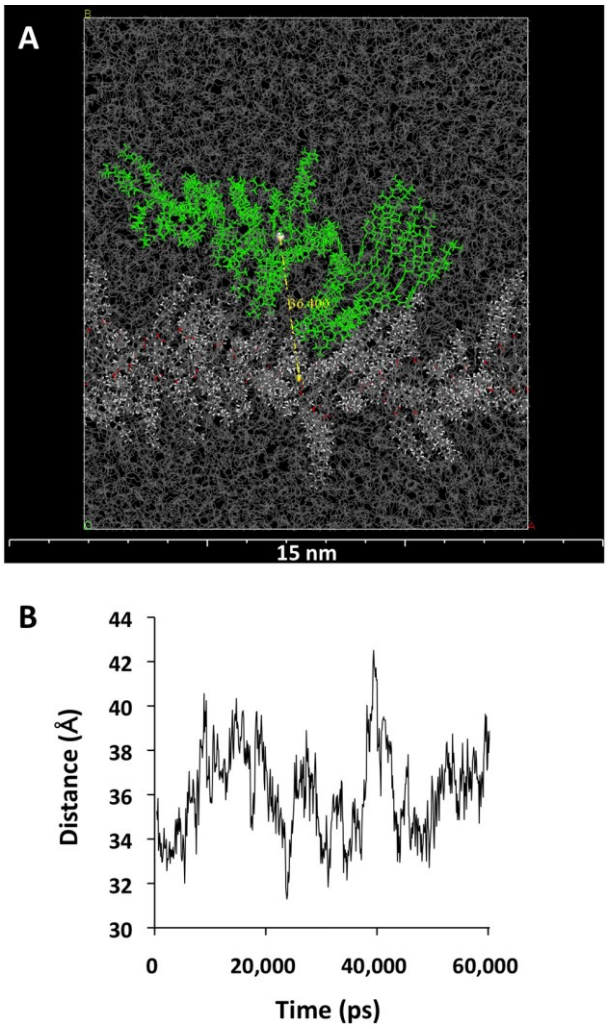

Fig. 4.4 (A) A snap shot of all-atom MD simulation at 50.0 ns. The distance between atoms located approximately at the center of a walking short chain (green) and a rail of a long chain was 3.64 nm. (B) The time change of the distance. The distance fluctuated and the average was 3.61 nm with the standard deviation of 0.2 nm (n = 600).

4.3 Results and Discussion

A para-substituted phenylacetylene polymer with bulky, optically active cholesteryl groups [(–)-poly(ChOCPA)] was synthesized (**Scheme 4.1**). The chiral helical structure was confirmed by circular dichroism (CD) spectroscopy (**Fig. 4.1**).[14,15] A dilute THF solution of the helical polymer was spin-cast onto a substrate of APS-coated mica, and the single polymer chains were adsorbed and moderately

fixed. Subsequently, fast-scanning AFM images were obtained in *n*-octylbenzene at room temperature (**Fig. 4.5**). As a result, a string-like structure with a length of approximately 300 nm was observed, and because this size almost agreed with the value derived from the molecular model, a single polymer chain was confirmed.

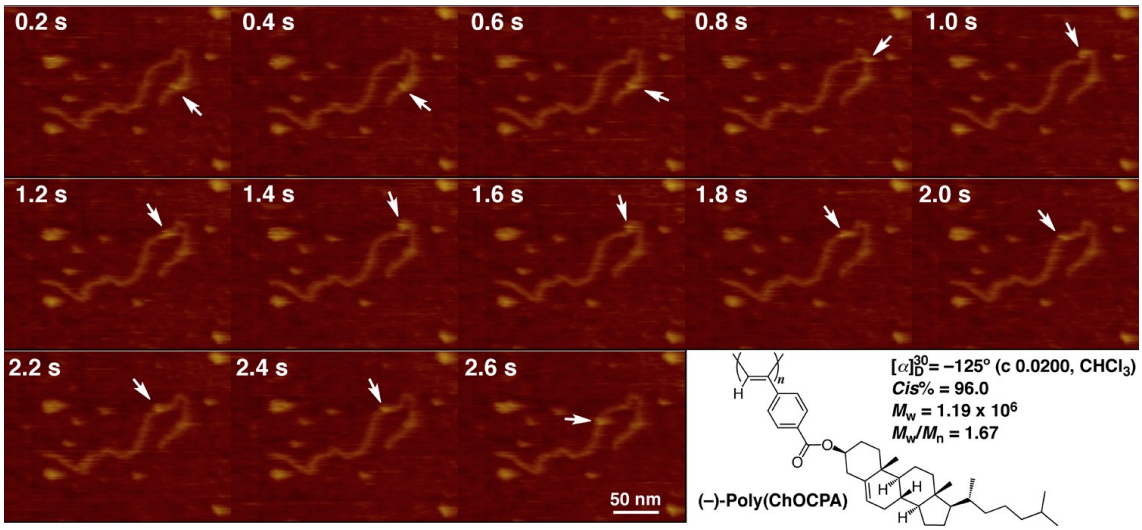

Fig. 4.5 A polymer molecular motor. Single-molecule imaging of macromolecular motor function along a chiral helical *π*-conjugated polymer chain, (–)-poly(ChOCPA), on 3-aminopropyltriethoxysilane (APS)-coated mica under *n*-octylbenzene at 25 ± 1 °C. White arrows indicate the positions of a walking molecule. XY: 250 nm × 188 nm (320 pixels × 240 pixels), Z: 8.40 nm. Frame rate: 5.0 frames per second (fps). X-Scan frequency: 1.47 kHz.

We obtained AFM video images of a short chain (indicated by arrows in **Fig. 4.5**) walking along a single long chain comprising a chiral helical polymer. This walking short chain was approximately 8 nm long and its molecular weight was estimated to be several tens of thousands (**Fig. 4.3**). The walking phenomenon was observed over a long distance (100 nm or more) and for 4 min or more. The rail consisting of the polymer chain was appropriately fixed on the APS-coated mica substrate, and molecular walking was easily observed using AFM. The instantaneous speed reached 100 nm/s. In particular, as shown in **Fig. 4.5**, the observation time was 0.6 to 1.2 s. The short chain walked along the long chain (the rail) without dissociating, even in the region where the rail polymer chain curved (with a radius of curvature of 10 nm or less). This is important for the function of a molecular motor.

The molecular walking was driven by thermal fluctuation. Many walking short-chain molecules have been confirmed, and the results are reproducible. The diversity of the walking properties was presumed to be due to the variation in the molecular weight of the walking molecule.

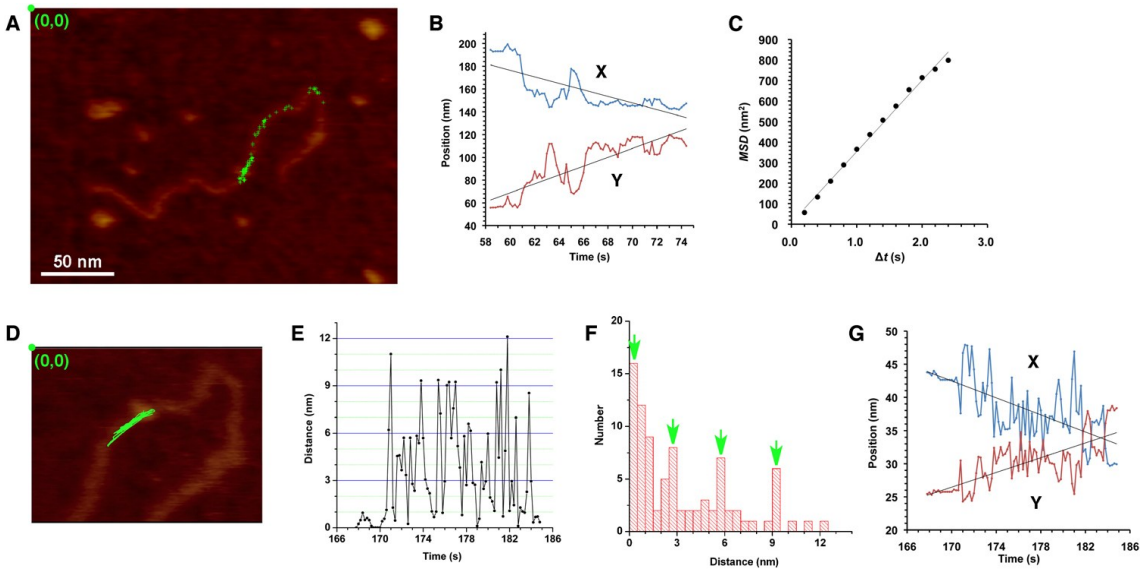

Fig. 4.6 Unidirectional processive movement of a short chain along a chiral helical polymer chain. (A) A short chain walking, observed by atomic force microscope (AFM) video imaging. The X and Y coordinates of the walking molecule were plotted as a green cross in an AFM image. XY: 250 nm × 188 nm (320 pixels × 240 pixels), Z: 8.40 nm. Frame rate: 5.0 fps. The origin (0,0) is in the upper left of the AFM image. (B) Time course of the walking molecule position as X and Y coordinates; the lines were linearly approximated. Unidirectional movement was confirmed. (C) Mean square displacement (MSD) plots based on the trajectory data from (B); the line linearly approximated the MSD-Δ*t* plots. *D* = 86.7 nm^2/s. (D) Trajectories of the walking molecule and a snapshot from the AFM movie. XY: 90.0 nm × 67.5 nm (320 pixels × 240 pixels), Z: 8.40 nm. Frame rate: 5.0 fps. The origin (0,0) is in the upper left of the AFM image. (E) Time course of the walking distance. (F) Histogram of the distance data from (E). The green arrows indicate distances of approximately 0, 3, 6, and 9 nm, which correspond to the walking step. (G) Time course of the walking molecule position as X and Y coordinates; the lines were linearly approximated. Unidirectional movement was confirmed.

In the observation of the processive movement of the short-chain molecule along the long polymer chain using AFM video imaging (**Fig. 4.6A**), unidirectionality was confirmed based on analysis of the trajectory of the centroid of the short-chain molecule (**Fig. 4.6B**). An MSD plot with a linear slope indicates that the molecular motion followed Einstein's law of Brownian motion (**Fig. 4.6C**). The diffusion coefficient was calculated as 86.7 nm^2/s. The distribution of the center of gravity of the walking short-chain molecule is shown in **Fig. 4.6A**. The short chain walked in the direction in which there was a higher density of strong binding sites due to van der Waals interactions. At high resolution (0.28 nm/pix; **Fig. 4.6D**), 3-nm steps were measured (**Fig. 4.6E**, **F**). As shown in **Fig. 4.7A**, a pitch of approximately 3 nm was confirmed on the molecular surface of the optimized model by molecular mechanics (MM) simulation of the helical structure of (–)-poly(ChOCPA). This periodic structure was considered to function as a "scaffold" for molecular walking. The snapshot structure calculated by all-atom MD simulation of the molecular walking model shown in **Fig. 4.7B** supports the existence of dynamic multipoint interaction and molecular engaged structures. In the all-atom atomic MD calculation, a molecular model–in which the repeating units were bonded at a dihedral angle of 155 degrees, the long chain was infinite, and the short chain comprised a 35-mer (expressed in green)–was placed in the MD cell. The solvent molecules (*n*-octylbenzene) were packed at a density of 0.858 g/cm^3. A production run was performed with the microcanonical ensemble (NVE) after an equilibration calculation at 298 K from 0 to 60 ns (126,174 atoms). Long-chain movement as a rail has also been confirmed, and seems to function as a "moving walkway" carrying short-chain molecules at short distances of a few nm. Along the flexible rail of the helical structure, the short chain moved in steps by dynamic multipoint interactions in which "walking motion by weak bond" and "walking stop by strong bond" were repeated, and a walking principle that was reminiscent of the crawling locomotion of an inchworm was proposed (**Fig. 4.7C**).

Unidirectional processive movement was confirmed. Although this may be due to biased Brownian motion, it remains controversial. This is because even (random) Brownian motion can be unidirectional when observed locally. To settle this discussion, a statistical analysis involving a greater number of observable samples (*n*) is necessary in the future.

Because biased Brownian motion requires an asymmetric potential, the use of chemical energy and

macromolecular design for high robustness are considered effective.

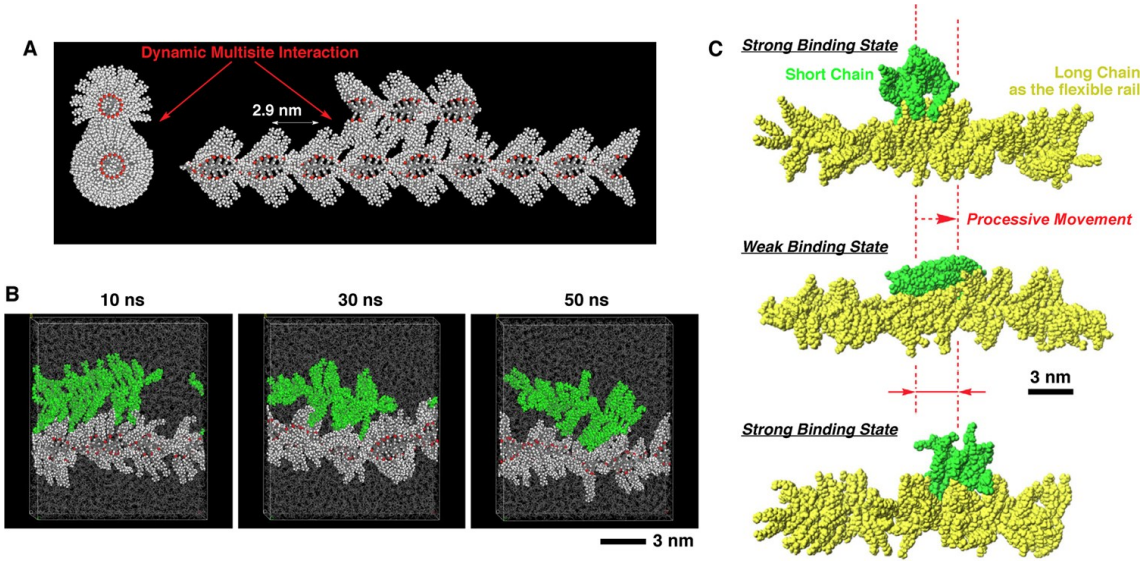

Fig. 4.7 A molecular walking mechanism. (A) An optimized model of an interaction between a short chain (35-mer) and a long chain (120-mer) of (–)-poly(ChOCPA) by molecular mechanics (MM) simulation. (B) Snapshots of all-atom molecular dynamics (MD) by the microcanonical ensemble (NVE) after equilibration at 298 K in *n*-octylbenzene. (C) A proposed model of the molecular walking of a short chain (green) along a helical polymer chain (yellow).

During the processive motion of the short-chain molecule along the polymer chain (**Fig. 4.8A**), although the short chain sometimes dissociated from the rail polymer chain, it eventually resumed its progress along the rail. The step size distribution between the adjacent frames (**Fig. 4.8B**, **C**) was biased in the positive X direction (toward the right in the AFM image) except for in the dwell state, and unidirectionality of movement was confirmed (**Fig. 4.8D**). The MSD plot reveals that the motion was Brownian (**Fig. 4.8E**). Except for −4.5 nm < ΔX < +4.5 nm, the step size data in **Fig. 4.8B** was used for the statistical analysis. Taking 16 steps, the step size was above +4.5 nm 13 times and below −4.5 nm 3 times. If the statistical analysis method of coin tossing is adopted, there are 2^{16} = 65,536 combinations (1) of obverse and reverse sides of the coin in 16 trials. There is 1 combination with 16 obverse and 0 reverse sides of the coin; ${}_{16}C_1$ = 16 combinations with 15 obverse and 1 reverse side of the coin; ${}_{16}C_2$ = 120 combinations with 14 obverse and 2 reverse sides of the coin; and ${}_{16}C_3$ = 560 combinations with 13 obverse and 3 reverse sides of the coin. Therefore, there are 1 + 16 + 120 + 560

= 697 combinations (2) in which the coin is tossed 16 times and the reverse occurs 3 times or fewer. The probability of the reverse occurring 3 times or fewer when tossing a coin 16 times is 697/65,536 = 0.0106 (3) from (1) and (2). Similarly, when a coin is tossed 16 times, the probability that the obverse will occur 3 times or fewer is also 0.0106 (4). If we focus only on the bias, the probability that one occurs more than 13 times and the other occurs fewer than 3 times is 0.0212. During molecular walking, the probability that a step of +4.5 nm or more would occur was 13 out of 16, and the probability that a step of –4.5 nm or less would occur was 3 out of 16. As with the coin-toss proposition, such a bias occurs with a probability of 2.12%, so it was proven to be predominantly biased at a significance level of 5%.

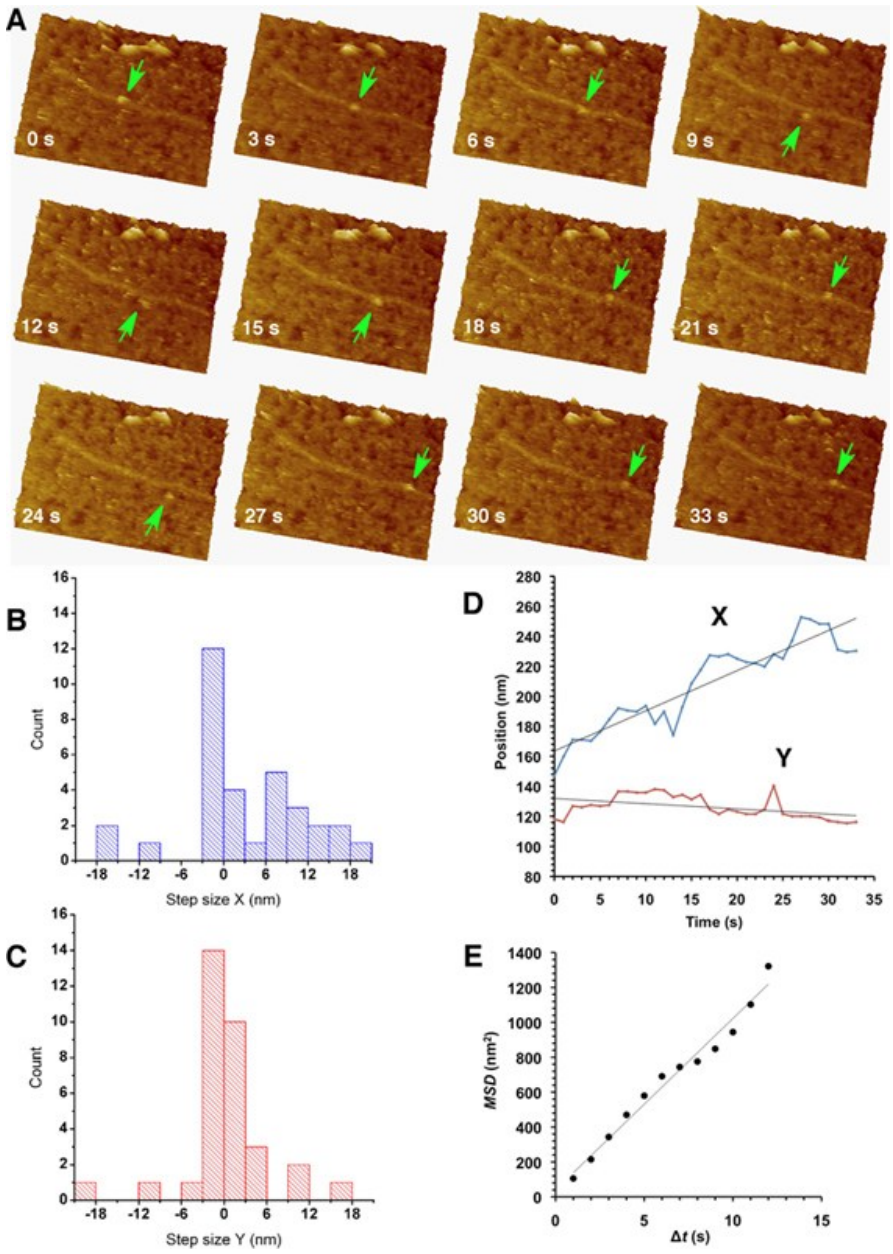

Fig. 4.8 Unidirectional processive movement of a short chain along a chiral helical polymer chain. (A) A short chain walking, observed by atomic force microscope (AFM) video imaging. The walking short chain is indicated by a green arrow in the snapshots from the AFM movie. XY: 300 nm × 225 nm (192 pixels × 144 pixels), Rate: 1.0 fps. The origin (0,0) is in the upper left of the AFM image. (B) Distribution of the step size of X (ΔX) of the walking molecule between frames ($\Delta X = X_{n+1} - X_n$). (C) Distribution of the step size of Y (ΔY) of the walking molecule between frames ($\Delta Y = Y_{n+1} - Y_n$). (D) Time course of the walking molecule position as X and Y coordinates. Unidirectional movement was confirmed. (E) Mean square displacement (MSD)

plots based on the trajectory data from (D). D = 24.6 nm^2/s.

4.4 Conclusion

In this study, we observed the function of a molecular motor where a short-chain molecule "walks" along a polymer chain using a chiral helical substituted phenylacetylene polymer with cholesteryl groups ((–)-poly(ChOCPA)). Single-molecule imaging with FS-AFM revealed that the short-chain molecule exhibited unidirectional processive movement in steps of approximately 3 nm, driven by thermal fluctuations. A walking mechanism resembling inchworm locomotion was proposed, involving dynamic multipoint interactions and the repetition of weak and strong molecular bonds. All-atom molecular dynamics simulations supported the interactions between the short-chain molecule and the long-chain polymer, confirming molecular-level behavior consistent with the experimental results. Statistical analysis suggested that the motion of the short-chain molecule was unidirectional, potentially due to biased Brownian motion.

Molecular walking in aqueous solutions is well known in the myosin/actin and kinesin/microtubule systems, but it has also been demonstrated in non-aqueous solutions. We believe that the present study of synthetic polymer motors will lead to the creation of artificial functional materials such as artificial muscles driven by thermal fluctuations. To create an artificial muscle, it is necessary to assemble the molecules; bundling the polymer chains is expected to make the structure more robust and to improve the molecular motor properties.

4.5 *Spectral Data*

4.5.1 *^{1}H and ^{13}C NMR Spectra*

4-{(–)-Cholesteryloxycarbonyl}bromobenzene (1)

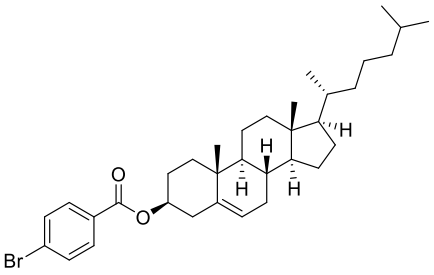

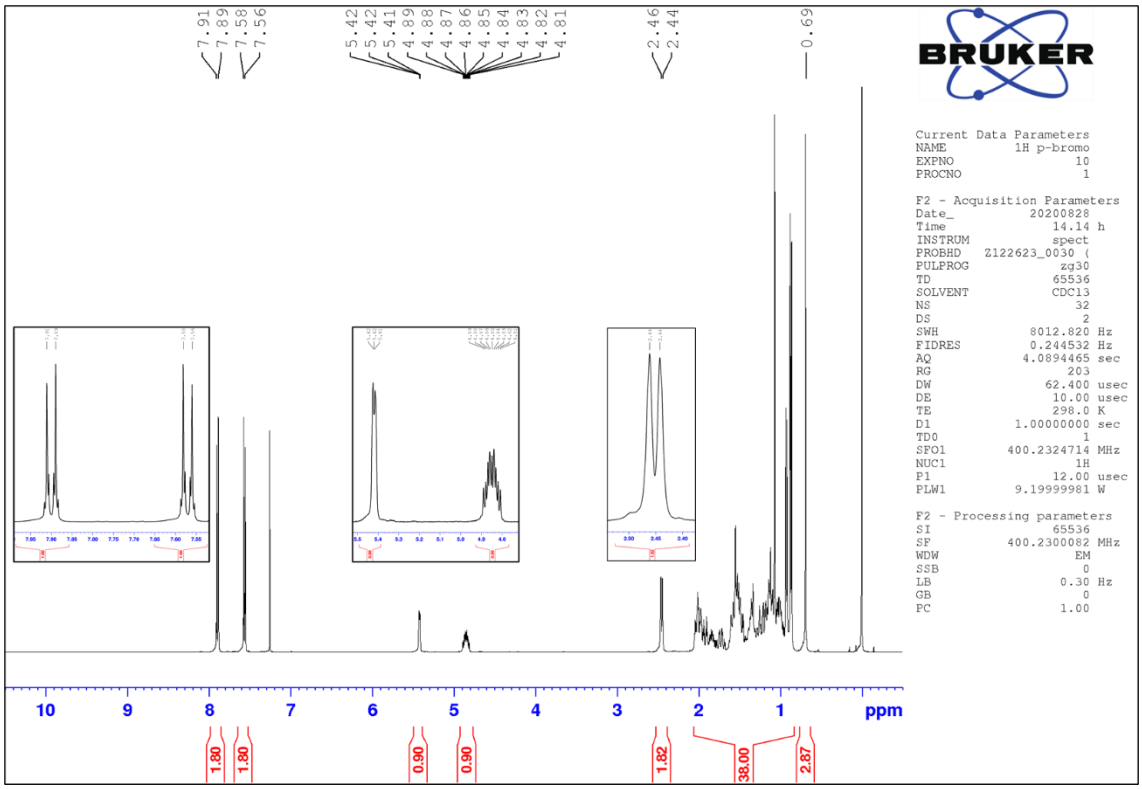

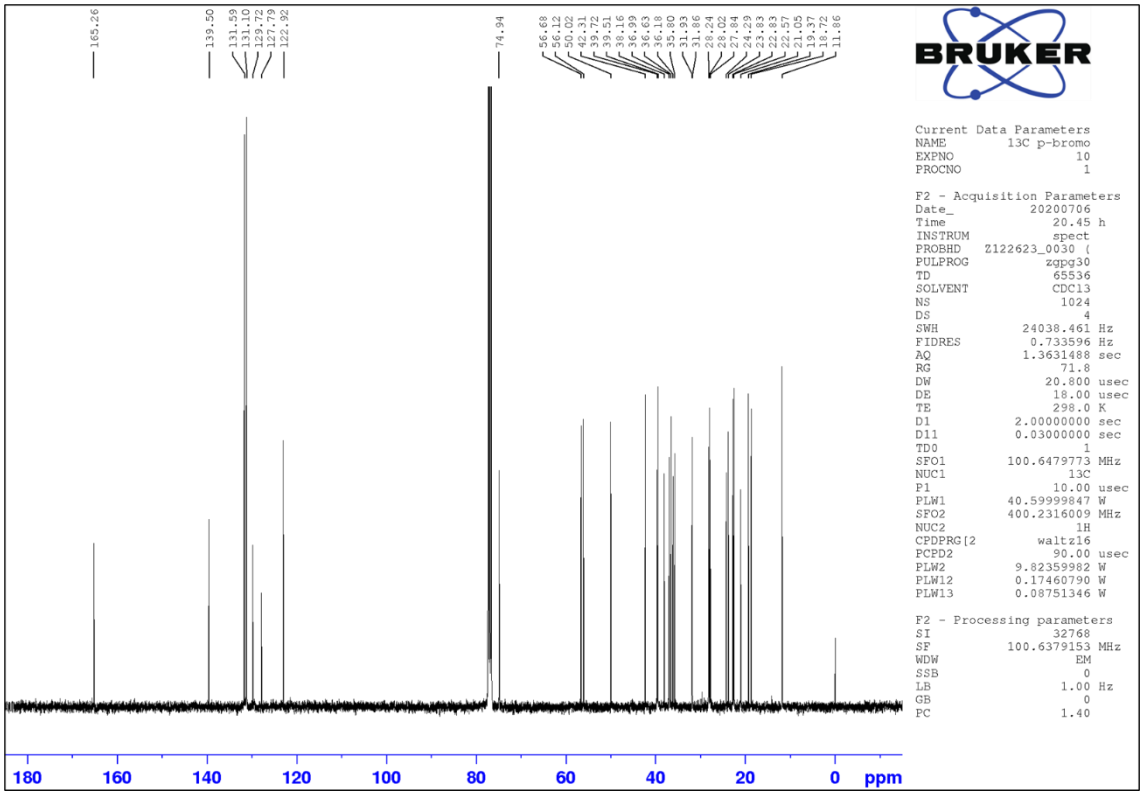
165.26
139.50
131.59
131.10
129.72
127.79
122.92
74.94
56.68
56.12
50.02
42.31
39.72
39.51
38.16
36.99
36.63
36.18
35.80
31.93
31.86
28.24
28.02
27.84
24.29
23.83
22.83
22.57
21.05
19.37
18.72
11.86
180
160
140
120
100
80
60
40
20
0
ppm
BRUKER
Current Data Parameters
NAME 13C p-bromo
EXPNO 10
PROCNO 1
F2 - Acquisition Parameters
Date_ 20200706
Time 20.45 h
INSTRUM spect
PROBHD Z122623_0030 (
PULPROG zgpg30
TD 65536
SOLVENT CDCl3
NS 1024
DS 4
SWH 24038.461 Hz
FIDRES 0.733596 Hz
AQ 1.3631488 sec
RG 71.8
DW 20.800 usec
DE 18.00 usec
TE 298.0 K
D1 2.00000000 sec
D11 0.03000000 sec
TD0 1
SFO1 100.6479773 MHz
NUC1 13C
P1 10.00 usec
PLW1 40.59999847 W
SFO2 400.2316009 MHz
NUC2 1H
CPDPRG[2 waltz16
PCPD2 90.00 usec
PLW2 9.82359982 W
PLW12 0.17460790 W
PLW13 0.08751346 W
F2 - Processing parameters
SI 32768
SF 100.6379153 MHz
WDW EM
SSB 0
LB 1.00 Hz
GB 0
PC 1.40

(–)-Cholesteryl 4-(3-hydroxy-3-methyl-1-butynyl)benzoate (2)

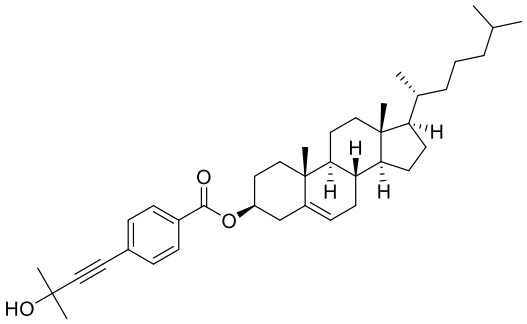

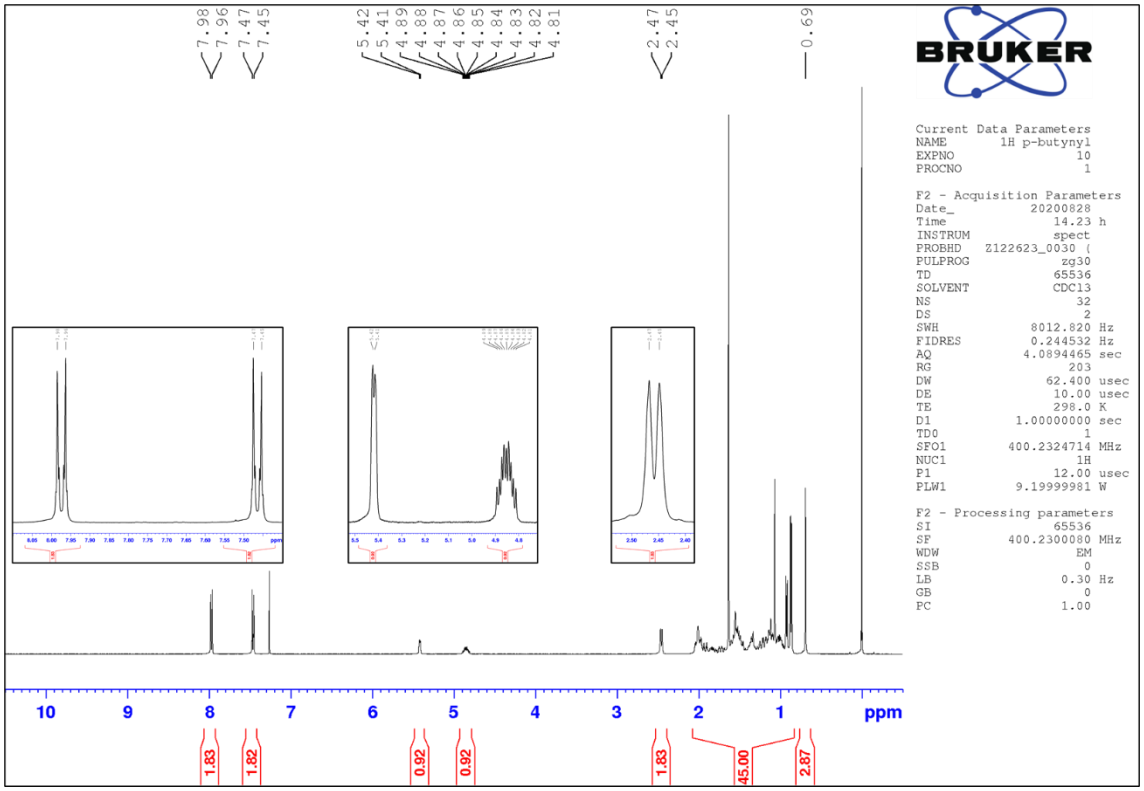

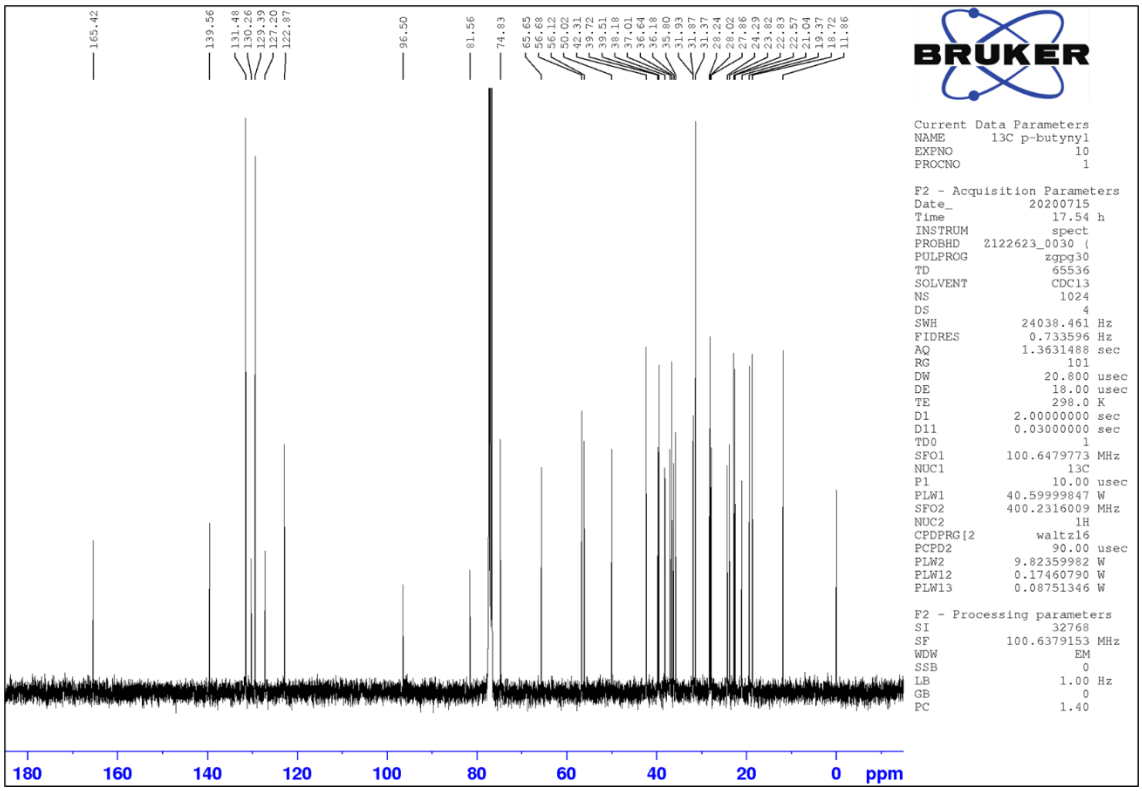
165.42
139.56
131.48
130.26
129.39
127.20
122.87
96.50
81.56
74.83
65.65
56.68
56.12
50.02
42.31
39.72
39.51
38.18
37.01
36.64
36.18
35.80
31.93
31.87
31.37
28.24
28.02
27.86
24.29
23.82
22.83
22.57
21.04
19.37
18.72
11.86
180
160
140
120
100
80
60
40
20
0
ppm
BRUKER
Current Data Parameters
NAME 13C p-butynyl
EXPNO 10
PROCNO 1
F2 - Acquisition Parameters
Date_ 20200715
Time 17.54 h
INSTRUM spect
PROBHD Z122623_0030 (
PULPROG zgpg30
TD 65536
SOLVENT CDCl3
NS 1024
DS 4
SWH 24038.461 Hz
FIDRES 0.733596 Hz
AQ 1.3631488 sec
RG 101
DW 20.800 usec
DE 18.00 usec
TE 298.0 K
D1 2.00000000 sec
D11 0.03000000 sec
TD0 1
SFO1 100.6479773 MHz
NUC1 13C
P1 10.00 usec
PLW1 40.59999847 W
SFO2 400.2316009 MHz
NUC2 1H
CPDPRG[2 waltz16
PCPD2 90.00 usec
PLW2 9.82359982 W
PLW12 0.17460790 W
PLW13 0.08751346 W
F2 - Processing parameters
SI 32768
SF 100.6379153 MHz
WDW EM
SSB 0
LB 1.00 Hz
GB 0
PC 1.40

(–)-*p*-Cholesteryloxycarbonylphenylacetylene (3) [(–)-ChOCPA]

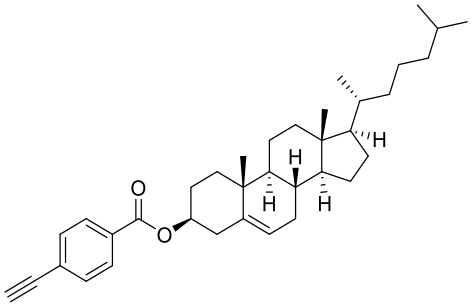

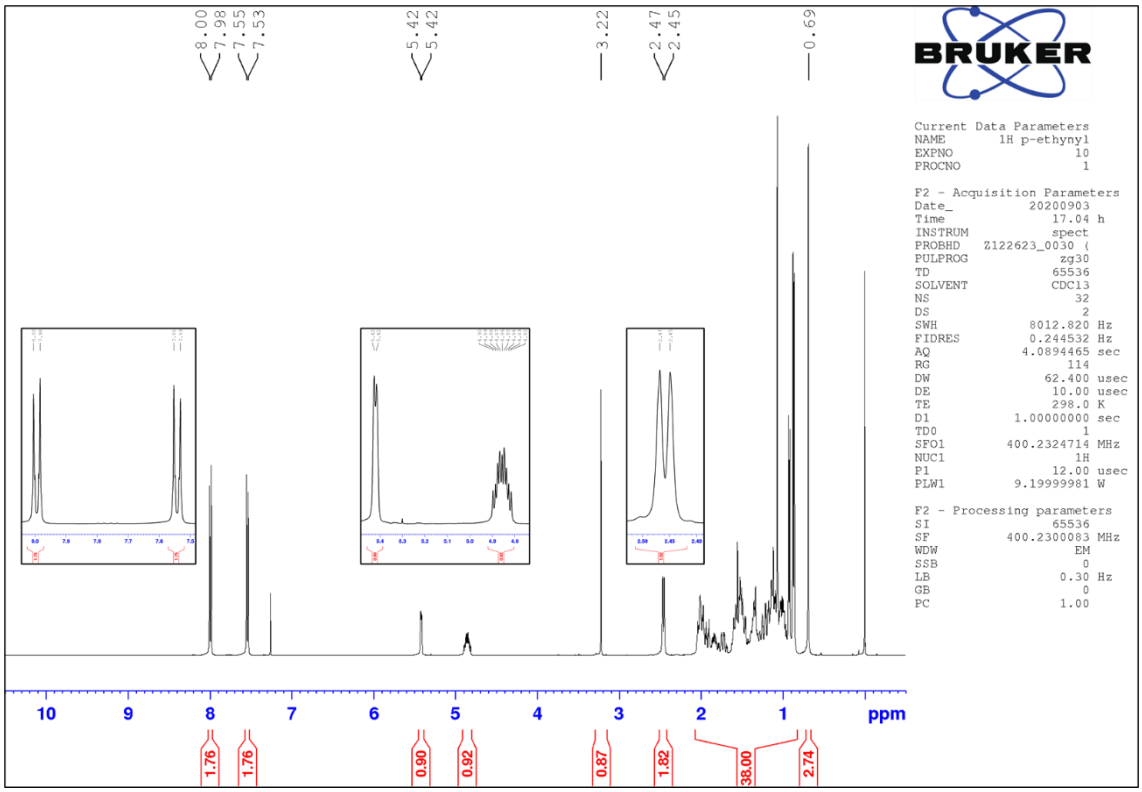

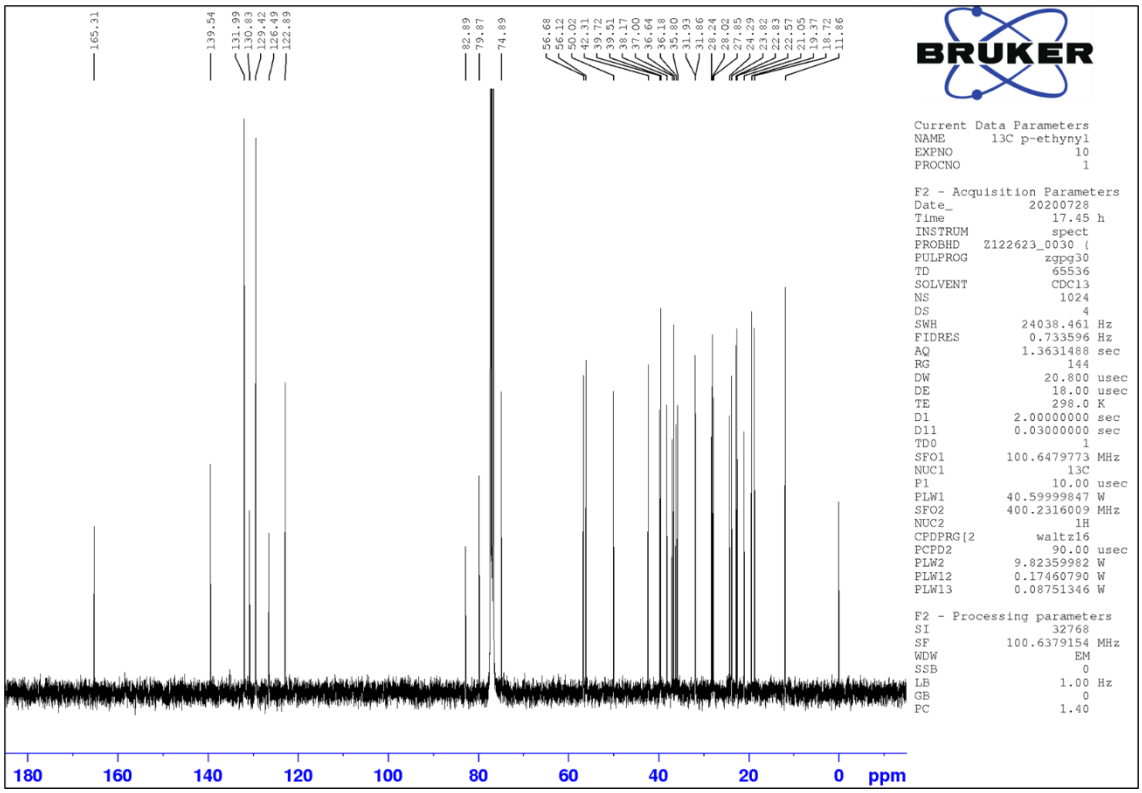
165.31
139.54
131.99
130.83
129.42
126.49
122.89
82.89
79.87
74.89
56.68
56.12
50.02
42.31
39.72
39.51
38.17
37.00
36.64
36.18
35.60
33.93
31.86
28.24
28.02
27.85
24.29
23.82
22.83
22.57
21.05
18.37
14.72
11.86
180
160
140
120
100
80
60
40
20
0
ppm
BRUKER
Current Data Parameters
NAME 13C p-ethynyl
EXPNO 10
PROCNO 1
F2 - Acquisition Parameters
Date_ 20200728
Time 17.45 h
INSTRUM spect
PROBHD Z122623_0030 (
PULPROG zgpg30
TD 65536
SOLVENT CDC13
NS 1024
DS 4
SWH 24038.461 Hz
FIDRES 0.733596 Hz
AQ 1.3631488 sec
RG 144
DW 20.800 usec
DE 18.00 usec
TE 298.0 K
D1 2.00000000 sec
D11 0.03000000 sec
TD0 1
SFO1 100.6479773 MHz
NUC1 13C
P1 10.00 usec
PLW1 40.59999847 W
SFO2 400.2316009 MHz
NUC2 1H
CPDPRG[2 waltz16
PCPD2 90.00 usec
PLW2 9.82359982 W
PLW12 0.17460790 W
PLW13 0.08751346 W
F2 - Processing parameters
SI 32768
SF 100.6379154 MHz
WDW EM
SSB 0
LB 1.00 Hz
GB 0
PC 1.40

(–)-Poly[4-(cholesteryloxycarbonyl)phenylacetylene]

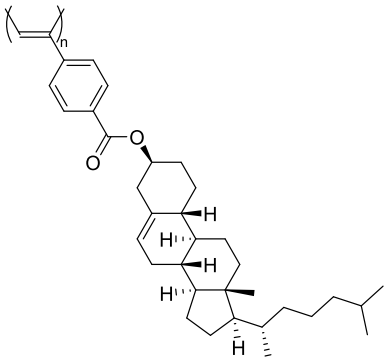

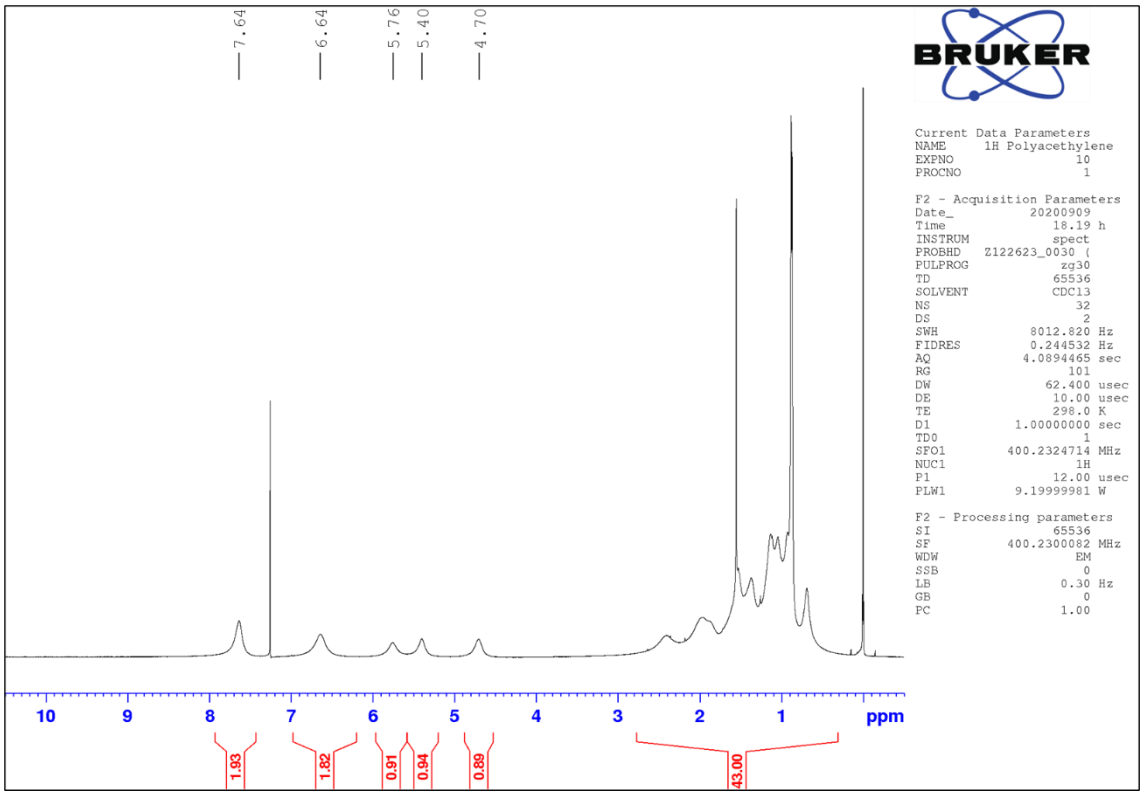

4.6 Reference

1 M. Kaya, H. Higuchi, Nonlinear Elasticity and an 8-nm Working Stroke of Single Myosin Molecules in Myofilaments. *Science* **2010**, *329*, 686-689. https://doi.org/10.1126/science.1191484

2 N. Kodera, D. Yamamoto, R. Ishikawa, T. Ando, Video imaging of walking myosin V by high-speed atomic force microscopy. *Nature* **2010**, *468*, 72-76. https://doi.org/10.1038/nature09450

3 Y. Okada, H. Higuchi, N. Hirokawa, Processivity of the single-headed kinesin KIF1A through biased binding to tubulin. *Nature* **2003**, *424*, 574-577. https://doi.org/10.1038/nature01804

4 M. Cesario, C. O. Dietrich-Buchecker, J. Guilhem, C. Pascard, J. P. Sauvage, Molecular structure of a catenand and its copper(I) catenate: complete rearrangement of the interlocked macrocyclic ligands by complexation. *J. Chem. Soc., Chem. Commun.* **1985**, *5*, 244-247. https://doi.org/10.1039/C39850000244

5 P. R. Ashton, D. Philp, N. Spencer, J. F. Stoddart, A new design strategy for the self-assembly of molecular shuttles. *J. Chem. Soc., Chem. Commun.* **1992**, *16*, 1124-1128. https://doi.org/10.1039/C39920001124

6 N. Koumura, R. W. J. Zijlstra, R. A. van Delden, N. Harada, B. L. Feringa, Light-driven monodirectional molecular rotor. *Nature* **1999**, *401*, 152–155. https://doi.org/10.1038/43646

7 T. Kudernac, N. Ruangsupapichat, M. Parschau, B. Maciá, N. Katsonis, S. R. Harutyunyan, K. Ernst, B. L. Feringa, Electrically driven directional motion of a four-wheeled molecule on a metal surface. *Nature* **2011**, *479*, 208–211. https://doi.org/10.1038/nature10587

8 K. Shinohara, Single-Molecule Imaging of a Polymer: Direct Observation of Structure and Dynamics in a Polymer Chain. *Kobunshi Ronbunshu* **2016**, *73*, 491-504. https://doi.org/10.1295/koron.2016-0034

9 K. Shinohara, *Applied Scanning Probe Methods X -Biomimetics and Industrial Applications*, Chapter 31: Scanning Probe Microscope Application for Single Molecules in a π-Conjugated

Polymer toward the Molecular Devices based on Polymer Chemistry, pp 153–182, B. Bhushan, H. Fuchs, M. Tomitori (Eds.), Springer (Berlin, Heidelberg), ISBN: 978-3-540-74084-1 (2008). https://doi.org/10.1007/978-3-540-74085-8_5

10 K. Shinohara, Dynamic Analysis Method for Polymer Chain, Manufacturing Method for Polymer, Polymer, Manufacturing Method for Synthetic Polymer, and Synthetic Polymer. WO 2014104172 A1 (2014), Jpn. Pat., P6061277 (2016).

11 K, Shinohara, M. Yanagisawa, Y. Makida, Direct Measurement of Long-Chain Branch in a Low-Density Polyethylene, *Sci. Rep.* 2019, *9*, 9791. https://doi.org/10.1038/s41598-019-46035-9

12 K. Shinohara, Y. Makida, Direct observation of dynamic interaction between a functional group in a single SBR chain and an inorganic matter surface. *Sci. Rep.* **2018**, *8*, 13982. https://doi.org/10.1038/s41598-018-32382-6

13 L. Green, M. Schotanus, M. A. McAlear, E. A. Howell, Atomic Force Microscopy Can Detect the Binding of Yeast Replication Factor C to DNA. *Nano Lett.* **2003**, *3*, 39-41. https://doi.org/10.1021/nl025831c

14 K. Shinohara, S. Yasuda, G. Kato, M. Fujita, H. Shigekawa, Direct Observation of the Chiral Quaternary Structure in a π-Conjugated Polymer at Room Temperature, *J. Am. Chem. Soc.* **2001**, *123*, 3619-3620. https://doi.org/10.1021/ja003023m

15 T. Aoki, M. Kokai, K. Shinohara, E. Oikawa, Chiral Helical Conformation of the Polyphenylacetylene Having Optically Active Bulky Substituent, *Chem. Lett.* **1993**, *22*, 2009-2012. https://doi.org/10.1246/cl.1993.2009

16 Y. Wada, K. Shinohara, H. Asakawa, S. Matsui, T. Taima, T. Ikai, One-step synthesis of one-dimensional supramolecular assemblies composed of helical macromolecular building blocks. *J. Am. Chem. Soc.* **2019**, *141* (35), 13995–14002. https://doi.org/10.1021/jacs.9b07417

Chapter 5. Synthesis and Direct Observation of Chiral Supramolecular Polymer of Porphyrin having Cholesteryl Groups

5.1 Introduction

Porphyrins are dye molecules that have broad π-conjugation planes. They form obliquely stacked J-aggregates and one-dimensionally stacked H-aggregates by π–π interactions, which originate from the broad conjugation plane. The aggregates grow into supramolecular polymers, which comprise higher-order structures such as superhelices[1] and ribbons.[2, 3] Therefore, porphyrin supramolecular polymers have diverse forms.[4, 5] The forming of porphyrin aggregates is influenced by their pendant groups.[6, 7] For example, if the porphyrin has amide groups as pendants, H-aggregates are easily formed owing to the formation of hydrogen bonds between amide bonds.[8, 9] Or if the porphyrin has pendant substituents that engage in hydrophobic–hydrophobic interactions, or strong van der Waals interactions, it is easier to form aggregates because of these interactions.[2] And, the presence of chiral substituents on the pendant groups can give rise to chiral helical structures during aggregate formation.[6]

Myosin and kinesin are motor proteins. They function as biomolecular machines that moves in parallel on a rail molecule by hydrolyzing adenosine triphosphate (ATP): myosin motors move on actin filaments, whereas kinesin motors move on microtubules. There is an expectation that they will be exploited in industrial applications.[10-12] But, these biomolecular machines only work under certain conditions, i.e., in an aqueous environment, at an appropriate temperature, and in the presence of ATP. Therefore, the expansion of the application environment is one of the challenges facing the use of molecular machines. Recently, researchers have focused on creating molecular machines that mimic the biomolecules described above using synthetic molecules. Several molecules have already been synthesized. They include catenane,[13] rotaxane,[14] light-driven molecular rotors,[15] and a nanocar,[16] all of which have been prepared and driven in a variety of environments by substituents and other devices. Synthetic molecular machines are able to operate in various environments, and therefore have a major advantage over biomolecular machines. However, synthetic molecular machines have not achieved the dynamic motion of biomolecular machines, and it has not been possible to develop molecules with

practical functions.

We recently investigated chiral helical poly(phenylacetylene) with cholesteryl groups as pendants using fast-scanning atomic force microscope (FS-AFM) video imaging. At 25 ± 1 °C and in a non-polar solvent, the short-chain molecules move along the long-chain molecules by Brownian motion.[17, 18] This suggests that it is possible to create synthesized macromolecular machines that are capable of long-distance parallel motion, such as that observed in kinesin and myosin, using synthetic polymers. This polymer was capable of multipoint interactions between a short- and a long-chain molecule owing to the periodic structure of its helix, and the phenomenon was caused by combining the multipoint interaction and Brownian motion. However, it has only been observed in poly(phenylacetylenes) with cholesteryl groups as pendants, and further extension of the generality is one of the issues to be addressed.

In this study, we synthesized porphyrin chiral helical supramolecular polymers with cholesteryl groups (**Fig. 5.1**), investigated their structure, and observed the interaction between the polymer chains.[19] Imaging interactions between polymer chains means confirming the origin of biomolecular motors that interact with the rails and move on them. We have already reported an artificial molecular motor in which short-chain molecules walk in one direction along a single chiral helical polymer chain.[17, 18] Observing the incremental steps of interaction and movement provides fundamental information for the evolutionary process of biomolecular motors such as Myosin along Actin filament. We also report a hierarchical pathway for forming higher-order structures in these supramolecular polymers based on the images obtained by microscopy. The present study provided a rare opportunity to observe the most straightforward supramolecular rods and the various higher-order structures they form.

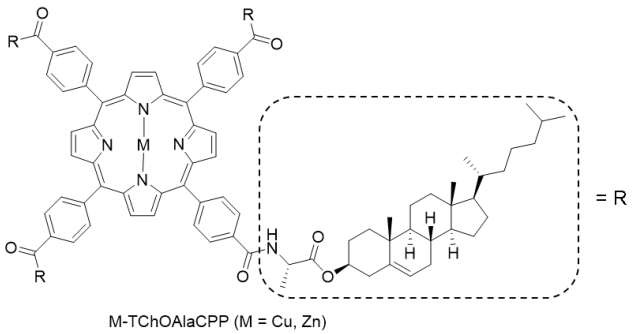

Fig. 5.1 Structure of porphyrin with bulky pendant chiral cholesteryl groups.

5.2 Experimental

5.2.1 Materials

(−)-Cholesterol, *N*-Boc-L-alanine, 4-dimethylaminopyridine (DMAP), copper(II) acetate were purchased from Kanto Chemical (Tokyo, Japan). *N*-(3-Dimethylaminopropyl)-*N*′-ethylcarbodiimide hydrochloride, trifluoroacetic acid, tetrakis(4-carboxyphenyl)porphyrin (TCPP) were purchased from Tokyo Chemical Industry (Tokyo, Japan). Zinc acetate was purchased from FUJIFILM Wako Pure Chemical (Osaka, Japan).

5.2.2 Synthesis of M-TChOAlaCPP

Method: Porphyrin supramolecular polymers ware prepared following section ^{1}H NMR spectra were recorded on an AVANCE III 400 MHz (Bruker, MA, USA). MASS spectra measured using matrix or surface assisted laser desorption/ionization fourier transform ion cyclotron resonance mass spectrometry (MALDI or SALDI FT-ICR MS) scimaX (Bruker, MA, USA). IR spectra were measured using Spectrum 100 (PerkinElmer, USA). CD spectra were measured using J-820 spectropolarimeter (Jasco, Tokyo, Japan). Concentration of porphyrin solutions was 2×10^{-6} M.

Cu- and Zn-TChOAlaCPP were synthesized as follows (**Scheme 5.1**).

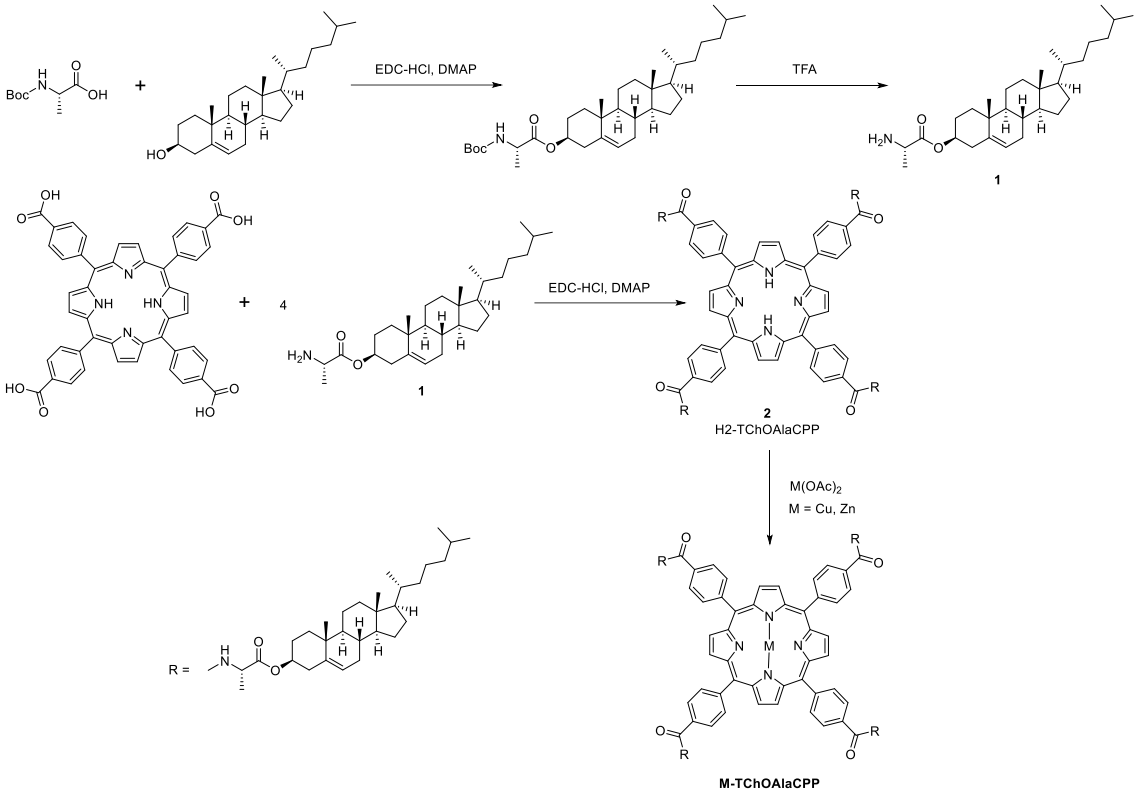

Scheme 5.1 Synthesis of Cu- and Zn-TChOAlaCPP supramolecular polymers.

L-Alanine cholesteryl ester (1)

(−)-Cholesterol (2.01 g, 5.20 mmol), *N*-(tert-butoxycarbonyl)-L-alanine (1.18 g, 6.24 mmol), and 4-dimethylaminopyridine (0.76 g, 6.22 mmol) were weighed. After nitrogen replacement, dichloromethane (26.0 mL) was added. The resulting solution was cooled to 0 °C and *N*-(3-dimethylaminopropyl)-*N*′-ethylcarbodiimide hydrochloride (2.00 g, 10.4 mmol) was added. The solution was then stirred for 30 min and refluxed for 18 h. When the reaction was complete, dichloromethane was added and the solution was washed with 1 M aqueous HCl, saturated aqueous $NaHCO_3$, and brine. The organic layer was dried with Na_2SO_4. The solvent was removed leaving crude *N*-(tert-butoxycarbonyl)-L-alanine cholesteryl ester. The crude product was dissolved in anhydrous dichloromethane (37.2 mL) under a nitrogen atmosphere. Trifluoroacetic acid (3.72 mL) was then

slowly added dropwise and the solution was stirred at room temperature for 7 h. When the reaction was complete, the solvent was removed, dichloromethane was added, the solution was washed with saturated $NaHCO_3$ solution and brine, and the organic layer was dried with Na_2SO_4. The solvent was removed, and the residue was dissolved in chloroform. The resulting solution was subjected to column chromatography with chloroform/methanol in ratios of 150/1 (*v*/*v*) and 20/1 (*v*/*v*), and L-alanine cholesteryl ester **1** (2 steps, 2.28 g, 96%) was obtained from the chloroform/methanol 20/1 (*v*/*v*) eluate. ^{1}H-NMR (400 MHz, $CDCl_3$, TMS) δ (ppm): 5.38 (d, *J* = 3.72 Hz, 1H, C=C*H*), 4.72–4.55 (m, 1H, O–C*H*), 3.51 (q, *J* = 7.03 Hz, 1H, NH_2–C*H*), 2.31 (d, *J* = 7.64 Hz, 2H, CH_2–C=CH), 2.06–1.93 (m, 2H), 1.93–1.77 (m, 3H), 1.70–0.76 (m, 38H), 0.68 (s, 3H, CH_3–C–CH–C_8H_{17}); ^{13}C-NMR (100 MHz, $CDCl_3$, TMS) δ (ppm): 175.9 (*C*O), 139.5 (*C*=CH), 122.8 (C=*C*H), 74.5 (COO*C*), 56.7, 56.1, 50.2 (NH–*C*H), 50.0, 42.3, 39.7, 39.5, 38.0 (*C*H_2–C=CH), 37.0, 36.6, 36.2, 35.8, 31.9, 31.9, 28.2, 28.0, 27.7, 24.3, 23.8, 22.8, 22.6, 21.0, 20.6, 19.3, 18.7, 11.9 (*C*H_3–C–CH–C_8H_{17}); IR (cm^{-1}) 3374 (NH), 1730 (CO); MS (SALDI-FT-ICR): *m*/*z* calcd. for $C_{30}H_{51}KNO_2$ ($[M^+K]^+$) 496.356; found 496.356.

Tetrakis(cholesteryloxy-L-alanylcarbonylphenyl)porphyrin (H_2-TChOAlaCPP) (2)

Tetrakis(4-carboxyphenyl)porphyrin (TCPP) (100 mg, 126 μmol), L-alanine cholesteryl ester **(1)** (350 mg, 765 μmol), and 4-dimethylaminopyridine (93.5 mg, 765 μmol) were weighed. After nitrogen replacement, a chloroform/dimethyl sulfoxide = 3/1 (*v*/*v*) mixture (5.00 mL) was added. The solution was cooled to 0 °C. *N*-(3-dimethylaminopropyl)-*N*′-ethylcarbodiimide hydrochloride (155 mg, 809 μmol) was added. The solution was stirred for 30 min and refluxed for 21 h. When the reaction was complete, the mixture was poured into methanol and the precipitate was filtered. The residue was dissolved in chloroform and subjected to column chromatography with a chloroform/methanol/triethylamine = 1000/1/1 (*v*/*v*/*v*) mixture to produce H_2-TChOAlaCPP **2** (189 mg, 59%), which was a purple solid. ^{1}H-NMR (400 MHz, $CDCl_3$, TMS) δ (ppm): 8.82 (s, 8H, β-pyrrol), 8.30 (d, *J* = 7.94 Hz, 8H, Ar*H*), 8.21 (d, *J* = 7.94 Hz, 8H, Ar*H*), 7.11 (d, *J* = 7.11 Hz, 4H, CO–N*H*),

5.44 (d, *J* = 4.28 Hz, 4H, C=C*H*), 4.95 (quin, *J* = 7.11 Hz, 4H, NH–C*H*), 4.86–4.73 (m, 4H, O–C*H*), 2.53–2.37 (m, 8H, CH_2–C=CH), 2.11–0.79 (m, 164H), 0.69 (s, 12H, CH_3–C–CH–C_8H_{17}), -2.82 (s, 2H, pyrrol N*H*).^{13}C-NMR (100 MHz, $CDCl_3$, TMS) δ (ppm): 172.9 (*C*O), 166.8 (*C*O), 145.4 (*Ar*), 139.3 (*C*=CH), 134.6 (*Ar*), 133.6 (*Ar*), 125.5 (*Ar*), 123.0 (C=*C*H), 119.3 (meso-*C*), 75.6 (COO*C*), 56.6, 56.1, 50.0, 48.9 (NH–*C*H), 42.3, 39.7, 39.5, 38.0 (*C*H_2–C=CH), 36.9, 36.6, 36.2, 35.8, 31.9, 31.8, 28.2, 28.0, 27.8, 24.3, 23.8, 22.8, 22.6, 21.0, 19.3, 19.0 (NH–CH–*C*H_3), 18.7, 11.8 (*C*H_3–C–CH–C_8H_{17}). IR (cm^{-1}) 3319 (pyrrol NH), 1736 (CO), 1656 (CO); MS (MALDI-FT-ICR): *m*/*z* calcd. for $C_{168}H_{227}N_8O_{12}$ ($[M^+H]^+$) 2549.743; found 2549.731.

Cu-Tetrakis(cholesteryloxy-L-alanylcarbonylphenyl)porphyrin (Cu-TChOAlaCPP)

H_2-TChOAlaCPP **(2)** (51.3 mg, 20.1 μmol) and copper(II) acetate (36.8 mg, 203 μmol) were weighed. After nitrogen replacement, chloroform (2.00 mL) was added, and the solution was refluxed for 24 h. When the reaction was complete, the mixture was subjected to column chromatography with chloroform to produce **Cu-TChOAlaCPP** (48.3 mg, 92%), which was a red solid. ^{1}H-NMR (400 MHz, $CDCl_3$, TMS) δ (ppm): 8.36–7.62 (br, Ar*H*), 7.14–6.66 (br, 4H, CO–N*H*), 5.59–5.30 (br, 4H, C=C*H*), 5.07–4.81 (br, 4H, NH–C*H*), 4.81–4.56 (br, 4H, O–C*H*), 2.50–2.30 (br, 8H, CH_2–C=CH), 2.15–0.77 (m, 164H), 0.68 (br_s, 12H, CH_3–C–CH–C_8H_{17}). ^{13}C-NMR (100 MHz, $CDCl_3$, TMS) δ (ppm): 172.8 (*C*O), 139.3 (*C*=CH), 123.0 (C=*C*H), 75.5 (COO*C*), 48.8 (NH–*C*H), 39.5, 38.0 (*C*H_2–C=CH), 36.9, 36.6, 36.1, 35.8, 31.9, 28.0, 27.7, 23.8, 22.8, 22.6, 19.3, 18.9 (NH–CH–*C*H_3), 18.7; IR (cm^{-1}) 1733 (CO), 1658 (CO), 1001 (Cu–N); MS (MALDI-FT-ICR): *m*/*z* calcd. for $C_{168}H_{225}N_8NaO_{12}$ ($[M^+H]^+$) 2610.657; found 2610.638.

Zn-Tetrakis(cholesteryloxy-L-alanylcarbonylphenyl)porphyrin (Zn-TChOAlaCPP)

H_2-TChOAlaCPP **(2)** (49.0 mg, 19.2 μmol) and zinc(II) acetate (35.7 mg, 195 μmol) were weighed. After nitrogen replacement, chloroform (2.00 mL) was added, and the solution was stirred at room

temperature for 24 h. When the reaction was complete, the mixture was subjected to column chromatography with chloroform/methanol (50/1 *v*/*v* ratio), and **Zn-TChOAlaCPP** (32.3 mg, 64%), which was a purple solid, was obtained from the eluate. ^{1}H-NMR (400 MHz, $CDCl_3$, TMS) δ (ppm): 8.91 (s, 8H, β-pyrrol), 8.29 (d, *J* = 7.92 Hz, 8H, Ar*H*), 8.15 (d, *J* = 7.92 Hz, 8H, Ar*H*), 7.08 (d, *J* = 7.11 Hz, 4H, CO–N*H*), 5.43 (d, *J* = 4.60 Hz, 4H, C=C*H*), 4.87 (quin, *J* = 7.11 Hz, 4H, NH–C*H*), 4.82–4.71 (m, 4H, O–C*H*), 2.50–2.36 (m, 8H, CH_2–C=CH), 2.08–0.80 (m, 164H), 0.69 (s, 12H, CH_3–C–CH–C_8H_{17}). ^{13}C-NMR (100 MHz, $CDCl_3$, TMS) δ (ppm): 172.8 (*C*O), 166.8 (*C*O), 149.9 (α-pyrrol), 146.4 (*Ar*), 139.3 (*C*=CH), 134.6 (*Ar*), 133.1 (*Ar*), 132.0 (β-pyrrol), 125.3 (*Ar*), 123.0 (C=*C*H), 120.1 (meso-*C*), 75.6 (COO*C*), 56.7, 56.1, 50.0, 48.8, 42.3, 39.7, 39.5, 38.0, 36.9, 36.6, 36.2, 35.8, 31.9. 31.8, 28.2, 28.0, 27.7, 24.3, 23.8, 22.8, 22.6, 21.0, 19.4, 18.9 (NH–CH–*C*H_3), 18.7, 11.9 (*C*H_3–C–CH–C_8H_{17}); IR (cm^{-1}) 1733 (CO), 1652 (CO), 996 (Zn–N); MS (MALDI-FT-ICR): *m*/*z* calcd. for $C_{168}H_{225}N_8O_{12}Zn$ ($[M^+H]^+$) 2611.657; found 2611.641.

5.2.3 Synthesis of Cu-TChOAlaCPP Supramolecular Polymer

A chloroform solution of **Cu-TChOAlaCPP** (0.2 mM) was made up to 2 μM in diethyl ether and diisopropyl ether, and allowed to stand in the dark for at least 5 h. To confirm the higher-order structure by electron microscopy, we prepared a high-concentration solution by adding anhydrous chloroform solution (0.5 mM) to diisopropyl ether to produce a concentration of 5 μM, and left it in the dark for at least 5 h. The Cu-TChOAlaCPP solutions did not exhibit fluorescence as shown in **Fig. 5.2A**. However, as shown in **Fig. 5.2B**, it is noted that *n*-octyl ether itself showed fluorescence.

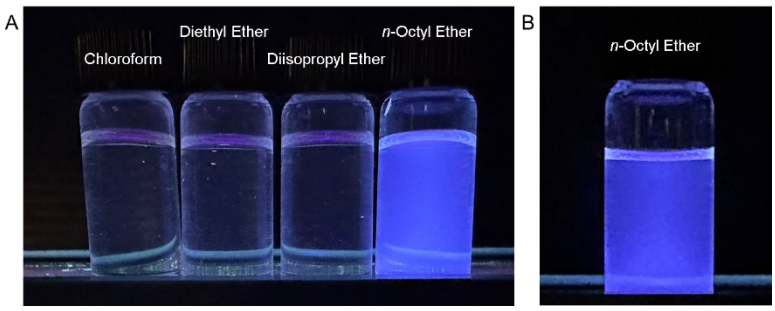

Fig. 5.2 Photographs of (A) Cu-TChOAlaCPP solutions, and (B) *n*-octyl ether excited at 365 nm.

5.2.4 Synthesis of Zn-TChOAlaCPP Supramolecular Polymer

A chloroform solution of **Zn-TChOAlaCPP** (1 mM) was made up to 10 μM in diethyl ether and diisopropyl ether, and allowed to stand in the dark for at least 5 h. The fluorescence spectra are shown in **Fig. 5.3**.

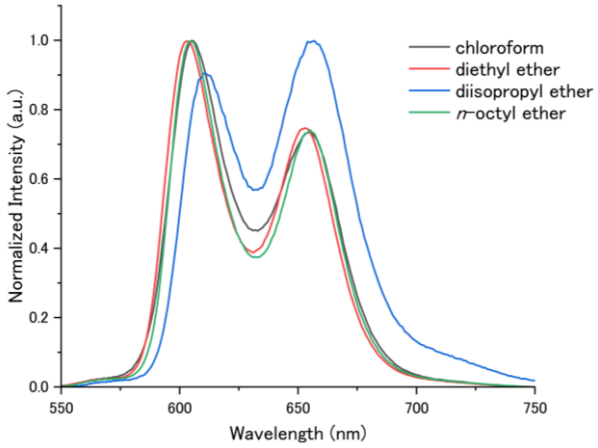

Fig. 5.3 Fluorescence spectra of Zn-TChOAlaCPP in chloroform (black line, λ_{ex} = 426 nm), in diethyl ether (red line, λ_{ex} = 423 nm), in diisopropyl ether (blue line, λ_{ex} = 431 nm), in *n*-octyl ether (green line, λ_{ex} = 428 nm).

The photographs of the Zn-TChOAlaCPP solutions excited at 365 nm are shown in **Fig. 5.4**. However, as shown in **Fig. 5.2B**, it is noted that *n*-octyl ether itself showed fluorescence.

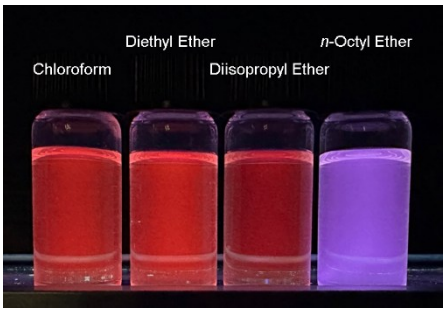

Fig. 5.4 Photographs of the Zn-TChOAlaCPP solutions excited at 365 nm.

5.2.5 AFM Imaging under Atmosphere

We used a PicoSPM II atomic force microscopies (AFM, Molecular Imaging, Tempe, USA) in tapping mode to obtain single-molecule images of the Cu- and Zn-TChOAlaCPP supramolecular polymers. The cantilever was an OMCL-AC160TS (Olympus, Tokyo, Japan).

The AFM samples were prepared as follows. For the Cu-TChOAlaCPP supramolecular polymer, the prepared solution (2 μM) was drop-cast onto a cleaved mica and dried thoroughly. For the Zn-TChOAlaCPP supramolecular polymer, the prepared solution (10 mM) was diluted with each solvent (< 1 μM) and spin-cast onto a cleaved mica. For the Cu- and Zn-TChOAlaCPP chloroform solutions, the prepared solutions (2 μM) were spin-cast onto a cleaved mica. **Fig. 5.5** (diisopropyl ether), **Fig. 5.6** (diethyl ether), and **Fig. 5.7** (chloroform) show AFM images of Cu-TChOAlaCPP supramolecular polymers, and **Fig. 5.8** (diisopropyl ether), **Fig. 5.9** (diethyl ether), and **Fig. 5.10** (chloroform) show AFM images of Zn-TChOAlaCPP supramolecular polymers.

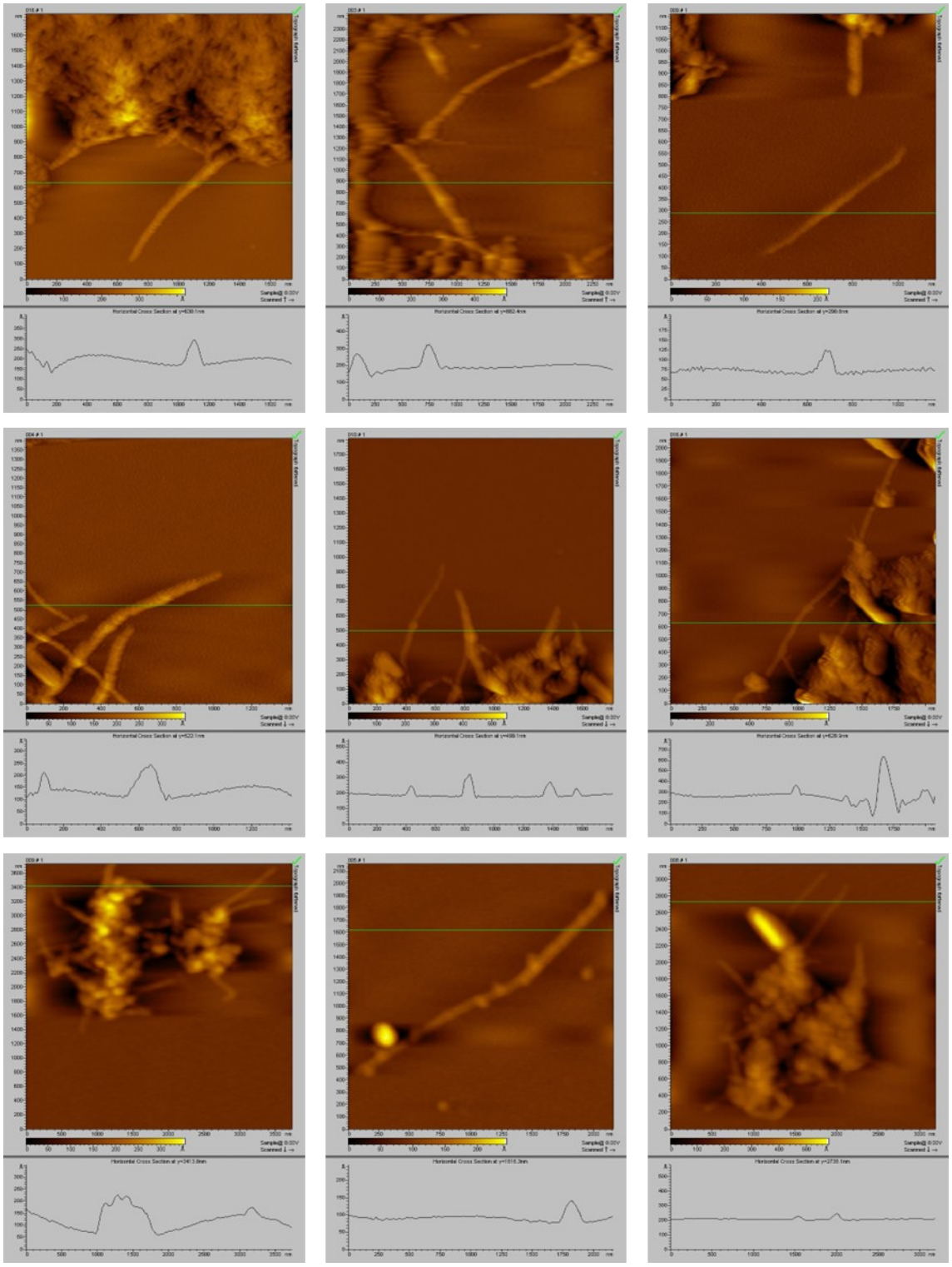

Fig. 5.5 AFM images and line profiles of Cu-TChOAlaCPP supramolecular polymers prepared in diisopropyl ether on mica under air at 25 ± 1 ºC.

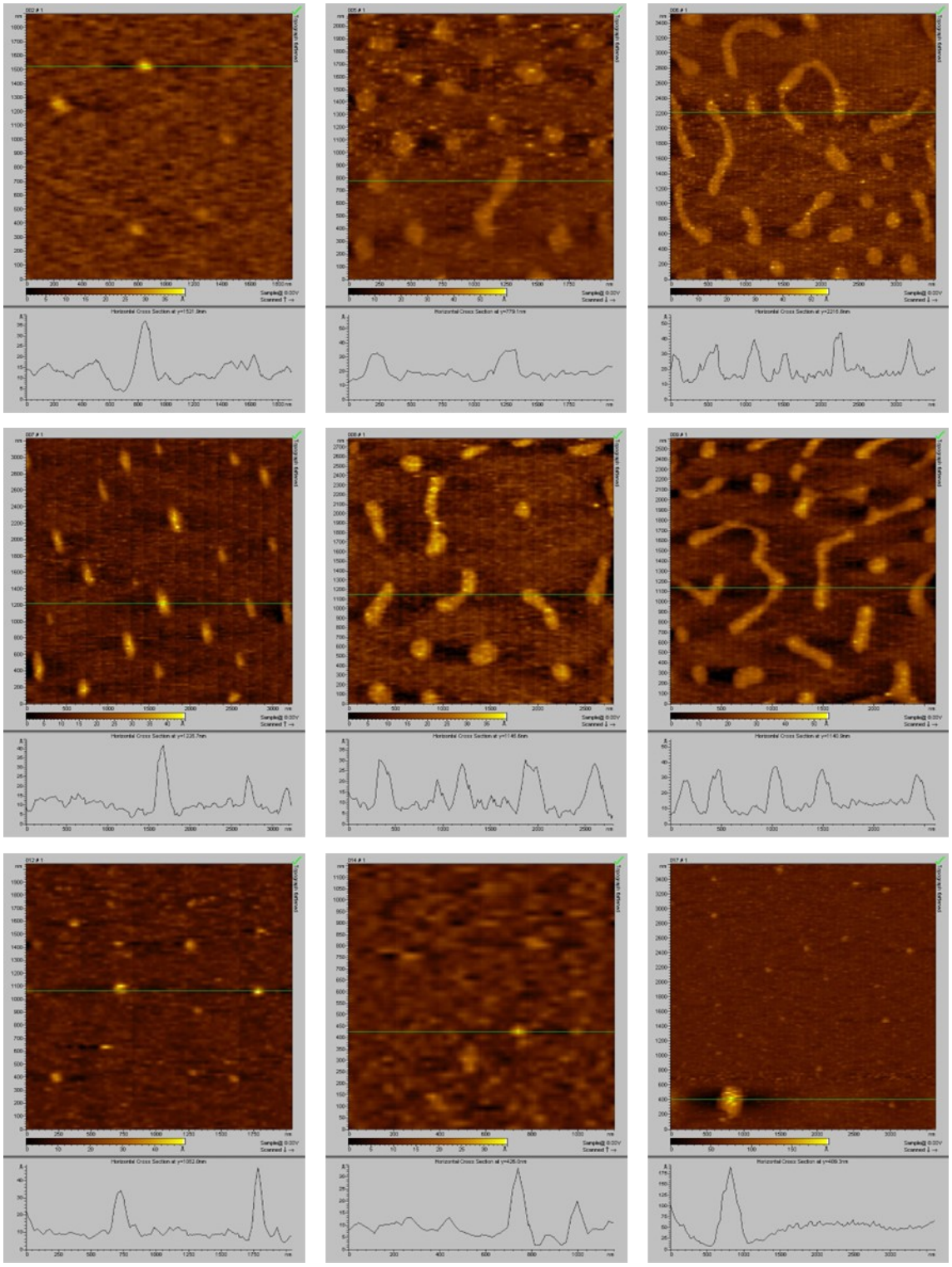

Fig. 5.6 AFM images and line profiles of Cu-TChOAlaCPP supramolecular polymers prepared in diethyl ether on mica under air at 25 ± 1 ºC.

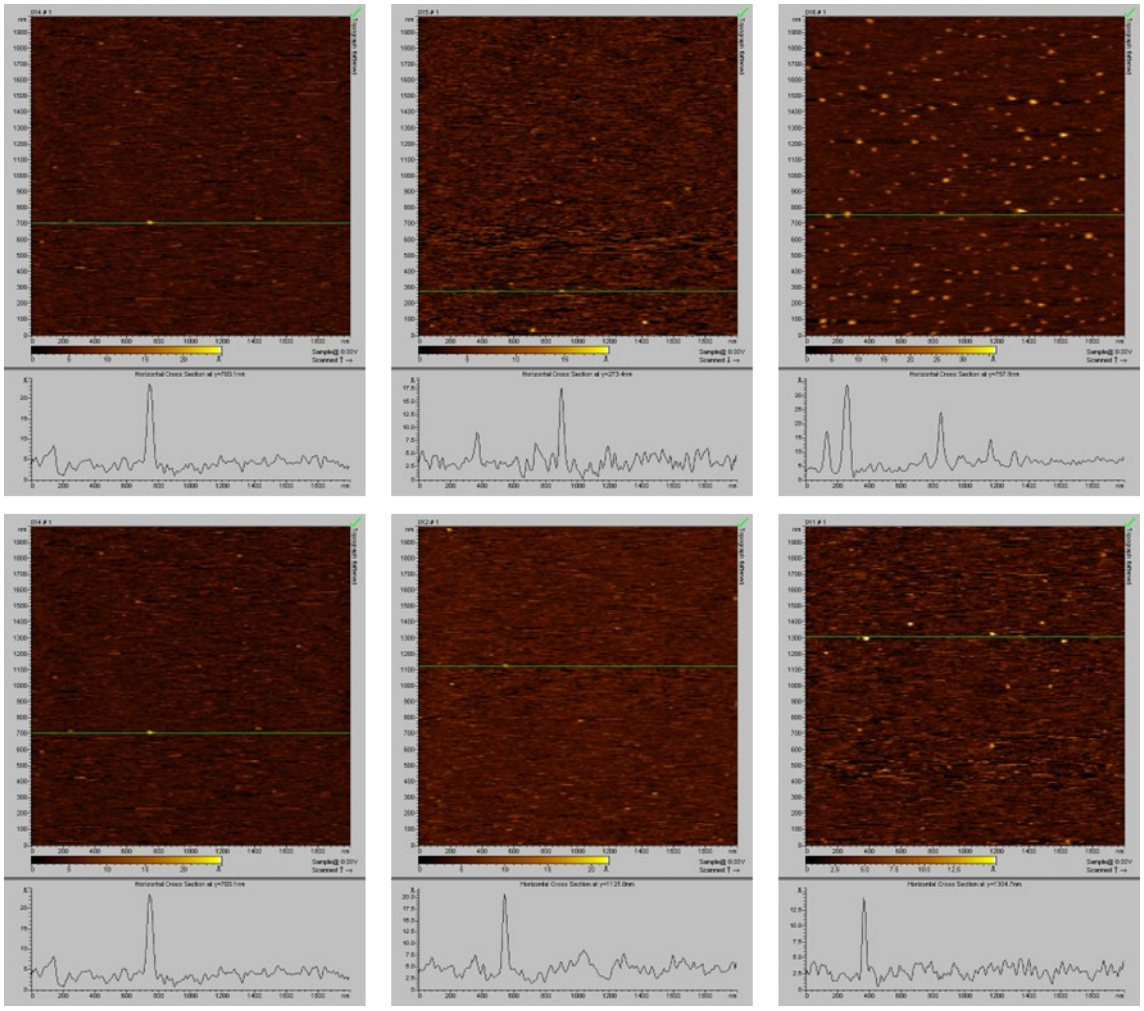

Fig. 5.7 AFM images and line profiles of Cu-TChOAlaCPP chloroform solution on mica under air at 25 ± 1 ºC.

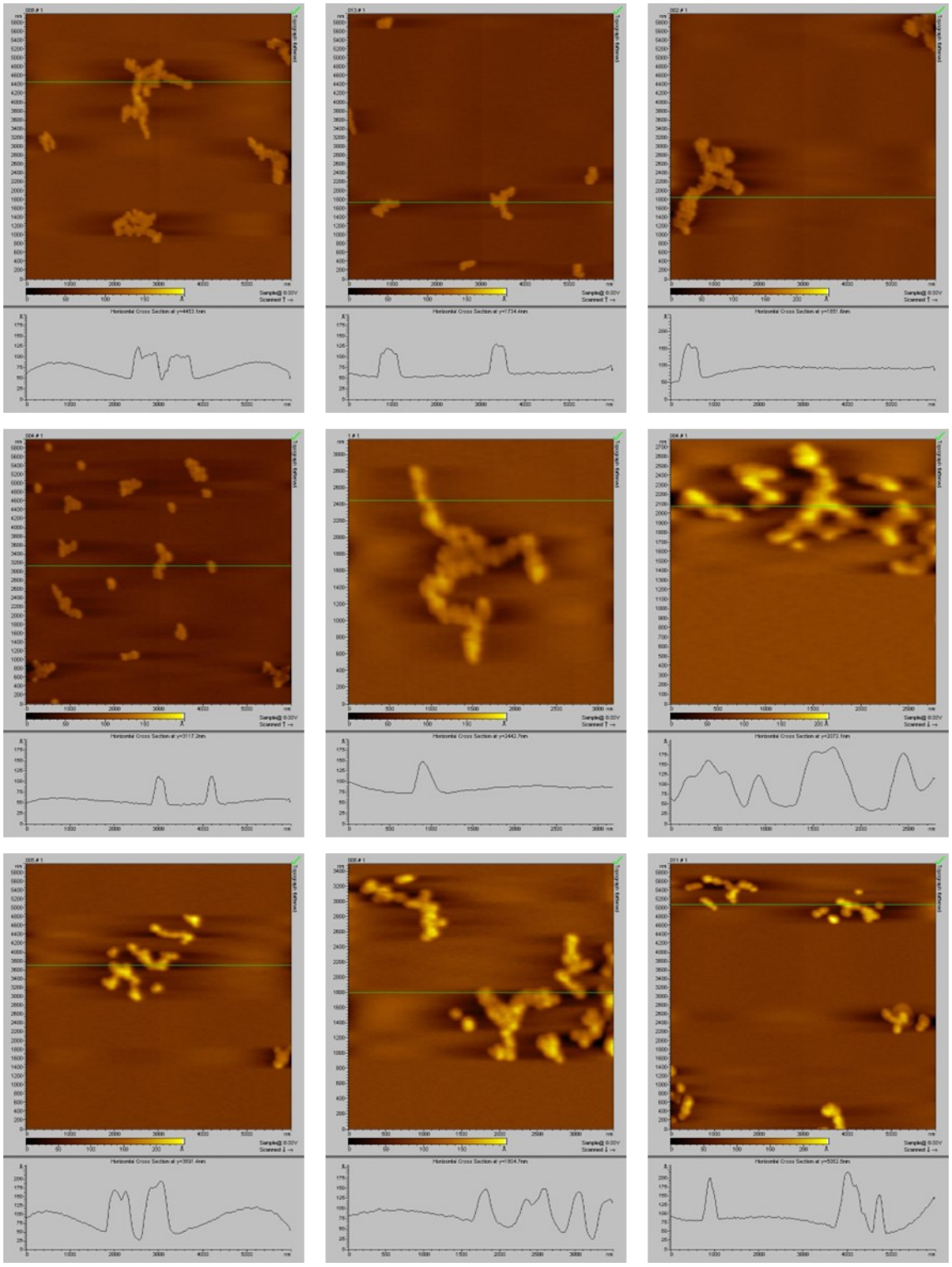

Fig. 5.8 AFM images and line profiles of Zn-TChOAlaCPP supramolecular polymers prepared in diethyl ether on mica under air at 25 ± 1 ºC.

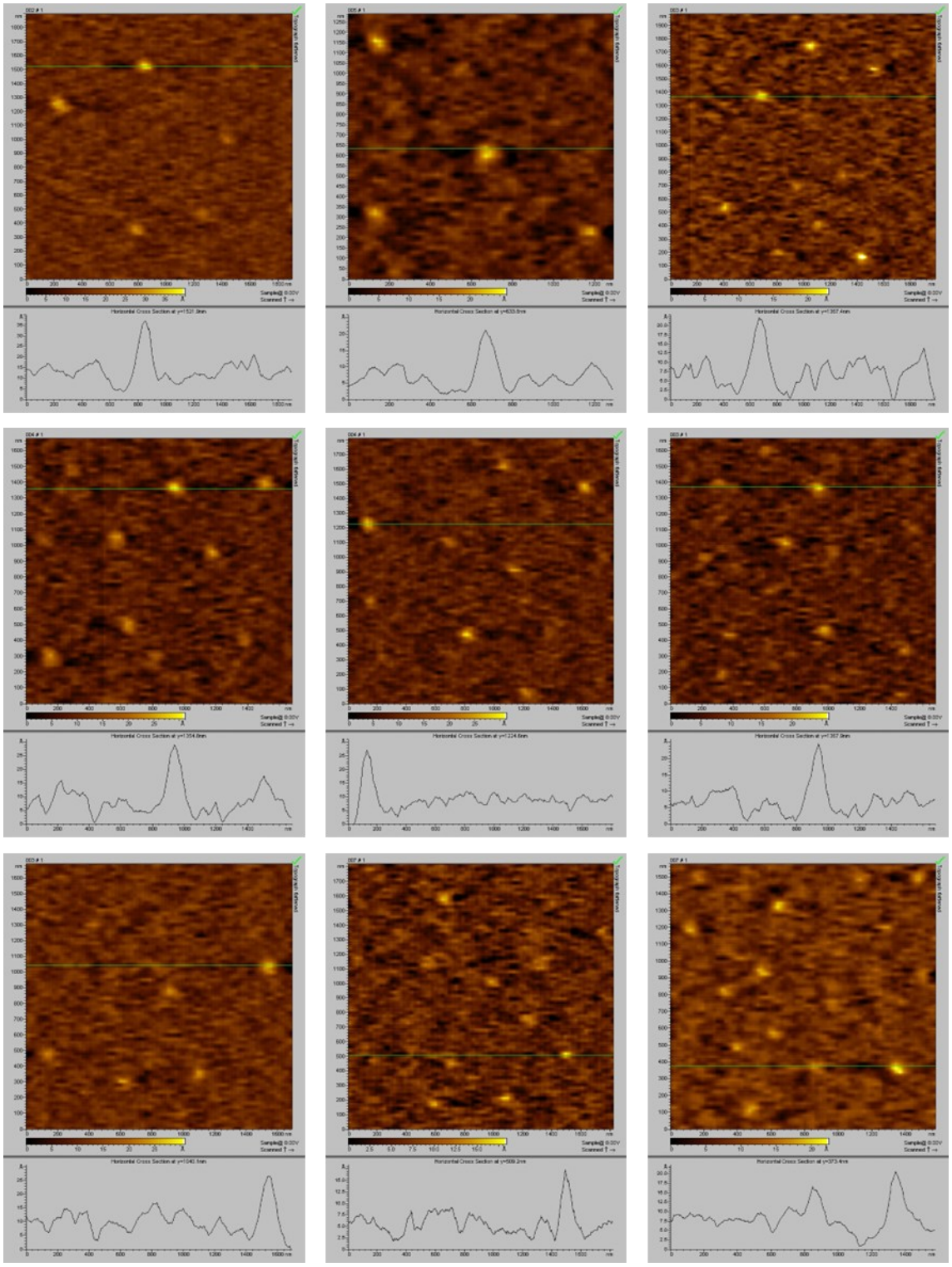

Fig. 5.9 AFM images and line profiles of Zn-TChOAlaCPP supramolecular polymers prepared in diisopropyl ether on mica under air at 25 ± 1 ºC.

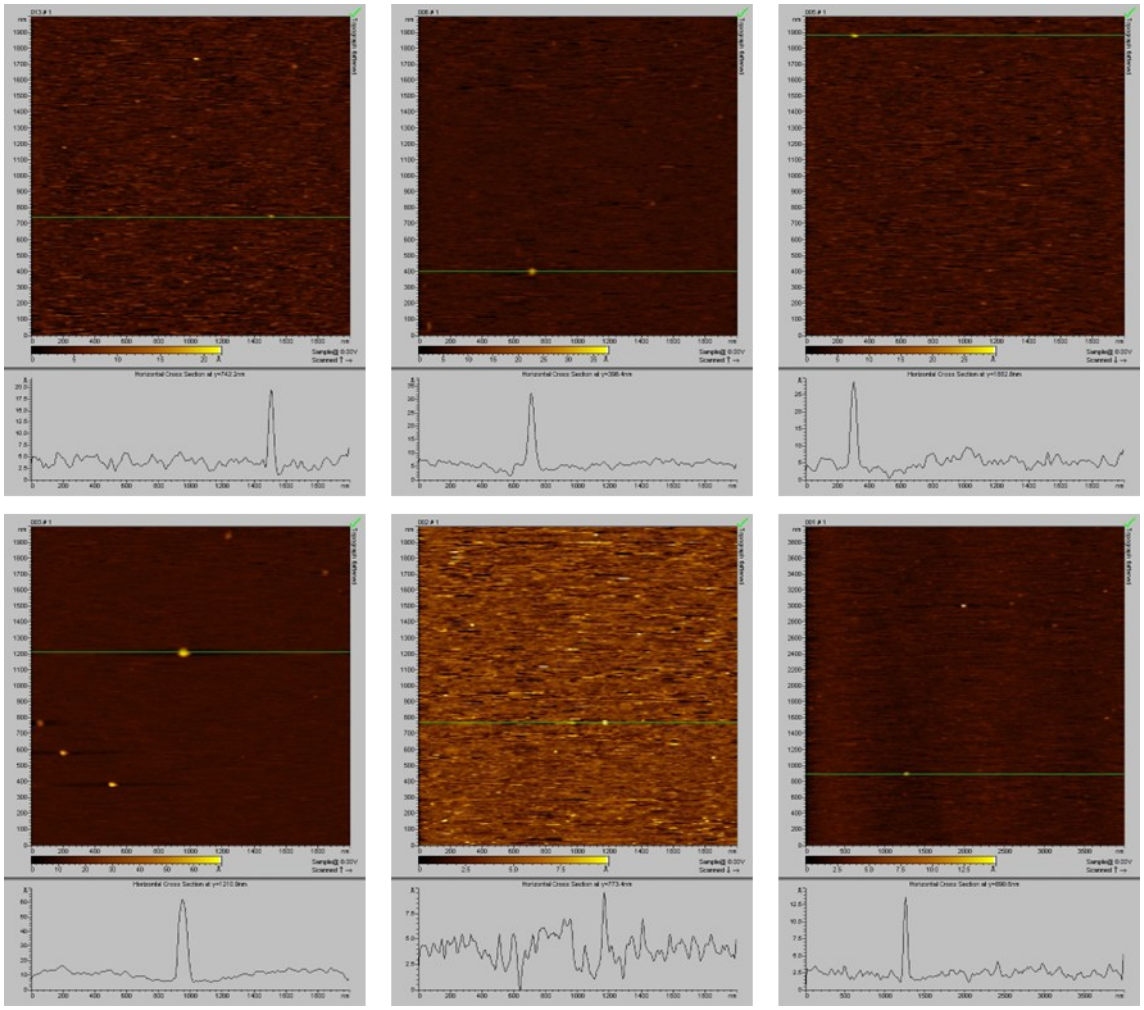

Fig. 5.10 AFM images and line profiles of Zn-TChOAlaCPP chloroform solution on mica under air at 25 ± 1 ºC.

5.2.6 FS-AFM Imaging

The FS-AFM video images were obtained in dynamic mode on a modified NVB500 FS-AFM (Olympus, Tokyo, Japan). An ultra-small cantilever USC-F1.2-k0.15 (NanoWorld AG, Neuchâtel, Switzerland) with a low spring constant of approximately 0.1 $N \cdot m^{-1}$ and a high resonance frequency above 1 MHz was used.

For the Cu-TChOAlaCPP, the diisopropyl ether solution (2 μM) of Cu-TChOAlaCPP was allowed to stand for more than 5 h and drop-cast onto the surface of a mica substrate to serve as the AFM video

imaging sample. AFM video imaging was carried out in *n*-octyl ether at 25 ± 1 ºC. A line profile is shown in **Fig. 5.11**.

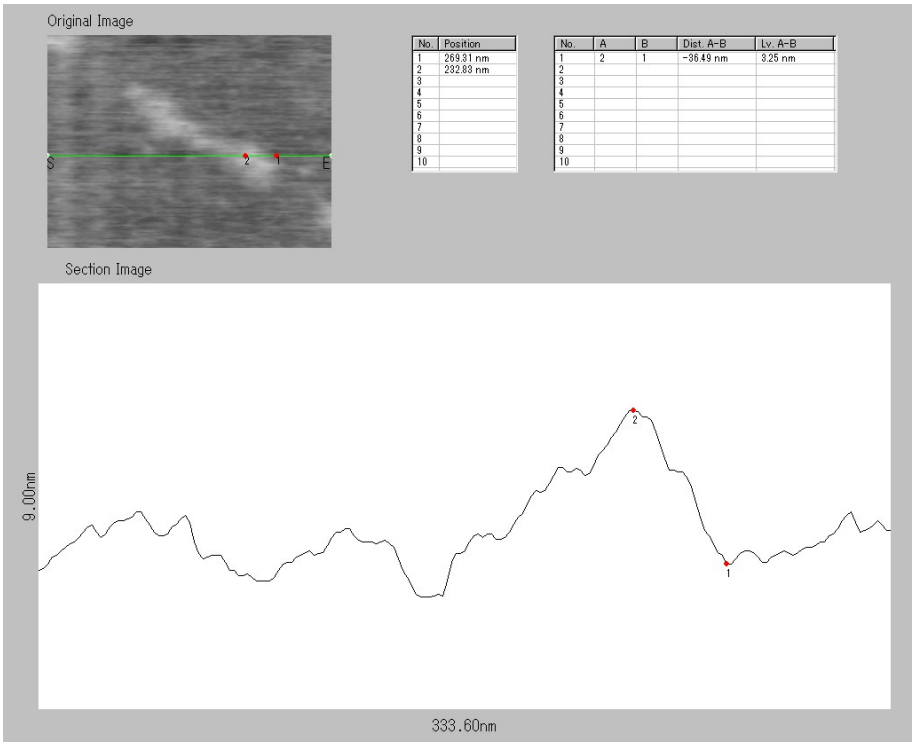

Fig. 5.11 A snapshot of FS-AFM video and line profile of Cu-TChOAlaCPP supramolecular polymer. FS-AFM image on mica under n-octyl ether at 25 ± 1 ºC. (XY, 334 × 250 nm; Z, 9.0 nm)

For the Zn-TChOAlaCPP, the diethyl ether solution (10 μM) of Zn-TChOAlaCPP was allowed to stand for more than 5 h, diluted 10-fold (< 1 μM), and drop-cast onto the surface of a mica substrate to serve as the AFM video imaging sample. AFM video imaging was carried out in *n*-octyl ether at 25 ± 1 ºC. A line profile is shown in **Fig. 5.12.**

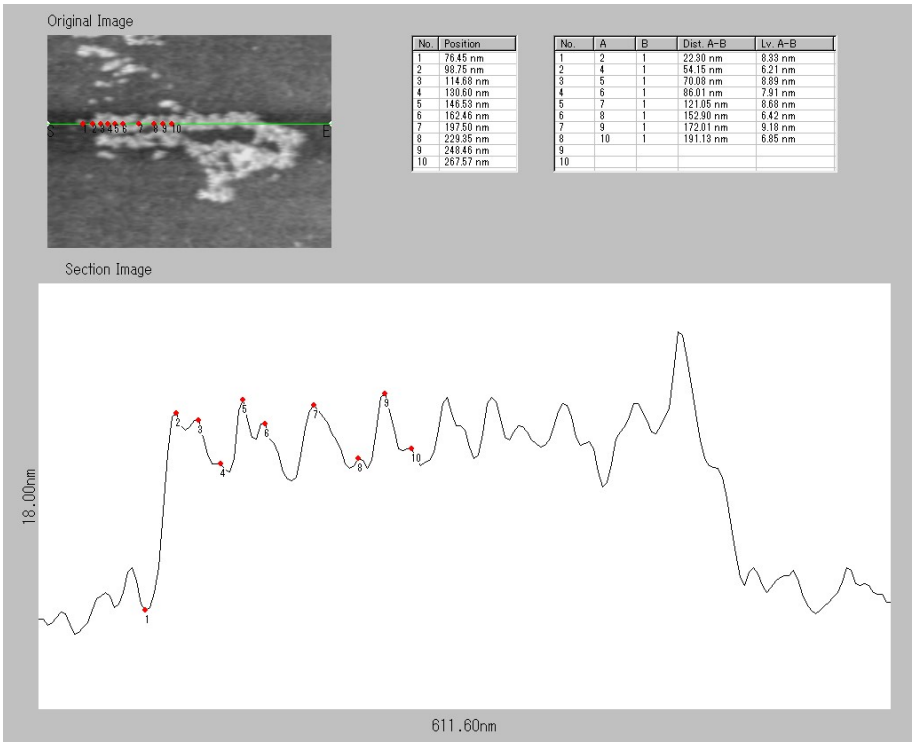

Fig. 5.12 A snapshot of FS-AFM video and line profiles of Zn-TChOAlaCPP supramolecular polymer. FS-AFM image on mica under n-octylether at 25 ± 1 ºC. (XY, 612 × 459 nm; Z, 18.0 nm)

5.2.7 SEM Imaging

We used a S-4500 or SU8230 scanning electron microscopy (SEM, Hitachi High-Tech Corporation., Tokyo, Japan) to obtain higher-order structure images of the Cu- and Zn-TChOAlaCPP supramolecular polymers.

The samples for SEM were prepared as follows. For the Cu-TChOAlaCPP supramolecular polymer, the prepared solution (5 μM) was drop-cast onto a Si single-crystal substrate, allowed to dry completely, and then coated with Pt-Pd to prepare the imaging sample (**Fig. 5.13**).

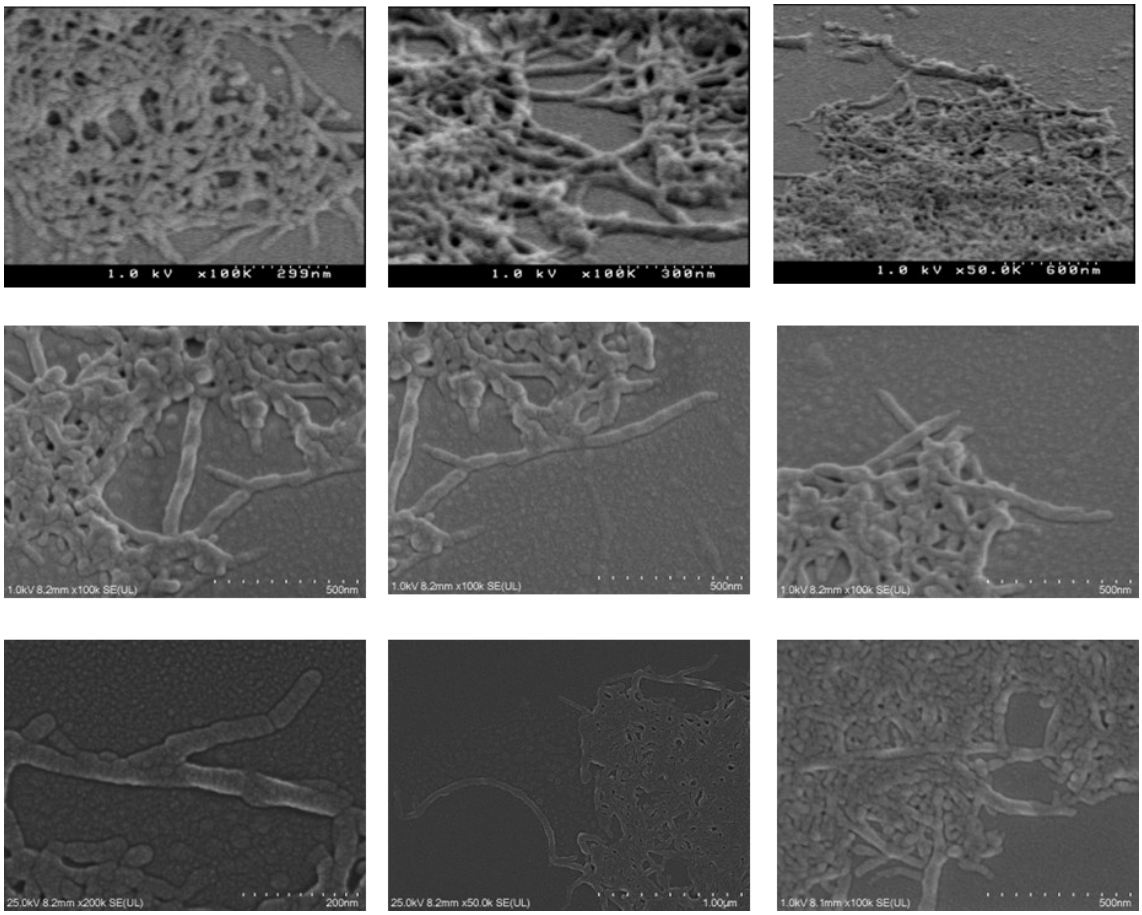

Fig. 5.13 SEM images of Cu-TChOAlaCPP supramolecular polymer on Si single crystal.

An identical method was used to prepare the Zn-TChOAlaCPP supramolecular polymer except that the solution comprised 10 μM diethyl ether. In each case, the supernatant solution was used because fibers were precipitated during the process (**Fig. 5.14**).

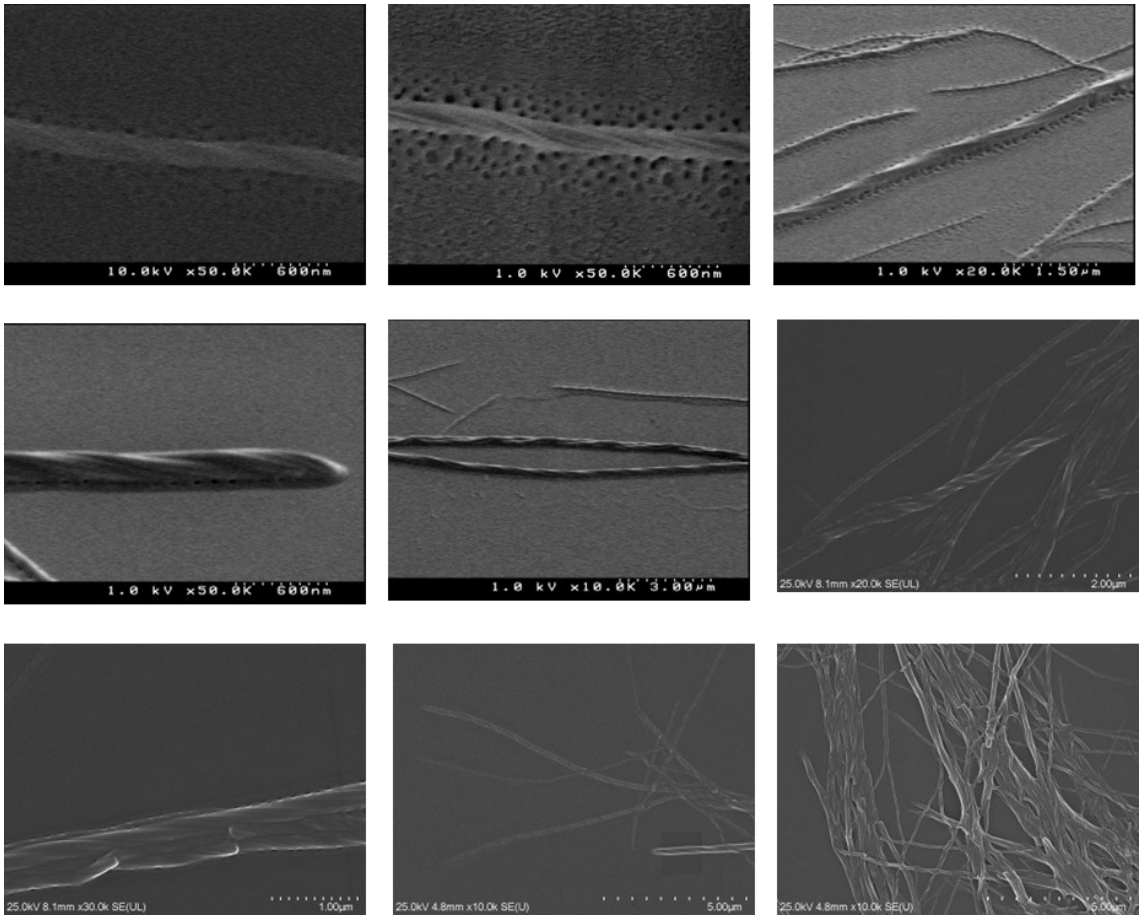

Fig. 5.14 SEM images of Zn-TChOAlaCPP supramolecular polymer on Si single crystal.

5.2.8 TEM Imaging

We used a H-7650 (Hitachi High-Tech Corporation., Tokyo, Japan) or JEM-2100Plus (JEOL Ltd., Tokyo, Japan) transmission electron microscopy (TEM) to obtain higher-order structure images of the Cu- and Zn-TChOAlaCPP supramolecular polymers.

The samples for TEM were prepared as follows. For the Cu-TChOAlaCPP supramolecular polymer, one or two drops of the prepared solution (5 μM) were placed on an ultra-high-resolution carbon support microgrid substrate and dried in a draft of air for 1 day (**Fig. 5.15**).

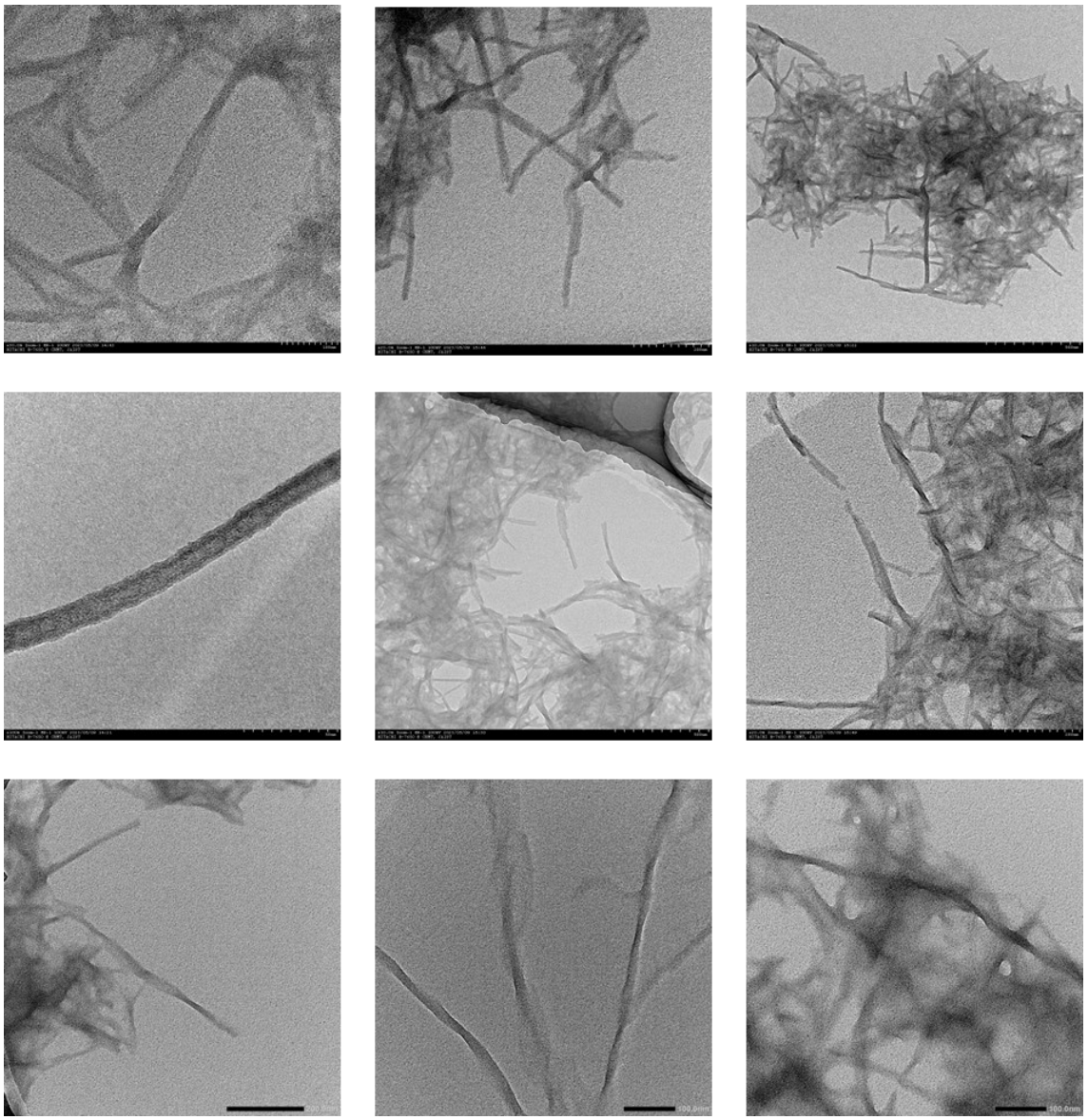

Fig. 5.15 TEM images of Cu-TChOAlaCPP supramolecular polymer on ultra-high-resolution carbon support microgrid substrate.

An identical method was used to prepare the Zn-TChOAlaCPP supramolecular polymer except that the supernatant solution was used owing to precipitation and its concentration was 10 μM (**Fig. 5.16**).

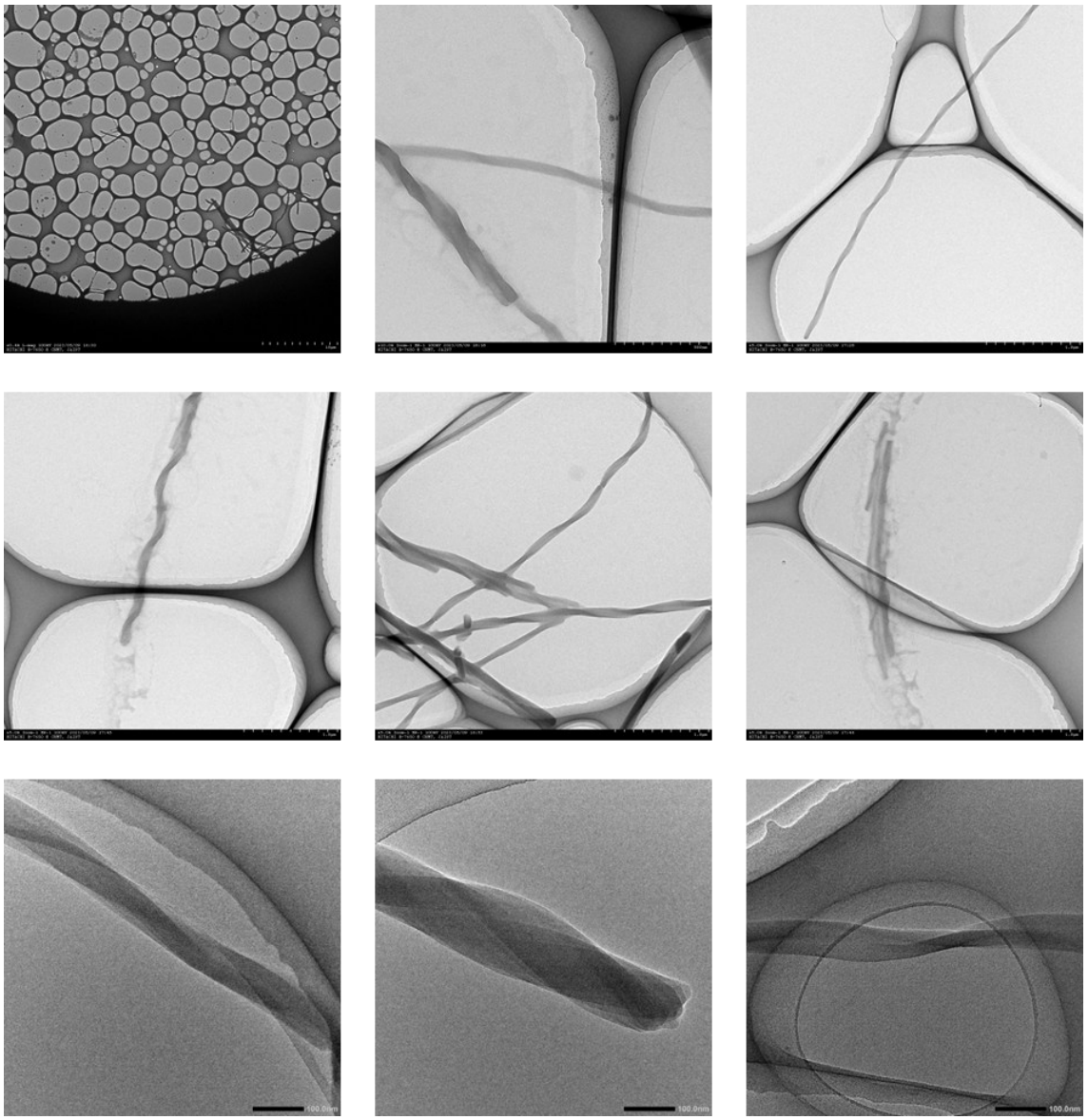

Fig. 5.16 TEM images of Zn-TChOAlaCPP supramolecular polymer on ultra-high-resolution carbon support microgrid substrate.

5.2.9 All-Atom MD Simulation

The molecular mechanics (MM) and all-atom molecular dynamics (MD) calculations were carried out using the Forcite module of BIOVIA Materials Studio 2023 (Dassault Systèmes BIOVIA, San Diego, CA, USA) on a supercomputer system (PowerEdge R6525, Dell Technologies Inc., Round Rock, TX, USA).

For the Cu-TChOAlaCPP polymer, 10 monomers were placed at 4 Å intervals and formed a right-handed helix structure without cutting hydrogen bonds. The geometry of the model was optimized and placed in an MD cell. The MD cell was built according to the usual procedure for an amorphous cell module. The MD cell dimensions and angles were: a = 80 Å, b = 80 Å, and c = 80 Å; and α = 90°, β = 90°, and γ = 90°, respectively. The supramolecular polymer was placed in the center of the cell, and the diethyl ether solvent molecules were packed in the cell at a density of 0.725 g cm^{-3}. The geometry of the MD cell was optimized sequentially. In the NVT ensemble (constant number of atoms, volume, and temperature), simulation was conducted at 298 K for 50 ps (time step of 0.2 fs; 250,000 steps), and in the NPT ensemble (constant number of atoms, pressure, and temperature), simulation was conducted at a pressure of 1.013×10^{-4} GPa at 298 K for 100 ps (time step of 1.0 fs; 100,000 steps) to equilibrate the MD cell. A Nosé–Hoover thermostat was used to control the temperature, and a Berendsen barostat was used to control the pressure. After equilibration at 298 K, simulation in the NVE ensemble (constant number of atoms, volume, and energy) was conducted for 10 ns (time step of 1.0 fs; 10,000,000 steps) as the production run. The Universal forcefield was used, and the charges were assigned by the forcefield. A snapshot structure is indicated in **Fig. 5.17**.

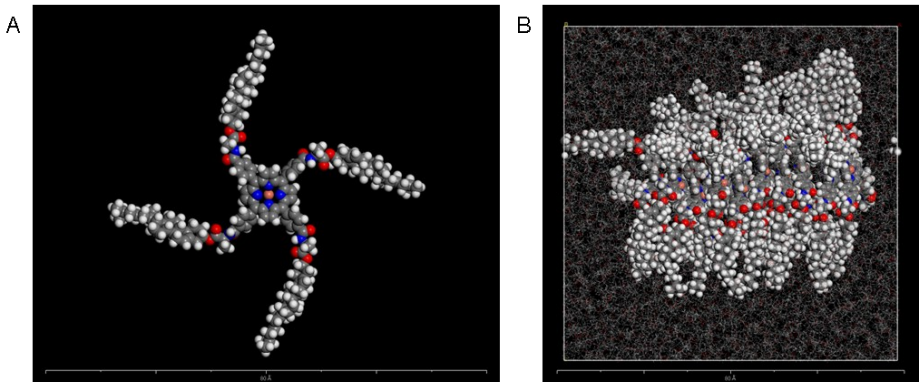

Fig. 5.17 A snapshot of MM and MD calculation. (A) A snapshot of MM calculation for the Cu-TChOAlaCPP. (B) A snapshot of all-atom MD simulation at 10 ns of Cu-TChOAlaCPP 10-mer.

For the Zn-TChOAlaCPP polymer, 10 main-chain monomers and 3 branching-chain monomers were placed without porphyrin stacking and formed a right-handed helix structure. The geometry of the model was optimized and the supramolecular polymer was placed in MD cell. The MD cell was built according to the usual procedure for an amorphous cell module. The MD cell length and angle were a = 185 Å, b = 110 Å, and c = 90 Å; and α = 90°, β = 90°, and γ = 90°, respectively. The supramolecular polymer was placed in the center of the cell, and the diisopropyl ether solvent molecules were packed in the cell at a density of 0.713 g cm^{-3}. The geometry of the MD cell was sequentially optimized. Simulation in the NVT ensemble (constant number of atoms, volume, and temperature) was conducted at 298 K for 100 ps (time step of 0.5 fs; 200,000 steps). The Zn-TChOAlaCPP polymer was then treated in the same way as the Cu-TChOAlaCPP polymer. A snapshot structure is indicated in **Fig. 5.18**.

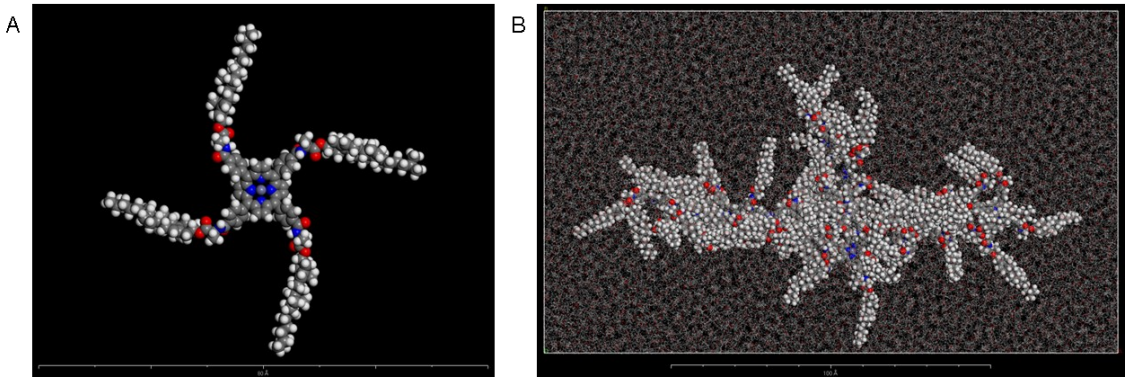

Fig. 5.18 A snapshot of MM and MD calculation. (A) A snapshot of MM calculation for the Zn-TChOAlaCPP. (B) A snapshot of all-atom MD simulation at 10 ns of Zn-TChOAlaCPP 10-mer with branching-chain.

5.3 Results and Discussion

5.3.1 Synthesis of M-TChOAlaCPP Supramolecular Polymers

Cu- and Zn-tetrakis(cholesteryloxyalanylcarbonylphenyl)porphyrin (TChOAlaCPP) were synthesized as follows (**Scheme 5.1**). Spectral data are provided in the Supporting Information. (−)-Cholesterol and *N*-Boc-L-alanine were subjected to a condensation reaction followed by deprotection to afford the pendant, L-alanine cholesteryl ester **1**. The 4-equivalent pendant **1** was subjected to condensation reaction with tetrakis(4-carboxyphenyl)porphyrin (TCPP) to afford H_2-TChOAlaCPP **2**. The monomers M-TChOAlaCPP (M = Cu, Zn) were obtained by reaction of H_2-TChOAlaCPP **2** with Cu or Zn acetates.

M-TChOAlaCPP supramolecular polymers were prepared by dissolving the synthesized M-TChOAlaCPPs in chloroform, pouring to diethyl ether or diisopropyl ether, and allowing the mixture to stand for at least 5 hours.

5.3.2 Aggregation Studies

The aggregation state was confirmed by ultraviolet–visible (UV-vis) absorption spectroscopy and circular dichroism (CD) spectroscopy (**Fig. 5.19**). Both Cu- and Zn-TChOAlaCPP were predominantly monomeric in chloroform, with maxima in the Soret band at 417 (Cu) and 426 nm (Zn), and no CD signal was observed for either monomer (**Fig. 5.19 black line**).

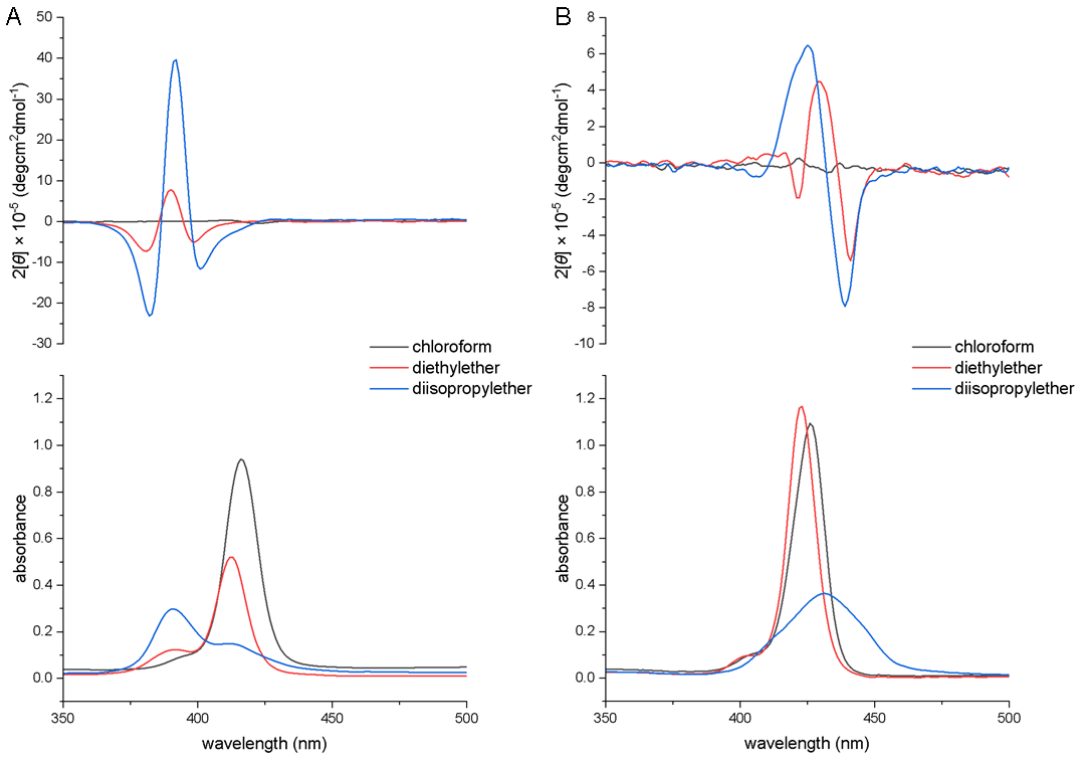

Fig. 5.19 UV-vis absorption (bottom) and CD (upper) spectra of (A) Cu- and (B) Zn-TChOAlaCPP.

For Cu-TChOAlaCPP, the maximum absorption wavelength in the Soret band of the aggregates formed in diisopropyl ether was 390 nm, indicating a blue shift compared with the monomer (**Fig. 5.19A blue line**). This indicates that Cu-TChOAlaCPP formed H-aggregates in diisopropyl ether. However, when formed in diethyl ether, a slight peak at 392 nm suggests the formation of H-aggregates, although a monomeric peak remained (**Fig. 5.19A red line**). The CD spectrum of Cu-TChOAlaCPP featured −/+/− CD peaks at 401, 392, and 382 nm. This pattern is similar to those reported by Mabesoone et al.[1] and Lorecchio et al.,[2] and it is thought that the helical porphyrin aggregates form higher-order structures.[20, 21] The signals attributable to a positive Cotton effect at short wavelengths (392 and 382 nm) are due to the aggregation of the porphyrins. In general, porphyrins are adaptable to the exciton chirality method,[22] so it is assumed that right-handed chiral helical H-aggregates are

formed. The three CD signal patterns of −/+/− are derived from higher-order structures formed by stacked porphyrins. According to Didraga et al.,[20] the intensity of a CD signal attributable to higher-order structures varies with the length of that structure, suggesting the formation of well-grown higher-order structures.

For Zn-TChOAlaCPP, the maximum absorption wavelength in the Soret band of the aggregates formed in diethyl ether was 423 nm, and it showed no significant shift compared with the monomer. Normally, a blue shift is observed when H-aggregates are formed, and a red shift is observed when J-aggregates are formed. So, the porphyrin rings of Zn-TChOAlaCPP aggregates in diethyl ether are thought to be so far apart that only weak exciton interactions take place between them. The CD spectra of Zn-TChOAlaCPP in diethyl ether features −/+/− CD signals at 441, 429, and 422 nm. It is similar to that of Cu-TChOAlaCPP; the positive Cotton effect at short wavelengths (429, 422 nm) is due to the weak exciton interaction between the porphyrin rings arranged in a right-handed helix. Furthermore, the three −/+/− CD signal patterns suggest the formation of higher-order structures. These facts suggest that the Zn-TChOAlaCPP is aggregated by the van der Waals interactions of its cholesteryl groups. On the other hand, the aggregates formed in diisopropyl ether produced a broad peak at 431 nm. The CD spectrum of Zn-TChOAlaCPP in diisopropyl ether featured −/+ CD peaks at 439 and 425 nm, respectively. In contrast to the CD spectrum produced by Zn-TChOAlaCPP in diethyl ether solution, there were only two peaks, suggesting the formation of a left-handed helical J-aggregate without the formation of higher-order structures.

5.3.3 Imaging of Cu-TChOAlaCPP Supramolecular Polymer

We observed the Cu-TChOAlaCPP supramolecular polymer grown in diisopropyl ether using AFM, SEM and TEM. The polymer shown in **Fig. 5.20A** is a rod that was 442 nm long. The height of the chain was approximately 4.4 nm, which was consistent with the MM calculation (**Fig. 5.17A**) when the effect of tapping[23] was considered. But the chain was very linear and wider than a single chain

even considering the curvature radius of the AFM probe. Therefore, it is considered as a bundle structure in which several chains lined up. As shown in the UV-vis spectrum, Cu-TChOAlaCPP formed H-aggregates due to π–π interactions between porphyrin rings. And then, the aggregates grew into rods and were lined up. It was easy for the rods to line up because the porphyrin has cholesteryl groups that express strong van der Waals forces. The polymer shown in **Fig. 5.20B** has a left-handed helical structure with a width of 17 nm and a helical pitch of 6 nm. There are darker and lighter regions in this structure. It means this structure is hollow structure. The width of the lighter region is approximately 6 nm, and the width of the darker region is also approximately 6 nm. These observations are consistent with the size of a porphyrin molecule. Based on its size and structural features, the structure in **Fig. 5.20B** is a superhelix formed by torsional strain from a single H-aggregate rod. As with higher-order structures in general, it formed a left-handed helix, which was the opposite direction of torsion between the porphyrin rings indicated by the CD spectrum. It is considered that the helical pitch was so small despite the higher-order structure owing to the interaction between the pendant cholesteryl groups. The polymer shown in **Fig. 5.20C** is a ribbon forming a loose right-handed helix with a width of 25 nm and a helical pitch of 206 nm. The contrast of the TEM image suggests that this supramolecular polymer had a ribbon structure with uniformly aligned porphyrins. The ribbon was 13 nm thick, which was smaller than the superhelix structure shown in **Fig. 5.20A**, and approximately twice the size of the single molecule of Cu-TChOAlaCPP suggested by the MM calculation. We note here that both of the torsional direction between the porphyrin rings suggested by the CD spectrum and the ribbon structure are same. In general, single helical supramolecular polymers form higher-order structures with helices in the opposite direction, owing to torsional strain. However, Meijer et al. reported that the rod structure of a H-aggregate collapses and rearranges to maximize the interaction between the pendants, resulting in the same helical direction in the higher-order structure and H-aggregate.[1] Because TChOAlaCPP has pendant cholesteryl groups that express strong van der Waals interactions, it was possible to rearrange the aggregation form to maximize the interactions and form

higher-order structures similar to those in the porphyrin supramolecular polymer reported by Meijer et al. Therefore, we think that the torsional direction between the porphyrin rings and the higher-order structure was the same.

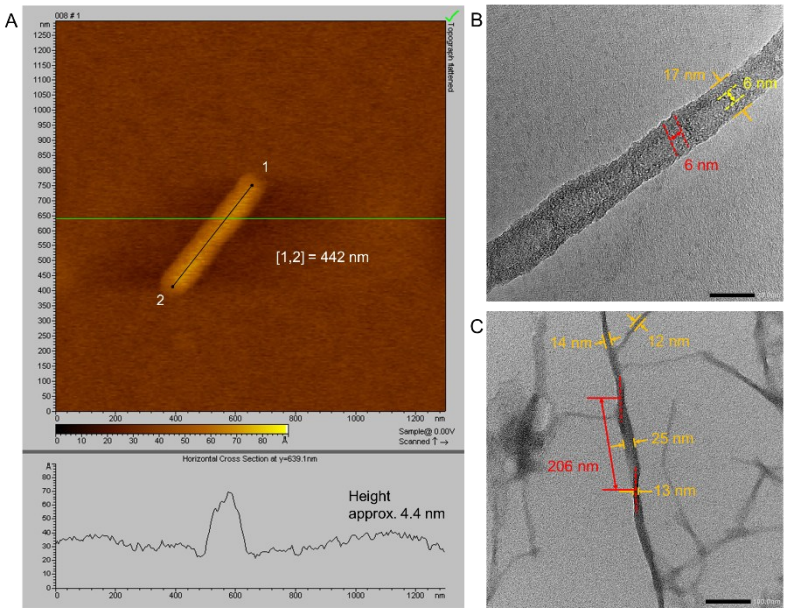

Fig. 5.20 Microscopic images of Cu-TChOAlaCPP supramolecular polymers; (A) bundle structure in which several chains lined up; (B) superhelix; and (C) ribbon. (A) AFM imaging was carried out on mica under air at 25 ± 1 ºC (Topography image, X: 1298 nm, Y: 1298 nm). (B, C) TEM imaging was carried out on an ultra-high-resolution carbon support membrane.

Cu-TChOAlaCPP supramolecular polymers grown in diethyl ether were also drop cast onto a mica substrate and imaged using AFM (**Fig. 5.6**). Supramolecular polymers similar to the rods grown in diisopropyl ether were observed. However, many spherical structures were observed that were not well grown. This is due to insufficient association, as indicated by spectroscopy. We didn't analyze further detailed structures because the aggregates must be well grown to function as rail molecules in molecular motors.

5.3.4 Imaging of Zn-TChOAlaCPP Supramolecular Polymer

We also observed the Zn-TChOAlaCPP supramolecular polymer grown in diethyl ether using AFM, SEM and TEM. The polymer shown in **Fig. 5.21A** is the most straightforward structure, rod having branching-chains. This polymer with a main chain that was 3792 nm in length and seven branching chains ranging in length from 65 to 675 nm.[24, 18] In addition, a 179 nm branch-on-branch structure was identified in the longest 675 nm branching chain. The height of the polymer was approximately 6–9 nm, which corresponds to one to two molecules according to the MM calculation **(Fig. 5.18A**). This suggests that monomers or a short chain partially adsorbed to a single chain. Porphyrin supramolecular polymers do not usually have branching chains. However, several branching chains were observed in the identified Zn-TChOAlaCPP supramolecular polymer. This porphyrin has four cholesteryl groups, and the supramolecular polymers were formed by van der Waals interactions of them. So, there are multiple parts that can interact, and this enables to be formed branching structures. The polymers shown in **Fig. 5.21B**, **C top** and **C bottom** are isolated fibers which were the most common of higher-order structures. The thickness and helical pitch of the fiber structure varied. This is due to the number of rods forming the fiber structure. The chirality of the fiber structure is unity (right-handed) as far as we have observed. Some of the fibers were formed long-range helix such as **Fig. 5.21B**. The polymers shown in **Fig. 5.21D**, **E** and **F** are ribbons. It formed both right- and left-handed helices. The ribbons were 134 and 157nm wide, 50 and 190 nm thick, and its helical pitch ranged from 369 to 589 and 2304 nm, respectively. The polymers shown in **Fig. 5.21C middle** and **G** are multiple-helix structures. We confirmed the double- (**Fig. 5.21C middle**) and triple-helix (**Fig. 5.21G**). These structures were formed by entanglement of two or three fibers. Fibers constructing double- and triple helix are with width of 181, 24–32 nm and a helical pitch of 2205, 582 nm, respectively. We were also imaged a rod with branching chains that appeared to be the simplest Zn-TChOAlaCPP supramolecular polymer (**Fig. 5.21H**). Although we could not confirm its helical structure, TEM did not reveal any overlap of polymer chains (contrast difference) at the branching point, which strongly suggests that the branching

structure was formed by van der Waals forces between cholesteryl groups.

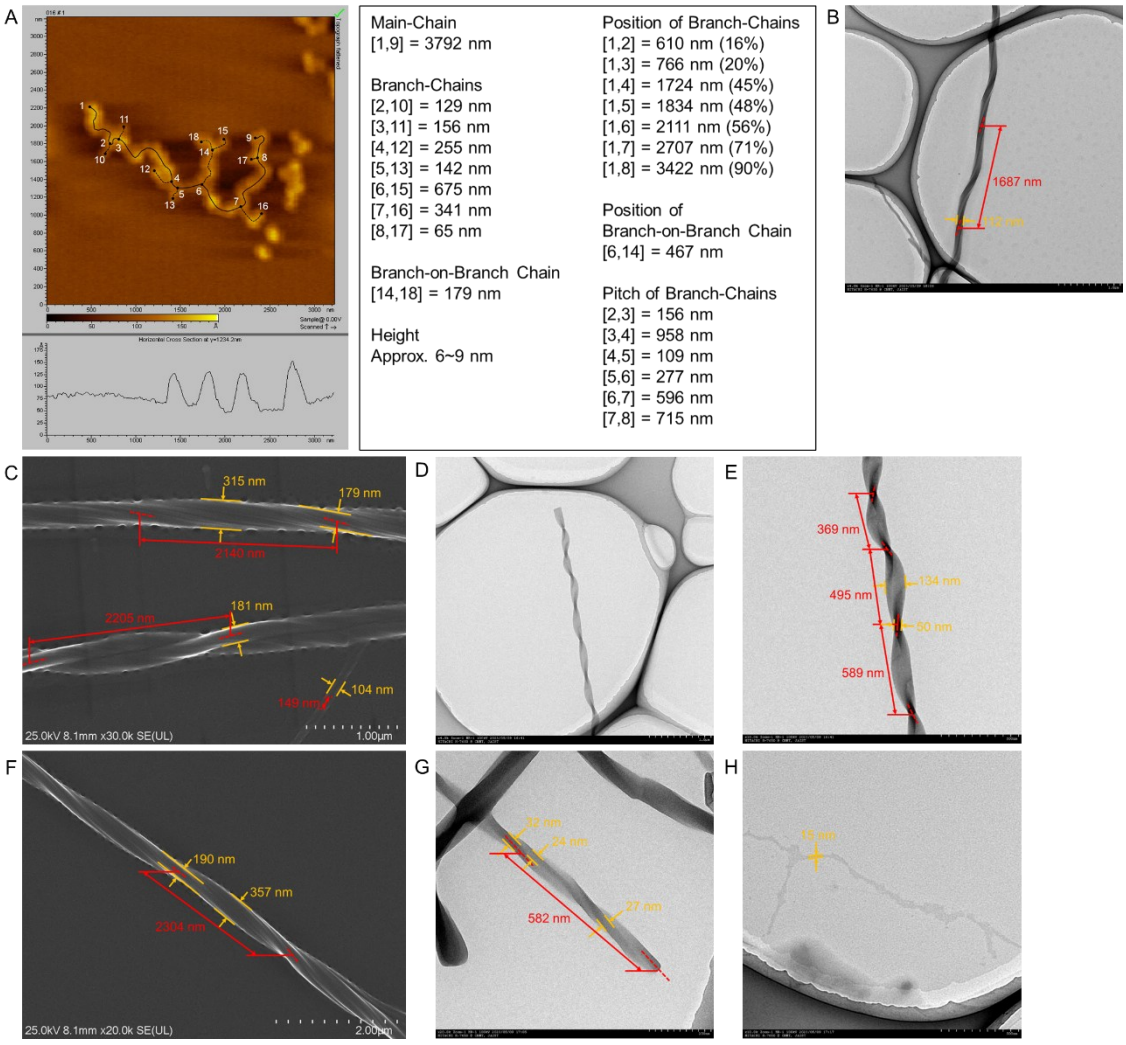

Fig. 5.21 Microscopic images of various structure of Zn-TChOAlaCPP supramolecular polymer: (A) an image and analysis data pertaining to the branching structure; (B, C top and bottom) rod; (D, E and F, E is an enlarged view of D) ribbon; and (C middle) double-helix structure; (G) triple-helix structure; and (H) fiber with branched chains. (A) AFM imaging was carried out on mica under air at 25 ± 1 ºC (Topography image, X: 3224 nm, Y: 3224 nm). (C, F) SEM imaging was carried out on a single Si crystal, and the samples were spatter-coated with Pt-Pd. (B, D, E, G, H) TEM imaging was carried out on an ultra-high-resolution carbon support membrane.

5.3.5 All-Atom MD

We used all-atom MD calculations to confirm the stability of the aggregates in solvents. In the Cu-TChOAlaCPP, we made 10 monomers placed at 4 Å intervals and formed right-handed helix structures (H-aggregates) without cutting hydrogen bonds. The model was placed in the MD cell, packed with diisopropyl ether (d = 0.725), optimized, equilibrated at 298 K, and finally subjected to a production run at 298 K from 0 to 10 ns in the microcanonical ensemble (NVE, **Fig. 5.22**).

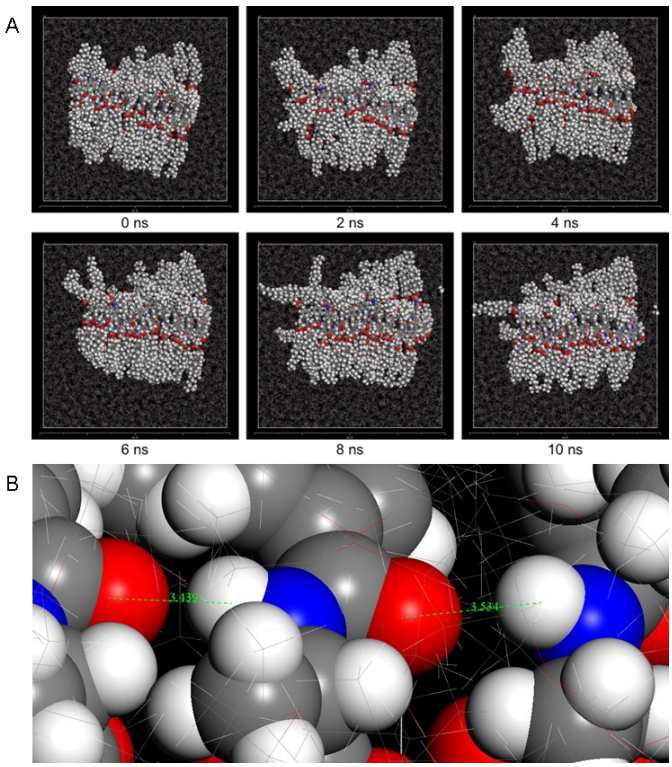

Fig. 5.22 MD calculation of Cu-TChOAlaCPP 10-mer. (A) Snapshots of all-atom MD of Cu-TChOAlaCPP obtained by the microcanonical ensemble (NVE) after equilibration at 298 K in diisopropyl ether. (B) Hydrogen bonding between amide groups after a 10 ns production run.

The Cu-TChOAlaCPP supramolecular polymer in diisopropyl ether did not collapse, retaining the porphyrin association state throughout the simulation (**Fig. 5.22A**). The helical structure was also retained, indicating the validity of the helical direction inferred from the CD spectra and the exciton chirality method. The calculations for Cu-TChOAlaCPP indicated that there were hydrogen bonds

(approximately 3.5 Å) between amide groups (NH-O), it was partial (**Fig. 5.22B**).[25] It is thought that hydrogen bonding acted in addition to π–π interactions between the porphyrin rings when the monomers were stacked. Although it was not possible to confirm the formation of hydrogen bonds by infrared spectroscopy owing to the precipitation of the polymer at high concentrations, these results suggest that hydrogen bonds contribute to the formation of H-aggregates in addition to π–π interactions between the porphyrin rings.

In the Zn-TChOAlaCPP, we made the model as linked by van der Waals interactions between the cholesteryl groups (**Fig. 5.23A**). In this interaction form, up to four porphyrins are able to interact around one porphyrin, which explains the formation of the branching chains. We made a branching polymer model (main chain = decamer, branching chain = trimer) and placed it in the MD cell. The model was optimized with diethyl ether packing (d = 0.713), optimized, equilibrated at 298 K, and finally subjected to a production run at 298 K from 0 to 10 ns in the NVE ensemble (**Fig. 5.23B**).

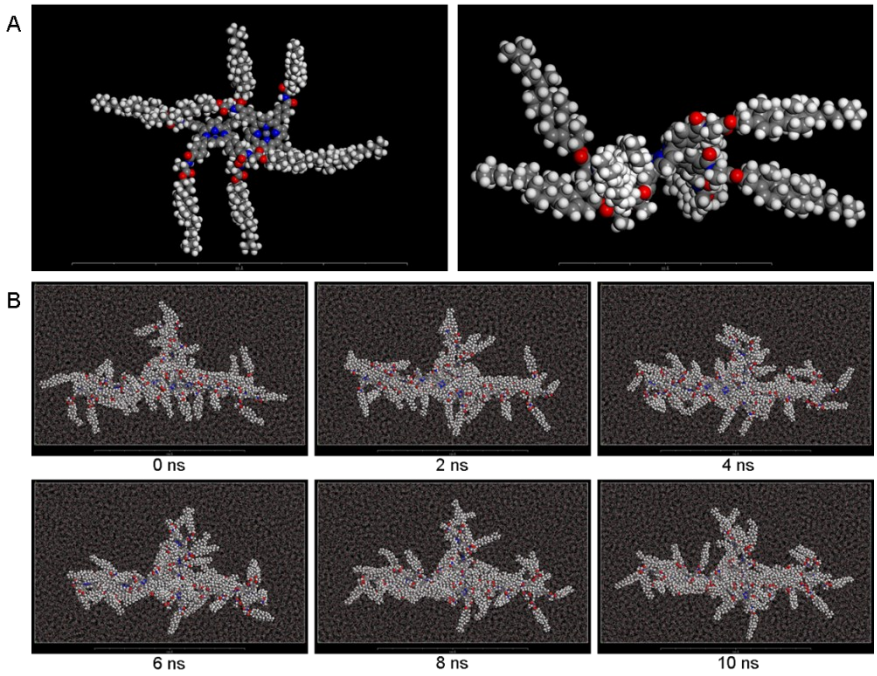

Fig. 5.23 MD calculation of Zn-TChOAlaCPP 10-mer with branching chain. (A) Estimated structure of Zn-TChOAlaCPP aggregation formed by van der Waals interactions. (B) Snapshots of all-atom MD of Zn-TChOAlaCPP obtained by the microcanonical ensemble (NVE) after

equilibration at 298 K in diethyl ether.

The Zn-TChOAlaCPP supramolecular polymer in diethyl ether did not collapse, retaining the porphyrin association state throughout the simulation (**Fig. 5.23B**). The helical structure was also retained, indicating the validity of the helical direction inferred from the CD spectrum and the exciton chirality method. However, unlike in Cu-TChOAlaCPP, no hydrogen bonds formed. The supramolecular polymer model had a flexible structure, which was consistent with the characteristics of flexible branched polymers confirmed by AFM imaging. Nor were the branched chains cleaved throughout the simulation. These results supported the validity of the proposed association state.

5.3.6 Polymer Growth Process

Based on spectroscopy, all-atom MD calculations, and microscopy (AFM, SEM, and TEM) imaging, we will discuss the growth processes of the Cu- and Zn-TChOAlaCPP supramolecular polymers as follows. In the Cu-TChOAlaCPP supramolecular polymers (**Fig. 5.24A**), the monomers form a right-handed helical rod (**Fig. 5.19A** and **Fig**. 5.20**A**) by forming H-aggregates. In addition to the π–π interactions between porphyrin rings, hydrogen bonds between amide groups are the driving force for the formation of H-aggregates. As the rod grow, it is transformed into a left-handed superhelix (**Fig. 5.20B**) by torsional strain. The collapse of this superhelix structure and the parallel alignment of multiple rods resulted in a ribbon structure (**Fig. 5.20C**). As far as we were able to determine, this ribbon structure was restricted to a right-handed helix. In the Zn-TChOAlaCPP supramolecular polymers (**Fig. 5.24B**), the monomers are linked by the van der Waals interactions of the pendant cholesteryl groups to form a right-handed helical (**Fig. 5.19B**) flexible rod (**Fig. 5.21A, H**) with branching chains. With further growth, it changes into an unbranched right-handed helical fiber structure (**Fig. 5.21B, C top,** and **C bottom**), which is formed by the entanglement of multiple rods. This fiber grows into two types of higher-order structures: a ribbon (**Fig. 5.21D, E, F**), which is formed

by the parallel alignment and rearrangement of fibers; and a multiple-helix structure (**Fig. 5.21C middle, G**), which is formed by the entanglement of multiple fibers. We successfully imaged the double (**Fig. 5.21C middle)** and triple helix structures (**Fig. 5.21G**). Although the fibers we examined were all right-handed and chiral-controlled, the chirality of the ribbon and multiple-helix structures was diverse.

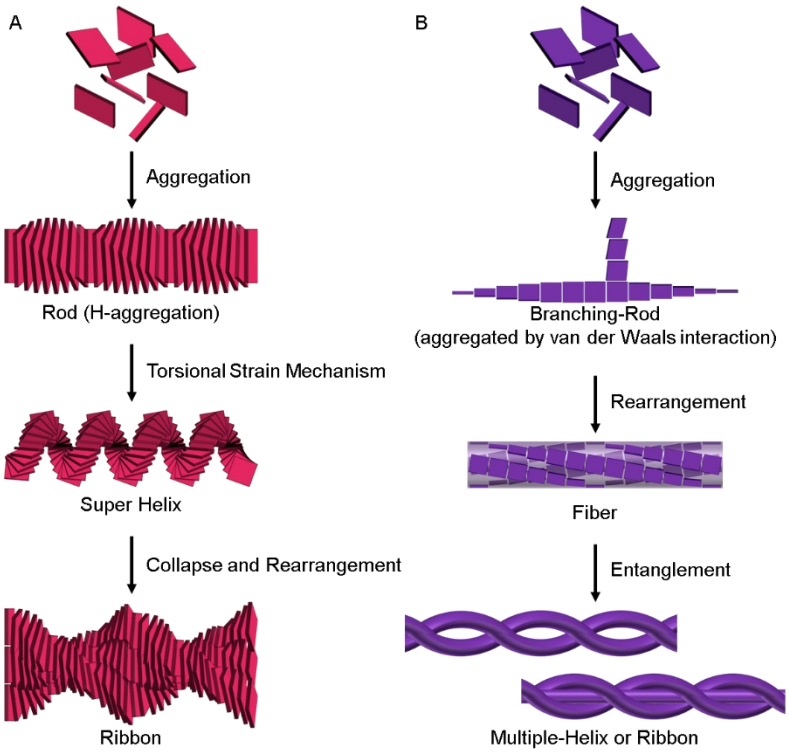

Fig. 5.24 Schematic diagrams representing the growth processes of (A) Cu- and (B) Zn-TChOAlaCPP supramolecular polymers.

The significant differences in the secondary and higher-order structures of the two metal-coordinated porphyrin supramolecular polymers are due to the different association states of the porphyrins in the respective solvents. As shown by the UV-vis spectra, in diisopropyl ether, Cu-TChOAlaCPP formed H-aggregates, and Zn-TChOAlaCPP formed J-aggregates. The J-aggregates of Zn-TChOAlaCPP were unable to grow sufficiently and remained as small granular aggregates. However, in diethyl ether, Cu-TChOAlaCPP formed a small amount of H-aggregates, and Zn-

TChOAlaCPP formed aggregates by van der Waals interactions of its pendant groups without porphyrin stacks. This very different aggregation state affects the higher-order structure, which explains why we obtained completely different microscopic images.

5.3.7 FS-AFM Imaging

Finally, FS-AFM imaging was performed to confirm the interaction between the polymer chains. All imaging was performed in *n*-octyl ether (UV-vis and CD spectra of *n*-octyl ether solutions are shown in the spectral data section). In the Cu-TChOAlaCPP supramolecular polymer, even *n*-octyl ether forms H-aggregates, so it is expected that the rod structure can be observed without structural collapse. The diisopropyl ether solution of Cu-TChOAlaCPP was drop-cast onto a mica substrate and imaged at 25 ± 1 ºC (**Fig. 5.25A**).

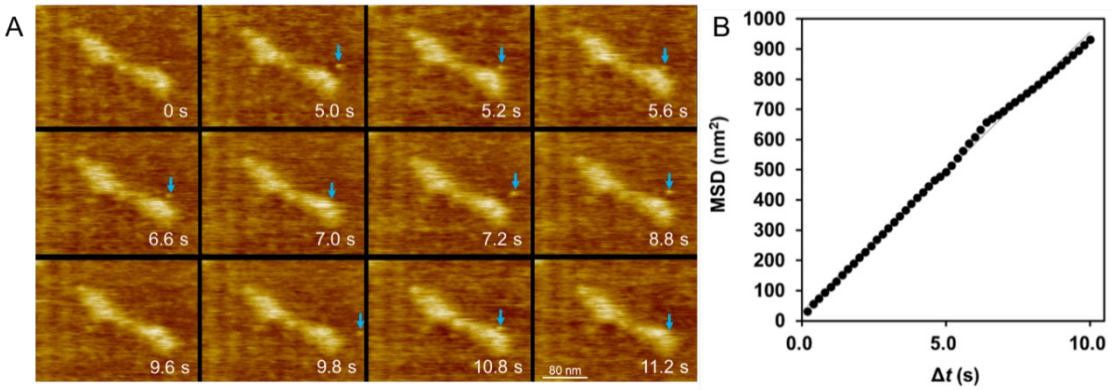

Fig. 5.25 FS-AFM: (A) Interaction between long- and short-chain of Cu-TChOAlaCPP supramolecular polymers driven by thermal fluctuations on mica under *n*-octyl ether at 25 ± 1 °C. The red arrows indicate the positions of the short-chain. (XY, 289 × 217 nm; Z, 9.0 nm; frame rate, 5.0 frames per second). (B) Mean square displacement (MSD) plots based on the trajectory data of the short-chain. The line profile is shown in Fig. 5.11.

As expected, a structure similar to the supramolecular polymer observed by atmospheric AFM imaging was confirmed. The structure did not collapse throughout the imaging and was shown to be

stable under the FS-AFM imaging environment. In addition, interaction between short and long chains was confirmed. The short-chain molecule repeatedly adsorbed and desorbed from the long-chain molecule. Long-term interactions and long-range processive motions were not observed because the short-chain molecules were too short, but they are necessary for molecular motor function. This suggests that the Cu-TChOAlaCPP supramolecular polymers can be used as the macromolecular motor. We made an MSD plot for the motion of the short-chain. An MSD plot with a linear slope indicates that the molecular motion follows Einstein's law of Brownian motion (**Fig. 5.25B**). The diffusion coefficient was found to be 23.2 nm^2/s.

FS-AFM imaging was also performed on Zn-TChOAlaCPP. The CD spectrum suggests that Zn-TChOAlaCPP forms different aggregates in *n*-octyl ether than in diethyl ether. Therefore, it is expected that it will disassociate during imaging. The diluted diethyl ether solution of Zn-TChOAlaCPP was drop-cast onto a mica substrate and imaged at 25 ± 1 ºC (**Fig. 5.26**).

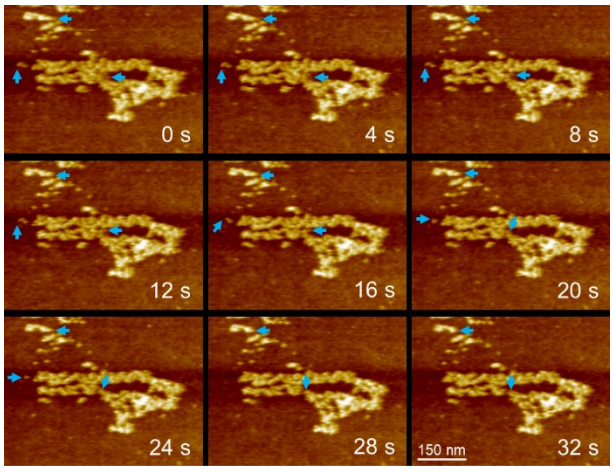

Fig. 5.26 FS-AFM: Single-molecule images revealing the disassembly of a Zn-TChOAlaCPP supramolecular polymer on mica under *n*-octyl ether at 25 ± 1 °C. The red arrows indicate the positions of the polymer ends. (XY, 612 × 459 nm; Z, 18.0 nm; frame rate, 5.0 frames per second). The line profile is shown in Fig. 5.12.

Although no short-chain and long-chain interactions were observed, we obtained a FS-AFM video image of the supramolecular polymer as it disassembled and shortened. The polymer chain ends shortened over time, as indicated by the red arrows in **Fig. 5.26**. This indicates that the Zn-TChOAlaCPP supramolecular polymers formed branched rods by non-covalent interactions, and disassembly was caused by thermal fluctuations and changing to the association state. Therefore, Zn-TChOAlaCPP cannot maintain long-chain molecules under the environment of FS-AFM imaging, making it difficult to use it as a rail molecule for molecular motors. However, since aggregates are formed even in *n*-octyl ether, it is expected to be used as short-chain molecules.

5.4 Conclusion

In the present study, we demonstrated the supramolecular polymerization and a hierarchical pathway for the formation of higher-order structures of Cu- and Zn-TChOAlaCPP with pendant cholesteryl groups. In spectroscopy, each porphyrins formed completely different association states. It was suggested the formation of higher-order structures by CD spectra except for the J-aggregates of Zn-TChOAlaCPP. The different association states revealed by spectroscopy were reflected in the marked differences in the shapes of the supramolecular polymers demonstrated by microscopy (AFM, FS-AFM, SEM, and TEM). We were able to image the secoundary and higher-order structures of both porphyrin supramolecular polymers. The all-atom MD calculations corroborated the stability of the supramolecular polymers in solvents. The results also confirmed the validity of the proposed association state. Based on these results, we proposed a mechanism by which the hierarchical higher-order structures of the supramolecular polymers were formed by different interactions. This is expected to provide a basis for controlling the higher-order structures of supramolecular polymers for the development of supramolecular materials.

We also confirmed the interaction between short- and long-chains in Cu-TChOAlaCPP supramolecular polymer. This phenomenon is the basis of the molecular motor function and supports

that this polymer can function as a molecular motor. We also consider that the observation of interactions confirmed the origins of biomolecular motors. We believe that the interactions observed in this study and processive movement observed in previous studies[17, 18] will provide hints to reveal the evolutionary process of biomolecular motors such as Myosin along Actin fulament.

5.5 *Spectral Data*

5.5.1 *^{1}H-NMR and ^{13}C-NMR spectra*

L-Alanine cholesteryl ester (1)

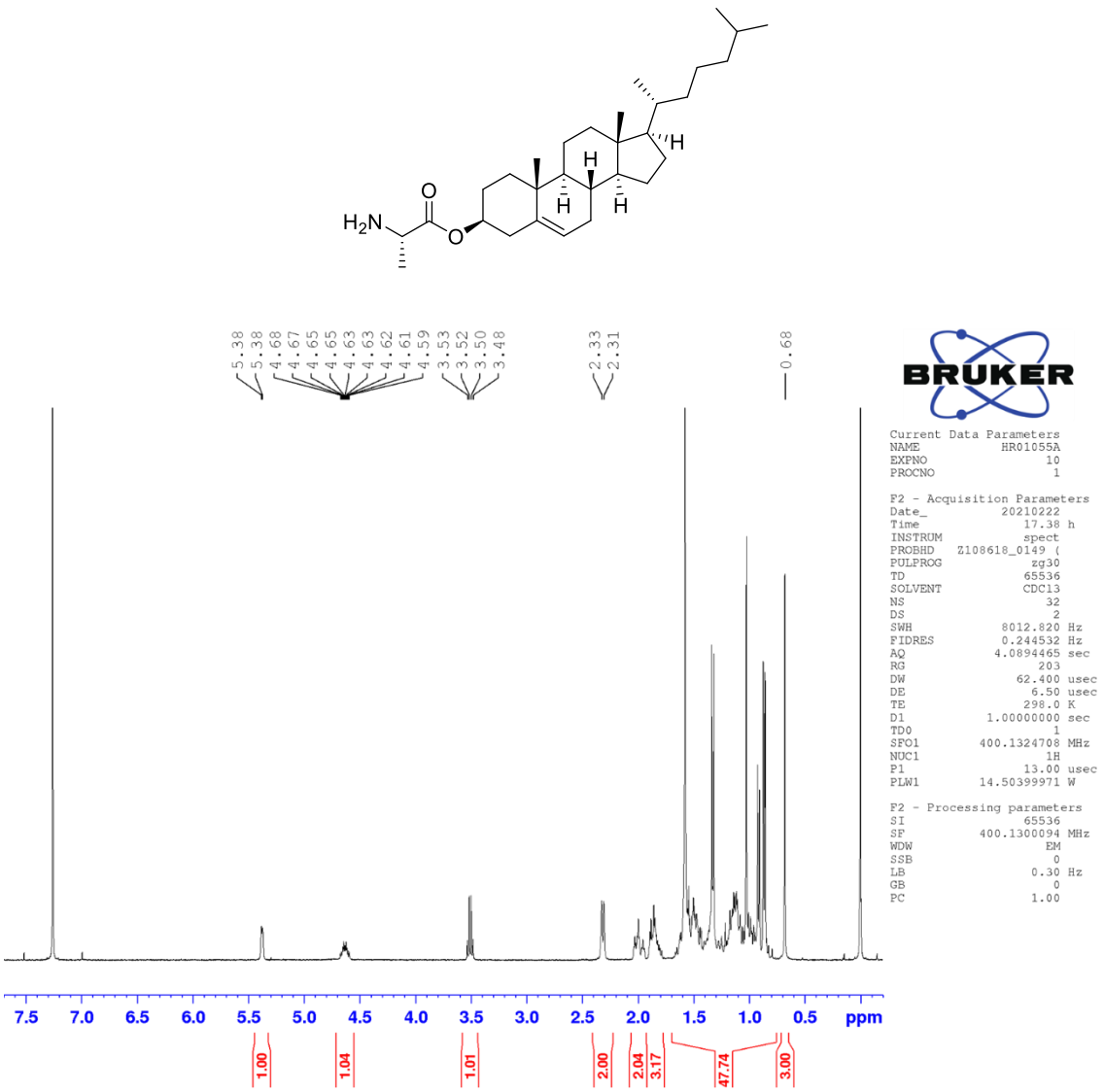

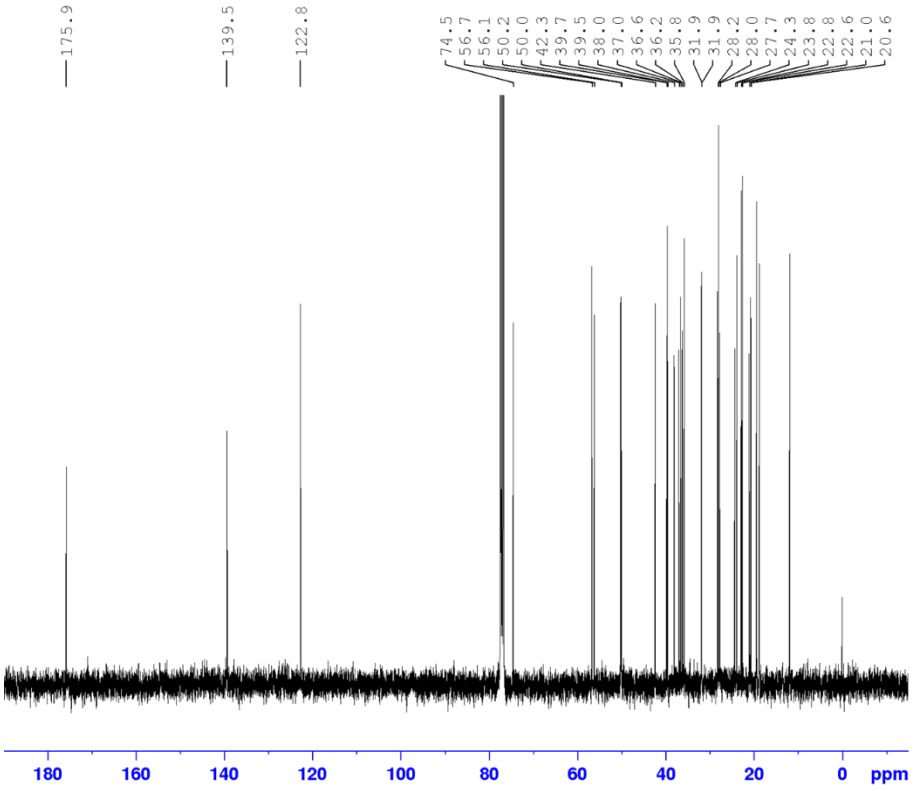

Current Data Parameters
NAME HR01055A_2023035
EXPNO 11
PROCNO 1

F2 - Acquisition Parameters
Date_ 20230324
Time 18.00 h
INSTRUM Avance
PROBHD Z122623_0030 (
PULPROG zgpg30
TD 65536
SOLVENT CDCl3
NS 256
DS 4
SWH 23809.523 Hz
FIDRES 0.726609 Hz
AQ 1.3762560 sec
RG 5.41667
DW 21.000 usec
DE 18.00 usec
TE 298.0 K
D1 2.00000000 sec
D11 0.03000000 sec
TD0 1
SFO1 100.6479773 MHz
NUC1 13C
P0 3.33 usec
P1 10.00 usec
PLW1 50.17800140 W
SFO2 400.2316009 MHz
NUC2 1H
CPDPRG[2 waltz65
PCPD2 90.00 usec
PLW2 8.51379967 W
PLW12 0.15136001 W
PLW13 0.07613100 W

F2 - Processing parameters
SI 32768
SF 100.6379135 MHz
WDW EM
SSB 0
LB 1.00 Hz
GB 0
PC 1.40

Tetrakis(cholesteryloxy-L-alanylcarbonylphenyl)porphyrin (H_2-TChOAlaCPP) (2)

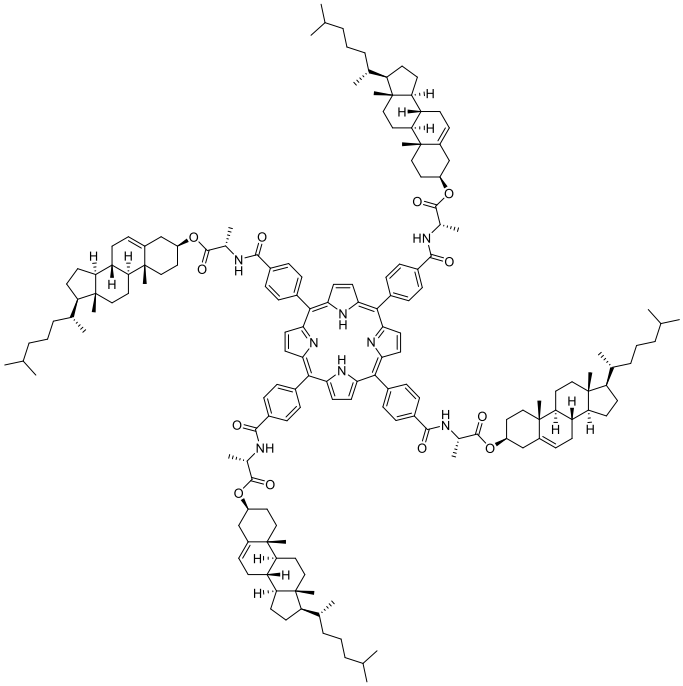

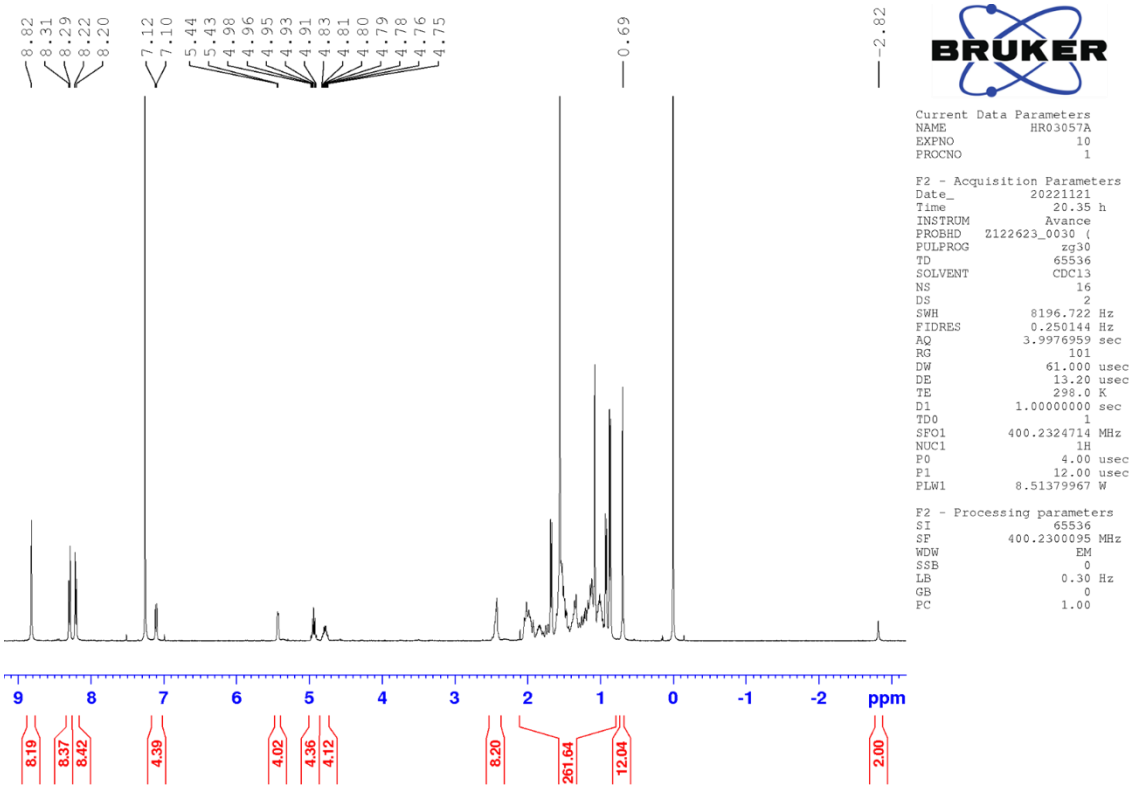

BRUKER

```
Current Data Parameters
NAME              HR03057A
EXPNO                   10
PROCNO                   1

F2 - Acquisition Parameters
Date_             20221121
Time                20.35 h
INSTRUM             Avance
PROBHD   Z122623_0030 (
PULPROG              zg30
TD                  65536
SOLVENT             CDCl3
NS                     16
DS                      2
SWH               8196.722 Hz
FIDRES            0.250144 Hz
AQ               3.9976959 sec
RG                    101
DW                 61.000 usec
DE                 13.20 usec
TE                 298.0 K
D1              1.00000000 sec
TD0                     1
SFO1           400.2324714 MHz
NUC1                   1H
P0                  4.00 usec
P1                 12.00 usec
PLW1            8.51379967 W

F2 - Processing parameters
SI                  65536
SF             400.2300095 MHz
WDW                    EM
SSB                     0
LB                 0.30 Hz
GB                      0
PC                   1.00
```

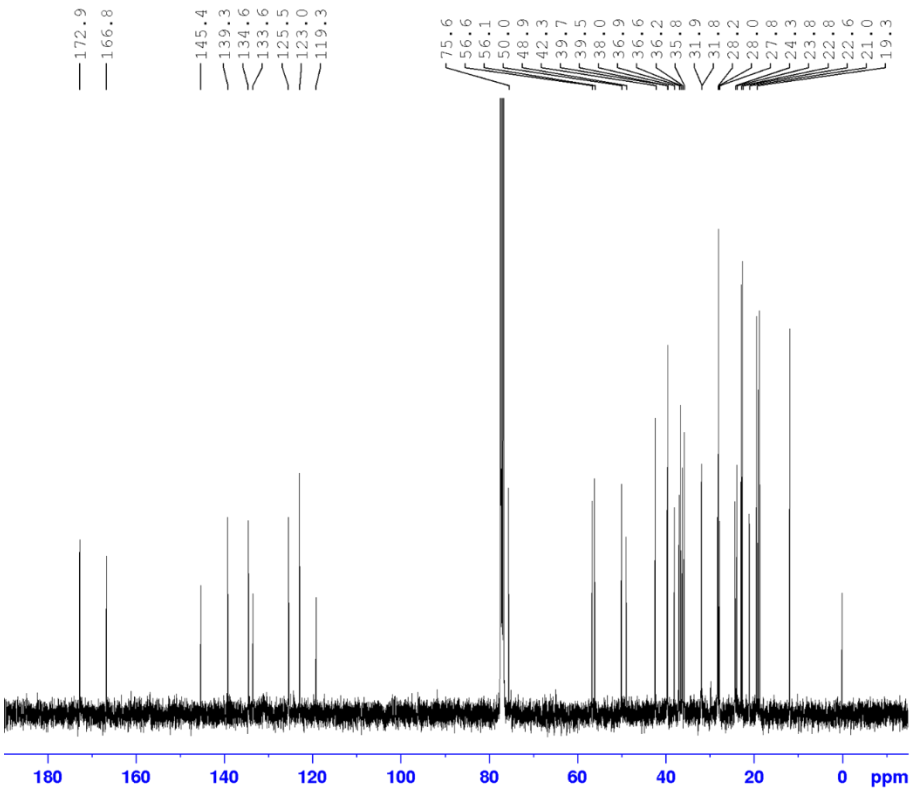

Current Data Parameters
NAME HR01048A-carbon
EXPNO 10
PROCNO 1

F2 - Acquisition Parameters
Date_ 20210208
Time 17.34 h
INSTRUM spect
PROBHD Z122623_0030 (
PULPROG zgpg30
TD 65536
SOLVENT CDCl3
NS 512
DS 4
SWH 24038.461 Hz
FIDRES 0.733596 Hz
AQ 1.3631488 sec
RG 90.5
DW 20.800 usec
DE 18.00 usec
TE 298.0 K
D1 2.00000000 sec
D11 0.03000000 sec
TD0 1
SFO1 100.6479773 MHz
NUC1 13C
P1 10.00 usec
PLW1 43.00000000 W
SFO2 400.2316009 MHz
NUC2 1H
CPDPRG[2 waltz16
PCPD2 90.00 usec
PLW2 11.00000000 W
PLW12 0.19555999 W
PLW13 0.09820800 W

F2 - Processing parameters
SI 32768
SF 100.6379161 MHz
WDW EM
SSB 0
LB 1.00 Hz
GB 0
PC 1.40

Cu-Tetrakis(cholesteryloxy-L-alanylcarbonylphenyl)porphyrin (Cu-TChOAlaCPP)

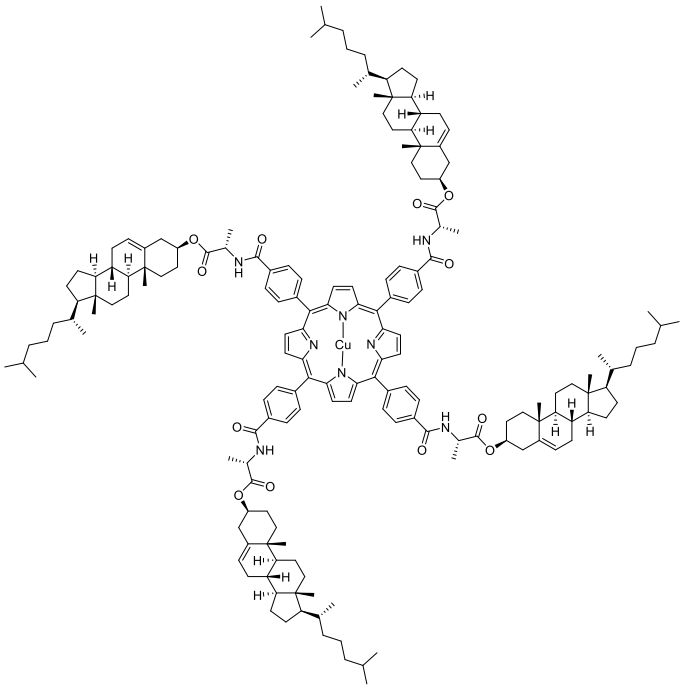

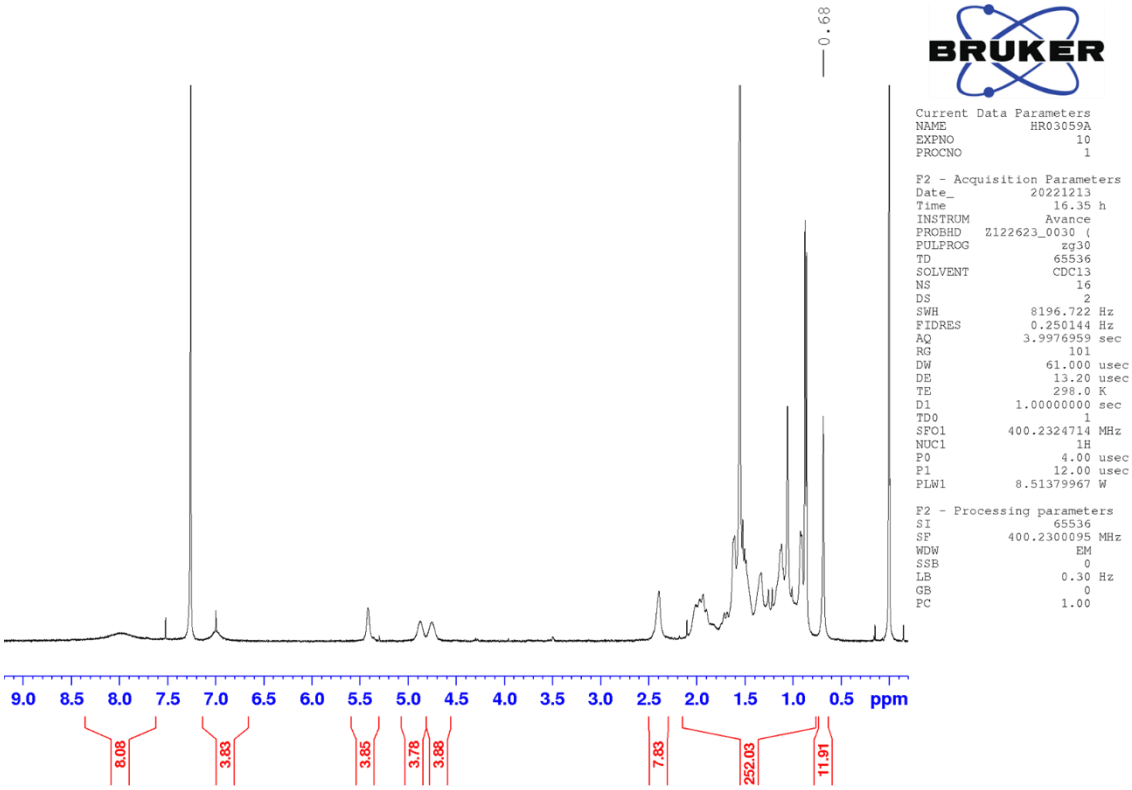

BRUKER

```
Current Data Parameters
NAME                  HR03059A
EXPNO                       10
PROCNO                       1

F2 - Acquisition Parameters
Date_               20221213
Time                    16.35 h
INSTRUM                 Avance
PROBHD     Z122623_0030 (
PULPROG                 zg30
TD                      65536
SOLVENT                 CDCl3
NS                         16
DS                          2
SWH                8196.722 Hz
FIDRES             0.250144 Hz
AQ                 3.9976959 sec
RG                        101
DW                   61.000 usec
DE                   13.20 usec
TE                   298.0 K
D1                1.00000000 sec
TD0                         1
SFO1            400.2324714 MHz
NUC1                       1H
P0                    4.00 usec
P1                   12.00 usec
PLW1              8.51379967 W

F2 - Processing parameters
SI                      65536
SF              400.2300095 MHz
WDW                        EM
SSB                         0
LB                     0.30 Hz
GB                          0
PC                     1.00
```

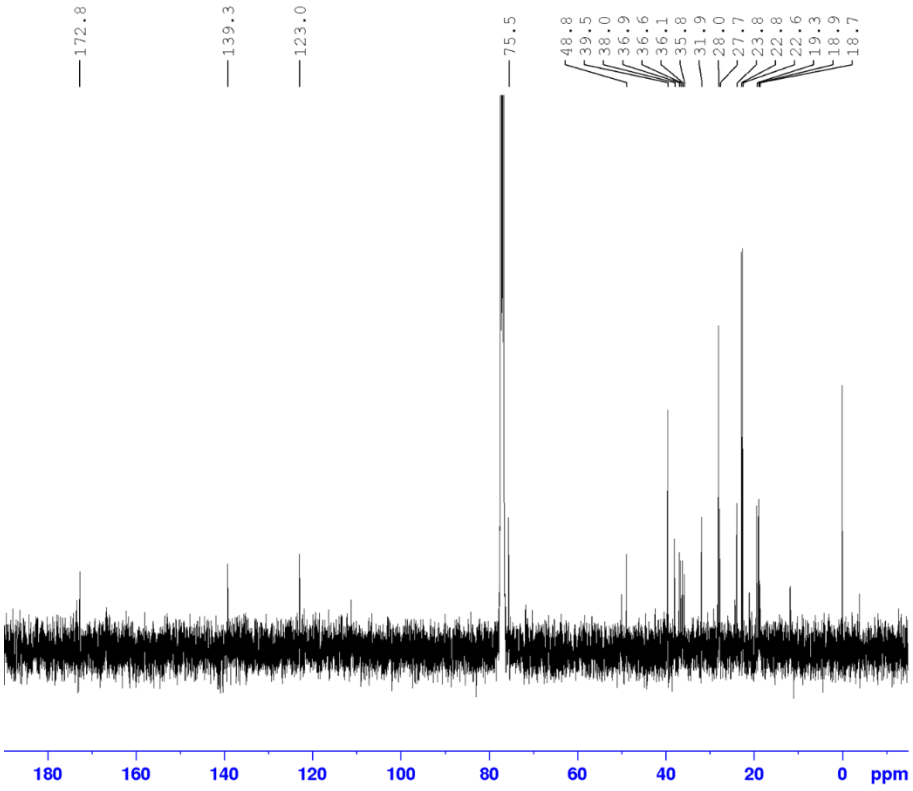

BRUKER

```
Current Data Parameters
NAME      HR03059A_20230324
EXPNO                   12
PROCNO                   1

F2 - Acquisition Parameters
Date_           20230324
Time              22.53 h
INSTRUM           Avance
PROBHD    Z122623_0030 (
PULPROG           zgpg30
TD                65536
SOLVENT           CDCl3
NS                 1024
DS                    4
SWH           23809.523 Hz
FIDRES         0.726609 Hz
AQ             1.3762560 sec
RG              5.41667
DW               21.000 usec
DE                18.00 usec
TE                298.0 K
D1            2.00000000 sec
D11           0.03000000 sec
TD0                   1
SFO1         100.6479773 MHz
NUC1                13C
P0                 3.33 usec
P1                10.00 usec
PLW1         50.17800140 W
SFO2         400.2316009 MHz
NUC2                1H
CPDPRG[2          waltz65
PCPD2             90.00 usec
PLW2          8.51379967 W
PLW12         0.15136001 W
PLW13         0.07613100 W

F2 - Processing parameters
SI                32768
SF           100.6379145 MHz
WDW                  EM
SSB                   0
LB                 1.00 Hz
GB                    0
PC                 1.40
```

Zn-Tetrakis(cholesteryloxy-L-alanylcarbonylphenyl)porphyrin (Zn-TChOAlaCPP)

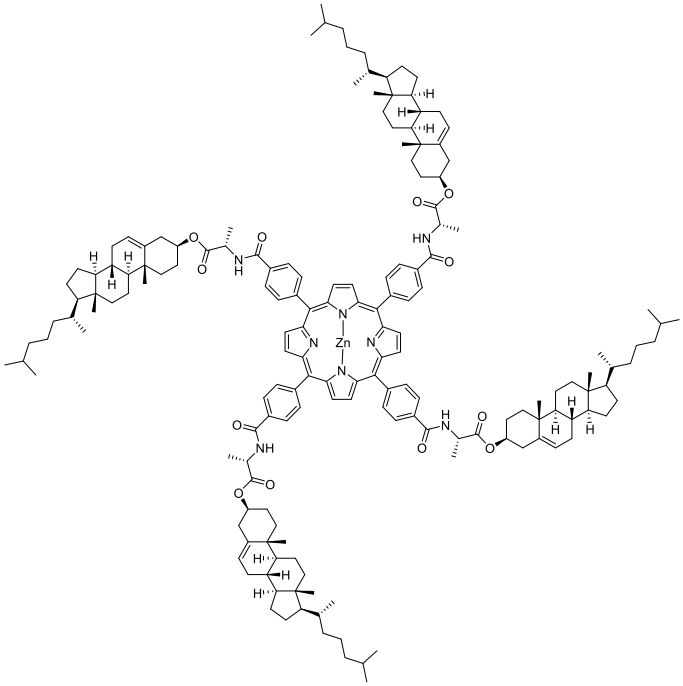

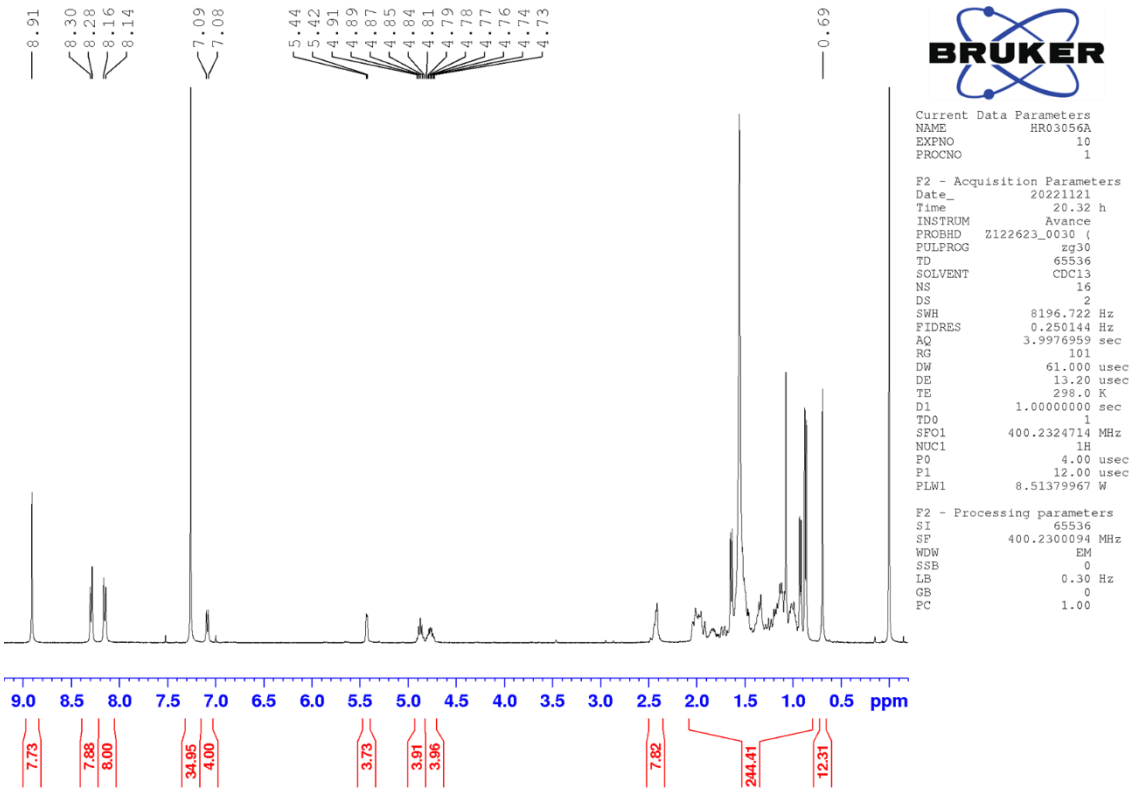


```
Current Data Parameters
NAME                  HR03056A
EXPNO                       10
PROCNO                       1

F2 - Acquisition Parameters
Date_               20221121
Time                    20.32 h
INSTRUM                 Avance
PROBHD     Z122623_0030 (
PULPROG                 zg30
TD                      65536
SOLVENT                 CDCl3
NS                         16
DS                          2
SWH                  8196.722 Hz
FIDRES               0.250144 Hz
AQ                   3.9976959 sec
RG                        101
DW                     61.000 usec
DE                     13.20 usec
TE                     298.0 K
D1                1.00000000 sec
TD0                         1
SFO1              400.2324714 MHz
NUC1                       1H
P0                     4.00 usec
P1                     12.00 usec
PLW1               8.51379967 W

F2 - Processing parameters
SI                      65536
SF                400.2300094 MHz
WDW                        EM
SSB                         0
LB                     0.30 Hz
GB                          0
PC                     1.00
```

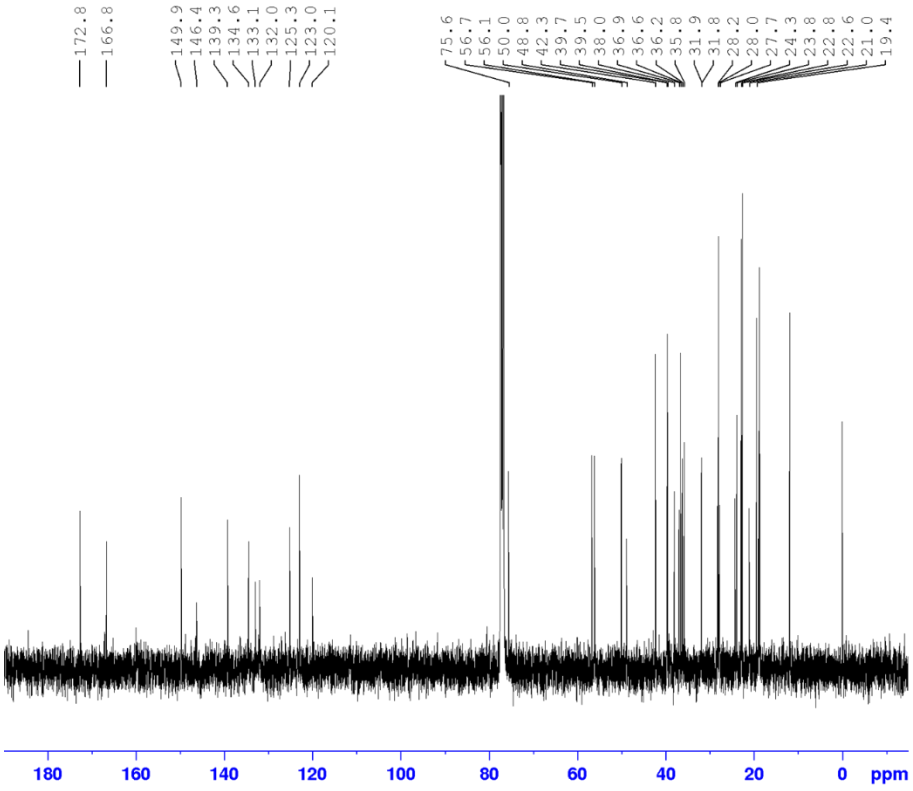


```
Current Data Parameters
NAME      HR03056A_20230324-2
EXPNO                      10
PROCNO                      1

F2 - Acquisition Parameters
Date_               20230324
Time                   21.04 h
INSTRUM                Avance
PROBHD    Z122623_0030 (
PULPROG                zgpg30
TD                      65536
SOLVENT                CDCl3
NS                      1024
DS                         4
SWH                23809.523 Hz
FIDRES             0.726609 Hz
AQ                 1.3762560 sec
RG                    5.41667
DW                    21.000 usec
DE                    18.00 usec
TE                    298.0 K
D1                 2.00000000 sec
D11                0.03000000 sec
TD0                        1
SFO1              100.6479773 MHz
NUC1                      13C
P0                     3.33 usec
P1                    10.00 usec
PLW1              50.17800140 W
SFO2              400.2316009 MHz
NUC2                      1H
CPDPRG[2               waltz65
PCPD2                 90.00 usec
PLW2               8.51379967 W
PLW12              0.15136001 W
PLW13              0.07613100 W

F2 - Processing parameters
SI                        32768
SF                100.6379145 MHz
WDW                        EM
SSB                         0
LB                     1.00 Hz
GB                          0
PC                     1.40
```

5.5.2 UV-vis and CD Spectra

Cu-TChOAlaCPP

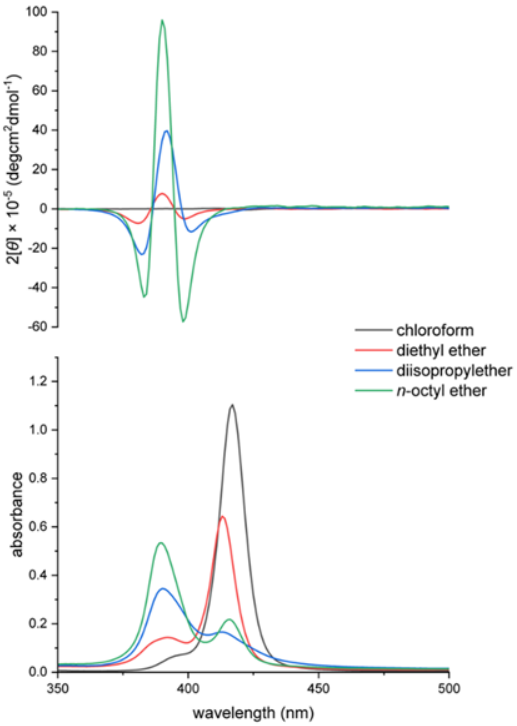

Zn-TChOAlaCPP

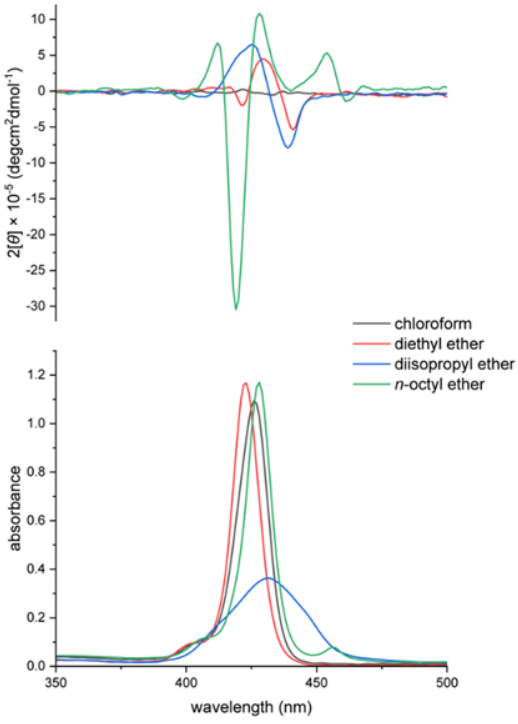

5.5.3 Fluorescence Spectra

Zn-TChOAlaCPP

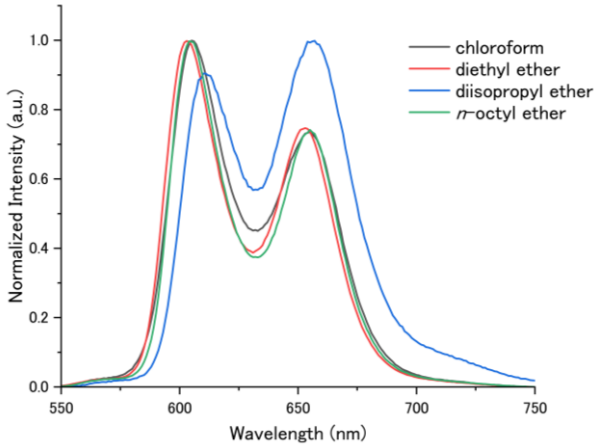

5.6 Reference

1. M. F. J. Mabesoone, A. J. Markvoort, M. Banno, T. Yamaguchi, F. Helmich, Y. Naito, E. Yashima, A. R. A. Palmans, and E. W. Meijer, Competing Interactions in Hierarchical Porphyrin Self-Assembly Introduce Robustness in Pathway Complexity. *J. Am. Chem. Soc.* **2018**, *140* (25), 7810–7819. https://doi.org/10.1021/jacs.8b02388
2. C. Lorecchio, M. Venanzi, C. Mazzuca, R. Lettieri, A. Palleschi, T. H. N. Thi, L. Cardová, P. Drasar, and D. Monti, Tuning the chiroptical and morphological properties of steroidal-porphyrin aggregates: a mechanistic, structural, and MM investigation. *Org. Biomol. Chem.* **2014**, *12*, 3956–3963. https://doi.org/10.1039/C4OB00134F
3. A. Rananaware, D. D. La, M. A. Kobaisi, R. S. Bhosale, S. V. Bhosale, and S. V. Bhosale, Controlled chiral supramolecular assemblies of water soluble achiral porphyrins induced by chiral counterions. *Chem. Commun.* **2016**, *52*, 10253–10256. https://doi.org/10.1039/C6CC04427A
4. Y. Rong, P. Chen, and M. Liu, Self-assembly of water-soluble TPPS in organic solvents: from nanofibers to mirror imaged chiral nanorods. *Chem. Commun.* **2013**, *49*, 10498–10500. https://doi.org/10.1039/C3CC46467A
5. Z. Li, C. J. Zeman IV, S. R. Valandro, J. P. O. Bantang, and K. S. Schanze, Adenosine Triphosphate Templated Self-Assembly of Cationic Porphyrin into Chiral Double Superhelices and Enzyme-Mediated Disassembly. *J. Am. Chem. Soc.* **2019**, *141* (32), 12610–12618. https://doi.org/10.1021/jacs.9b04133
6. R. van der Weegen, A. J. P. Teunissen, and E. W. Meijer, Directing the Self-Assembly Behaviour of Porphyrin-Based Supramolecular Systems *Chem. Eur. J.* **2017**, *23*, 3773–3783. https://doi.org/10.1002/chem.201605872
7. Y. Li, T. Wang, and M. Liu, Gelating-induced supramolecular chirality of achiral porphyrins: chiroptical switch between achiral molecules and chiral assemblies. *Soft Matter*, **2007**, *3*, 1312–

1317. https://doi.org/10.1039/B710165A

8. M. Shirakawa, S. Kawano, N. Fujita, K. Sada, and S. Shinkai, Hydrogen-Bond-Assisted Control of H versus J Aggregation Mode of Porphyrins Stacks in an Organogel System. *J. Org. Chem.* **2003**, *68* (13), 5037–5044. https://doi.org/10.1021/jo0341822

9. B. N. Ortega, F. J. Ramírez, D. B. Amabilino, M. Linares, D. Beljonne, J. T. L. Navarrete, and J. Casado, Electronic and vibrational circular dichroism spectroscopies for the understanding of chiral organization in porphyrin aggregates. *Chem. Commun.* **2012**, *48*, 9147–9149. https://doi.org/10.1039/C2CC34374F

10. M. Kaya, and H. Higuchi, Nonlinear Elasticity and an 8-nm Working Stroke of Single Myosin Molecules in Myofilaments. *Science* **2010**, *329*, 686–689. https://doi.org/10.1126/science.1191484

11. N. Kodera, D. Yamamoto, R. Ishikawa, and T. Ando, Video imaging of walking myosin V by high-speed atomic force microscopy. *Nature* **2010**, *468*, 72–76. https://doi.org/10.1038/nature09450

12. Y. Okada, H. Higuchi, and N. Hirokawa, Processivity of the single-headed kinesin KIF1A through biased binding to tubulin. *Nature* **2003**, *424*, 574–577. https://doi.org/10.1038/nature01804

13. M. Cesario, C. O. Dietrich-Buchecker, J. Guilhem, C. Pascard, and J. P. Sauvage, Molecular structure of a catenand and its copper(I) catenate: Complete rearrangement of the interlocked macrocyclic ligands by complexation. *J. Chem. Soc., Chem. Commun.* **1985**, 244–247. https://doi.org/10.1039/C39850000244

14. P. R. Ashton, D. Philp, N. Spencer, and J. F. Stoddart, A new design strategy for the self-assembly of molecular shuttles. *J. Chem. Soc., Chem. Commun.* **1992**, 1124–1128. https://doi.org/10.1039/C39920001124

15. N. Koumura, R. D. W. J. Zijlstra, R. A. van Delden, N. Harada, and B. L. Feringa, Light-driven

monodirectional molecular rotor. *Nature* **1999**, *401*, 152–155. https://doi.org/10.1038/43646

16. T. Kudernac, N. Ruangsupapichat, M. Parschau, B. Maciá, N. Katsonis, S. R. Harutyunyan, K. Ernst, and B. L. Feringa, Electrically driven directional motion of a four-wheeled molecule on a metal surface. *Nature* **2011**, *479*, 208–211. https://doi.org/10.1038/nature10587
17. K. Shinohara, Y. Makida, T. Oohashi, and Ryoga Hori, Single-Molecule Unidirectional Processive Movement along a Helical Polymer Chain in Non-aqueous Medium. *Langmuir* **2022**, *38* (40), 12173–12178. https://doi.org/10.1021/acs.langmuir.2c01704
18. K. Shinohara, Single-Molecule Imaging of a Polymer: Direct Observation of Structure and Dynamics in a Polymer Chain. *Kobunshi Ronbunshu*, **2016**, *73* (6), 491–504. https://doi.org/10.1295/koron.2016-0034
19. T. Fukui, T. Uchihashi, N. Sasaki, H. Watanabe, M. Takeuchi, K. Sugiyasu, Direct Observation and Manipulation of Supramolecular Polymerization by High-Speed Atomic Force Microscopy. *Angew. Chem.* **2018**, *130*, 15691–15696. https://doi.org/10.1002/anie.201809165
20. C. Didraga, J. A. Klugkist, and J. Knoester, Optical Properties of Helical Cylindrical Molecular Aggregates: The Homogeneous Limit. *J. Phys. Chem. B* **2002**, *106* (44), 11474–11486. https://doi.org/10.1021/jp026217s
21. V. I. Prokhorenko, D. B. Steensgaard, and A. R. Holzwarth, Exciton Theory for Supramolecular Chlorosomal Aggregates: 1. Aggregate Size Dependence of the Linear Spectra. *Biophys. J.*, **85** (5), 3173–3186. https://doi.org/10.1016/S0006-3495(03)74735-3
22. N. Harada, S. M. L. Chen, and K. Nakanishi, Quantitative definition of exciton chirality and the distant effect in the exciton chirality method. *J. Am. Chem. Soc.* **1975**, *97* (19), 5345–5352. https://doi.org/10.1021/ja00852a005
23. Y. C. Chang, C. S. Chang, D. C. Wang, M. H. Lee, T. F. Wang, M. Y. Wu, T. Y. Fu, and T. T. Tsong, Nanoscale Imaging of Biomolecules by Controlled Carbon Nanotube Probes. *Jpn. J. Appl. Phys.* **2004**, *43*, 4517–4520. https://doi.org/10.1143/JJAP.43.4517

24. K. Shinohara, M. Yanagisawa, and Y. Makida, Direct Observation of Long-Chain Branches in a Low-Density Polyethylene. *Sci. Rep.* **2019**, *9* (9791). https://doi.org/10.1038/s41598-019-46035-9

25. Y. Wada, K. Shinohara, H. Asakawa, S. Matsui, T. Taima, and T. Ikai, One-Step Synthesis of One-Dimensional Supramolecular Assemblies Composed of Helical Macromolecular Building Blocks. *J. Am. Chem. Soc.* **2019**, *141* (35), 13995–14002. https://doi.org/10.1021/jacs.9b07417

Chapter 6. Direct Observation and Force Measurement of Ionic Polymer Molecular Motor

6.1 Introduction

In biological systems, molecules such as actomyosin[1,2] and microtubule–kinesin[3,4] are known as "molecular motors," which perform unidirectional movements driven by thermal fluctuations using adenosine triphosphate (ATP) and exhibit highly sophisticated functionalities. Recently, research on synthetic molecular machines that mimic these biomolecular motors using synthetic compounds has garnered significant attention. To date, several synthetic molecular machines, including catenanes,[5] rotaxanes,[6] light-driven molecular rotors,[7] and nano-cars,[8] have been developed. However, these are small molecules, and there are limitations in developing advanced functionalities. If molecular machines capable of generating substantial forces using polymers can be created, highly functional molecular systems comparable to biomolecular motors could be realized using synthetic polymers.

In recent years, we have observed molecular motor functions using polymers capable of dynamic interactions at multiple points.[9–11] The fact that synthetic polymers, previously considered mere structural entities, exhibit controlled movements at room temperature in solvents provides strong evidence that they can behave similarly to biomolecular motors. This opens the door to realizing practical synthetic molecular machines with functionalities based on polymers. However, previous studies have been limited to imaging the movements, and the most critical aspect of molecular motors, namely "force generation," has not been addressed. The primary reasons for this are the lack of reports on force generation at the single-molecule level in synthetic polymers and the absence of established measurement conditions. Additionally, optical trapping systems that have enabled single-molecule force measurements of biomolecular motors are optimized for measurements in aqueous solutions, making measurements in the organic solvents where molecular motor functions were observed challenging.[2–4]

Therefore, in this study, we employed water-soluble anionic and cationic polymers to conduct fast-scanning atomic force microscope (FS-AFM) video imaging of movements similar to reported molecular motors and performed force measurements of interactions between ionic polymer chains

using an optical trapping system. For the anionic polymers, we used poly(2-acrylamido-2-methyl-1-propanesulfonic acid) (PAMPS) with sulfonic acid groups at the side-chain termini, and for the cationic polymers, we used poly(allylamine hydrochloride) (PAA-HCl) with ammonium groups at the side-chain termini. These polymers are commercially available, and if such common polymers can function as molecular motors, the preparation of synthetic polymer motors would become significantly simplified, offering advantages over biomolecular motors. Furthermore, this paper reports the first force measurements of interactions between polymer chains using an optical trapping system.

6.2 Experimental

6.2.1 Materials

Poly(2-acrylamido-2-methyl-1-propanesulfonic acid) (PAMPS, $M_w = 2 \times 10^6$ g/mol) was purchased from Sigma-Aldrich (Missouri, USA). Poly(allylamine hydrochloride) (PAA-HCl, $M_w = 1.5 \times 10^4$ g/mol for AFM imaging; $M_w = 1.5 \times 10^5$ g/mol for force measurement) was provided from NITTOBO MEDICAL (Tokyo, Japan). The structures are shown in **Scheme 6.1**.

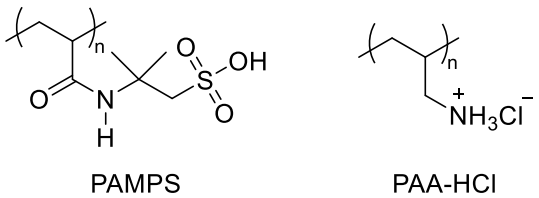

Scheme 6.1 The structures of ionic polymer (left: PAMPS, right: PAA-HCl).

6.2.2 FS-AFM Imaging

To observe the single molecule of the polymer chain, we modified the specifications of an NVB500 fast-scanning atomic force microscope (FS-AFM) (Olympus, Tokyo, Japan) in dynamic (tapping) mode (**Fig. 6.1**).[9,12] An ultra-small cantilever with a low spring constant of approximately 0.1 N/m and a high resonance frequency of over 1 MHz in air was used (AC-10EGS, Olympus, Tokyo, Japan or

USC-F1.2-k0.15, NanoWorld AG, Switzerland).

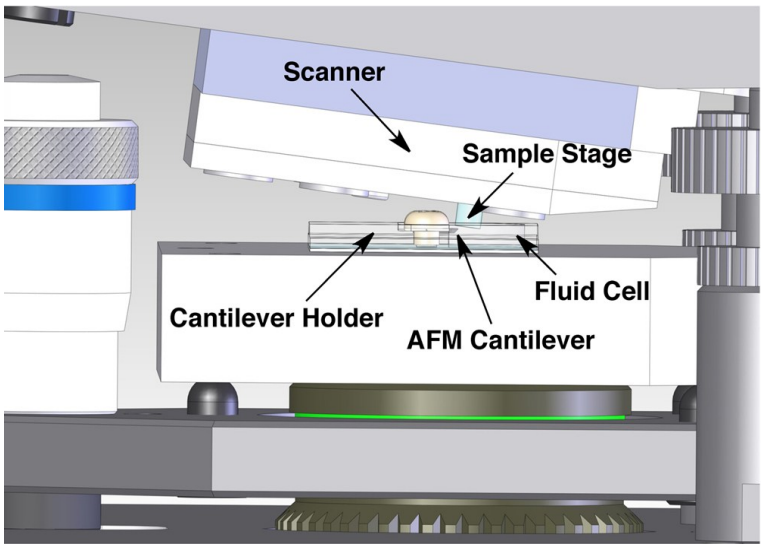

Fig. 6.1 AFM head with a fluid cell.

The polymers were dissolved in water to prepare a solution with a concentration of approximately 1×10^{-6} mol/L. A sample for imaging was prepared by casting PAMPS aqueous solution onto a mica substrate, followed by casting PAA-HCl aqueous solution.

6.2.3 MSD plots

To determine the dynamics of the walking short chain, the measurement point of the video-imaged short chain was tracked and the mean square displacement (MSD) for a certain time Δt was plotted against Δt,

$$MSD(\Delta t) = \overline{[\Delta x(\Delta t)]^2 + [\Delta y(\Delta t)]^2} \tag{6.1}$$

The diffusion coefficient D (nm^2/s) was calculated by dividing the slope of the linearly approximating the MSD-Δt plots of the measurement point by four.

6.2.4 All-atom MD simulations

All-atom molecular dynamics (MD) simulations were carried out using the Forcite module of the BIOVIA Materials Studio 2023 (Dassault Systèmes BIOVIA, San Diego, CA, USA) on a supercomputer system (PowerEdge R6525, Dell Technologies Inc., Round Rock, TX, USA). A model of PAMPS-deprotonation and PAA-protonation was build by use of the Polymer Builder module. The torsion angle between monomer units was set to +155 degree. A 20-mer of PAA-protonation model was put on the infinite-chain of PAMPS-deprotonation in a MD cell. The MD cell was built by means of usual procedure of the Amorphous Cell module. The MD cell length and angle were (a = 90 Å, b = 40 Å, c = 40 Å) and ($\alpha = 90°$, $\beta = 90°$, $\gamma = 90°$), respectively. Here, polymer chains, XXX protons, and XXX chloride ions put in the center of the cell, and the solvent molecules of H_2O were packed in the cell at density of 1.000 g cm^{-3}. Subsequently, the geometry of the MD cell was optimized. Simulation in the NVT ensemble (constant number of atoms, volume and temperature) was conducted at 298 K for 100 ps (time step of 1.0-fs, 100,000 steps) and the NPT ensemble (constant number of atoms, pressure and temperature) was conducted at pressure of 1.013×10^{-4} GPa and at 298 K for 100 ps (time step of 1.0-fs, 100,000 steps) to equilibrate the MD cell. The Nose thermostat was used to control the temperature. The Berendsen barostat was used to control the pressure. After the equilibration at 298 K, simulation in the NVE ensemble (constant number of atoms, volume and energy) was conducted for 27 ns (time step of 1.0 fs, 27,000,000 steps) as the production run. The COMPASS III (ver. 1.2) forcefield was used, and the charges were assigned by the forcefield. A snapshot structure was indicated in **Fig. 6.2** and **Fig**. 6.3.

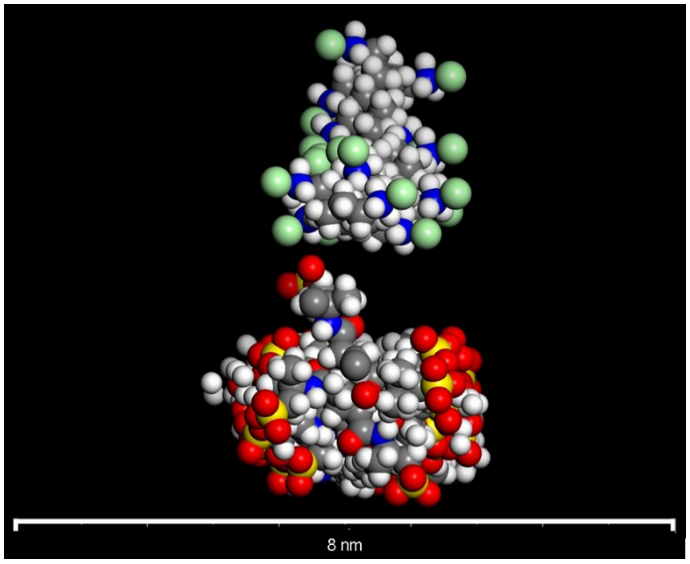

Fig. 6.2 A model of a PAA-HCl 20-mer on a PAMPS infinity chain.

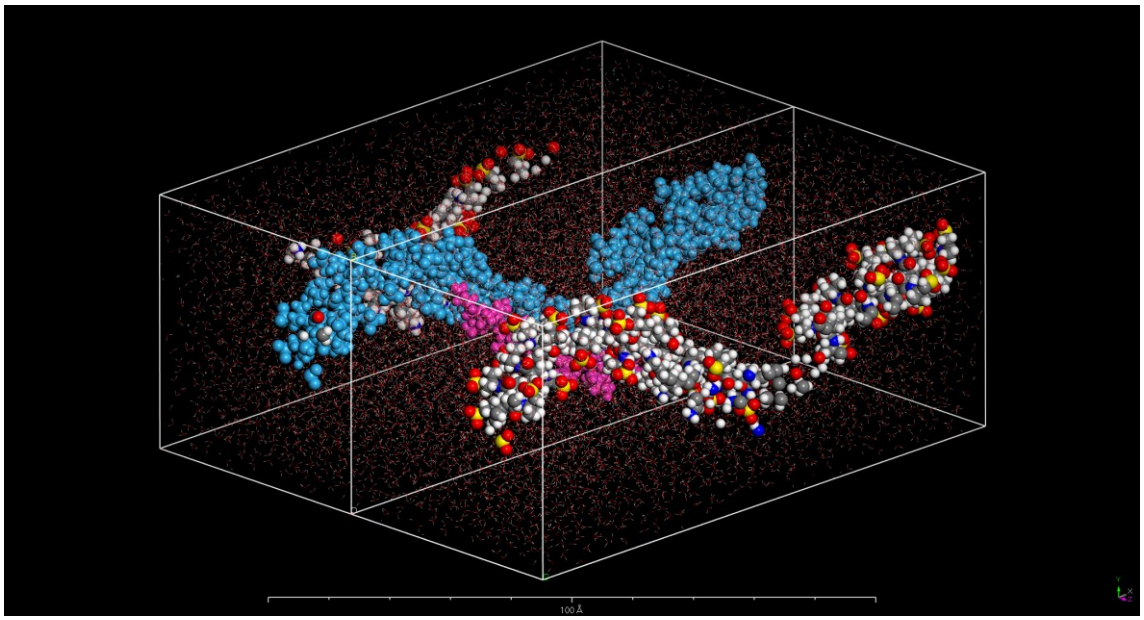

Fig. 6.3 A snap shot of all-atom MD simulation at 27.0 ns (pink: PAA-protonation chain; blue: PAMPS-deprotonation chain).

6.2.5 Force Measurement using Optical Trapping System

Force measurements of interactions between ionic polymer chains were conducted using an optical trapping system. [2–4] A 15 mM KCl aqueous solution of PAMPS (M_w = 2.0 × 10^6 g/mol, 2.0 × 10^3 μg/mL) was introduced into a chamber fabricated from glass cleaned with KOH aqueous solution and acetone. After allowing the solution to stand for three minutes, the chamber was washed with a 15 mM KCl and 2 mM phosphate buffer aqueous solution. Separately, PAA-HCl (M_w = 1.5 × 10^5 g/mol, 30 μg/mL) and carboxyl-modified polystyrene beads (φ1 μm) were mixed, diluted with a 15 mM KCl and 2 mM phosphate buffer aqueous solution, and then injected into the chamber as the measurement sample.

The measurement of single-molecule interactions was performed by laser trapping floating beads and bringing them close to the substrate, while moving the trap position along the x-axis using a stimulator to increase the probability of interactions.

The measurements of multi-molecular interactions were performed by laser-trapping beads adsorbed to the substrate and peeling them off for use. The peeled beads were then approached to the substrate, and the trap position was moved along the x-axis using a stimulator to increase the probability of interactions.

Since the trapped beads behave like springs, the energy was calculated using the equation below.

$$E = \frac{1}{2}kx^2 \tag{6.2}$$

Here, the trap stiffness was k = 0.749.

The number of PAA-HCl chains interacting with a PAMPS chain was calculated probabilistically. According to the Poisson distribution, the probability $p(m)$ that m PAA-HCl chains are bound to the surface of the bead when the expected value is λ is given by,

$$p(m) = \frac{\lambda^m e^{-\lambda}}{m!} \tag{6.3}$$

Therefore, the probability $p(interaction)$ that one or more PAA-HCl chains are bound to the bead

surface and interact with the PAMPS chain is,

$$p(interaction) = 1 - p(0) = 1 - e^{-\lambda} \tag{6.4}$$

Among these, the probability that only one PAA-HCl chain interacts with the PAMPS chain is,

$$\frac{p(1)}{p(interaction)} = \frac{\lambda e^{-\lambda}}{1 - e^{-\lambda}} \tag{6.5}$$

Even when multiple PAA-HCl chains are bound to a bead, if they are sufficiently separated, they do not interact simultaneously. Considering **Fig. 6.4**, the solid angle Ω within which two PAA-HCl chains can bind simultaneously is,

$$\Omega = \frac{\int_0^{\theta} 2\pi A \sin\theta \times A \, d\theta}{A^2} = 2\pi(1 - \cos 2\theta) \tag{6.6}$$

Thus, the probability $p(multiple)$ that two PAA-HCl chains exist within the range where they can simultaneously interact is given by dividing Ω by the total solid angle (4π),

$$p(multiple) = \frac{\Omega}{4\pi} \tag{6.7}$$

Assuming the distance from the substrate to the binding point of the bead–PAA-HCl chain is 10 nm, the distance x nm from the contact point of the bead and substrate to the PAA-HCl chain is determined by the Pythagorean theorem,

$$x = \sqrt{500^2 - (500 - 10)^2} \cong 99.5 \text{ [nm]} \tag{6.8}$$

Therefore,

$$\sin\frac{\theta}{2} = \frac{99.5}{500} = 0.199 \tag{6.9}$$

and,

$$\cos 2\theta = 2\cos^2\theta - 1 = 2\left(1 - 2\sin^2\frac{\theta}{2}\right) - 1 \cong 0.842 \tag{6.10}$$

At this time, since θ is approximately 16.3°, from equation (6.6), Ω is approximately 0.316π. Therefore, the probability that two molecules simultaneously interact is,

$$p(multiple) = \frac{\Omega}{4\pi} = \frac{0.842}{4\pi} \cong 0.079 \tag{6.11}$$

For example, when $p(interaction) = 0.3$, the expected value λ is,

$$p(0) = \frac{\lambda^0 e^{-\lambda}}{0!}$$

$$1 - 0.3 = e^{-\lambda}$$

$$\lambda \cong 0.357 \tag{6.12}$$

The probability that two PAA-HCl chains are bound to a bead is,

$$\frac{p(2)}{1 - p(0)} = \frac{\frac{\lambda^2 e^{-\lambda}}{2!}}{1 - e^{-\lambda}} = \frac{\frac{(0.357)^2 e^{-0.357}}{2}}{1 - e^{-0.357}} \cong 0.149 \tag{6.13}$$

At that time, the probability that two molecules simultaneously interact with the PAMPS chain is $0.149 \times 0.079 \times {}_2C_2 \cong 1.18\%$. Similarly, it is calculated that the probability that two PAA-HCl chains interact with the PAMPS chain while three PAA-HCl chains are bound to the bead is approximately $0.0176 \times 0.079 \times {}_3C_2 \cong 0.42\%$, and the probability that three PAA-HCl chains interact with the PAMPS chain while three PAA-HCl chains are bound to the bead is approximately $0.0177 \times (0.079)^{3-1} \times {}_3C_3 \cong 0.01\%$. The probability of more than three molecules binding simultaneously is negligible. Therefore, if 30% of the beads interact with PAMPS, the probability that the interaction is a single-molecule interaction is calculated as, $100\% - 1.18\% - 0.42\% - 0.01\% = 98.39\%$. By summarizing these equations, the probability PPP of a single-molecule interaction is expressed as,

$$P = 1 - \sum_{n=2}^{m} \left[\frac{\lambda^n e^{-\lambda}}{n! \times (1 - e^{-\lambda})} \times \sum_{k=2}^{n} \left(\binom{n}{k} \times 0.079^{k-1} \right) \right] \tag{6.14}$$

Table 6.1 shows the expected values λ and the probabilities P of single-molecule interactions for interaction rates $p(interaction) = 0.1, 0.3, 0.5, 0.7, 0.9$.

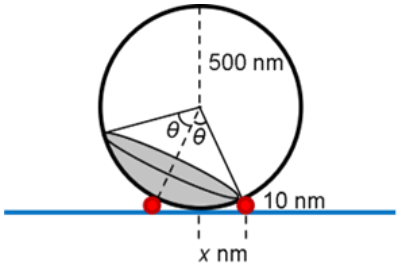

Fig. 6.4 The range within which multiple PAA-HCl chains bound to a bead can simultaneously interact with PAMPS chains is depicted. The blue line represents the substrate, and the red circles denote PAA-HCl chains that have interacted with PAMPS chains.

Table 6.1 Expected values λ and probabilities P (%) of single-molecule interactions for interaction rates p(interaction)=0.1,0.3,0.5,0.7,0.9.

p(*interaction*)	λ	P (%)
0.1	0.1053605	99.56
0.3	0.356675	98.31
0.5	0.6931472	96.13
0.7	1.2039728	91.55
0.9	2.3025851	75.27

6.3 Results and Discussion

6.3.1 FS-AFM Imaging

Using a modified FS-AFM for polymer observation, imaging of each polymer chain was performed in a 30 mM KCl aqueous solution at 25 ± 1 °C. For PAMPS alone, rigid molecules adsorbed to the mica substrate was observed (**Fig. 6.5** and a line profile is shown in **Fig. 6.6**). In contrast, PAA-HCl alone exhibited self-shrinking globule and randomly moved on the mica substrate due to Brownian motion (**Fig. 6.7** and a line profile is shown in **Fig. 6.8**). By casting both polymer chains onto the mica substrate, electrostatic interaction between PAMPS and PAA-HCl was observed (**Fig. 6.9A**). It was confirmed that PAA-HCl chain undergoing random Brownian motion on the mica substrate repeatedly

bound and dissociated with the PAMPS chain upon approaching them. This behavior was not observed in the imaging of PAMPS and PAA-HCl alone. Furthermore, since this phenomenon was reproduced in all-atom molecular dynamics (MD) simulations, it was concluded that the binding and dissociation were due to electrostatic interactions between PAMPS and PAA-HCl (**Fig. 6.9B**).

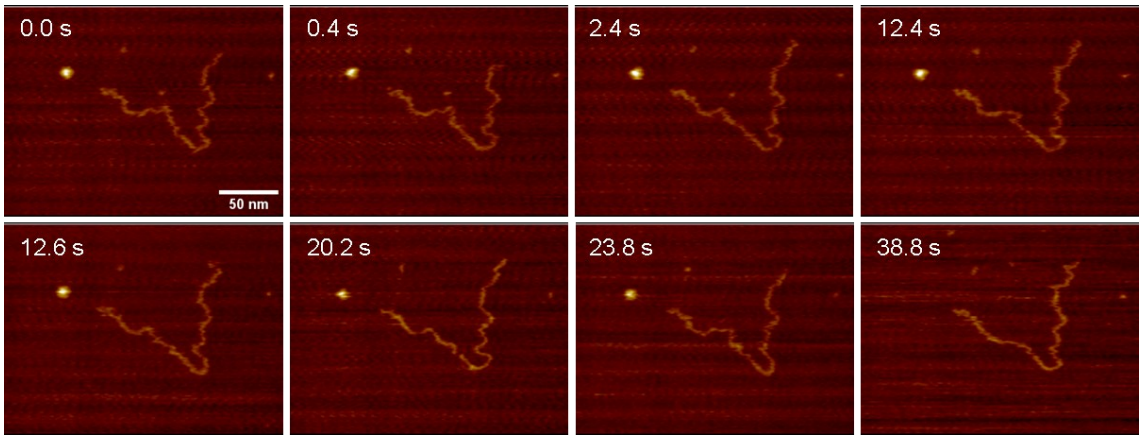

Fig. 6.5 Snapshots from FS-AFM movie of a single PAMPS chain forming a rigid linear

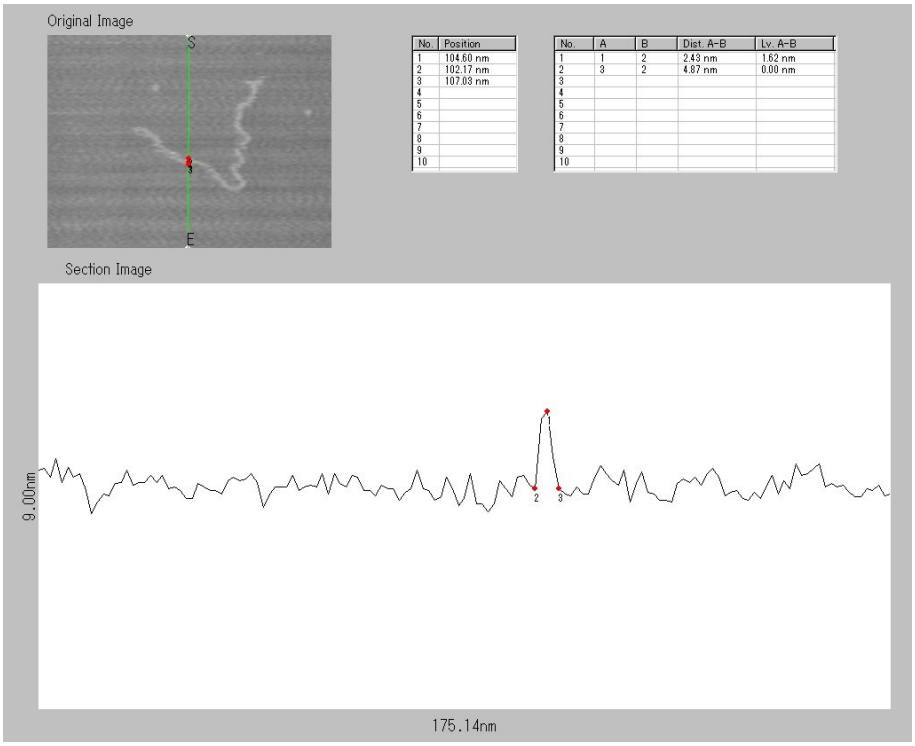

Fig. 6.6 Line profile of a PAMPS chain in 30 mM KCl aqueous solution at 25 ± 1 ºC.

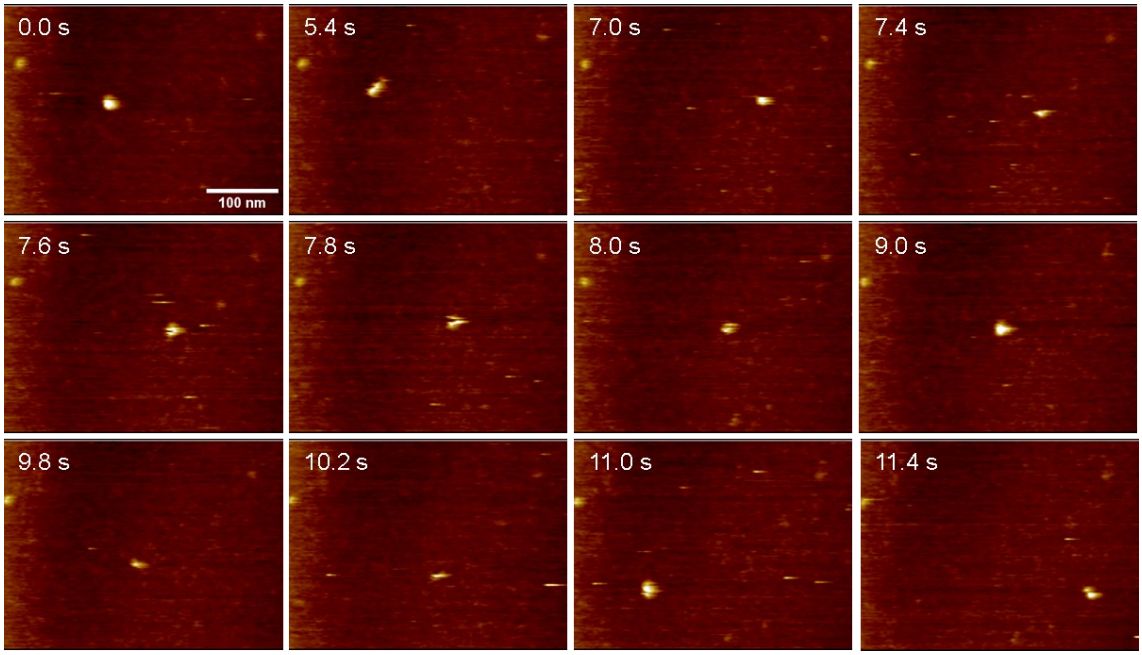

Fig. 6.7 Snapshots from FS-AFM movie of a single PAA-HCl chain forming a globule. XY: 389 nm × 292 nm, Z: 18.00 nm. Frame rate: 5.0 frames per second (fps).

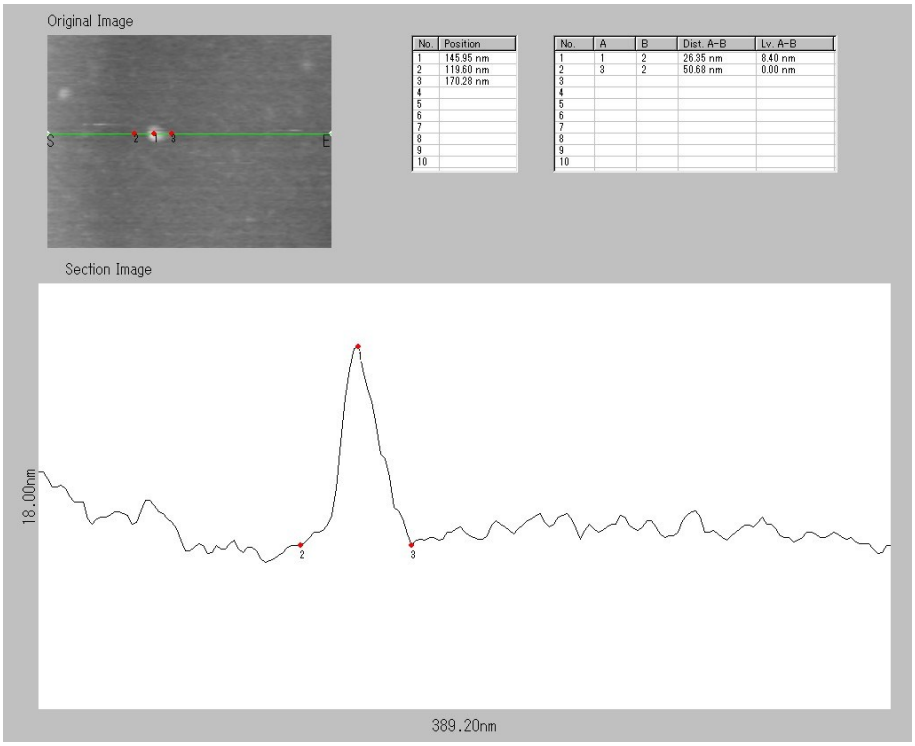

Fig. 6.8 Line profile of PAA-HCl a chain in 30 mM KCl aqueous solution at 25 ± 1 ºC.

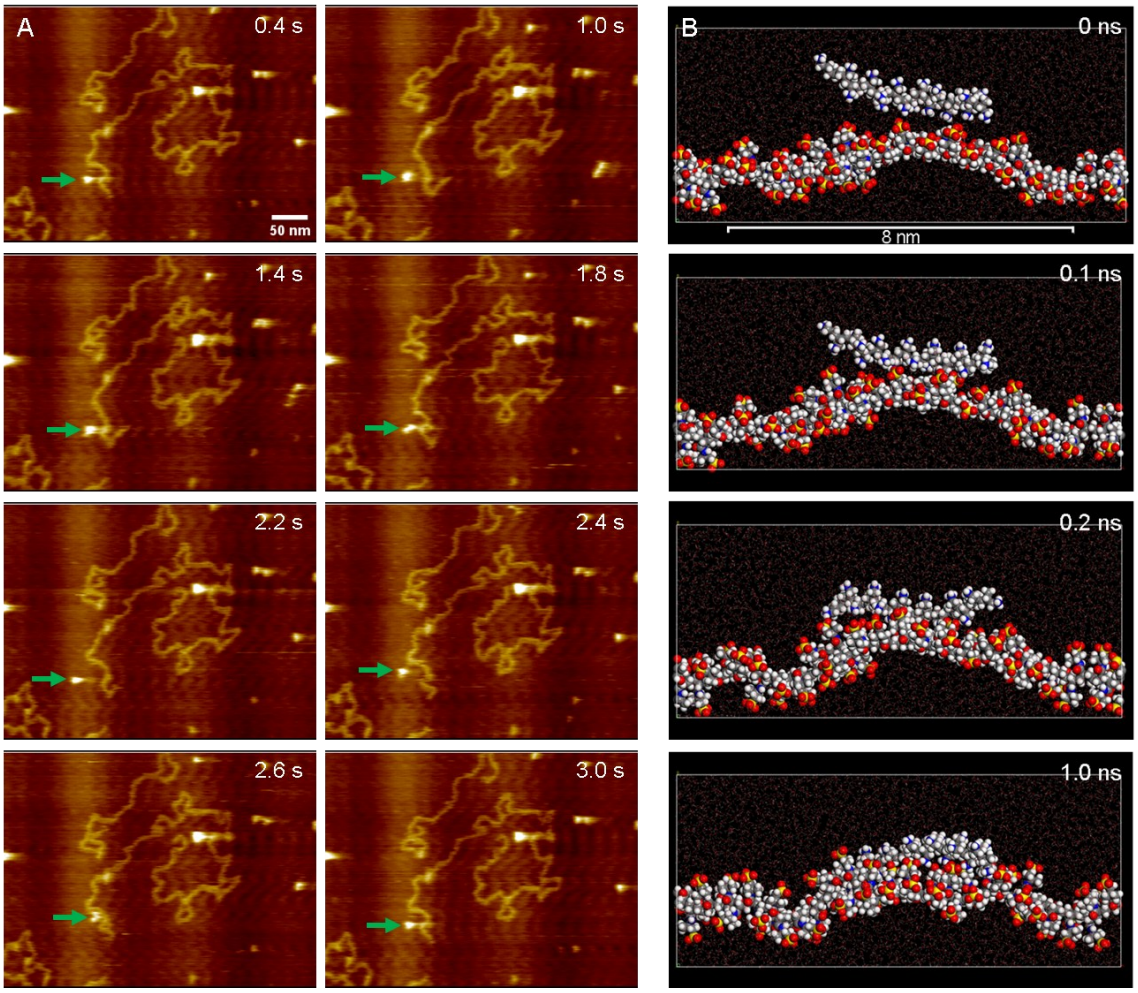

Fig. 6.9 Electrostatic interactions between PAMPS and PAA-HCl. (a) FS-AFM: Repeated binding and dissociation resulting from electrostatic interactions between PAMPS and PAA-HCl (green arrow: Position of PAA-HCl). Scale: XY, 434 × 325 nm; Z, 9.0 nm. (b) All-atom MD Simulation: Interaction dynamics between PAMPS chains and PAA-HCl chains.

We also observed the PAA chains (short-chain molecule) undergoing translational motion along the PAMPS chains (rail-chain molecule) driven by thermal fluctuations (**Fig. 6.10**, and a line profile is shown in **Fig. 6.11**). This movement was sustained over long distances (several hundred nanometers) and persisted for more than two minutes. We attribute this behavior to the short-chain molecule binding through multiple electrostatic interactions between polymer chains while moving along the rail

molecule due to Brownian motion. The short-chain molecule was able to traverse the rails without dissociating, even in bent regions. Numerous instances of this walking motion were observed, and the diversity of movements is attributed to variations in molecular weight.

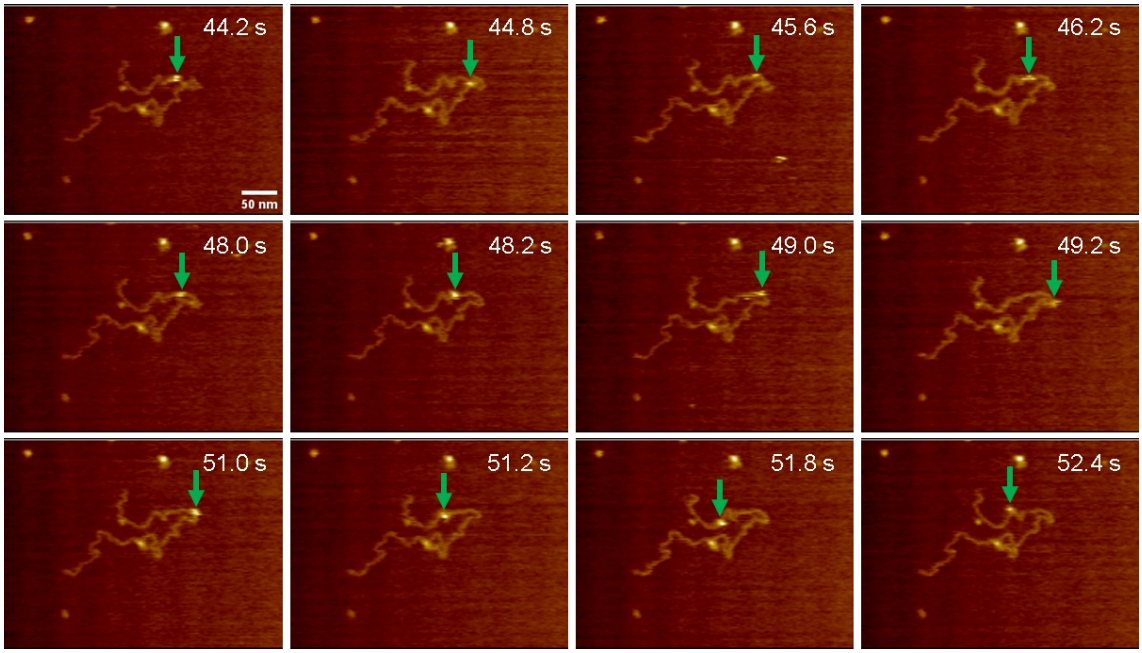

Fig. 6.10 Snapshots from FS-AFM movie. A PAA-HCl chain moves along PAMPS chain due to thermal fluctuation. Green arrows indicate the positions of a PAA-HCl chain. XY: 389 nm × 296 nm, Z: 18.00 nm. Frame rate: 5.0 frames per second (fps).

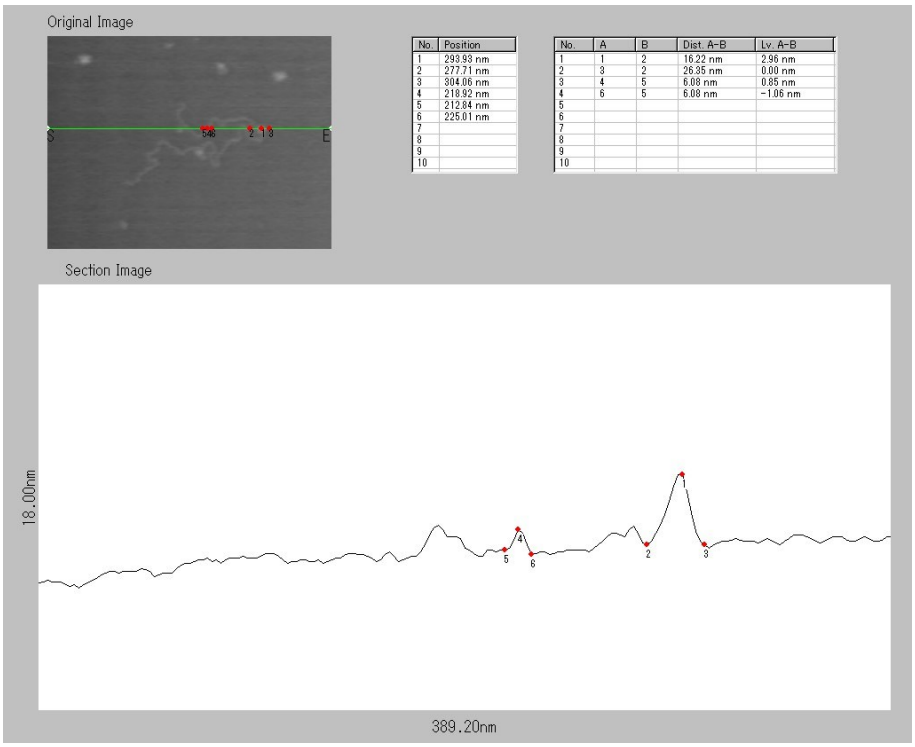

Fig. 6.11 Line profile of PAA-HCl chain moving along a PAMPS chain in 30 mM KCl aqueous solution at 25 ± 1 ºC.

Details of the motion are shown in **Fig. 6.12**. While multiple steps corresponding to multiples of the helical pitch were frequently observed in the previously reported chiral helical poly(phenyl acetylene), the step sizes in the current motion were disordered (**Fig. 6.12A**, **B** and **C**).[10] This is attributed to the fact that both PAMPS and PAA-HCl form random coil structures, lacking periodic binding points on their molecular surfaces. For the same reason, the direction of the steps was random (**Fig. 6.12D** and **E**). The ratio of the direction of movement to the right side : the left side was 121 : 139. No bias was also observed in step sizes, leading to the conclusion that the movement direction is random. For this movement, a Mean Squared Displacement (MSD) plot was generated (**Fig. 6.12F**). The linear slope of the MSD indicates that the movement is driven by Brownian motion, and the diffusion coefficient was calculated to be D = 19.5 nm²/s. To investigate the disorder in step sizes, an analysis was performed using all-atom MD simulations. The distance between sulfonate groups of PAMPS

interacting with PAA-HCl was measured (**Fig. 6.12G**). The ammonium groups of PAA interact with sulfonate groups every 1 to 3 monomer units, and the distance between sulfonate groups interacting with ammonium groups is approximately 7 Å. Therefore, the minimum step size is about 7 Å. Upon detailed examination of step sizes of 5.5 nm or less observed by FS-AFM, step sizes of approximately multiple of 0.7 nm were confirmed (**Fig. 6.12H**). However, there is variability in the spacing between sulfonate groups, which leads to disorder in larger step sizes.

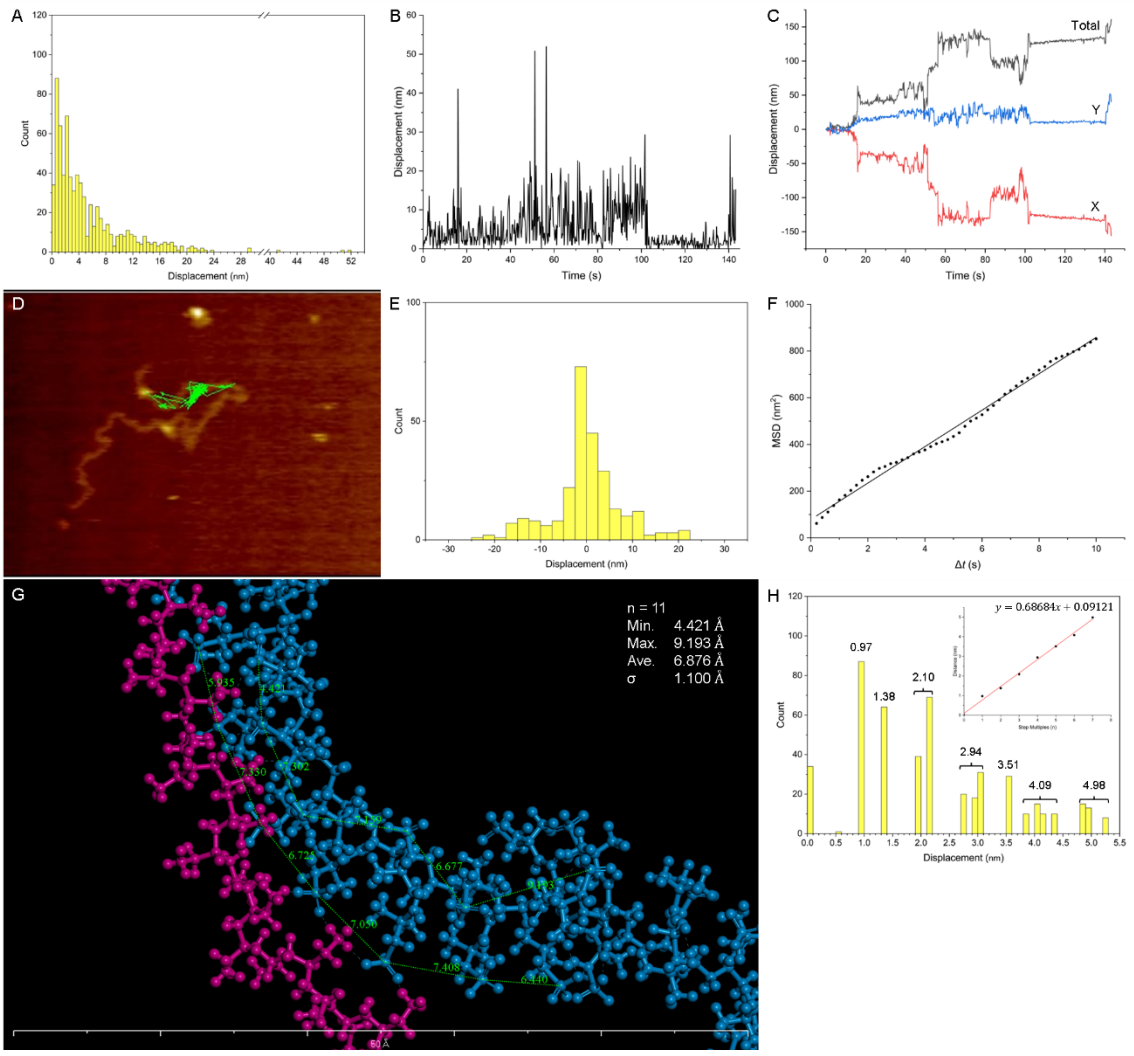

Fig. 6.12 Analysis of FS-AFM Imaging. (A) Histogram of step sizes. (B) Plots of displacement at each time point. (C) Displacement-time plots. The lower left corner of the AFM image was set as the origin *O*(0,0). (black: total displacement, red: *x*-axial displacement, blue: *y*-axial

displacement) (D) Trajectories of PAA-HCl used for analyzing movement direction from 80 to 143.2 seconds. (E) Distribution of step sizes towards the right and left side. (F) Mean square displacement (MSD) plots based on the trajectory data from (D); the line linearly approximated the MSD-Δ*t* plots. *D* = 19.5 nm^2/s. (G) Snapshot from all-atom MD simulation. It shows the distance between the sulfonate groups of PAMPS that are interacting with the ammonium groups of PAA-HCl. (H) Details of step sizes up to 5.5 nm. The numbers represent the average value of elements within the range. The upper right panel displays a distance-step multiples plot. The slope is approximately 0.7, reflecting the spacing between sulfonate groups.

Furthermore, we confirmed the existence of PAMPS–PAA-HCl complex molecular chains driven by thermal fluctuations (**Fig. 6.13**). These complex molecular chains exhibited a structure in which thread-like PAMPS molecules were entwined with globule-shaped PAA-HCl chains. This movement was caused by the entire complex molecular chain being dragged by PAA-HCl chains that interact with PAMPS chains and are driven by Brownian motion. Additionally, we observed that the movement ceased when PAA-HCl chains detached from the complex molecular chains (**Fig. 6.14**). This phenomenon indicates that unidirectional movement is characteristic of the complex molecular chains.

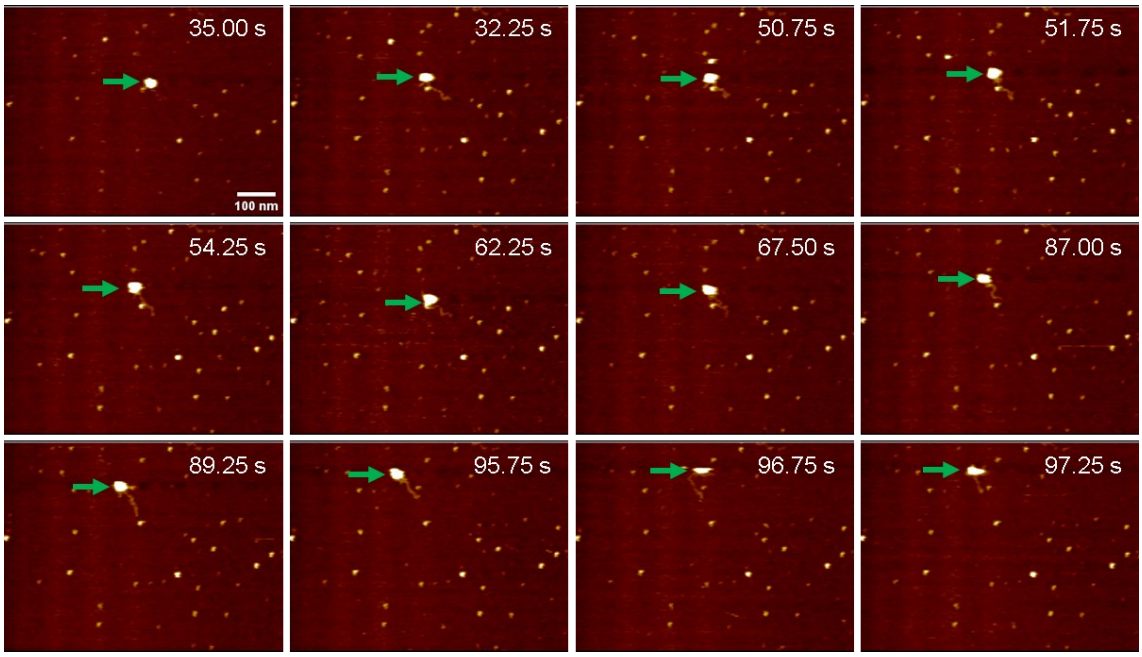

Fig. 6.13 Snapshots from FS-AFM movie. A complex molecular chain moves in one direction due to thermal fluctuation. Green arrows indicate the positions of a PAA-HCl chain. XY: 734 nm × 550 nm, Z: 18.00 nm. Frame rate: 4.0 frames per second (fps).

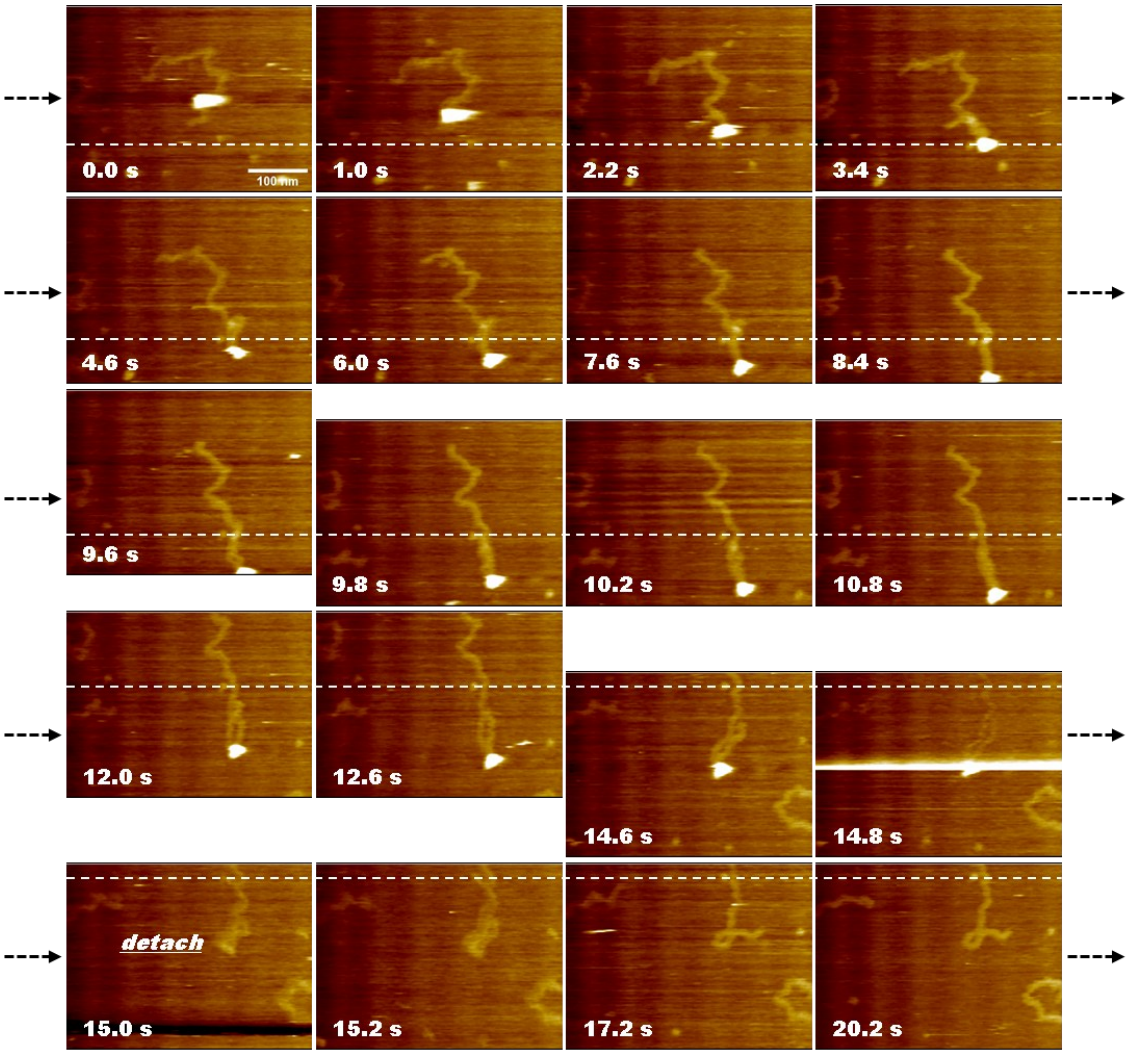

Fig. 6.14 Snapshots from FS-AFM movie. A complex molecular chain moves in one direction due to thermal fluctuation. White dashed line indicates the positions of the particles strongly bound to the substrate. XY: 411 nm × 309 nm, Z: 18.00 nm. Frame rate: 5.0 frames per second (fps). Fifteen seconds after starting imaging, the PAA-HCl chain detached from the PAMPS chain. Concurrently, the movement of the PAMPS chain ceased.

The movement of the complexes also exhibited disordered step sizes (**Fig. 6.15A, B and C**). The complex molecular chains moved across the surface of the mica substrate, which we attributed to the irregular interaction points between the polymers and the substrate. However, the direction of

movement showed a bias (**Fig. 6.15D**). This bias depended on the shape of the complex molecular chains, with the position of PAA-HCl within the complex aligning with the direction of movement. For instance, when PAA-HCl was located at the upper part of the complex molecular chain, the movement occurred in the upward direction. A detailed analysis of the directional bias was conducted. The ratio of the direction of movement to the upper side : left side was 146 : 109. This means that movements towards the plus end occurred 1.3-times more frequently than those towards the minus end. Notably, for larger step sizes exceeding 5 nm, the ratio was 65 : 33, indicating a 2.0-times difference. This bias was consistently observed across all complex molecular chains studied, suggesting that the complex chains exhibit directional movement (**Fig. 6.14** and **Fig**. 6.16). Regarding this movement, Mean Square Displacement (MSD) plots were generated (**Fig. 6.15E**). The linear slope of the MSD indicates that the movement of the complex molecular chains is driven by Brownian motion. The diffusion coefficient was calculated to be D = 21.3 nm^2/s.

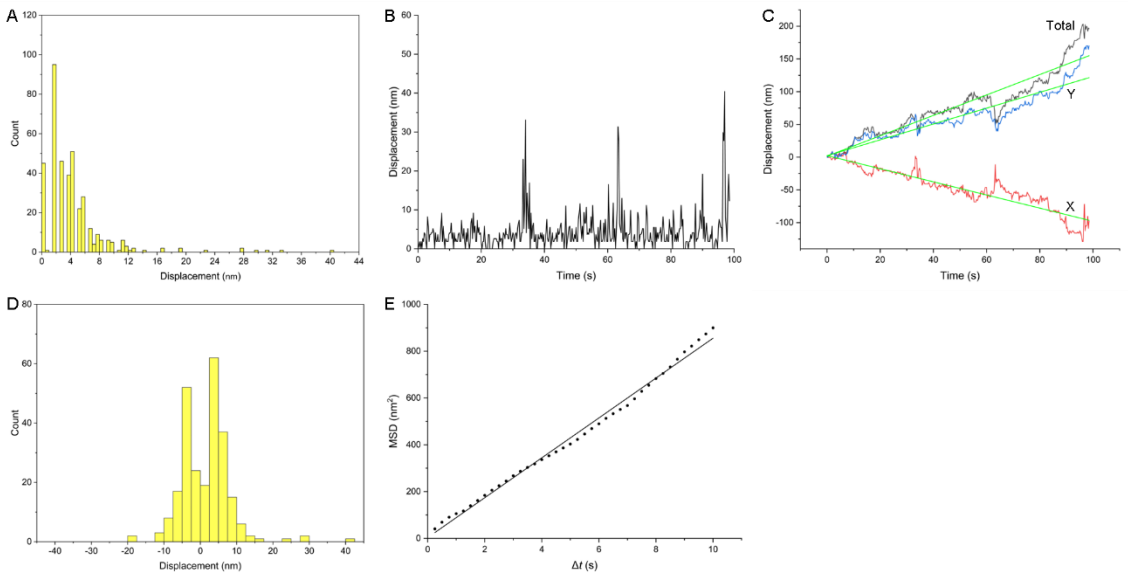

Fig. 6.15 Analysis of FS-AFM Imaging. (A) Histogram of step sizes. (B) Plots of displacement at each time point. (C) Displacement-time plots. The lower left corner of the AFM image was set as the origin *O*(0,0). (black: total displacement, red: *x*-axial displacement, blue: *y*-axial displacement) (D) Distribution of step sizes towards the upper and bottom side. (E) Mean square

displacement (MSD) plots based on the trajectory data from Fig. 6.13; the line linearly approximated the MSD-Δ*t* plots. D = 21.3 nm^2/s.

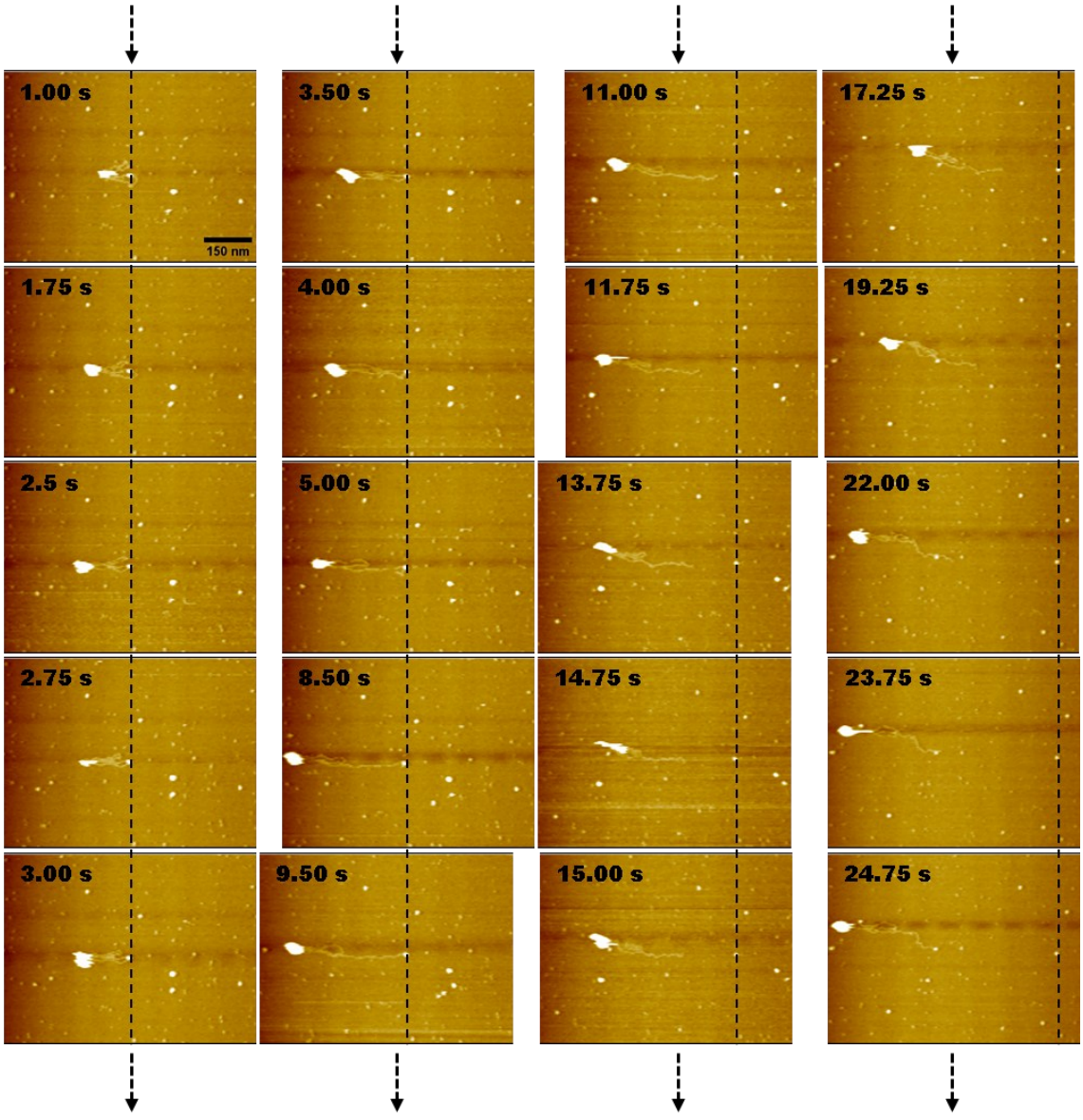

Fig. 6.16 Snapshots from FS-AFM movie. A complex molecular chain moves in one direction due to thermal fluctuation. Black dashed line indicates the positions of the particles strongly bound to the substrate. XY: 790 nm × 600 nm, Z: 36.00 nm. Frame rate: 4.0 frams per second (fps).

The directional bias in the movement was attributed to the asymmetric molecular structure. Under aqueous conditions, PAA-HCl formed globules, and moved on the substrate due to the reduced contact area (**Fig. 6.7** and **Fig**. 6.8). In contrast, size information obtained from line profiles (**Fig. 6.6**) and MD simulations (**Fig. 6.3**) indicated that PAMPS adopted an extended conformation under aqueous conditions. This rigid structure resulted from ionic repulsion and amide bonds between pendant groups. Considering that the substrate surface contains silanol groups that repel the sulfonate groups in PAMPS, PAMPS was weakly anchored to the substrate due to the salt effect of the added KCl. Consequently, when PAA-HCl is nearby, PAMPS easily detaches from the substrate and binds to PAA-HCl, allowing the PAMPS segment bound to PAA-HCl to gain mobility.

We propose an explanation for the directional bias in movement based on information obtained from AFM images. **Fig. 6.17** shows AFM images and schematic diagrams illustrating (**A**) forward and (**B**) backward steps. The forward step is hypothesized to occur when the mobile moiety near PAA-HCl pulls the PAMPS segment, which is weakly attached to the substrate. As indicated by size measurements (**Fig. 6.6**), the PAMPS chain adopts an extended conformation. Therefore, when the mobile moiety moves in a direction that stretches the PAMPS chain beyond its capacity, the chain can no longer extend and is dragged along, causing the entire composite molecular chain to move. This hypothesis is supported by the molecular positions observed in the AFM images (**Fig. 6.17A**). In contrast, the backward step is hypothesized to occur when the mobile moiety pushes the PAMPS segment, causing it to shrink. As discussed in **Chapter 2**, polymer chains with bulky pendants can also form flexible structures in solution. PAMPS chains under aqueous conditions are expected to adopt metastable, contracted conformations. Consequently, part of the energy associated with the mobile moiety's backward step is thought to be consumed by these conformational changes. The bending of the PAMPS segment observed in the AFM images supports this hypothesis (**Fig. 6.17B**). However, during continuous backward steps or motion involving large step sizes, the PAMPS segment is eventually dragged backward, resulting in the entire complex chain moving backward (**Fig. 6.13**;

54.25 s to 62.25 s). Because conformational changes occur during the backward step, the energy required to move differs from that in the forward step. This discrepancy is thought to facilitate unidirectional motion. In addition, perturbations from the probe's tapping may also contribute to this phenomenon.

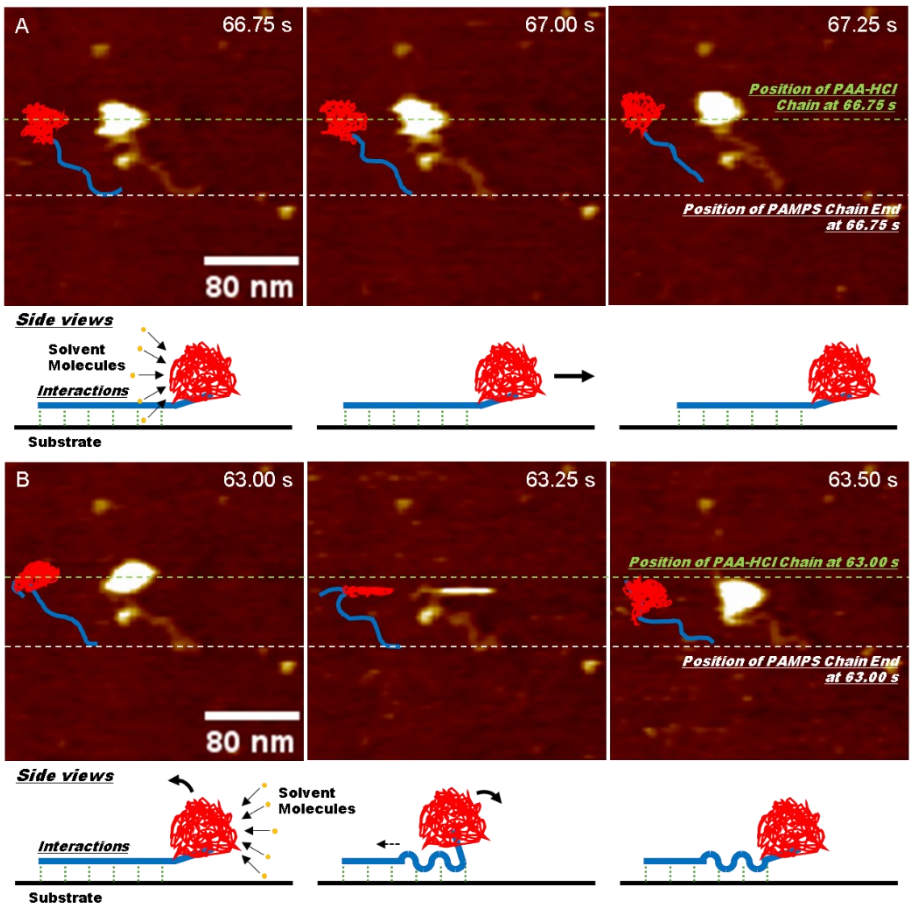

Fig. 6.17 Schematic Diagram of Unidirectional Movement. (A) Forward and (B) backward steps. The complex molecular chains, comprising PAA-HCl chains (red) bound to PAMPS chains (blue), exhibit differences in mobility between the PAA-HCl-bound segments and the unbound segments. The difference in energy required to move between forward and backward steps causes the observed directional bias in movement.

At present, no further conclusions can be drawn from the available data. To gain a more detailed understanding of this mechanism, innovative techniques will be required to visualize conformational changes at the atomic level or to clarify the energy states of each conformation. Nevertheless, the emergence of unidirectional movement is an extremely important finding for motor proteins and the future of molecular motor research.

6.3.2 Force Measurement of Interaction Between Single Molecules

Understanding the extent of energy generated in molecular motor characteristics is crucial. Therefore, force measurements were conducted using an optical trapping system. Additionally, while FS-AFM only provides data every few hundred milliseconds, the optical trapping system can obtain data every few tens of microseconds, allowing for the expected confirmation of intermediate states of motor function. Measurements were performed in a mixed solution of 15 mM KCl and 2 mM phosphate buffer at 25 ± 1 °C. To use a higher concentration sample compared to the sample concentration used for FS-AFM observations, phosphate buffer was employed to clarify the charge state. Furthermore, to prevent PAA-HCl chains from being buried in the surface irregularities of polystyrene beads, PAA-HCl with a molecular weight ten times larger than that used for FS-AFM imaging (M_w = 1.5 × 10^5 g/mol) was employed.

When the concentration of PAA-HCl was 10 μg/mL, the interaction rate was $p(interaction) = 14\%\ (n = 90)$ during the 30-minute period following sample preparation. From equation (6.14), the probability of single-molecule chain interactions was $P = 99.3\%$, suggesting that the observed displacements are due to single-molecule interactions. Moreover, compared to the interaction rate of $p(interaction) = 7\%\ (n = 83)$ at a PAA-HCl concentration of 0 μg/mL, the higher interaction rate indicates that the interactions between PAMPS and PAA-HCl were measured. Displacements accompanied by binding occurring on extremely short timescales of tens of microseconds were confirmed. Displacements occurring in a few stages were also observed (**Fig. 6.18**).

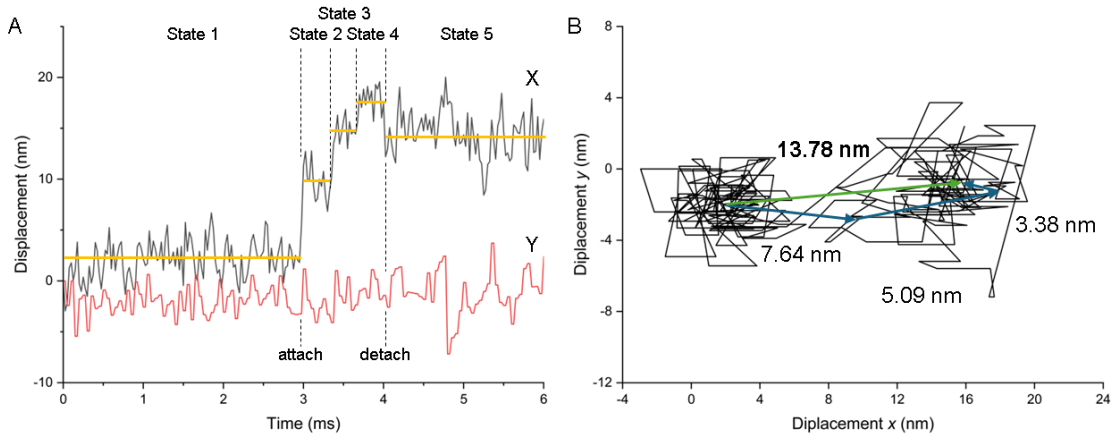

Fig. 6.18 Force measurement results of interactions between PAMPS–PAA-HCl using an optical trapping system. Four stages of displacement were observed. (A) Displacement-time plot (black: X axis, red: Y axis). (B) X-Y displacement plot. The first stage (State 1 to 2) exhibited a displacement of 7.64 nm, the second stage (State 2 to 3) 5.09 nm, the third stage (State 3 to 4) 3.38 nm, and the displacement between the start and end points (State 1 to 4) was 13.78 nm.

A detailed analysis was conducted on the displacements shown in **Fig. 6.18**. The standard deviations of the *x* and *y* displacements for each state are presented in **Table 6.2**. This variability is attributed to Brownian motion. When intermolecular interactions occur, Brownian motion is constrained, resulting in smaller standard deviations. However, no difference was observed in the standard deviations between State 1 and State 5. This suggests that the displacement from State 4 to State 5 is not driven by interactions but rather by detaching. Therefore, **Fig. 6.18** depicts movement with three stages of displacement: the first stage (State 1 to 2) exhibits a displacement of 7.64 nm, the second stage (State 2 to 3) 5.09 nm, and the third stage (State 3 to 4) 3.38 nm, with an overall displacement from the start to the end point (State 1 to 4) of 13.78 nm. Additionally, this detachment indicates that PAMPS and PAA-HCl can easily dissociate, suggesting that the energy generation is due to translational movement along rail molecules rather than within the complex molecular chains. Using the displacement from the start to the end point (State 1 to 4) and equation (6.2), the energy generated by this interaction was

calculated to be 34.71 k_BT, indicating significant energy generation. In myosin V, biological molecular motors, a combination of lever arm swing and Brownian motion (the hand-over-hand mechanism) enables the motor to perform work of 16 k_BT per step.[13] Although the interactions between single molecules involve a small number of samples (n), making statistical evaluation impossible, it has been confirmed that they can perform work comparable to that of biological molecular motors.

Table 6.2 Standard deviation of x, y displacements in each state

	State 1	State 2	State 3	State 4	State 5
σ_x	2.12	1.75	1.18	1.29	2.17
σ_y	1.92	1.61	1.70	1.07	2.17

Currently, only a few instances of displacements resulting from interactions between single molecules have been confirmed. To facilitate more detailed analyses, it is necessary to increase the sample size (n) and perform statistical analyses. Nevertheless, the finding that energy is generated through interactions between synthetic polymer chains is entirely novel. It is expected to have a significant impact on the field of polymer motors and, more broadly, on the entire polymer science domain in the future.

6.3.3 Force Measurement of Interaction Between a few Molecules

If polymer motors can be driven cooperatively, they would generate forces comparable to motor proteins, thereby increasing the potential for applications in devices such as artificial muscles. Therefore, force measurements were conducted using a 30 μg/mL aqueous solution of PAA-HCl. The interaction rate was $p(interaction) = 96\%$ ($n = 23$), and from equation (6.14), the probability of interactions between single molecules was $P = 59.7\%$, indicating a high probability of a few molecule binding. Furthermore, the improvement in binding rates corresponding to PAA-HCl concentrations supported that the force measured in **Chapter 6.3.2** was due to interactions between

single molecules. Similar to interactions between single molecules, displacements accompanied by binding occurring on extremely short timescales of tens of microseconds were confirmed. Displacements occurring in a few stages were also observed. The displacements shown in **Fig. 6.19** consisted of two stages: the first stage exhibited a displacement of 15.82 nm, the second stage 19.79 nm, and the overall displacement from the start point to the end point was 13.31 nm.

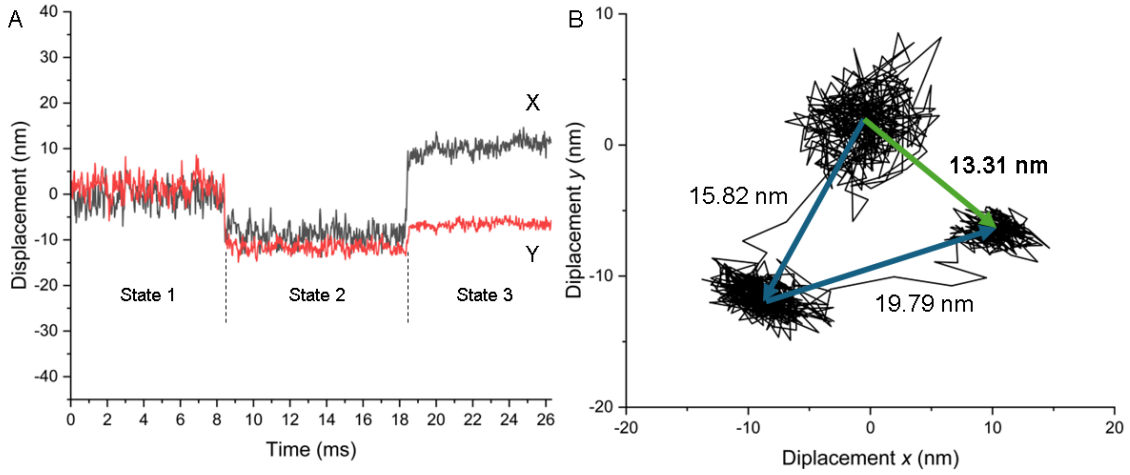

Fig. 6.19 Force measurement results of interactions between a few molecules using an optical trapping system. Two stages of displacement were observed. (A) Displacement-time plot (black: X axis, red: Y axis). (B) X-Y displacement plot. The first stage (State 1 to 2) exhibited a displacement of 15.82 nm, the second stage (State 2 to 3) 19.79 nm, and the displacement between the start and end points (State 1 to 3) was 13.31 nm.

Focusing on the noise sizes of each step in **Fig. 6.19A**, it is observed that they gradually decrease. When calculating the standard deviations $(\sigma_{xn}, \sigma_{yn})$ for each step (n), the values are $(\sigma_{x1}, \sigma_{y1}) = (2.49, 2.28)$, $(\sigma_{x2}, \sigma_{y2}) = (2.00, 1.14)$, and $(\sigma_{x3}, \sigma_{y3}) = (1{,}44, 0.78)$, indicating a progressive reduction in variability. This variability is attributed to Brownian motion; therefore, a decrease in variability signifies a transition to stronger binding. From MD calculations (**Fig. 6.12G**), it is considered that PAMPS and PAA-HCl interact at the Ångström scale, making it unlikely for single-molecule bindings to transition to progressively stronger bindings on a millisecond timescale.

Consequently, the reduction in variability is reasonably attributed to an increase in the number of interacting polymer chains. This suggests the potential for cooperative movement of polymer molecular motors. Detailed measurement results are presented in **Fig. 6.20**. It is important to note that analyzing interactions between a few molecules is more complex compared to interactions between single molecules, and thus, these data do not guarantee elucidation at the molecular level. To further discuss the displacements caused by interactions between a few molecules, future studies will require statistical analyses with larger sample sizes (n). Calculating the energy from the measured displacements using equation (6.2) reveals that most of the observed movements generate significant forces exceeding 5 k_BT (**Fig. 6.20C**). The fact that energy up to 178 k_BT (7.30×10^{-19} J) was generated suggests that organizing polymer motors to behave like motor proteins could enable applications in devices such as artificial muscles.

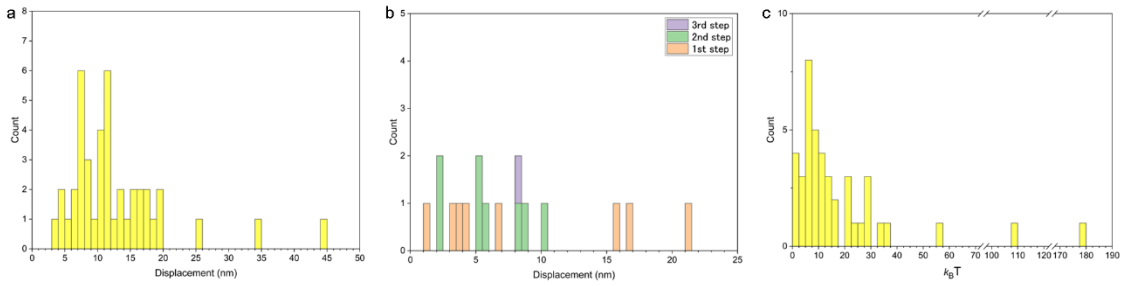

Fig. 6.20 Analysis of force measurements. (a) Histogram of displacements between start and end points. (b) Histogram of displacements at each step, using data that exhibited two or more displacement stages (1st step: n = 8; 2nd step: n = 8; 3rd step: n = 1). (c) Histogram of energy generated by displacements between start and end points.

6.4 Conclusion

In this study, we observed molecular motor functions and conducted force measurements using commercially available ionic polymers, specifically PAMPS and PAA-HCl. The translational movement of PAA-HCl chains along PAMPS chains was driven by thermal fluctuations. The step size

was multiple of 0.7 nm, which corresponds to the distance between the sulfonic acid groups interacting with PAA-HCl chains at the ends of PAMPS chains. Additionally, we confirmed the phenomenon of complex molecular chains, composed of the PAMPS chain bound to the PAA-HCl globule, moving unidirectionally. This unidirectionality was considered to result from structural asymmetry and the tapping effects of the probe.

Regarding these movements, force measurements were conducted using an optical trapping system. This study is the first report applying an optical trapping system to polymeric polymers, demonstrating that single-molecule level mechanical measurements are feasible in synthetic polymers. Mechanical measurements using low-concentration PAA-HCl aqueous solutions confirmed the generation of forces due to translational movement along rail molecules, presumed to be interactions between single molecules. Furthermore, using high-concentration PAA-HCl aqueous solutions resulted in force generation presumably due to interactions between a few molecules, suggesting that organizing polymer motors can generate significant forces akin to motor proteins.

This study demonstrated that synthetic polymer motors driven by thermal fluctuations at room temperature generate forces similar to motor proteins. This strongly supports the feasibility of artificial muscles driven by thermal fluctuations. The distinct movement mechanism, which allows for long-distance translational movement, suggests potential applications not only in artificial muscles but also in molecular transport and other areas. The discovery that energy is generated through interactions between synthetic polymer chains is entirely novel and is expected to have a significant impact on the field of polymer motors and, more broadly, on the entire polymer science domain.

6.5 Reference

1. N. Kodera, D. Yamamoto, R. Ishikawa, T. Ando, Video Imaging of Walking Myosin V by High-Speed Atomic Force Microscopy. *Nature* **2010**, *468* (7320), 72–76. https://doi.org/10.1038/nature09450

2. M. Kaya, H. Higuchi, Nonlinear Elasticity and an 8-Nm Working Stroke of Single Myosin Molecules in Myofilaments. *Science* **2010**, *329* (5992), 686–689. https://doi.org/10.1126/science.1191484

3. M. Nishiyama, E. Muto, Y. Inoue, T. Yanagida, H. Higuchi, Substeps within the 8-Nm Step of the ATPase Cycle of Single Kinesin Molecules. *Nat. Cell Biol.* **2001**, *3* (4), 425–428. https://doi.org/10.1038/35070116

4. Y. Okada, H. Higuchi, N. Hirokawa, Processivity of the Single-Headed Kinesin KIF1A through Biased Binding to Tubulin. *Nature* **2003**, *424* (6948), 574–577. https://doi.org/10.1038/nature01804

5. M. Cesario, C. O. D. Buchecker, J. Guilhem, C. Pascard, J. P. Sauvage, Molecular Structure of a Catenand and Its Copper(I) Catenate: Complete Rearrangement of the Interlocked Macrocyclic Ligands by Complexation. *J. Chem. Soc. Chem. Commun.* **1985**, *5*, 244–247. https://doi.org/10.1039/C39850000244

6. P. R. Ashton, D. Philp, N. Spencer, J. F. Stoddart, A New Design Strategy for the Self-Assembly of Molecular Shuttles. *J. Chem. Soc. Chem. Commun.* **1992**, *16*, 1124–1128. https://doi.org/10.1039/C39920001124

7. N. Koumura, R. W. J. Zijistra, R. A. V. Delden, N. Harada, B. L. Feringa, Light-Driven Monodirectional Molecular Rotor. *Nature* **1999**, *401* (6749), 152–155. https://doi.org/10.1038/43646

8. T. Kudernac, N. Ruangsupapichat, M. Parschau, B. MacIá, N. Katsonis, S. R. Harutyunyan, K. H. Ernst, B. L. Feringa, Electrically Driven Directional Motion of a Four-Wheeled Molecule on a Metal Surface. *Nature* **2011**, *479* (7372), 208–211. https://doi.org/10.1038/nature10587

9. K. Shinohara, Single-Molecule Imaging of a Polymer: Direct Observation of Structure and Dynamics in a Polymer Chain. *Kobunshi Ronbunshu* **2016**, *73* (6), 491–504. https://doi.org/10.1295/koron.2016-0034

10. K. Shinohara, Y. Makida, T. Oohashi, R. Hori, Single-Molecule Unidirectional Processive Movement along a Helical Polymer Chain in Non-Aqueous Medium. *Langmuir* **2022**, *38* (40), 12173–12178. https://doi.org/10.1021/acs.langmuir.2c01704
11. R. Hori, K. Higashimine, O. Notoya, K. Shinohara, Synthesis and Direct Observation of Chiral Supramolecular Polymer of Porphyrin Having Cholesteryl Groups. *Langmuir* **2024**, *40* (10), 5535–5544. https://doi.org/10.1021/acs.langmuir.4c00164
12. K. Shinohara, *Applied Scanning Probe Methods X -Biomimetics and Industrial Applications*, Chapter 31: Scanning Probe Microscope Application for Single Molecules in a π-Conjugated Polymer toward the Molecular Devices based on Polymer Chemistry, pp 153–182, B. Bhushan, H. Fuchs, M. Tomitori (Eds.), Springer (Berlin, Heidelberg), ISBN: 978-3-540-74084-1 (2008). https://doi.org/10.1007/978-3-540-74085-8_5
13. K. Fujita, M. Iwaki, Myosin V is a biological Brownian machine. *Biophysics* **2014**, *10*, 69–75. https://doi.org/10.2142/biophysics.10.69

Chapter 7. General Conclusion

In each chapter, the following findings were elucidated:

Chapter 2

We synthesized poly(phenylacetylene), which forms a one-handed helical structure, and conducted motion analysis at the solid-liquid interface using FS-AFM. The analytical method developed in this study effectively clarified structural changes occurring within a single polymer chain, establishing a new technique for the precise analysis of polymers at solid-liquid interfaces. Although the synthesized helical poly(phenylacetylene) was expected to possess a rigid structure due to its π-conjugated backbone and bulky pendant groups, it was observed to have a flexible structure with substantial molecular-level dynamics. Understanding the dynamics of polyacetylene, a conductive polymer, contributes to the enhancement of material properties.

Chapter 3

We performed motion analysis at the solid-liquid interface using FS-AFM on PEG@*α*-CD polypseudorotaxane, which can be conveniently prepared by simple mixing. While PEG@*α*-CD polypseudorotaxane is frequently utilized as a supramolecular material, issues such as solubility and the exclusion of *α*-CDs during dissolution have hindered strict structural analysis. In this study, by fixing the complex to the substrate before *α*-CDs exclusion, we enabled dynamic analysis of polypseudorotaxane in an aqueous solution. In polypseudorotaxane with high molecular weight PEG, an "end-capping effect" was confirmed, where the formation of globules at the PEG chain ends inhibited the exclusion of *α*-CDs. Additionally, stretching and contracting movements accompanied by *α*-CDs shuttling were observed. These findings provide fundamental information for the design of supramolecular materials.

Chapter 4

We synthesized poly(phenylacetylene), forming a one-handed helical structure, and discovered molecular motor functions through FS-AFM imaging. The observed translational movement extended over distances

exceeding 100 nm, achieving dynamic motions not previously realized in synthetic molecular machines. Analysis of the observed motor functions revealed that the movements of short chains were driven by Brownian motion. Furthermore, the unidirectional movement was induced by the chiral helical structure and perturbations from the probe's tapping. This suggests that, with a more precise molecular design, it is possible to create synthetic polymer molecular motors with functionalities comparable to motor proteins.

Chapter 5

Inspired by the molecular motor functions confirmed in poly(phenylacetylene), we synthesized porphyrin-based supramolecular polymers capable of interaction between polymer chains. Structural observations using various microscopes revealed stepwise formation processes of higher-order structures depending on the coordinating metals. Notably, supramolecular polymers using Zn-porphyrin formed branched structures unprecedented in previous studies. FS-AFM imaging of supramolecular polymers using Cu-porphyrin confirmed the interactions considered the origin of molecular motor functions. This study provides foundational information for the design of supramolecular polymers and the elucidation of polymer motor functionalities.

Chapter 6

Using ionic polymers with opposite charges, we observed molecular motor functions and conducted force measurements. The polymers employed are commercially available versatile polymers, and the induction of molecular motor functions by these polymers indicates the feasibility of realizing affordable and high-functioning molecular motors. Additionally, the formed complex molecular chains possessed asymmetric structures with varying mobility, resulting in unidirectional movement. To confirm that these motor functions generate energy, force measurements were performed using an optical trapping system. This study is the first report applying an optical trapping system to synthetic polymers. The measurements confirmed force generation due to motor functions. Furthermore, force generation presumably resulting from interactions

between a few molecules was also observed, suggesting that organizing synthetic polymer motors can generate significant forces comparable to motor proteins. This research is an extremely important report demonstrating that synthetic polymer motors generate energy.

The findings obtained in each chapter collectively provide sufficient evidence for the utility of FS-AFM in analyzing single polymer chains. The dynamic analyses conducted in this study represent a unique analytical method not achievable with methods other than FS-AFM. It is well-known that the structure of single polymer chains influences the physical properties of polymer materials. With growing interest in single-molecular imaging, the development of methods to elucidate structures and dynamics in solution is an important and socially valuable invention contributing to the further advancement of polymer materials.

Additionally, this study reports on synthetic polymer motors driven by thermal fluctuations. Until now, all developed synthetic molecular machines had been low-molecular-weight entities, and dynamic movements akin to motor proteins had not been achieved. The motor functions confirmed in this study realized long-distance translational movements exceeding 100 nm, demonstrating that functionalities comparable to motor proteins are achievable with synthetic polymers. Moreover, the observation of polymer chains undergoing binding and dissociation due to intermolecular interactions is considered the origin of molecular motor functions, suggesting that research on synthetic polymers is a valuable approach for elucidating the evolutionary process of motor proteins.

Furthermore, we conducted force measurements using an optical trapping system on synthetic molecular motors utilizing water-soluble polymers. Previously, optical trapping systems were applied exclusively to biological molecules, but this study is the first to report their application to synthetic polymers. The discovery that synthetic polymers, previously considered merely structural entities, can generate energy is entirely novel and is expected to have a significant impact on the field of polymer science.

In an era where energy issues garner substantial attention and innovative solutions are sought, the invention of synthetic polymer motors driven by thermal fluctuations presents a novel and useful approach. This thesis includes discoveries that contribute to the Sustainable Development Goals (SDGs) and address

energy problems, making it important information that will be utilized widely across various fields, particularly in polymer science.

Achievements

Original Articles Related to This thesis

1. K, Shinohara, Y. Makida, T. Oohashi and R. Hori, Single-Molecule Unidirectional Processive Movement along a Helical Polymer Chain in Non-aqueous Medium. *Langmuir* **2022**, *38* (40), 12173–12178. https://doi.org/10.1021/acs.langmuir.2c01704
2. R. Hori, K. Higashimine, O. Notoya and K. Shinohara, Synthesis and Direct Observation of Chiral Supramolecular Polymer of Porphyrin Having Cholesteryl Groups. *Langmuir* **2024**, *40* (10), 5535–5544. =***Selected for the Supplementary Cover***= https://doi.org/10.1021/acs.langmuir.4c00164
3. R. Hori and K. Shinohara, Direct Observation of the "End-Capping Effect" of a PEG@α-CD Polypseudorotaxane in Aqueous Media, *Macromolecules* **2025**, *published online.* https://doi.org/10.1021/acs.macromol.4c02491.

Other Articles

1. T. Kamei, J. Miyazaki, R. Hori, H. Saito, T. Takahashi, K. Shinohara, M. Miura and H. Suzuki, Spectral and HPLC Analyses of Synthesized Butin and Butein. *Chem. Pharm. Bull.* **2024**, *72* (7), 648–657. https://doi.org/10.1248/cpb.c24-00239
2. T. Yashima, R. Hori, T. Maruyama, K. Nakashima, H. Fujihara, M. Naito, S. Miyagawa and Y. Tokunaga, Synthesis of a cross–chain bridging cryptand. *Org. Chem. Front.*, **2025**, *in press*. https://doi.org/10.1039/D4QO02330G
3. R. Hori, K. Shinohara, Synthesis and Direct Observation of Branched Chiral Helical Poly(phenylacetylene) with Cholesteryl Groups, *submitted*.

International Conference

1. R. Hori, K. Shinohara, Synthesis and Single-Molecule Imaging of Porphyrin Supramolecular Polymer with Cholesteryl Groups. *The 13th SPSJ International Polymer Conference (IPC 2023)*, Sapporo,

Japan, July 18–21, 2023, Poster.

Domestic Conference

1. 堀 諒雅, 篠原 健一, ポリマー1 分子の直視：分岐構造を有するキラルらせん高分子の合成と 1 分子イメージング, 日本化学会第 102 春季年会, オンライン開催, 2022 年 3 月 23–26 日, 口頭発表.
2. 篠原 健一, 大貫 佑河, 堀 諒雅, 樋口 秀男, ポリマー1 分子の直視：イオン性ポリマー分子モーターの高速 AFM イメージングとレーザートラップ法による力学計測, 第 71 回高分子討論会, オンライン開催, 2022 年 9 月 5–7 日, 口頭発表.
3. 堀 諒雅, 篠原 健一, ポリマー1 分子の直視：コレステリル基を有する Zn-ポルフィリンの合成とキラルらせん超分子分岐ポリマーの 1 分子イメージング, 日本化学会第 103 春季年会, 東京理科大学 野田キャンパス, 2023 年 3 月 22–25 日, 口頭発表.
4. 篠原 健一, 大貫 佑河, 堀 諒雅, 樋口 秀男, ポリマー1 分子の直視：イオン性ポリマー鎖による力発生, 第 72 回高分子学会年次大会, G メッセ群馬, 2023 年 5 月 24–26 日, 口頭発表.
5. 堀 諒雅, 東嶺 孝一, 能登屋 治, 篠原 健一, ポリマー1 分子の直視：コレステリル基を有する Cu-および Zn-ポルフィリンの合成とキラルらせん超分子ポリマーのイメージング, 第 72 回高分子討論会, 香川大学, 2023 年 9 月 26–28 日, 口頭発表.
6. 堀 諒雅, 篠原 健一, ポリマー1 分子の直視：ポリ擬ロタキサン鎖一本の高速 AFM イメージング, 第 73 回高分子学会年次大会, 仙台国際センター, 2024 年 6 月 5–7 日, 口頭発表.
7. 篠原 健一, 大橋 崇, 堀 諒雅, ポリマー 1 分子の直視：コレステリル基を有するキラルらせんポリマー鎖一本の動態イメージング, 第 73 回高分子討論会, 新潟大学, 2024 年 9 月 25–27 日, 口頭発表.
8. 堀 諒雅, 大貫 佑河, 樋口 秀男, 篠原 健一, ポリマー1 分子の直視：レーザートラップ法によるイオン性ポリマー鎖同士の力学計測, 第 73 回高分子討論会, 新潟大学, 2024 年 9 月 25–27 日, 口頭発表.

Grant

JST SPRING: Support for Pioneering Research Initiated by the Next Generation, Grant Number JPMJSP2102.

Acknowledgements

The reported research was conducted under the supervision of Dr. Ken-ichi Shinohara, Area of Materials Chemistry Frontiers, Japan Advanced Institute of Science and Technology (JAIST), spanning the period from 2022 to 2025. I would like to express my heartfelt gratitude to Dr. Ken-ichi Shinohara for his invaluable guidance throughout this research. I would also like to sincerely thank Dr. Hideo Higuchi, New Industry Creation Hatchery Center (NICHe), Tohoku University, for lending me the optical trapping system equipment and guiding me in the experiments. Furthermore, I extend my heartfelt appreciation to Dr. Takashi Kamei, Faculty of Pharmacy, Hokuriku University, and Dr. Takumi Yamaguchi, Area of Bioscience, Biotechnology, and Biomedical Engineering, JAIST, for their significant guidance in advancing the minor research. I am sincerely grateful to Mr. Akio Miyazato, the Center for Nano Materials and Technology, JAIST, for performing the MS measurements; to Mr. Koichi Higashimine for TEM imaging; to Mr. Osamu Notoya for SEM imaging; and to Ms. Kanae Miyashita, Research Center for Advanced Computing Infrastructure, for supporting the molecular dynamics simulations. Additionally, I would like to express my heartfelt gratitude to Dr. Toshiaki Taniike, Dr. Noriyoshi Matsumi, Dr. Masayuki Yamaguchi, and Dr. Tomoyuki Ikai, Graduate School of Engineering, Nagoya University, for their review and advice during the writing of this thesis. This work was supported by JST SPRING, Japan (Grant Number JPMJSP2102). Finally, I would like to thank my family for their financial and emotional support.

Ryoga Hori

Graduated School of Advanced Science and Technology

Japan Advance Institute of Science and Technology

March 2025.